



universität
wien

DISSERTATION

Titel der Dissertation

„Vibrational Properties and Thermodynamical Stabilities of Alloys and Compounds: A First-Principles study“

Verfasser

Mag. David Reith

angestrebter akademischer Grad

Doktor der Naturwissenschaften (Dr. rer. nat.)

Wien, 2011

Studienkennzahl lt. Studienblatt: A 091 411

Dissertationsgebiet lt. Studienblatt: Studium der Naturwissenschaften Physik

Betreuerin / Betreuer: Ao. Univ.-Prof. tit. Univ.-Prof. Dr. Raimund Podloucky

For Samuel Alexander Reith

Kurzfassung

Das grundsätzliche Ziel dieser Arbeit ist es, Materialeigenschaften basierend auf „First Principles“ Rechnungen, d.h. ohne Verwendung empirischer Parameter, zu beschreiben. Dazu wurden insbesondere die aktuellsten Ansätze der Dichtefunktionaltheorie (DFT) verwendet. Besonderes Augenmerk galt auch dem wichtigen Beitrag der Schwingungen zur Freien Energie. Dabei lieferte die Standard DFT die Grundzustandsenergie und die elektronische Struktur bei $T = 0$ K, aus der viele physikalische Eigenschaften einer geordneten Struktur hergeleitet werden können. Hierfür wurde das „Vienna Ab-initio Simulation Package“ (VASP) verwendet. Kräfte, die auf Atome wirken, können mit DFT berechnet werden und in weiterer Folge dazu verwendet werden, um Schwingungseigenschaften, wie Phononenspektren und die Freie Energie der Schwingungen, herzuleiten. In der Praxis wurde dazu das Programm *f*PHON verwendet, eine eigene Adaption von PHON, welches nun auch für allgemeine Kristallstrukturen angewandt werden kann.

Zwei unterschiedliche Materialien wurden genau untersucht, und zwar die Verbindung $\text{Mo}_3\text{Al}_2\text{C}$ und Fe-Cu Legierungen.

Die $\text{Mo}_3\text{Al}_2\text{C}_{1-x}$ Verbindung ist von besonderem Interesse, da diese supraleitende Eigenschaften aufweist, aber die Kristallstruktur keine Inversionsymmetry beinhaltet. Durch Phononenrechnungen wurde festgestellt, dass die Verbindung ohne Kohlenstoffleerstellen dynamisch instabil ist, d.h. um Stabilität zu erreichen muss x größer als 0 sein. Jedoch zeigen die Standard DFT Rechnungen bei $T = 0$ K, dass Kohlenstoffleerstellen energetisch ungünstig sind. Die Berücksichtigung der Freien Energie der Schwingungen in einem thermodynamischem Modell korrigierten dies für die Temperaturen, bei denen die Proben experimentell hergestellt wurden, d.h. die Kohlenstoffleerstellen werden energetisch stabil. Eine Untersuchung des durch Leerstellen herfergerufene „Phonon Softening“ im Zusammenhang mit diesem thermodynamischen Modell erlaubten es, den Bereich, in dem $\text{Mo}_3\text{Al}_2\text{C}_{1-x}$ stabil ist, auf $0.09 < x < 0.14$ einzuschränken. Eine wohl definierte Leerstellenkonzentration ist wichtig für das Verständnis der supraleitenden Eigenschaften, da die Fermiflächen stark von der Kohlenstoffleerstellenkonzentration x abhängig sind.

Kupfer ist ein technologisch wichtiger Härtezusatz zu Stahl. Das Ziel war nun, die Kupferlöslichkeit in Eisen basierend auf „First Principles“ Rechnungen vorherzusagen. Dabei muss erwähnt werden, dass es im gesamten Mischungsbereich keine stabilen Verbindungen gibt. Basierend auf Superzellenrechnungen wurde ein thermodynamisches Modell für isolierte Einzel- und Paar-Atom Defekte entwickelt. Wird der Schwingungsanteil der Freien Energie berücksichtigt, dann erhöht sich die Kupferlöslichkeit in Eisen dramatisch auf Werte, die den experimentellen Ergebnisse gleichen. Dieses Modell ist jedoch nur auf isolierte, nicht interagierende Defekte anwendbar und daher nur für verdünnte Lösungen richtig.

Für ein konzentrationsabhängiges Model des Fe-Cu Phasendiagrammes wurde die „Cluster Expansion“ (CE) Methode, so wie sie im „UNiversal CLuster Expansion“ (UNCLE) Programmpacket implementiert ist, gewählt. Basierend auf einer großen Anzahl von Inputstrukturen, die mit spin-polarisierten DFT berechnet wurden, wurde mit CE die effektiven Clusterwechselwirkungsenergien (ECIs) des dazugehörigen Satzes von Figuren ermittelt. Dies stellte sich wegen der fehlenden Fe-Cu Mischverbindungen als besonders schwierig heraus. Nach Abschluss der CE wurde eine Monte-Carlo (MC) Simulation mit den ECIs und dem dazugehörigen Figurensatz durchgeführt. Dabei wurde die Simulationszelle in zwei Blöcke aufgeteilt, die bei $T = 0$ K aus reinem Eisen und Kupfer bestanden. Unter Berücksichtigung der Temperatur und nach Erreichen des thermodynamischen Gleichgewichtes wurde die Kupferlöslichkeit in Eisen durch Zählen der gelösten Kupferatome im Eisenblock ermittelt. Die so gefundenen Werte stellten sich als viel zu niedrig heraus.

Erneut wurde die Freie Energie der Schwingungen berücksichtigt, indem für jede Inputstruktur die Kraftkonstanten berechnet und die dazugehörigen dynamischen Matrizen diagonalisiert wurden. Dadurch sind die ECIs auch temperatur-abhängig, d.h. es muss bei jeder Temperatur eine eigene CE gemacht werden. Es stellte sich heraus, dass dies massive Konvergenzprobleme verursacht, welches nur durch ein Mitteln der ECIs und Figursätze gelöst werden kann. Dies führt zu einem viel größeren Satz an Figuren als bei der Standard CE. Die Verwendung dieser mittleren Figursätze in der MC resultiert in einer signifikant höheren Kupferlöslichkeit, die den Werten des Defektmodelles gleichen. Diese konzentrations- und temperatur-abhängige CE Studie macht es nun möglich, die Bildung von Kupferausscheidungen richtig zu beschreiben.

Abstract

The fundamental aim of the thesis is to describe properties of solid materials from first-principles without the need of any empirical parameter and with the accuracy of up-to-date density functional theory (DFT) approaches. A particular effort is made to include the most important contribution to the temperature dependent free energy of the material in terms of the vibrational free energy. Standard DFT applications yield the ground state total energy and electronic structure at $T = 0$ K, for which many physical properties of structurally ordered systems are derived. In this work, this was achieved by making use of the Vienna *ab-initio* simulation package (VASP). Forces acting on the atoms can be obtained from DFT calculations which are then used for deriving vibrational properties such as phonon spectra and vibrational free energies. In practice, this was done within the harmonic approximation by applying the program package *f*PHON, which works for general crystal structures. It was developed as part of this thesis by substantially extending the package PHON, which is available on the web.

Two types of material classes were studied in detail, namely the compound $\text{Mo}_3\text{Al}_2\text{C}$ and the Fe-Cu alloy system.

The compound $\text{Mo}_3\text{Al}_2\text{C}_{1-x}$ is of particular interest because it is superconducting but its crystal structure has no centre of inversion. From phonon calculations it was found that it is dynamically unstable without carbon vacancies, i.e. for $x = 0$. Yet, from standard DFT $T = 0$ K supercell calculations it turned out that carbon vacancies are energetically very costly. However, by including the corresponding vibrational free energies in a thermodynamic model at temperatures, at which the experimental samples were fabricated, carbon vacancy formation became favourable. By analysis of the vacancy dependent phonon softening and thermodynamic stability the carbon vacancy concentration range, for which $\text{Mo}_3\text{Al}_2\text{C}_{1-x}$ is dynamically and thermodynamically stable, was derived to be $0.09 < x < 0.14$. A well-defined vacancy concentration is important for understanding the superconducting properties because the Fermi surface strongly depends on x .

Cu enrichment of steel is technologically important for hardening the material. The task for the first-principles theory now is to derive the solubility of Cu in Fe, whereby no thermodynamic stable compound phase exists in the whole composition range. Based on a supercell description for isolated single-atom and pairwise defects a thermodynamic model was developed. When vibrational formation energies were taken into account the solubility of Cu in Fe increased dramatically and the result is in very good agreement to experiment. The described model is limited to non-interacting defects which in practice refers to very dilute concentrations.

For a truly concentration dependent modelling of the Fe-Cu phase diagram the cluster expansion (CE) technique as implemented in the universal cluster expansion (UNCLE)

package was chosen. Based on a large set of spin-polarised DFT calculations as input structures for the CE the effective cluster interaction energies (ECI) and the corresponding set of CE figures were derived. Achieving DFT accuracy for the CE was a particularly difficult task in this case because of the non-miscibility of the Fe-Cu system. After the CE was completed Monte Carlo (MC) simulations were performed, which were initiated by partitioning the simulation cell into two blocks of materials consisting at $T = 0$ K of pure Fe and Cu. Switching on temperature and reaching the thermodynamic equilibrium allows then the determination of the Cu solubility in Fe by counting the number of dissolved Cu atoms in the Fe block. Thereby, it is found that the resulting Cu solubility is far too small.

Again, vibrational free energies were now taken into account by calculating force-constants and diagonalising the dynamical matrix for each of the DFT input structures of the CE. Including temperature dependent vibrational free energies in the CE results in ECI's also becoming temperature dependent. Hence, at each temperature of interest a separate CE needed to be done. This caused severe convergency problems, finally requiring the averaging of figure-sets from different CE's at the same temperature leading to a substantially larger figure-set than typically used for standard CE applications. Applying the averaged figure-sets in MC runs resulted in significantly increased Cu-solubilities, as similarly found with the isolated defect model. With the concentration dependent treatment of the CE the study of the formation of Cu precipitation became possible.

Acknowledgements

At this point I want to take the opportunity to thank all the people without whose support this thesis would not have been possible.

Special thanks and gratitude go to my advisor Raimund Podloucky. Next to his valuable guidance I would like to thank him for the team spirit in the group that exist primarily because of him. I would also like to thank Claudia Blaas-Schenner, her help and support in correcting this thesis have been invaluable.

I wish to thank Markus Stöhr for his moral support and help in understanding the working of cluster expansion and UNCLE. I would also like to thank Tobias Kerscher for supplying me and our group with the latest and newest versions of UNCLE and Stefan Müller for giving our group access to UNCLE.

Furthermore, I want to thank Georg Kresse for the strong support to our group, in particular in providing our group with the latest versions of the VASP code and pseudopotentials.

Special thanks also go to the other group members: Marcel Hieckel, Georg Kastlunger, Mingxing Chen, Martin Leitner, Petr Lazar and René Moser; the discussions with them were of great help. I would like to thank especially Cesare Franchini for his support and friendship.

To my family: I wish to thank my parents for their support over the years and my wife Annabella for her patience and moral support.

To all the family members, friends and people I have neglected in the past year, thank you for your patience and understanding.

Contents

Kurzfassung	i
Abstract	iii
Acknowledgements	v
List of Figures	xi
List of Tables	xix
Abbreviations	xxi
1 Introduction	1
2 Density Functional Theory	5
2.1 Density Functional Theory	7
2.2 Approximations and Implementation	9
3 Lattice Dynamics	11
3.1 Force-Constant Matrix	12
3.2 Equation of Motion	13
3.3 Quantum Mechanical Formulation	15
3.4 <i>Ab-initio</i> Phonon Calculations	18
3.4.1 Force-Constant Method	18
3.4.2 Example: Diamond	21
3.4.3 Supercell Size	27
3.5 Imaginary Frequency	31
3.6 Physical Properties	32
3.6.1 Displacements	32
3.6.2 Density of States	32
3.6.3 Partition Function	34
3.6.4 Free Energy	35
3.6.5 Internal Energy	36
3.6.6 Entropy	37
3.6.7 Specific Heat	37

3.7	Implementation in <i>f</i> PHON	38
4	Isolated Defect Model	41
4.1	Configurational Entropy	42
4.2	Grand Canonical Approach	43
4.3	Solubility	45
5	Cluster Expansion	47
5.1	Theoretical Background	47
5.2	Implementation in UNCLE	51
5.2.1	Genetic Algorithm	52
5.2.2	Monte Carlo	53
5.3	Solubility and Phase Boundaries	55
5.3.1	Grand Canonical Approach	55
5.3.2	Canonical Approach	57
5.3.3	Local Grand Canonical Approach	59
5.4	Temperature Dependent CE	61
6	Mo₃Al₂C: Phonons and Phase stability	65
6.1	Vibrational Properties	66
6.2	Formation Energy	73
6.3	Conclusions	78
7	Fe_{1-x}Cu_x	79
7.1	Bulk Fe and Cu	81
7.1.1	Vibrational Properties	82
7.1.2	Thermal Expansion - Quasiharmonic Approach	84
7.2	Independent Defect Model for Fe-Cu	86
7.2.1	Formation Energies	86
7.2.2	Vibrational Formation Energies	91
7.2.3	Phase diagram	94
7.3	Cluster Expansion	98
7.3.1	Temperature Dependent CE	99
7.3.2	Monte Carlo simulation: Solubility of Cu	105
7.3.3	Supersaturation and Precipitations	106
7.4	Interface Entropy	113
7.5	Conclusion	116
A	Brillouin Zone Sampling	119
B	<i>f</i>PHON Manual	121
B.1	Files used by <i>f</i> PHON	121

B.1.1	INPHON	121
B.1.2	OUTPHON	122
B.1.3	POSCAR	122
B.1.4	SPOSCAR	123
B.1.5	DISP	124
B.1.6	FORCES	124
B.1.7	DYNMAT	125
B.1.8	QPOINTS	125
B.1.9	DOS, DOS.meV and DOS.cm	126
B.1.10	ENTRO	126
B.1.11	FREQ, FREQ.meV and FREQ.cm	127
B.1.12	FPROJ and EIGENPHON	128
B.1.13	HARMONIC	128
B.1.14	DYNPHON	128
B.2	Configuration Options in INPHON	129
B.2.1	MASS	129
B.2.2	RMAX	129
B.2.3	ISYM	129
B.2.4	LHARMONIC	130
B.2.5	INTI and LSYMM	130
B.2.6	Finding Displacements and Constructing Supercells	131
B.2.6.1	LDISP and DISP	131
B.2.6.2	LZFORCE	132
B.2.6.3	IBCELL and NDIM	132
B.2.7	Phonon Density of States, F , U , S and C_V Calculations	133
B.2.7.1	LFREE	133
B.2.7.2	QA, QB, QC and LGAMMA	133
B.2.7.3	TEMPERATURE, LDELAT, TMIN, TMAX, ITSTEP	134
B.2.7.4	DOSIN, DOSEND, DOSSTEP and DOSSMEAR	134
B.2.7.5	IPDOS	134
B.2.8	Calculating the Phonon Dispersion Relation	135
B.2.8.1	IND, INPOINT, LRECIP, QI and QF	135
B.2.8.2	LPFREQ and LDPHON	136
B.2.9	IMOV, ISTEP, TSTEP, IBRANCH and Q	136
B.2.10	LO–TO Splitting	137
B.2.10.1	LBORN	137
B.2.10.2	BORN	137
B.2.10.3	INELEC, RDIELECTRIC and RDIETENSOR	138
B.2.10.4	RESIGMA	138
B.3	Example	139
B.3.1	Dispersion Relation	140
B.3.2	Phonon DOS	141
B.3.3	F, U, S and C_V	142

C Special Points in the First Brillouin Zone	145
C.1 Simple Cubic (sc)	145
C.2 Body-Centred Cubic (bcc)	146
C.3 Face-Centred Cubic (fcc)	147
C.4 Hexagonal and Hexagonal Close-Packed (hcp)	148
C.5 Simple Tetragonal (st)	149
C.6 Body-Centred Tetragonal (bct) and Face-Centred Tetragonal (fct)	150
C.6.1 Body-Centred Tetragonal (bct):	151
C.6.2 Face-Centred Tetragonal (fct):	151
Bibliography	153
List of Publications	159
Talks and Conference Contributions	161
Curriculum Vitae	163

List of Figures

3.1	Sketch illustrating the position of atom κ in unit cell l , with lattice vector $\vec{R}_{l\kappa}$, displacement $\vec{u}_{l\kappa}$ and current position $\vec{r}_{l\kappa}$	11
3.2	Force-field for graphene, due to the displacement of the central atom by $ u = 0.02 \text{ \AA}$ in the direction of the black arrow. The direction of the forces is indicated by arrows which are scaled as well as colour coded according to their magnitude. Supercell boundaries are indicated by the solid lines.	20
3.3	Displacement $\vec{u}_{l\kappa}$ is mirrored by the periodic boundary leading to further three equidistant displacements to the atom on $\vec{R}_{l'\kappa'}$. Thus, the force acting on atom $l'\kappa'$ is overestimated by a factor of four.	21
3.4	A sketch of the diamond structure for which the underlying lattice is face-centred cubic. The primitive unit cell contains two atoms coloured orange at $\vec{R}_{01} = (0, 0, 0)$ and $\vec{R}_{02} = (0.25, 0.25, 0.25)a$. The cartesian coordinates are scaled by lattice constant a . Both atoms have four nearest neighbours, of which three are situated outside the primitive unit cell and are coloured yellow.	22
3.5	First Brillouin zone of a face-centred cubic cell with the high symmetry points and the reciprocal basis B . The coordinates of the high symmetry points are given in direct and cartesian coordinates. The direct coordinates are scaled by factor $2\pi a^{-1}$	26
3.6	The force-field of graphene resulting from the displacement $\vec{u} = 0.02\vec{e}_1 \text{ \AA}$ for a unit cell, for a $2 \times 2 \times 1$ supercell and for a $4 \times 4 \times 1$ supercell are shown in the upper panels. In the lower panel the magnitude of the forces $ F $ as a function of the distance $ R $ from the displaced atom are compared to those of a $6 \times 6 \times 1$ supercell.	28
3.7	The dispersion relation of graphene calculated for a unit cell (green solid lines), for a $2 \times 2 \times 1$ supercell (red dashed-dotted lines), for a $4 \times 4 \times 1$ supercell (blue dashed lines) and for a $6 \times 6 \times 1$ supercell (black solid lines).	29
3.8	The phonon dispersions for diamond calculated with <i>f</i> PHON and VASP using a supercell with 2 atoms (red lines), 16 atoms (blue lines) and 54 atoms (black lines) are compared to experimental values [26] (circles). The phonons were calculated with a displacement of 0.02 \AA	30
3.9	The phonon dispersions for face-centred cubic aluminium calculated with <i>f</i> PHON and VASP using a supercell with 4 atoms (red lines), 8 atoms (blue lines) and 27 atoms (black lines) are compared to experimental values [27] (circles). The phonons were calculated with a displacement of 0.02 \AA	31

3.10	The phonon dispersions for body-centred cubic zirconium is shown as calculated for a supercell with 32 atoms and using a displacement of 0.02 Å. Imaginary frequencies are indicated by negative values.	32
3.11	Phonon density of states (DOS) for face-centred tetragonal indium calculated by <i>f</i> PHON and VASP.	34
3.12	For face-centred tetragonal indium the vibrational free energy F_{phon} (green solid line) is shown in comparison to the vibrational internal energy U_{phon} (blue dotted line) and the vibrational entropy S_{phon} times temperature T (red dashed line). These values were calculated with <i>f</i> PHON and VASP.	35
3.13	Vibrational specific heat C_V of face-centred tetragonal indium, calculated using <i>f</i> PHON and VASP.	37
4.1	Example of the grand canonical potential J' for a $A_{1-x}B_x$ alloy at a given temperature for thermodynamically stable solid solutions at the A-rich and B-rich sides. The common tangent defining the limits of solubility touches J' at x_I and x_{II} , between which the alloy decomposes into a mixture of phases with concentrations x_I and x_{II} , respectively. The thermodynamically stable phase I exists in the range $0 \leq x \leq x_I$, whereas phase II is stable for $x_{II} \leq x \leq 1$	45
5.1	The CE decomposition of the crystal into points, pairs, triplets and many-body figures is illustrated.	48
5.2	The formation enthalpy $\Delta H(x)$ versus the concentration of A-atoms x in A_xB_{1-x} is shown for different structures. The red line represents the ground-state line. Note, that the structure below the ground-state line, marked with a red circle, is an important structure and it has to be included as an additional input structure in the CE.	50
5.3	The standard workflow for the CE is sketched. The formation enthalpies of an initial set of configurations defined by N_{set} input structures calculated with DFT is used for an initial CE. With the fitted set of interaction energies $\{J_f\}$ the enthalpies $\Delta H_{\text{CE}}(\{\sigma\}_{\text{all}})$ of all possible N_{all} configurations (limited by the maximum number of atoms allowed in the structures) are predicted by CE. Configurations predicted to be below the ground-state line defined by the N_{set} input configurations are then identified and the N_{new} structures describing these configurations are calculated with DFT and added to the set of N_{set} input structures. If no new configuration below the ground-state line is found then the CE has converged.	51
5.4	Illustration of the genetic algorithm: In a) an example of crossover is given. Two ‘parent’ solutions marked red and green are used to create a ‘child’ solution. The sketch in b) shows mutation. A random bit in the binary string is flipped into the opposite state.	53

5.5	A standard MC workflow is shown. In the system with state σ the spin of two arbitrary atoms i and j , which have the opposite pseudo spins, is exchanged. If the energy of the new state σ' is lower than the original state, than that state is kept. Otherwise the Boltzmann factor of the energy is calculated and compared to a random number in the range $\{0, 1\}$. If the random number is smaller than the Boltzmann factor, then the new state is kept. If this is not the case the state is discarded and the process is reinitiated.	54
5.6	Sketch of the common tangent method. The effective chemical potential μ , i.e. the derivative of G is a constant in the concentration range where the two phases coexist marked by I + II while it varies in the one phase regions of both phase I and II.	56
5.7	Effective chemical potential of Cu (μ_{Cu}) versus Cu concentration shown for a grand canonical Monte Carlo simulation with 512000 atoms at $T = 1200$ K. The phase boundary is estimated by fitting two lines onto the curve. At the point where these lines intersect an arrow indicates the phase boundary between the Fe phase and the Fe+Cu phase.	57
5.8	Concentration of Cu dissolved (red diamonds), Cu in precipitate (green circles) and enthalpy ΔE (blue squares) plotted versus T for a canonical MC simulation with $x = 1$ at. % of Cu in the simulation cell.	58
5.9	Sketch of the metastability problem. If the simulation cell with $x = 1$ at. % is cooled below the correct phase boundary (black solid line) the Cu atoms stay in solution, as shown by the simulation cell cross-section in the insets where only the Cu atoms are indicated by red squares, since the formation of a stable Cu precipitate needs a larger computational timespan. This results in a overestimation of the Cu solubility.	59
5.10	Cross sections along $[111]$ of the simulation cell with Fe atoms coloured in black and Cu in red. The initial setup (i.e. one slab Cu and one slab Fe) is brought to thermodynamical equilibrium. The volume used to determine the concentration of dissolved Cu (i.e Cu solubility in Fe) is indicated by the two green lines.	60
5.11	Cu solubility in bcc Fe calculated from figure-sets of twenty separate CE's (blue crosses) compared to results using a merged figure-set (red diamonds and dotted line).	62
6.1	Properties of $\text{Mo}_3\text{Al}_2\text{C}$. Panel a): crystal structure; panel b): experimental electrical resistivity (yellow circles) [55]. Inset in panel b) sketches the pressure dependency of conducting transition temperature T_c	67

6.2	Vibrational properties of $\text{Mo}_3\text{Al}_2\text{C}_x$ with $x \leq 1$, i.e. vacancies on the C sublattice. In panel a) for $\text{Mo}_3\text{Al}_2\text{C}$ the calculated phonon dispersion derived from the displaced-atoms force-constant method (black line) is compared to a calculations with force-constants derived from linear response (red line). In panels b), c) and d) the dispersion relation, as calculated directly from the displaced-atoms force-constants, are presented for $\text{Mo}_3\text{Al}_2\text{C}_{0.96875}$, $\text{Mo}_3\text{Al}_2\text{C}_{0.875}$ and $\text{Mo}_3\text{Al}_2\text{C}_{0.75}$, respectively. It should be noted, that the paths in reciprocal space are different, because for $\text{Mo}_3\text{Al}_2\text{C}_{0.875}$ a $2 \times 1 \times 1$ simple tetragonal supercell has been used but for the other cases a $1 \times 1 \times 1$ or a $2 \times 2 \times 2$ simple cubic supercell.	69
6.3	Carbon vacancy concentration x versus the frequency of the lowest optical mode at Γ	70
6.4	Panels a) and b) prsent the dispersion relation, as derived from the displaced-atoms force-constant method for $\text{Mo}_{2.75}\text{Al}_2\text{C}_1$ and $\text{Mo}_3\text{Al}_{1.75}\text{C}_1$	70
6.5	Vacancies on the C sublattice: Phonon DOS (black solid line) and the partial phonon DOS of Mo (purple dashed line), Al (green dotted line) and C (blue dashed-dotted line) are shown in panels a), b), c) and d) for $\text{Mo}_3\text{Al}_2\text{C}$, $\text{Mo}_3\text{Al}_2\text{C}_{0.96875}$, $\text{Mo}_3\text{Al}_2\text{C}_{0.875}$ and $\text{Mo}_3\text{Al}_2\text{C}_{0.75}$, respectively. In the inset the total DOS at low frequencies is compared to a Debye-like ω^2 behaviour (red dashed line).	72
6.6	Vacancies on the Mo or Al sublattice: Phonon DOS (black solid line) and the partial phonon DOS of Mo (purple dashed line), Al (green dotted line) and C (blue dashed-dotted line) are shown in a)for $\text{Mo}_{2.75}\text{Al}_2\text{C}_1$ and in b) for $\text{Mo}_3\text{Al}_{1.75}\text{C}_1$. The inset compares the increase of the total DOS at low frequencies is compared to a Debye-like ω^2 behaviour (red dashed line).	73
6.7	Total vacancy formation energy (sum of the DFT ε and vibrational f formation energies) versus temperature for a Mo vacancy (purple dashed line), an Al vacancy (green dotted line) and a C vacancy (blue dashed-dotted line) in a unit cell ($1 \times 1 \times 1$ supercell). Also the result for a carbon vacancy in a $2 \times 1 \times 1$ supercell is shown (red solid line).	75
6.8	Total vacancy formation energy, $\varepsilon + f(T)$, times carbon vacancy concentration x versus x at temperatures of 1250°C (blue diamond) and 1500°C (red circles). The dashed lines (blue for 1250°C and red for 1500°C) are obtained by parabolic interpolation between the calculated data.	76
6.9	Temperature dependent carbon vacancy concentration plotted as a solid red line. Experimental preparation temperatures are indicated as dashed black lines. The critical carbon vacancy concentration, below which the structure becomes dynamically unstable, is shown by a green dash-dotted line, while the carbon vacancy concentrations of the calculated supercells are drawn as blue dotted lines.	77
7.1	Atom probe microscope image as derived by Harald Leitner and Michael Schober at the Montan University of Leoben of Cu precipitates in Fe after the alloy has been annealed for 500000 seconds at 773 K	79

7.2	Change in hardness versus time at $T = 773$ K for $\text{Fe}_{1-x}\text{Cu}_x$, $x = 1.17$ at.%. Experimental data of Ref. [60].	80
7.3	DFT total energies E_{DFT} (PBE parametrisation) for Fe and Cu as a function of volume V , whereby the energy zero corresponds to the minimum of E_{DFT} . The ground states are bcc ferromagnetic (FM) Fe and fcc Cu. Left panel: results for Fe bcc and fcc non-spinpolarised (NM), antiferromagnetic (AFM) and ferromagnetic (FM). Right panel: results for fcc and bcc Cu.	81
7.4	Phonon dispersion for bcc FM Fe along some high symmetry directions. DFT results (black line) for the equilibrium lattice parameter at $T = 0$ K, $a_0 = 2.831$ Å are compared to experiment [69] (circles), as measured at $T = 296$ K. A further DFT calculation was made for $a = 2.841$ Å (red line), corresponding to the DFT derived thermal expansion at $T = 296$ K. For details see text.	83
7.5	Phonon dispersion relation for fcc Cu along high-symmetry paths. DFT results (black line) are compared to experiment measured at $T = 49$ K [74] (circles).	83
7.6	Differences $\Delta g(E) = g_{a_0}(\omega) - g_a(\omega)$ of normalised phonon DOS of fcc Cu. Blue dotted line: result for the lattice constant $a = 3.622$ Å; red dashed line: $a = 3.650$ Å. The inset shows the phonon DOS for the $T = 0$ K equilibrium lattice constant of $a_0 = 3.636$ Å.	85
7.7	Volume dependent DFT total energy $E_{\text{DFT}}(a)$ (black solid line) and the total free energy $F_{\text{tot}}(a, T) = E_{\text{DFT}}(a) + F_{\text{phon}}(a, T)$ (dashed lines) for $T = 100$ K, 250 K, 300 K and 350 K vs. the lattice parameter a . For each curve the lattice constant at minimum energy is indicated by a red dot. The energy zero coincides with the minimum of $E_{\text{DFT}}(a_0)$	85
7.8	DFT derived thermal expansion of Fe (red solid line) in comparison to experiment [79] (black circles and dashed line). The Curie temperature T_C is indicated by an arrow.	86
7.9	DFT derived thermal expansion of Cu. Present study: blue solid line; other calculation [78]: magenta dotted line; experiment [80]: black circles and dashed line.	87
7.10	Phonon free energies for temperature dependent equilibrium parameters $a(T)$, $F_{\text{phon}}(a(T), T)$ (solid lines) are compared to $F_{\text{phon}}(a_0, T)$ (dashed lines) for both Fe (red and orange) and Cu (dark blue and light blue). The lattice parameter a_0 corresponds to the DFT minimum.	88
7.11	Differences Δg of normalised phonon DOS for substitutional Cu defects in comparison to pure bcc Fe: single-atom Cu defect (yellow dashed line) and pair-wise Cu defect (red solid line). The phonon DOS for bcc Fe is shown in the inset.	92
7.12	Differences Δg of normalised phonon DOS for substitutional Fe defects in comparison to pure fcc Cu: single-atom Fe defect (turquoise dashed line) and pair-wise Fe defect (blue solid line). The phonon DOS for bulk fcc Cu is shown in the inset.	93

7.13	Temperature dependence of changes of differences of vibrational free energies $f(T)$ (see Eq. 7.6). Defects in bcc Fe: single Cu atom (yellow dashed line) and pairs of Cu atoms (red solid line); defects in fcc Cu: single Fe atom (turquoise dashed line) and pairs of ferromagnetic Fe atoms (blue dashed-dotted line). The plotted values for pair-wise defects correspond to the vibrational defect energy of the two atoms (not divided by 2).	94
7.14	Phase diagram of the Fe-Cu system at the Fe-rich and Cu-rich side. Panel a: Comparison between the experimental data of Ref. [62] (black solid line) to the calculations including the vibrational energy according to Eq. 4.10. Hatched areas: regions of metastable phases. The upper boundaries of the hatched areas mark the thermodynamically stable phase boundaries. Panel b: Analysis the calculated results for the thermodynamically stable phase boundaries. Without vibrational energies: dashed lines, with vibrational energies: full lines. Results for single and both (single and pair-wise) defects at the Fe-rich side are shown in yellow and red colours, correspondingly. On the Cu-rich side only the results for both (or rather pair-wise) defects are shown (blue colour), because the effect of single defects is hardly visible.	95
7.15	Enthalpy of formations vs. atomic fraction x of the $\text{Fe}_{1-x}\text{Cu}_x$ alloy system. Comparison of DFT input values (green squares) to CE predictions (black crosses). The random mixing energy of this work (dashed black line) is compared to a CE of Liu <i>et al.</i> [63] (blue circles). The averaging is done over all 8 atom unit cell structures with a bcc parent lattice.	99
7.16	Magnetic moment per atom versus Cu concentration x for $\text{Fe}_{1-x}\text{Cu}_x$. . .	100
7.17	Enthalpy of formation ΔH as derived from temperature dependent CE by taking into account vibrational free energies, representation similar to Fig. 7.15. The percentage of imaginary frequency indicates how much of the total vibrational spectrum is affected by the non-vibrational modes. . .	101
7.18	Frequency of imaginary modes occuring in Fig. 7.17.	102
7.19	Temperature dependency the cross validation score $S_{\text{CV}}(T)$. At each temperature several figure-sets with varying $S_{\text{CV}}(T)$ are obtained. Average of $S_{\text{CV}}(T)$ indicated by solid line.	102
7.20	Effective cluster interaction energies \bar{J} of the merged figure-set for $ \bar{J} > 5$ are shown for the cases without and with vibrational free energies for $T = 600$ K and 1200 K. The vertex-vertex v distance is given in multiples of the lattice constant a , i.e. the correct distance of the pair figures is described by $d_{\text{pair}} = 2v$	104
7.21	Pair figure ECI's of the merged figure-set \bar{J} versus temperature up to the sixth nearest neighbour pair interactions.	106
7.22	Random mixing energies without and with vibrational free energies for temperatures $T = 0$ K (no phonons), 5 K, 300 K, 600 K, 900 K and 1200 K.	107

7.23	Cross-sections of the simulation box the in [111] direction with and without vibrational contributions as well as the layer concentration of Cu at the $T = 900$ K, 1050 K and 1200 K. The Fe atoms are coloured black and Cu atoms red. Area (volume) in which the Cu atoms were counted is marked by two green lines (planes).	108
7.24	Fe-Cu phase diagram at the Fe-rich side: CALPHAD according to Landolt and Börnstein [62] (black solid line); CE results with vibrational contributions (red dashed line and diamond) and without the (blue dashed line and triangle). Independent defect model indicated by (orange solid line).	109
7.25	Cu distribution in a $50 \times 50 \times 50$ simulation cell with $x = 3$ at.% at $T = 800$ K is shown at different MC steps. The initially randomly distributed Cu atoms (red spheres) coalesce into Cu precipitates as time progresses.	111
7.26	Panel a) plots the concentration of dissolved Cu atoms in the Fe-matrix and the concentration of Cu atoms in precipitates as well as the the energy change per atom versus MC steps. In panel b) the change in average precipitate size and its standard deviation and the number of precipitates are shown. In the 'time' regions distinguished by I, II and III a nucleation and two separate Ostwald ripening processes, a fast and a slow one, are shown.	112
7.27	Entropy versus temperature calculated using CE without vibrational free energy (blue diamonds and blue dotted line) and with vibrational free energy (red circles and red dotted line) compared to values calculated using the isolated defect model without vibrational free energy (blue dashed line) and with (red dashed line). The inset gives the difference $S_{\text{intf}} = S_{\text{CE}} - S_{\text{def}}^{\text{av}}$ for both, without (blue line) and with (red line) vibrational free energy. The black dashed-dotted line extrapolates the values for the case with vibrational free energy assuming that it has a similar behavior to the one without.	115
B.1	Phonon dispersion relation for $\text{D0}_3 \text{Fe}_3\text{Al}$.	141
B.2	Density of states for $\text{D0}_3 \text{Fe}_3\text{Al}$.	142
B.3	Vibrational free energy F , internal energy U and entropy times temperature $-k_B T S$ for $\text{D0}_3 \text{Fe}_3\text{Al}$.	143
B.4	Specific heat C_V for $\text{D0}_3 \text{Fe}_3\text{Al}$.	143

List of Tables

3.1	Conversion factors for phonons.	33
6.1	Physical properties of $\text{Mo}_3\text{Al}_2\text{C}$	66
6.2	Formation energies for vacancies in $\text{Mo}_3\text{Al}_2\text{C}$ for $1 \times 1 \times 1$ and $2 \times 1 \times 1$ unit cells without vibrational contributions (DFT T=0 only), adding $f^X(T)$, and finally completing with the configurational entropy $S_{\text{conf}}(c_X) = -[c_X \ln(c_X) + (1 - c_X) \ln(1 - c_X)]$ at temperatures of 1250°C and 1500°C.	74
7.1	Results of several VASP and <i>flair</i> calculations and experimental data for ground state properties of bcc Fe and fcc Cu: lattice parameter a_0 , total magnetic moment M and bulk modulus B . PAW: projected augmented wave pseudopotentials, USPP: ultrasoft pseudopotentials. GGA parametrisations of the exchange-correlation functionals according to Ref. [12] (PBE) and Ref. [67] (PW91).	82
7.2	Formation energy per atom for the single atom defect, ε^{X_1} , and pair-wise substitutional defects, $\varepsilon^{X_2}/2$ per atom for Cu in bcc Fe and Fe in Cu. All geometrical parameters are relaxed.	89
7.3	DFT derived formation energy of one Cu defect in bcc-Fe, $\varepsilon^{\text{Cu}_1}$, for several test cases for 16 and 64 atoms supercells. The corresponding defect energy of Fe in fcc Cu, $\varepsilon^{\text{Fe}_1}$, was calculated only for a 64 atom supercell. Results are shown for no relaxation, relaxation of atomic positions, as well as relaxation of volume and positions. Several \vec{k} -point sets were also tested, the number given is the total number of all \vec{k} -points in the BZ. A comparison with the data of Ref. [64] is made for the calculations of $\varepsilon^{\text{Cu}_1}$ with a supercell of 16 atoms. Abbreviations for potentials and methods are given as in Table 7.1	90
7.4	Temperature dependence of the differences of vibrational free energy, f^{X_1} and $f^{X_2}/2$, according to Eq. 7.6.	91
7.5	Relative distribution of one atom and pair-wise defects (in % of x) at 800 K and 1200 K, and the corresponding total concentration x of the solute species.	94
7.6	Cross validation score $\bar{S}_{\text{CV}}(T)$ averaged over twenty figure-sets for CE's without the vibrational contributions and with vibrational contributions at 600 K, 900 K and 1200 K.	103
7.7	Mean solubility of Cu $\bar{c}_{\text{Cu}}(F)$ as derived from 20 individual CE fits in comparison to the value $c_{\text{Cu}}(\bar{F})$ corresponding to the merged figure-sets.	107

7.8	Estimated interface entropy S_{intf} versus temperature without and with vibrational free energy ($\Delta f(T)$). The value in the bracket is given under the assumption that the interface entropy with vibrational free energy increases continuously.	114
-----	---	-----

Abbreviations

QM	Q uantum M echanics
DFT	D ensity F unctional T heory
CE	C luster E xpansion
MC	M onte C arlo
CALPHAD	C ALculation of P HAse D iagrams
VASP	V ienna A b-initio S imulation P ackage
UNCLE	U Niversal C Luster E xpansion code
<i>f</i> PHON	full-symmetry P HON
LDA	L ocal D ensity A pproximation
GGA	G eneralised G radient A pproximation
PBE	GGA, parametrisations according to P erdew, B urke and E rnzerhof
PAW	P rojector A ugmented W ave
USPP	U ltra S oft P seudo P otentials
NM	N on M agnetic
FM	F erro M agnetic
AFM	A nti F erro M agnetic
DOS	D ensity O f S tates
BZ	first B rillouin Z one

Chapter 1

Introduction

The fundamental aim of the thesis is to describe properties of solid materials from first-principles without the need of any empirical parameter and with the accuracy of up-to-date density functional theory (DFT) approaches. A particular effort is made to include the most important contribution to the temperature dependent free energy of the material in terms of the vibrational free energy. Standard DFT applications yield the ground state total energy and electronic structure at $T = 0$ K, for which many physical properties of structurally ordered systems are derived.

In this thesis, this was achieved by making use of the Vienna *ab-initio* simulation package (VASP). Forces acting on the atoms are obtained from DFT calculations which are then used for deriving vibrational properties such as phonon spectra and vibrational free energies. In practice, this was done within the harmonic approximation by applying the program package *f*PHON, which works for general crystal structures. It was developed as part of this thesis by extending the package PHON.

Two types of material classes were studied in detail, namely the ordered compound $\text{Mo}_3\text{Al}_2\text{C}_{1-x}$ and the Fe-Cu alloy system.

The compound $\text{Mo}_3\text{Al}_2\text{C}_{1-x}$ is of particular interest because it is superconducting but its crystal structure has no centre of inversion. Obviously, the phonon dispersion and in particular soft modes are searched for to get a hint about the superconducting mechanism. On the other hand, carbides and carbid-like compounds are known to have vacancies on the carbon sublattice. Therefore, also thermodynamical stabilities are of importance, for which the vibrational free energy is essential.

Cu enrichment of steel is technologically important for hardening the material. The task for the first-principles theory now is to derive the solubility of Cu in Fe, whereby no thermodynamic stable compound phase exists in the whole composition range. Because the concentration of Cu in Fe (which is the most interesting case for these alloys) is rather

small, modelling the solubility by isolated defects seems reasonable and therefore will be applied as a first step.

For a truly concentration dependent modelling of the Fe-Cu phase diagram the cluster expansion (CE) technique as implemented in the universal cluster expansion (UNCLE) package was chosen. Standard CE applications are done for alloy system with stable ordered phases, which is not the case for Fe-Cu alloys. The major task will be to include vibrational free energies for generating the effective cluster interactions (ECI's). In doing this, the ECI's will become temperature dependent which means that for each temperatures a different CE has to be done.

To the knowledge of the author first-principles studies of an alloy system in such a temperature dependent manner are rather rare.

Chapter 2 provides a short overview about the underlying fundamental theory, the density functional theory (DFT) and its application in the Vienna *ab-initio* simulation package (VASP) [1–4].

Continuing with chapter 3 a thorough theoretical discussion about modelling of vibrational properties within the harmonic approximation is given. For the calculations the direct force-constant matrix is used which relies on the forces as derived from DFT. The described method is implemented in the program *f*PHON, which is an extension of the package PHON of D. Alfè's [5, 6] PHON.

For describing solubility of dilute alloys in terms of isolated defects, DFT supercell energies at $T = 0$ K and temperature dependent vibrational free energies are combined within a thermodynamical model elaborated in chapter 4. A general description of the configurational entropy for single and pair-wise defects was developed, which was then used to construct a grand canonical potential.

Chapter 5 introduces the cluster expansion (CE), for which the universal cluster expansion (UNCLE) code [7, 8] is applied. The standard CE approach is extended to include vibrational free energies for each of the DFT input structures which results in temperature dependent ECI's.

In chapter 6 the vibrational and thermodynamical stabilities of the superconducting carbide $\text{Mo}_3\text{Al}_2\text{C}_{1-x}$ are discussed.

Finally, in chapter 7 the results of the *ab-initio* calculations for the Fe-Cu alloy are discussed in great detail elaborating on the difficulties caused by including vibrational free energies.

Appendix A overviews to the most widely used scheme for Brillouin zone sampling. A manual for applying the program package *f*PHON is given in the appendix B and the

special points in the first Brillouin Zone for a selection of crystal structures are found in appendix [C](#).

Chapter 2

Density Functional Theory

The time-independent non-relativistic Schrödinger equation for the groundstate (GS) is defined by

$$\hat{H} \Psi_{\text{GS}}(\vec{X}_1 \dots \vec{X}_{N_e}, \vec{R}_1 \dots \vec{R}_{N_n}) = \bar{E}_{\text{GS}} \Psi_{\text{GS}}(\vec{X}_1 \dots \vec{X}_{N_e}, \vec{R}_1 \dots \vec{R}_{N_n}) \quad (2.1)$$

for a many-body system consisting of N_e electrons and of N_n nuclei, where the positions of the atomic nuclei are defined by \vec{R}_k , and the electronic coordinates are defined by $\vec{X}_j(\vec{x}_j, s_j)$ comprising both, spin s_j and position \vec{x}_j . The Hamiltonian is built up according to

$$\hat{H} = \hat{T}_e + \hat{V}_{ee} + \hat{T}_n + \hat{V}_{nn} + \hat{V}_{en} . \quad (2.2)$$

The different terms are the the electronic kinetic energy

$$\hat{T}_e = -\frac{\hbar^2}{2m} \sum_{j=1}^{N_e} \nabla_j^2 , \quad (2.3)$$

the electronic Coulomb interaction

$$\hat{V}_{ee} = \frac{1}{2} \sum_{j=1}^{N_e} \sum_{k=1}^{N_e} \frac{e^2}{|\vec{X}_j - \vec{X}_k|} , \quad (2.4)$$

the kinetic energy of the nuclei

$$\hat{T}_n = -\frac{\hbar^2}{2} \sum_{l=1}^{N_n} \frac{\nabla_l^2}{M_l} , \quad (2.5)$$

the nuclei-nuclei interaction

$$\hat{V}_{\text{nn}} = \frac{1}{2} \sum_{l=1}^{N_n} \sum_{m=1}^{N_n} \frac{Z_l Z_m e^2}{|\vec{R}_l - \vec{R}_m|} , \quad (2.6)$$

and the electron-nuclei Coulomb interaction

$$\hat{V}_{\text{en}} = -\frac{1}{2} \sum_{l=1}^{N_n} \sum_{j=1}^{N_e} \frac{Z_l e^2}{|\vec{R}_l - \vec{X}_j|} . \quad (2.7)$$

The mass of the electrons is defined by m while that of nucleus i is given by M_i , and its charge by Z_i . The ground state energy eigenvalue \bar{E}_{GS} is the lowest of the eigenvalue spectrum of the Hamiltonian and gives the total ground state energy of the system of electrons and nuclei. If, as usual the Born-Oppenheimer approximation is assumed the motion of the nuclei can be taken out from the Hamiltonian and the ground state total energy of the system is written as

$$\bar{E}_{\text{GS}} =: E_{\text{GS,tot}} = E_{\text{GS}} + V_{\text{nn}} , \quad (2.8)$$

where E_{GS} is now the ground state total energy of the electronic system and V_{nn} is the Coulomb energy of the nuclei-nuclei interaction. It should be noted that the Hamiltonian for deriving E_{GS} still contains the Coulomb interaction between electrons and nuclei, \hat{V}_{ne} . This is called in the phraseology of density functional theory the external potential. The electronic wavefunctions must obey Pauli's exclusion principle, i.e. being antisymmetric about exchanging electrons, and further must fulfill the normalisation condition

$$\langle \Psi | \Psi \rangle = 1 . \quad (2.9)$$

Here and later on one is only interested in the ground state of the system. Schrödinger's equation for the ground state can now be reformulated in terms of a variational principle making use of the total energy as a functional of Ψ ,

$$E[\Psi] = \langle \Psi | \hat{H} | \Psi \rangle , \quad (2.10)$$

under the constraint of the normalisation condition in Eq. 2.9 introducing a Lagrangian multiplier. This, after minimisation will become the ground state energy eigenvalue \bar{E}_{GS} . The variational principle requires that

$$E[\Psi_{\text{GS}}] \leq E[\Psi] , \quad (2.11)$$

with Ψ_{GS} for the ground state wavefunction. The ground state energy describing the minimum of the functional is defined by,

$$\bar{E}_{\text{GS}} = \min E[\Psi] . \quad (2.12)$$

2.1 Density Functional Theory

From the ground state wavefunction a ground state density for the electronic system

$$\rho_{\text{GS}}(\vec{X}) = \int \Psi_{\text{GS}}(\{\vec{X}_i\}) d\vec{X}_1 \dots \vec{X}_{N_e-1} \quad (2.13)$$

is integrated out fulfilling the condition of classical electronic density by

$$\int \rho_{\text{GS}}(\vec{X}) d\vec{X} = N_e , \quad (2.14)$$

whereby the integration also includes the summation over the spin coordinates.

The original concept of Hohenberg and Kohn's [9] density functional theory (DFT) was to replace the ground state functional of Eq. 2.10 and its minimisation by

$$E_{\text{GS}} := E[\rho_{\text{GS}}] = \min E[\rho] . \quad (2.15)$$

The total energy of the ground state is derived from an energy functional of the density ρ under the constraint of Eq. 2.14, instead of the many-body wavefunction Ψ . After mastering all problems concerning uniqueness a direct equation for the ground state density is derived. However, it turns out to be useless for deriving a quantitative useful ground state density and thus the ground state total energy for realistic atomic systems. Immediately following the publication of the original DFT the concept of Kohn and Sham was presented [10], in which a step backwards is made towards a wavefunction-like concept. This is done by introducing single particle like wave functions defined by,

$$\rho_{\text{GS}}(\vec{X}) = \sum_i \phi_i^*(\vec{X}_i) \phi_i(\vec{X}_i) , \quad (2.16)$$

i.e. the orbitals ϕ_i build up the true ground state density $\rho_{\text{GS}}(\vec{X})$. This requirement is, strictly speaking, the only physical meaning of the Kohn-Sham orbitals ϕ_i . In other words, one searches for a fictitious system of independent quasi-particles described by the orbitals ϕ fulfilling Eq. 2.16. The total energy functional as utilised in Eq. 2.15 is replaced by functional $E[\{\phi_i\}]$. Again, its uniqueness and existence had to be proven, which resulted in a vast amount of studies and publications. Searching for the ground

state total energy by minimizing the functional $E[\{\phi_i\}]$ under the constraint

$$\int \rho_{\text{GS}}(\vec{X}) d\vec{X} = \sum_i \int \phi_i^*(\vec{X}_i) \phi_i(\vec{X}_i) d\vec{X} = N_e \quad (2.17)$$

leads to the renowned Kohn-Sham equations

$$\hat{h}_{\text{KS}}\phi_i = \epsilon_i\phi_i \quad (2.18)$$

which appear to be Schrödinger-like equations for single, or rather, quasi particle like states. The Kohn-Sham Hamiltonian

$$\hat{h}_{\text{KS}}\phi_i = -\frac{\hbar^2}{2m}\nabla^2 + V_{\text{eff}} \quad (2.19)$$

consists of a single-particle kinetic energy and an effective potential, which at a first glance looks like a local quantity only dependent on the coordinates \vec{X} . It is however obvious, that if the Kohn-Sham equations express the correct physics then V_{eff} must also contain all non-local interactions. In particular, the interactions due to the exchange and correlation properties of the many-body electronic system. The big technical advantage of single-particle equations like the Kohn-Sham equation (Eq. 2.18) is, that there exists a vast experience pool to numerically solve these types of self-consistent equations very efficiently. Of course, the crucial point for deriving quantitatively useful results is how well the many-body exchange-correlation interactions can be approximated as discussed later on.

The effective potential

$$V_{\text{eff}}(\vec{X}) = V_{\text{ext}}(\vec{X}) + V_{\text{coul}}(\rho_{\text{GS}}) + V_{\text{xc}} \quad (2.20)$$

consists of the classical external potential $V_{\text{ext}}(\vec{X})$ (i.e. the Coulomb electron-nuclei interactions), the classical Coulomb interaction of the electron density $V_{\text{coul}}(\rho_{\text{GS}})$ and the exchange correlation potential

$$V_{\text{xc}} = \frac{\delta E_{\text{xc}}[\rho]}{\delta \rho}, \quad (2.21)$$

which is a functional derivative of the unknown exchange-correlation functional $E_{\text{xc}}[\rho]$. Once the Kohn-Sham equations are solved self-consistently the two fundamental quantities of density functional theory, the ground state density ρ_{GS} and consequently the

ground state total energy

$$E_{\text{GS}} = \sum_i \epsilon_i - \frac{1}{2} \int \frac{\rho_{\text{GS}}(\vec{X}) \rho_{\text{GS}}(\vec{X}')}{|\vec{r} - \vec{r}'|} d\vec{X} d\vec{X}' + E_{\text{xc}}[\rho_{\text{GS}}] - \int V_{\text{xc}}[\rho_{\text{GS}}] \rho_{\text{GS}}(\vec{X}) d\vec{X} \quad (2.22)$$

can be derived (see Ref. [11]). Due to the Born-Oppenheimer approximation the total energy E_{GS} describes the potential energy $E_{\text{GS}}(\{\vec{R}_i\})$ with respect to the positions of the nuclei, i.e. the positions of the nuclei are fixed when minimizing the electronic state. Therefore, the force \vec{F}_i acting on atom i is defined as

$$\vec{F}_i := \vec{F}(\vec{R}_i) = - \frac{\partial E_{\text{GS}}(\vec{R}_1 \dots \vec{R}_{N_n})}{\partial \vec{R}_i} . \quad (2.23)$$

2.2 Approximations and Implementation

For the actual calculations the unknown exchange correlation functional E_{xc} for a realistic many-body system of interacting electrons and nuclei has to be approximated. In practical terms the success of any formal theory depends firstly on how well \hat{E}_{xc} can be approximated and secondly on how the formal machinery can be cast into an efficient computer code.

Concerning the first point, in this work the two most common local or semi-local approximations are applied the local density approximation (LDA) and its extended version the general gradient approximation (GGA). Within LDA the exchange-correlation energy is expressed in terms of the exchange-correlation energy $\epsilon_{xc}(\rho)$ per particle in the homogenous free electron gas,

$$E_{\text{xc}}^{\text{LDA}}[\rho] = \int \rho(\vec{X}) \epsilon_{\text{xc}}(\rho) d\vec{X} . \quad (2.24)$$

Within GGA the local expression are extended by including the density gradient in the functional,

$$E_{\text{xc}}^{\text{GGA}}[\rho, \nabla \rho] . \quad (2.25)$$

It is well known, that LDA suffers from over binding effects for bulk systems with smaller nuclear charges (e.g. the 3d-transition metal elements) or for surfaces in general. There the assumption of the charge density being comparable to an homogeneous electron gas is much worse than in the bulk. In such cases GGA solves most of the problems but is less accurate for bulk systems with large nuclear charges such as the 5d-transition metal elements. Therefore, a proper selection of the many-body approximation for the actual

calculations has to be made. This is sometimes not straightforward. Strictly speaking, due to the choice between either LDA or GGA the calculations are not truly *ab-initio*. On the other hand, for the actual calculations in this work only these two choices are made for the whole periodic table and the results are very or reasonably accurate for a wide class of materials. Of course, there exists a range of materials and properties at which these rather simple and computationally costless LDA and GGA approximations fail in some respects. These are strongly correlated systems (e.g. 3d-transition metal oxides), gap sizes in general (which is a more fundamental DFT problem), and van-der-Waals bonding. Cures to these problems exist, at least partially, but are computationally very demanding and on the forefront of research and code development.

For the actual calculations in this work the GGA parametrisation of Perdew, Burke and Ernzerhof (PBE) [12] was chosen.

The second crucial point for the *ab-initio* calculation of physical properties of large systems is the computational machinery, which largely depends on the choice of basis functions, i.e. the Kohn-Sham orbitals. For such orbitals in three-dimensional periodic systems plane waves are ideal candidates if the construction of pseudopotentials can be mastered. Relying on the projector-augmented wave (PAW) description of Blöchl [13] flexible and trustable pseudopotentials can be designed [4] which seem to work for all valence atomic orbitals (including 3d and 4f orbitals) if constructed and tested carefully. This fundamental requirement is the backbone of one of the most powerful DFT (and post-DFT) computer code, the Vienna *ab-initio* simulation package (VASP) as developed by G. Kresse and his group [1–4]. The reader who is interested in details and applications of this code is referred to the VASP manual [14]. With the VASP code, bulk and surface systems (in terms of a repeated slab) with up to 200-300 atoms can be studied with fully optimised atomic geometries. Of particular importance for the present work, which focusses on vibrational properties, is the possibility to reliably calculate the force for such large systems.

Chapter 3

Lattice Dynamics

In the crystal atom κ vibrates around its equilibrium position $\vec{R}_{l\kappa} = \vec{R}_l + \vec{\tau}_\kappa$, i.e. the sum of the Bravais lattice vector \vec{R}_l pointing at unit cell l and the basis vector $\vec{\tau}_\kappa$ pointing at atom κ in that cell. It is displaced from this equilibrium position by a displacement $\vec{u}_{l\kappa}$, and therefore its current position $\vec{r}_{l\kappa}$ is given by

$$\vec{r}_{l\kappa} = \vec{R}_{l\kappa} + \vec{u}_{l\kappa}, \quad (3.1)$$

as illustrated in Fig. 3.1. The index l denotes the unit cell in which the atom κ is positioned, whereby $l = 0, \dots, (C - 1)$ and $\kappa = 1, \dots, N$, where C describes the total number of unit cells and N the number of atoms per unit cell.

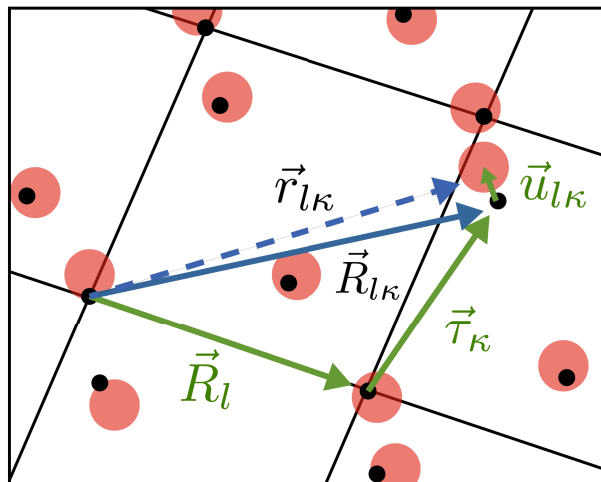


FIGURE 3.1: Sketch illustrating the position of atom κ in unit cell l , with lattice vector $\vec{R}_{l\kappa}$, displacement $\vec{u}_{l\kappa}$ and current position $\vec{r}_{l\kappa}$.

Assuming that the displacements $\vec{u} = \{\vec{u}_{l\kappa}, \vec{u}_{l'\kappa'}, \vec{u}_{l''\kappa''}, \dots\}$ are sufficiently small the corresponding total energy E of the crystal is expanded in a Taylor series at the equilibrium position $\vec{u} = 0$,

$$\begin{aligned}
 E(\vec{u}) = & E_0 + \sum_{l\kappa,\alpha} u_{l\kappa,\alpha} \left. \frac{\partial E_0}{\partial u_{l\kappa,\alpha}} \right|_{\vec{u}=0} + \frac{1}{2} \sum_{l\kappa,\alpha} \sum_{l'\kappa',\beta} u_{l\kappa,\alpha} u_{l'\kappa',\beta} \left. \frac{\partial^2 E_0}{\partial u_{l\kappa,\alpha} \partial u_{l'\kappa',\beta}} \right|_{\vec{u}=0} \\
 & + \frac{1}{6} \sum_{l\kappa,\alpha} \sum_{l'\kappa',\beta} \sum_{l''\kappa'',\gamma} u_{l\kappa,\alpha} u_{l'\kappa',\beta} u_{l''\kappa'',\gamma} \left. \frac{\partial^3 E_0}{\partial u_{l\kappa,\alpha} \partial u_{l'\kappa',\beta} \partial u_{l''\kappa'',\gamma}} \right|_{\vec{u}=0} + O(\vec{u}^4), \quad (3.2)
 \end{aligned}$$

in which E_0 describes the groundstate energy ($\vec{u} = 0$ for all atoms), which in the present work is the DFT equilibrium total energy. The indices α , β and γ label the three components of the displacement vectors (i.e. $\alpha, \beta, \gamma = 1, 2, 3$). The zeroth-order term is just a constant, whereas the first-order term comprises the forces acting on the atoms. If the atoms are at their equilibrium positions, i.e. all forces are zero, then the first-order term is zero. The second-order term is the harmonic potential energy term (V_{harm}), which is the quantity aimed for in terms of the force-constant matrix. Higher-order terms describing anharmonic effects will not be considered further on.

In the harmonic approximation the relation between atom displacement \vec{u} and the back-driving force $\vec{F}(\vec{u})$ is linear, i.e. $F = -Ku$ for the most simple one-dimensional case with spring-constant or force-constant $K = -F/u$. Obviously, K has to be replaced in the three-dimensional crystal by a suitably constructed force-constant matrix Φ .

3.1 Force-Constant Matrix

The force-constant matrix as defined by

$$\Phi \begin{pmatrix} l & l' \\ \kappa & \kappa' \end{pmatrix}_{\alpha\beta} = \left. \frac{\partial^2 E_0}{\partial u_{l\kappa,\alpha} \partial u_{l'\kappa',\beta}} \right|_{\vec{u}=0}, \quad (3.3)$$

appears in the harmonic potential [15],

$$V_{\text{harm}} = \frac{1}{2} \sum_{l\kappa,\alpha} \sum_{l'\kappa',\beta} \Phi \begin{pmatrix} l & l' \\ \kappa & \kappa' \end{pmatrix}_{\alpha\beta} u_{l\kappa,\alpha} u_{l'\kappa',\beta}, \quad (3.4)$$

with the vector component indices α and β . The force-constant matrix Φ has the following symmetry properties:

- As a direct result of the invariance of the interchange of derivatives in Eq. 3.3,

$$\Phi \begin{pmatrix} l & l' \\ \kappa & \kappa' \end{pmatrix}_{\alpha\beta} = \Phi \begin{pmatrix} l' & l \\ \kappa' & \kappa \end{pmatrix}_{\beta\alpha} . \quad (3.5)$$

- If the crystal structure has a centre of inversion, i.e. the potential energy of the crystal obeys $V(\vec{R}) = V(-\vec{R})$, then the stricter symmetry relation

$$\Phi \begin{pmatrix} l & l' \\ \kappa & \kappa' \end{pmatrix}_{\alpha\beta} = \Phi \begin{pmatrix} l' & l \\ \kappa' & \kappa \end{pmatrix}_{\alpha\beta} \quad (3.6)$$

is valid.

- Due to translational symmetry of the underlying Bravais lattice the summation l, l' can be reformulated to give

$$\Phi \begin{pmatrix} l'' \\ \kappa & \kappa' \end{pmatrix}_{\alpha\beta} = \Phi \begin{pmatrix} l-l' & 0 \\ \kappa & \kappa' \end{pmatrix}_{\alpha\beta} = \Phi \begin{pmatrix} l & l' \\ \kappa & \kappa' \end{pmatrix}_{\alpha\beta} . \quad (3.7)$$

Since the difference between two lattice vectors is also a lattice vector, as $\vec{R}_{l''} = \vec{R}_l - \vec{R}_{l'}$, the index $l'' = l - l'$ is introduced.

- If the same displacement $\vec{d} = \vec{u}$ acts on all atoms in the crystal, thereby displacing the entire crystal without a distortion, then $V_{\text{harm}}(\vec{d}) = V_{\text{harm}}(\vec{u} \rightarrow 0) = 0$. Hence,

$$\sum_{l\kappa, \alpha} \sum_{l'\kappa', \beta} \Phi \begin{pmatrix} l-l' & 0 \\ \kappa & \kappa' \end{pmatrix}_{\alpha\beta} d_\alpha d_\beta = \sum_{\alpha\beta} CN d_\alpha d_\beta \sum_{l'\kappa'} \Phi \begin{pmatrix} l-l' & 0 \\ \kappa & \kappa' \end{pmatrix}_{\alpha\beta} = 0 .$$

It follows that

$$\sum_{l'\kappa'} \Phi \begin{pmatrix} l'' \\ \kappa\kappa' \end{pmatrix}_{\alpha\beta} = 0 . \quad (3.8)$$

3.2 Equation of Motion

From the harmonic potential and Newton's second law the equations of motions are derived,

$$F_{l\kappa, \alpha} = M_\kappa \frac{\partial^2}{\partial t^2} u_{l\kappa, \alpha} = - \frac{\partial V_{\text{harm}}}{\partial u_{l\kappa, \alpha}} = - \sum_{l'\kappa', \beta} \Phi \begin{pmatrix} l-l' & 0 \\ \kappa & \kappa' \end{pmatrix}_{\alpha\beta} u_{l'\kappa', \beta} , \quad (3.9)$$

in which M_κ denotes the mass of atom κ .

To solve these equations a plane wave *ansatz* for the displacements is made [15],

$$u_{l\kappa,\alpha}(t) = \frac{1}{\sqrt{M_\kappa}} \epsilon_{\kappa,\alpha}(\vec{q}) e^{i(\vec{q}\cdot\vec{R}_{l\kappa} - \omega(\vec{q})t)}, \quad (3.10)$$

with angular frequency $\omega(\vec{q})$ and the polarization vector $\vec{\epsilon}_\kappa(\vec{q})$ for a chosen point \vec{q} which is due to the periodic boundary condition an element of the first Brillouin zone (BZ), i.e. $\vec{q} \in \text{BZ}$. Applying this *ansatz* to Eq. 3.9 and considering the translational symmetry from Eq. 3.7 the expression per unit cell

$$\omega^2(\vec{q}) \epsilon_{\kappa,\alpha}(\vec{q}) = \sum_{\kappa',\beta} \left[\sum_{l''} \frac{1}{\sqrt{M_\kappa M_{\kappa'}}} \Phi \left(\begin{matrix} l'' \\ \kappa \ \kappa' \end{matrix} \right)_{\alpha\beta} e^{i\vec{q}\cdot\vec{R}_{l''}} e^{i\vec{q}\cdot(\vec{\tau}_\kappa - \vec{\tau}_{\kappa'})} \right] \epsilon_{\kappa',\beta}(\vec{q}), \quad (3.11)$$

finally arises.

The expression in square brackets defines with

$$D_{\alpha\beta}^{\kappa\kappa'}(\vec{q}) = \sum_{l''} \frac{1}{\sqrt{M_\kappa M_{\kappa'}}} \Phi \left(\begin{matrix} l'' \\ \kappa \ \kappa' \end{matrix} \right)_{\alpha\beta} e^{i\vec{q}\cdot\vec{R}_{l''}} e^{i\vec{q}\cdot(\vec{\tau}_\kappa - \vec{\tau}_{\kappa'})} \quad (3.12)$$

element $\kappa \ \kappa'$ of the dynamical matrix

$$D(\vec{q}) = \begin{pmatrix} \{D_{\alpha\beta}^{11}\} & \cdots & \{D_{\alpha\beta}^{1N}\} \\ \vdots & \ddots & \vdots \\ \{D_{\alpha\beta}^{N1}\} & \cdots & \{D_{\alpha\beta}^{NN}\} \end{pmatrix}. \quad (3.13)$$

Thus, Eq. 3.11 is reformulated by

$$\omega^2(\vec{q}) \epsilon_{\kappa,\alpha}(\vec{q}) = \sum_{\kappa',\beta} D_{\alpha\beta}^{\kappa\kappa'}(\vec{q}) \epsilon_{\kappa',\beta}(\vec{q}). \quad (3.14)$$

This is an eigenvalue problem with eigenvalues $\omega^2(\vec{q})$ and eigenvectors $\vec{\epsilon}_\kappa(\vec{q})$. The square roots of these eigenvalues yield the dispersion relation $\omega(\vec{q})$. It is obvious, that negative eigenvalues for $\omega^2(\vec{q})$ will result in imaginary frequencies, i.e. non oscillating displacements. Conventionally when plotting $\omega(\vec{q})$ the imaginary frequencies are shown as negative values.

As the dynamical matrix $D(\vec{q})$ has dimension $3N \times 3N$ (N being the number of atoms in the unit cell), a total of $3N$ solutions exist for each wavevector \vec{q} , corresponding to a vibrational mode j . The eigenvectors of these modes, distinguished

by index $j = 1, \dots, 3N$ are orthonormal to each other, hence,

$$\sum_{\kappa} \vec{\epsilon}_{\kappa,j}^*(\vec{q}) \vec{\epsilon}_{\kappa,j'}(\vec{q}) = \delta_{jj'} . \quad (3.15)$$

Three of these branches describe acoustic modes, i.e. modes of vibration which vanish at the long-wavelength limit. Therefore $\omega(\vec{q}) \rightarrow 0$ if $\vec{q} \rightarrow \vec{0}$. The other $3(N-1)$ modes, which do not vanish at the long-wavelength limit, describe optical modes. Along high-symmetry paths in \vec{q} -space, the eigenvectors of a set of three modes can be classified in terms of a longitudinal ($\vec{\epsilon}_{\kappa,j} \parallel \vec{q}$) and two transversal polarisation ($\vec{\epsilon}_{\kappa,j} \perp \vec{q}$).

3.3 Quantum Mechanical Formulation

Using the harmonic potential of Eq. 3.4 and the kinetic energy for mass M_{κ} , the Hamiltonian is given by

$$\hat{H} = \hat{T} + \hat{V}_{\text{harm}} = \sum_{l\kappa} \frac{\hat{p}_{l\kappa}^2}{2M_{\kappa}} + \frac{1}{2} \sum_{l\kappa,\alpha} \sum_{l'\kappa',\beta} \Phi \begin{pmatrix} l-l' & 0 \\ \kappa & \kappa' \end{pmatrix}_{\alpha\beta} u_{l\kappa,\alpha} u_{l'\kappa',\beta} . \quad (3.16)$$

Both the momentum operator and the displacement vectors are redefined in terms of Fourier transformation

$$\hat{p}_{l\kappa} = \sqrt{\frac{M_{\kappa}}{CN}} \sum_{\vec{q}} \sum_j^{N_q} \sum_j^{3N} \vec{\epsilon}_{\kappa,j}(\vec{q}) \hat{P}_j(\vec{q}) e^{-i\vec{q} \cdot \vec{R}_{l\kappa}} \quad (3.17)$$

and

$$\vec{u}_{l\kappa} = \frac{1}{\sqrt{CNM_{\kappa}}} \sum_{\vec{q}} \sum_j^{N_q} \sum_j^{3N} \vec{\epsilon}_{\kappa,j}^*(\vec{q}) \hat{X}_j(\vec{q}) e^{i\vec{q} \cdot \vec{R}_{l\kappa}} , \quad (3.18)$$

whereby N_q defines the number of \vec{q} -points in the BZ.

In these definitions one introduces the normal coordinate operators $\hat{X}_j(\vec{q})$ and $\hat{P}_j(\vec{q})$ which are the Fourier transforms of $\vec{u}_{l\kappa}$ and $\hat{p}_{l\kappa}$ [16] utilizing

$$\hat{X}_j(\vec{q}) = \sum_{l\kappa} \sqrt{\frac{M_{\kappa}}{N_q}} \vec{\epsilon}_{\kappa,j}(\vec{q}) \vec{u}_{l\kappa} e^{-i\vec{q} \cdot \vec{R}_{l\kappa}} \quad (3.19)$$

$$\hat{P}_j(\vec{q}) = \sum_{l\kappa} \frac{1}{\sqrt{N_q M_{\kappa}}} \vec{\epsilon}_{\kappa,j}^*(\vec{q}) \hat{p}_{l\kappa} e^{i\vec{q} \cdot \vec{R}_{l\kappa}} . \quad (3.20)$$

It should be noted that both, $\vec{u}_{l\kappa}$ and $\hat{p}_{l\kappa}$, correspond to an observable quantity and, therefore, have to be self-adjoint (see page 88 in Ref. [17]). As a consequence,

$$\hat{P}_j(\vec{q}) = \hat{P}_j^\dagger(-\vec{q}) \quad (3.21)$$

and

$$\hat{X}_j(\vec{q}) = \hat{X}_j^\dagger(-\vec{q}) \quad (3.22)$$

has to be valid.

The Hamiltonian (Eq. 3.16) is simplified in two steps, starting with the kinetic energy. As \hat{p} is an observable, i.e. $\hat{p}_{l\kappa}^2 = \hat{p}_{l\kappa}\hat{p}_{l\kappa}$, the kinetic term is defined by

$$\hat{T} = \frac{1}{2CN} \sum_{l\kappa} \sum_{\vec{q}\vec{q}'} \sum_{jj'} \vec{e}_{\kappa,j}(\vec{q}) \vec{e}_{\kappa,j'}(\vec{q}') \hat{P}_j(\vec{q}) \hat{P}_{j'}(\vec{q}') e^{-i(\vec{q}+\vec{q}') \cdot \vec{R}_{l\kappa}}. \quad (3.23)$$

From the orthonormality of the polarisation vectors $\vec{e}_{\kappa,j}(\vec{q})$, $\vec{e}_{\kappa,j'}(\vec{q}')$ and from translational symmetry, i.e. $\sum_{l\kappa} e^{i(\vec{q}+\vec{q}') \cdot \vec{R}_{l\kappa}} = CN \delta_{\vec{q}+\vec{q}',0}$, [15] one derives

$$\vec{q} + \vec{q}' = 0 \Rightarrow \vec{q}' = -\vec{q}. \quad (3.24)$$

Rewriting Eq. 3.23 leads to

$$\hat{T} = \frac{1}{2} \sum_{\vec{q}} \sum_j \hat{P}_j(\vec{q}) \hat{P}_j^\dagger(\vec{q}). \quad (3.25)$$

Similar steps are now made for the potential energy part of the Hamiltonian

$$\begin{aligned} \hat{V}_{\text{harm}} = \frac{1}{2CN} \sum_{l\kappa,\alpha} \sum_{l'\kappa',\beta} \sum_{\vec{q}\vec{q}'} \sum_{jj'} \frac{1}{\sqrt{M_\kappa M_{\kappa'}}} \Phi \begin{pmatrix} l'-l & 0 \\ \kappa & \kappa' \end{pmatrix}_{\alpha\beta} \epsilon_{\kappa,j,\alpha}^*(\vec{q}) \epsilon_{\kappa',j',\beta}^*(\vec{q}') \\ \hat{X}_{j,\alpha}(\vec{q}) \hat{X}_{j',\beta}(\vec{q}') e^{i\vec{q} \cdot \vec{R}_{l\kappa}} e^{i\vec{q}' \cdot \vec{R}_{l'\kappa'}}. \end{aligned} \quad (3.26)$$

Rewriting the exponentials

$$e^{i(\vec{q} \cdot \vec{R}_{l\kappa} + \vec{q}' \cdot \vec{R}_{l'\kappa'})} = e^{i\vec{q} \cdot (\vec{R}_{l\kappa} - \vec{R}_{l'\kappa'})} e^{i\vec{R}_{l'\kappa'} \cdot (\vec{q} + \vec{q}')}, \quad (3.27)$$

and applying again translational symmetry one arrives at

$$\begin{aligned} \hat{V}_{\text{harm}} = \frac{1}{2} \sum_{\vec{q}} \sum_j \sum_{\kappa,\alpha} \sum_{\kappa',\beta} \left[\sum_{l''} \frac{1}{\sqrt{M_\kappa M_{\kappa'}}} \Phi \begin{pmatrix} l'' & \\ \kappa & \kappa' \end{pmatrix}_{\alpha\beta} e^{i\vec{q} \cdot \vec{R}_{l''}} e^{i\vec{q} \cdot (\vec{\tau}_\kappa - \vec{\tau}_{\kappa'})} \right] \\ \epsilon_{\kappa,j,\beta}(\vec{q}) \epsilon_{\kappa',j,\alpha}^*(\vec{q}) \hat{X}_{j,\alpha}(\vec{q}) \hat{X}_{j,\beta}^\dagger(\vec{q}). \end{aligned} \quad (3.28)$$

The part in the square brackets can be identified as matrix element $D_{\alpha\beta}^{\kappa\kappa'}(\vec{q})$ of the dynamical matrix (Eq. 3.12). Based upon the eigensolutions of the dynamical matrix in Eq. 3.14, the potential energy part (Eq. 3.28) can be simplified to

$$\hat{V}_{\text{harm}} = \frac{1}{2} \sum_{\vec{q}}^{N_q} \sum_j^{3N} \omega_j^2(\vec{q}) \hat{X}_j(\vec{q}) \hat{X}_j^\dagger(\vec{q}), \quad (3.29)$$

summing over all phonon modes j for each \vec{q} .

Thus, the Hamiltonian amounts to

$$\hat{H} = \frac{1}{2} \sum_{\vec{q}}^{N_q} \sum_j^{3N} \left(\hat{P}_j(\vec{q}) \hat{P}_j^\dagger(\vec{q}) + \omega_j^2(\vec{q}) \hat{X}_j(\vec{q}) \hat{X}_j^\dagger(\vec{q}) \right). \quad (3.30)$$

At this point it is convenient to introduce creation operator $\hat{a}_{\vec{q},j}^\dagger$ and annihilation operator $\hat{a}_{\vec{q},j}$ [16]

$$\hat{a}_{\vec{q},j}^\dagger = \sqrt{\frac{\omega_j(\vec{q})}{2\hbar}} \hat{X}_j^\dagger(\vec{q}) - i \sqrt{\frac{1}{2\hbar\omega_j(\vec{q})}} \hat{P}_j^\dagger(\vec{q}) \quad (3.31)$$

$$\hat{a}_{\vec{q},j} = \sqrt{\frac{\omega_j(\vec{q})}{2\hbar}} \hat{X}_j(\vec{q}) + i \sqrt{\frac{1}{2\hbar\omega_j(\vec{q})}} \hat{P}_j(\vec{q}). \quad (3.32)$$

With $[\hat{X}_j, \hat{X}_j^\dagger] = [\hat{P}_j, \hat{P}_j^\dagger] = 0$ and $[\hat{X}_j, \hat{P}_j] = i\hbar$ the creation and annihilation operators lead to the elegant formulation of the Hamiltonian

$$\hat{H} = \sum_{\vec{q}}^{N_q} \sum_j^{3N} \hbar\omega_j(\vec{q}) \left(\hat{a}_{\vec{q},j}^\dagger \hat{a}_{\vec{q},j} + \frac{1}{2} \right). \quad (3.33)$$

The creation and annihilation operators change the number of phonons of an eigenstate $|n_{\vec{q},j}\rangle$ consisting of n phonons with mode j and wavevector \vec{q} by

$$\hat{a}_{\vec{q},j}^\dagger |n_{\vec{q},j}\rangle = \sqrt{n_{\vec{q},j} + 1} |n_{\vec{q},j} + 1\rangle \quad (3.34)$$

and

$$\hat{a}_{\vec{q},j} |n_{\vec{q},j}\rangle = \sqrt{n_{\vec{q},j}} |n_{\vec{q},j} - 1\rangle. \quad (3.35)$$

Applying the creation and annihilation operators on $|n_{\vec{q},j}\rangle$ derives the number of phonons occupying the chosen state \vec{q}, j with

$$\hat{a}_{\vec{q},j}^\dagger \hat{a}_{\vec{q},j} |n_{\vec{q},j}\rangle = n_{\vec{q},j} |n_{\vec{q},j}\rangle, \quad (3.36)$$

defining the number operator $n_{\vec{q},j}$.

The commutator relations

$$[\hat{a}_{\vec{q},j}, \hat{a}_{\vec{q}',j}^\dagger] = \delta_{\vec{q}\vec{q}'} \quad (3.37)$$

$$[a_{\vec{q},j}, a_{\vec{q}',j}] = [a_{\vec{q},j}^\dagger, a_{\vec{q}',j}^\dagger] = 0 \quad (3.38)$$

identify the phonons as bosons.

Finally, the temperature dependent total energy of the oscillating system $E(T)$ can be described by,

$$E(T) = \sum_{\vec{q}}^{N_q} \sum_j^{3N} \hbar\omega_j(\vec{q}) \left(\bar{n}_{\vec{q},j}(T) + \frac{1}{2} \right) = \sum_{\vec{q}}^{N_q} \sum_j^{3N} E_j(T, \vec{q}) , \quad (3.39)$$

with the phonon energy $E_j(T, \vec{q})$ of mode j at \vec{q} and T , and the Bose-Einstein distribution function

$$\bar{n}_{\vec{q},j}(T) = \frac{1}{e^{\beta\hbar\omega_j(\vec{q})} - 1} , \quad (3.40)$$

wherein $\beta = 1/(k_B T)$ is defined using Boltzmann's constant k_B .

3.4 *Ab-initio* Phonon Calculations

For calculating the phonon dispersion on an *ab-initio* level mainly two approaches are used, namely the *linear response* approach [18–22] and the *direct* method [1, 23].

In this work, the *direct* force-constant method is used and will therefore be discussed in more detail.

3.4.1 Force-Constant Method

Starting with a crystal, where all atoms are at their equilibrium positions, the displacement of one atom from its equilibrium induces net forces on itself and all other atoms. Specifically, force $\vec{F}(\vec{u}_{l\kappa}, \vec{R}_{l'\kappa'})$ acts on the atom at $\vec{R}_{l'\kappa'}$ when atom $l\kappa$ is displaced by $\vec{u}_{l\kappa}$.

When calculating with DFT a cell with periodic boundary conditions (see Ref. [24] and chapter 8 in Ref. [25]) is used. Therefore, not a system with infinite proportions is described but a system containing periodically repeated simulation cells. If this simulation cell contains multiples of the primitive unit cell it is referred to by the term supercell.

The force-field of the supercell collects all forces acting on the atoms resulting from displacement $\vec{u}_{l\kappa}$ and is defined by

$$\mathfrak{F}(\vec{u}_{l\kappa}) = \left\{ \vec{F}(\vec{u}_{l\kappa}, \vec{R}_{11}), \dots, \vec{F}(\vec{u}_{l\kappa}, \vec{R}_{l\kappa}), \dots, \vec{F}(\vec{u}_{l\kappa}, \vec{R}_{l'\kappa'}), \dots, \vec{F}(\vec{u}_{l\kappa}, \vec{R}_{CN}) \right\}, \quad (3.41)$$

as sketched for graphene in Fig. 3.2.

When deriving the force-fields generated by displacement $\vec{u}_{l\kappa}$ a suitably large supercell has to be chosen, so that the interaction between the periodically repeated displaced atoms is insignificant. As it is not sure that this criteria is always fulfilled one has to consider under the nearest image convention (see chapter 8 in Ref. [25]) that the force acting on an atom at $\vec{R}_{l'\kappa'}$ due to displacement $\vec{u}_{l\kappa}$ also includes superimposed forces of the displacements $\vec{u}_{l''\kappa}$ via the nearest images in the adjacent supercells acting through the periodic boundary as sketched in Fig. 3.3. It is important to correct these superimposed forces for equidistant nearest images as shown in the example for diamond (Sec. 3.4.2) by normalizing the acting force by the number of images with $|\vec{R}_{l\kappa} - \vec{R}_{l'\kappa'}| = |\vec{R}_{l''\kappa} - \vec{R}_{l'\kappa'}|$. Further ramifications of the periodic boundary on the minimum supercell size are discussed later in section 3.4.3.

The choice of a set of three linear independent displacements is arbitrary, yet for the sake of convenience and simplicity the displacements are oriented along the axis of the coordinate system, i.e.,

$$\vec{u}_{l\kappa,1} = u_{l\kappa,1}\vec{e}_1, \quad \vec{u}_{l\kappa,2} = u_{l\kappa,2}\vec{e}_2 \quad \text{and} \quad \vec{u}_{l\kappa,3} = u_{l\kappa,3}\vec{e}_3, \quad (3.42)$$

using unit vectors $\vec{e}_1 = (1, 0, 0)$, $\vec{e}_2 = (0, 1, 0)$ and $\vec{e}_3 = (0, 0, 1)$.

The harmonic approximation requires a linear relationship between displacement and force (Eq. 3.9), i.e.,

$$\Phi \begin{pmatrix} l-l' & 0 \\ \kappa & \kappa' \end{pmatrix}_{\alpha\beta} = -\frac{F_\alpha(u_{l\kappa,\beta}\vec{e}_\beta, \vec{R}_{l'\kappa'})}{u_{l\kappa,\beta}}. \quad (3.43)$$

Force component α is divided by $u_{l\kappa,\beta}$, thus defining component $\alpha\beta$ of the force constant matrix Φ .

In principle, it is necessary to calculate $\mathfrak{F}(u_{l\kappa,\beta}\vec{e}_\beta)$ for all three orthonormal displacements of the chosen atom in the supercell. When choosing $u_{l\kappa} = u_{l\kappa,1} = u_{l\kappa,2} = u_{l\kappa,3}$ the number of possible displacements can be reduced if a point group operation S under which the crystal structure is invariant exists that applied to \vec{e}_β rotates it to $\vec{e}_{\beta'}$ with $\beta' \neq \beta$ with $\beta, \beta' = \{1, 2, 3\}$. This S can then be used to rotate all forces \vec{F} in the supercell with

$$S\vec{F}(u_{l\kappa}S\vec{e}_\beta, S^{-1}\vec{R}_{l'\kappa'}) = \vec{F}(u_{l\kappa}\vec{e}_\beta, \vec{R}_{l'\kappa'}). \quad (3.44)$$

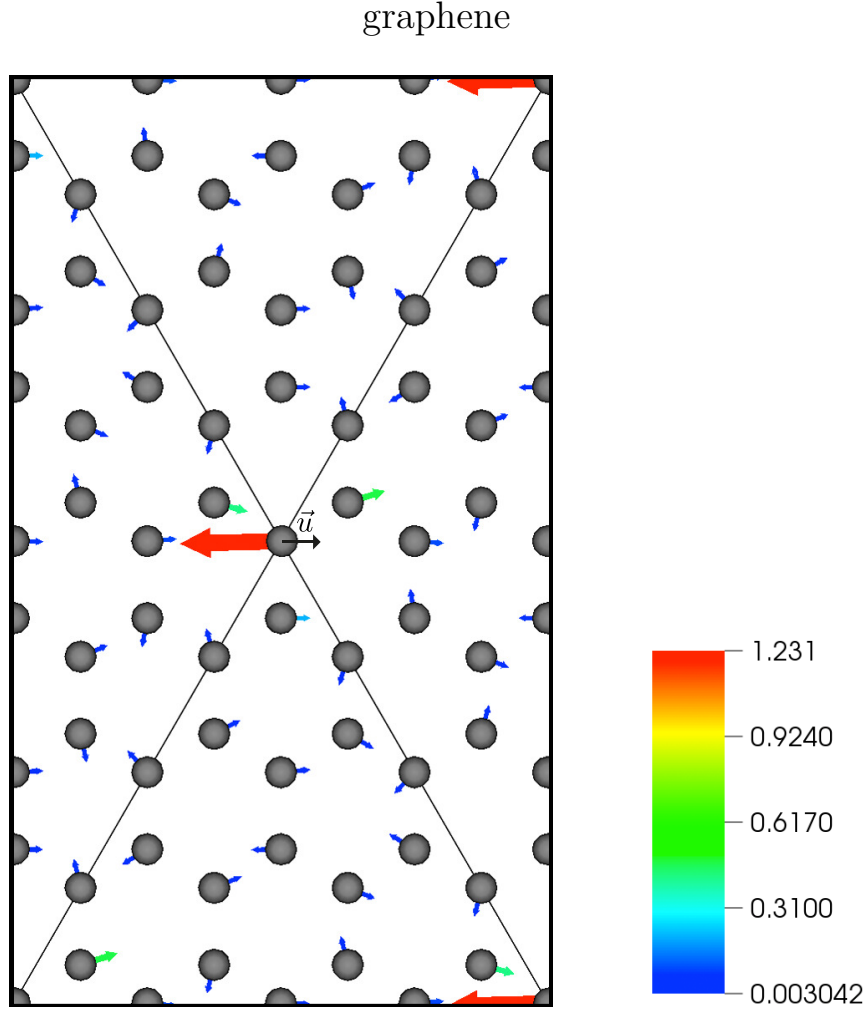


FIGURE 3.2: Force-field for graphene, due to the displacement of the central atom by $|u| = 0.02 \text{ \AA}$ in the direction of the black arrow. The direction of the forces is indicated by arrows which are scaled as well as colour coded according to their magnitude. Supercell boundaries are indicated by the solid lines.

Furthermore, the number of atoms that have to be displaced is reduced to those in the primitive unit cell that are under all invariant non-symmorphic space group operations $S_{\text{sg}} = \{S, \vec{t}\}$ and point group operations S of the primitive unit cell non equivalent. (Note that S_{sg} consists of S and a non-proper translation \vec{t} .) The force-constant $\Phi \begin{pmatrix} l-\tilde{l}' & 0 \\ \tilde{\kappa} & \tilde{\kappa}' \end{pmatrix}_{\alpha\beta}$ of the atoms at $\vec{R}_{l\tilde{\kappa}}$ and $\vec{R}_{\tilde{l}'\tilde{\kappa}'}$, equivalent to atoms at $\vec{R}_{l\kappa}$ and $\vec{R}_{l'\kappa'}$ under S_{sg} or S , can then be derived from $\Phi \begin{pmatrix} l-l' & 0 \\ \kappa & \kappa' \end{pmatrix}_{\alpha\beta}$ by

$$\Phi \begin{pmatrix} l-\tilde{l}' & 0 \\ \tilde{\kappa} & \tilde{\kappa}' \end{pmatrix}_{\alpha\beta} = S \Phi \begin{pmatrix} l-l' & 0 \\ \kappa & \kappa' \end{pmatrix}_{\alpha\beta} S^{-1}, \quad (3.45)$$

with

$$|\vec{R}_{l\kappa} - \vec{R}_{l'\kappa'}| = |\vec{R}_{l\tilde{\kappa}} - \vec{R}_{\tilde{l}'\tilde{\kappa}'}|. \quad (3.46)$$

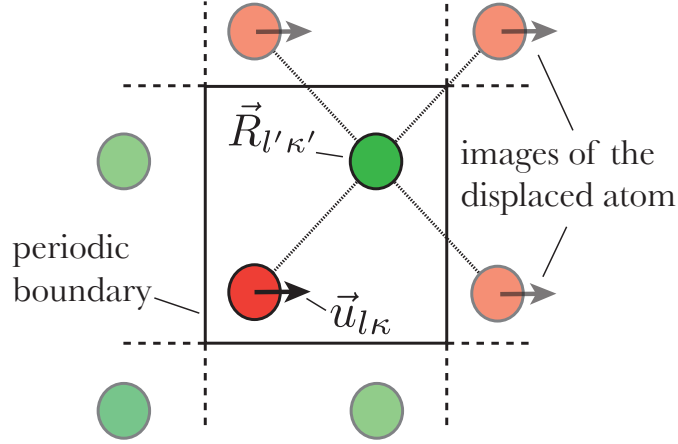


FIGURE 3.3: Displacement $\vec{u}_{l\kappa}$ is mirrored by the periodic boundary leading to further three equidistant displacements to the atom on $\vec{R}_{l'\kappa'}$. Thus, the force acting on atom $l'\kappa'$ is overestimated by a factor of four.

3.4.2 Example: Diamond

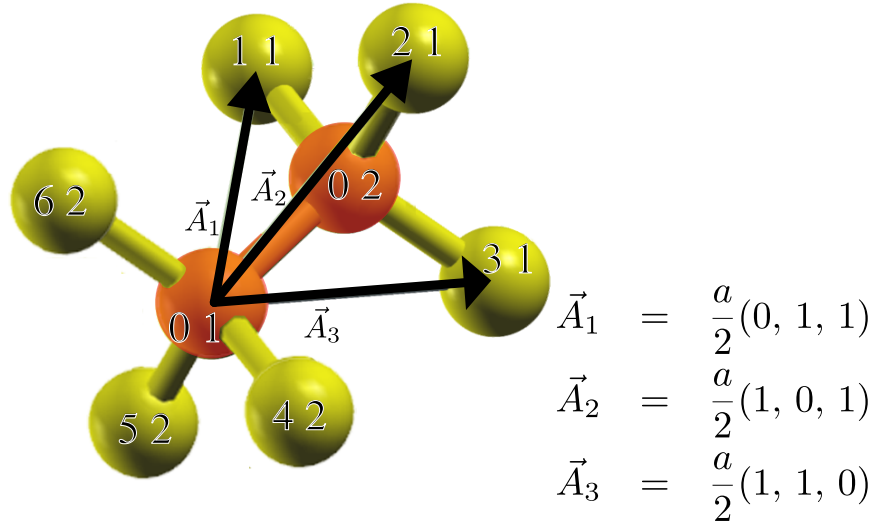
To illustrate the practical implementation of the force-constant method the phonon modes of diamond are derived by pencil for a supercell containing just one primitive unit cell in the cartesian coordinates.

Fig. 3.4 shows the primitive unit cell of diamond consisting of two carbon atoms whose positions with lattice constant a are $\vec{R}_{01} = (0, 0, 0)$ and $\vec{R}_{02} = (0.25, 0.25, 0.25)a$.

This diamond structure is invariant under 48 space group operations of which 24 are pure point group operations and 24 are non symmorphic space group operations.

The atom at \vec{R}_{02} is equivalent to the atom at \vec{R}_{01} under, for example, the space group operation,

$$S_{\text{sg}} = \left\{ \left(\begin{array}{ccc} -1 & 0 & 0 \\ 0 & -1 & 0 \\ 0 & 0 & -1 \end{array} \right), \left(\begin{array}{c} 0.25 \\ 0.25 \\ 0.25 \end{array} \right) a \right\}, \quad (3.47)$$



		direct	cartesian [a]
atoms in unit cell:	\vec{R}_{01}	(0, 0,0)	(0, 0, 0)
	\vec{R}_{02}	(1/4, 1/4, 1/4)	(1/4, 1/4, 1/4)
neighbours to \vec{R}_{01} :	\vec{R}_{02}	(1/4, 1/4, 1/4)	(1/4, 1/4, 1/4)
	\vec{R}_{42}	(-3/4, 1/4, 1/4)	(1/4, -1/4, -1/4)
	\vec{R}_{52}	(1/4,-3/4, 1/4)	(-1/4, 1/4, -1/4)
	\vec{R}_{62}	(1/4, 1/4,-3/4)	(-1/4, -1/4, 1/4)
neighbours to \vec{R}_{02} :	\vec{R}_{01}	(0, 0,0)	(0, 0, 0)
	\vec{R}_{11}	(1, 0, 0)	(0, 1/2,1/2)
	\vec{R}_{21}	(0, 1, 0)	(1/2, 0, 1/2)
	\vec{R}_{31}	(0, 0, 1)	(1/2, 1/2, 0)

FIGURE 3.4: A sketch of the diamond structure for which the underlying lattice is face-centred cubic. The primitive unit cell contains two atoms coloured orange at $\vec{R}_{01} = (0, 0, 0)$ and $\vec{R}_{02} = (0.25, 0.25, 0.25)a$. The cartesian coordinates are scaled by lattice constant a . Both atoms have four nearest neighbours, of which three are situated outside the primitive unit cell and are coloured yellow.

describing an inversion and a non primitive translation, as

$$\begin{aligned}
 S_{\text{sg}}\vec{R}_{02} &= \left\{ \begin{pmatrix} -1 & 0 & 0 \\ 0 & -1 & 0 \\ 0 & 0 & -1 \end{pmatrix}, \begin{pmatrix} 0.25 \\ 0.25 \\ 0.25 \end{pmatrix} a \right\} \vec{R}_{02} = \left\{ \begin{pmatrix} -1 & 0 & 0 \\ 0 & -1 & 0 \\ 0 & 0 & -1 \end{pmatrix}, \begin{pmatrix} 0.25 \\ 0.25 \\ 0.25 \end{pmatrix} a \right\} \begin{pmatrix} 0.25 \\ 0.25 \\ 0.25 \end{pmatrix} a \\
 &= \begin{pmatrix} -1 & 0 & 0 \\ 0 & -1 & 0 \\ 0 & 0 & -1 \end{pmatrix} \begin{pmatrix} 0.25 \\ 0.25 \\ 0.25 \end{pmatrix} a + \begin{pmatrix} 0.25 \\ 0.25 \\ 0.25 \end{pmatrix} a = - \begin{pmatrix} 0.25 \\ 0.25 \\ 0.25 \end{pmatrix} a + \begin{pmatrix} 0.25 \\ 0.25 \\ 0.25 \end{pmatrix} a \\
 &= \begin{pmatrix} 0.0 \\ 0.0 \\ 0.0 \end{pmatrix} = \vec{R}_{01} .
 \end{aligned} \tag{3.48}$$

Therefore, it is sufficient to consider the three orthonormal displacements for one of the two atoms. This can be further reduced to a single displacement when considering that the point group operator

$$S = \begin{pmatrix} 0 & 0 & 1 \\ 1 & 0 & 0 \\ 0 & 1 & 0 \end{pmatrix} , \tag{3.49}$$

describing a three-fold rotation, applied to unit vector \vec{e}_1 gives \vec{e}_2 and to \vec{e}_2 gives \vec{e}_3 .

As an example of a VASP DFT calculation displacing by $u_{01}\vec{e}_1$, with $u_{01} = 0.02 \text{ \AA}$, results in the force-field

$$\mathfrak{F}(u_{01}\vec{e}_1) = \left\{ \vec{F}(u_{01}\vec{e}_1, \vec{R}_{01}), \vec{F}(u_{01}\vec{e}_1, \vec{R}_{02}) \right\} = \left\{ \begin{pmatrix} -0.74 \\ 0 \\ 0 \end{pmatrix} \text{eV/\AA}, \begin{pmatrix} 0.74 \\ 0 \\ 0 \end{pmatrix} \text{eV/\AA} \right\} . \tag{3.50}$$

As the application of the inverse of the point group rotation (Eq. 3.49) on \vec{R}_{02} yields,

$$S^{-1}\vec{R}_{02} = \begin{pmatrix} 0 & 1 & 0 \\ 0 & 0 & 1 \\ 1 & 0 & 0 \end{pmatrix} \begin{pmatrix} 0.25 \\ 0.25 \\ 0.25 \end{pmatrix} a = \begin{pmatrix} 0.25 \\ 0.25 \\ 0.25 \end{pmatrix} a = \vec{R}_{02} , \tag{3.51}$$

the force-fields for $u_{01}\vec{e}_2$ and $u_{01}\vec{e}_3$ are derived by

$$\begin{aligned}
 \mathfrak{F}(u_{01}\vec{e}_2) &= \left\{ S\vec{F}(u_{01}S\vec{e}_1, S^{-1}\vec{R}_{01}), S\vec{F}(u_{01}S\vec{e}_1, S^{-1}\vec{R}_{02}) \right\} \\
 &= \left\{ S\vec{F}(u_{01}\vec{e}_2, \vec{R}_{01}), S\vec{F}(u_{01}\vec{e}_2, \vec{R}_{02}) \right\} \\
 &= \left\{ \begin{pmatrix} 0 \\ -0.74 \\ 0 \end{pmatrix} \text{eV/\AA}, \begin{pmatrix} 0 \\ 0.74 \\ 0 \end{pmatrix} \text{eV/\AA} \right\}
 \end{aligned} \tag{3.52}$$

and

$$\mathfrak{F}(u_{01}\vec{e}_3) = \left\{ \left(\begin{array}{c} 0 \\ 0 \\ -0.74 \end{array} \right) \text{eV}/\text{\AA}, \left(\begin{array}{c} 0 \\ 0 \\ 0.74 \end{array} \right) \text{eV}/\text{\AA} \right\}. \quad (3.53)$$

This allows, using Eq. 3.43, for the construction of the force-constant matrix

$$\begin{aligned} \Phi \binom{0}{11} &= - \begin{pmatrix} \vec{F}^T(u_{01}\vec{e}_1, \vec{R}_{01})/u_{01} \\ \vec{F}^T(u_{01}\vec{e}_2, \vec{R}_{01})/u_{01} \\ \vec{F}^T(u_{01}\vec{e}_3, \vec{R}_{01})/u_{01} \end{pmatrix} \\ &= \begin{pmatrix} 37.1 & 0 & 0 \\ 0 & 37.1 & 0 \\ 0 & 0 & 37.1 \end{pmatrix} \text{eV}/\text{\AA}^2 \end{aligned} \quad (3.54)$$

$$(3.55)$$

and using S of S_{sg} (Eq. 3.47),

$$\Phi \binom{0}{22} = S \Phi \binom{0}{11} S^{-1} = \begin{pmatrix} 37.1 & 0 & 0 \\ 0 & 37.1 & 0 \\ 0 & 0 & 37.1 \end{pmatrix} \text{eV}/\text{\AA}^2. \quad (3.56)$$

Constructing the force-constant matrix between the atoms at \vec{R}_{01} and \vec{R}_{02} can not be done so easily. As the supercell is much too small the nearest images of the displacement have to be considered correctly. When comparing the graphene unit cell (Fig. 3.4) with the sketch in Fig. 3.3 one realises, that the force $\vec{F}^T(u_{01}\vec{e}_1, \vec{R}_{02})$ also includes in addition to the force from $u_{01}\vec{e}_1$ through the periodic boundary the forces from $u_{11}\vec{e}_1$ at \vec{R}_{11} , $u_{21}\vec{e}_1$ at \vec{R}_{21} and $u_{31}\vec{e}_1$ at \vec{R}_{31} . Equivalently, the net acting force $\vec{F}^T(u_{02}\vec{e}_1, \vec{R}_{01})$ also includes in addition resulting forces from displacements $u_{42}\vec{e}_1$, $u_{52}\vec{e}_1$ and $u_{62}\vec{e}_1$. As such, the forces have to be normalised by a factor of four when constructing the force-constant matrix.

$$\begin{aligned} \Phi \binom{0}{12} &= \frac{1}{4} \begin{pmatrix} \vec{F}^T(u_{01}\vec{e}_1, \vec{R}_{02})/u_{01} \\ \vec{F}^T(u_{01}\vec{e}_2, \vec{R}_{02})/u_{01} \\ \vec{F}^T(u_{01}\vec{e}_3, \vec{R}_{02})/u_{01} \end{pmatrix} \\ &= \begin{pmatrix} -9.275 & 0 & 0 \\ 0 & -9.275 & 0 \\ 0 & 0 & -9.275 \end{pmatrix} \text{eV}/\text{\AA}^2. \end{aligned} \quad (3.57)$$

Furthermore, the nearest images allow for the derivation of the force-constant matrices

$$\Phi \begin{pmatrix} 1 \\ 12 \end{pmatrix} = \Phi \begin{pmatrix} 2 \\ 12 \end{pmatrix} = \Phi \begin{pmatrix} 3 \\ 12 \end{pmatrix} = \Phi \begin{pmatrix} 0 \\ 12 \end{pmatrix} . \quad (3.58)$$

Using S from S_{sg} (Eq.3.47) leads to the last four force-constant matrices with

$$\begin{aligned} \Phi \begin{pmatrix} 0 \\ 21 \end{pmatrix} &= S \Phi \begin{pmatrix} 0 \\ 12 \end{pmatrix} S^{-1} \\ &= \Phi \begin{pmatrix} 4 \\ 21 \end{pmatrix} = \Phi \begin{pmatrix} 5 \\ 21 \end{pmatrix} = \Phi \begin{pmatrix} 6 \\ 21 \end{pmatrix} \\ &= \begin{pmatrix} -9.275 & 0 & 0 \\ 0 & -9.275 & 0 \\ 0 & 0 & -9.275 \end{pmatrix} \text{eV}/\text{\AA}^2 . \end{aligned} \quad (3.59)$$

With this set of ten force-constant matrices all necessary ingredients to construct the dynamical matrix exist and

$$D(\vec{q}) = \begin{pmatrix} D^{11} & D^{12} \\ D^{21} & D^{22} \end{pmatrix} . \quad (3.60)$$

There are only carbon atoms in the primitive unit cell, with $M_{\text{carbon}} = 12.01$ amu (amu is a abbreviation for the unified atomic mass unit), hence the dynamical matrix becomes

$$D(\vec{q}) = \frac{1}{M_{\text{carbon}}} \begin{pmatrix} \Phi \begin{pmatrix} 0 \\ 11 \end{pmatrix} e^{i\vec{q} \cdot (\vec{R}_{01} - \vec{R}_{01})} & \sum_{\nu'}^{0,1,2,3} \Phi \begin{pmatrix} \nu' \\ 12 \end{pmatrix} e^{i\vec{q} \cdot (\vec{R}_{01} - \vec{R}_{\nu'2})} \\ \sum_{\nu'}^{0,4,5,6} \Phi \begin{pmatrix} \nu' \\ 21 \end{pmatrix} e^{i\vec{q} \cdot (\vec{R}_{02} - \vec{R}_{\nu'1})} & \Phi \begin{pmatrix} 0 \\ 22 \end{pmatrix} e^{i\vec{q} \cdot (\vec{R}_{02} - \vec{R}_{02})} \end{pmatrix} . \quad (3.61)$$

To solve the eigenvalues of the dynamical matrix one now has to choose a value for \vec{q} inside the first Brillouin zone of the face-centred cubic cell sketched in Fig. 3.5. The simplest high symmetry point is Γ , where $\vec{q} = \vec{0}$ and therefore the phase factor is one. At this \vec{q} -point the dynamical matrix is given by

$$D(\Gamma) = \begin{pmatrix} 3.087 & 0 & 0 & -3.087 & 0 & 0 \\ 0 & 3.087 & 0 & 0 & -3.087 & 0 \\ 0 & 0 & 3.087 & 0 & 0 & -3.087 \\ -3.087 & 0 & 0 & 3.087 & 0 & 0 \\ 0 & -3.087 & 0 & 0 & 3.087 & 0 \\ 0 & 0 & -3.087 & 0 & 0 & 3.087 \end{pmatrix} \frac{\text{eV}}{\text{amu } \text{\AA}^2} . \quad (3.62)$$

Before solving the eigenvalue problem one should consider its units. To derive angular frequencies in THz one needs to convert from $\text{eV}/(\text{amu } \text{\AA}^2)$ to $1/(2\pi)^2 \text{ J}/(\text{kg m}^2)$. This

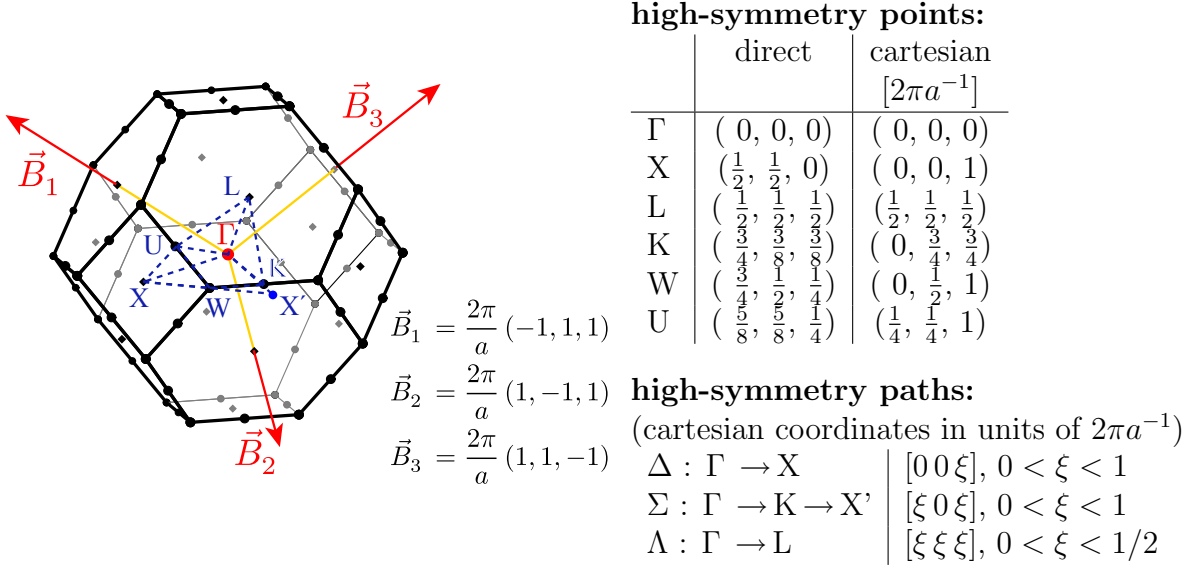


FIGURE 3.5: First Brillouin zone of a face-centered cubic cell with the high symmetry points and the reciprocal basis B . The coordinates of the high symmetry points are given in direct and cartesian coordinates. The direct coordinates are scaled by factor $2\pi a^{-1}$.

is done by multiplying the dynamical matrix with

$$\frac{1}{(2\pi)^2} \frac{[\text{eV} \rightarrow \text{J}]}{[\text{amu} \rightarrow \text{kg}][\text{\AA}^2 \rightarrow \text{m}^2]} = \frac{1}{(2\pi)^2} \frac{1.6022 \times 10^{-19} \text{ J}}{1.6605 \times 10^{27} \text{ kg } 1 \times 10^{-20} \text{ m}^2} = 244.4 \text{ THz}^2. \quad (3.63)$$

Two sets of three degenerate eigenvalues $\omega_1^2 = \omega_2^2 = \omega_3^2 = 0 \text{ THz}^2$ and $\omega_4^2 = \omega_5^2 = \omega_6^2 = 1508.68 \text{ THz}^2$ are now derived from Eq. 3.62. Therefore, the frequencies of the modes at Γ are $\omega_1 = \omega_2 = \omega_3 = 0 \text{ THz}$ and $\omega_4 = \omega_5 = \omega_6 = 38.84 \text{ THz}$.

Next, the dynamical matrix at $\vec{q} = X$ is derived. At this high symmetry point the off diagonal elements of the dynamical matrix become zero, because

$$\begin{aligned} \sum_{\nu'}^{0,1,2,3} \Phi \begin{pmatrix} \nu' \\ 12 \end{pmatrix} e^{i\vec{q} \cdot (\vec{R}_{01} - \vec{R}_{\nu'2})} &= \Phi \begin{pmatrix} 0 \\ 12 \end{pmatrix} e^{\frac{i\pi}{2}} + \Phi \begin{pmatrix} 4 \\ 12 \end{pmatrix} e^{-\frac{i\pi}{2}} + \Phi \begin{pmatrix} 5 \\ 12 \end{pmatrix} e^{-\frac{i\pi}{2}} + \Phi \begin{pmatrix} 6 \\ 12 \end{pmatrix} e^{\frac{i\pi}{2}} \\ &= -i\Phi \begin{pmatrix} 0 \\ 12 \end{pmatrix} + i\Phi \begin{pmatrix} 4 \\ 12 \end{pmatrix} + i\Phi \begin{pmatrix} 5 \\ 12 \end{pmatrix} - i\Phi \begin{pmatrix} 6 \\ 12 \end{pmatrix} = 0. \end{aligned} \quad (3.64)$$

Therefore, the dynamical matrix is now described by

$$D(\mathbf{X}) = \begin{pmatrix} 3.087 & 0 & 0 & 0 & 0 & 0 \\ 0 & 3.087 & 0 & 0 & 0 & 0 \\ 0 & 0 & 3.087 & 0 & 0 & 0 \\ 0 & 0 & 0 & 3.087 & 0 & 0 \\ 0 & 0 & 0 & 0 & 3.087 & 0 \\ 0 & 0 & 0 & 0 & 0 & 3.087 \end{pmatrix} \frac{\text{eV}}{\text{amu } \text{\AA}^2}. \quad (3.65)$$

The eigenvalues of this matrix are trivially degenerate according to $\omega_1^2 = \omega_2^2 = \omega_3^2 = \omega_4^2 = \omega_5^2 = \omega_6^2 = 754.4628 \text{ THz}^2$, from which $\omega = 27.47 \text{ THz}$ is derived.

From Fig. 3.8 one observes that the phonon dispersion for diamond using just the unit cell compared to calculations done with supercells is as expected wrong. The supercell is too small to accurately describe the phonon dispersion.

3.4.3 Supercell Size

An important question within the force-constant method to consider is the minimum size of the supercell necessary to accurately describe the phonons. For this one needs to take into account the superposition of the forces due to the periodic boundary condition. From the example of graphene in Fig. 3.6 one observes, that this effect can be substantial if the size of the supercell is too small. In the extreme case, where the supercell only consists of a single unit cell, then not only is $|\vec{F}|$ equal for both atoms but also spatial information on the force vector is lost, i.e. the direction of the force vectors are wrong.

To correctly calculate $D(\vec{q})$ the supercell has to be large enough so that in the direction where its diameter is the smallest the magnitude of the forces acting on the furthest atom away from the displaced atom, in regards to the nearest image convention, are sufficiently small. The contributions of any atom further away can then be safely omitted from the construction of the dynamical matrix. Further, to reduce the effect of force superposition on the atoms the supercell should be as isotropic as possible. If this is not the case a much larger supercell has to be used.

As can be seen in Fig. 3.7 for our case of the two dimensional graphene the supercell has to include at least 32 atoms (a supercell with $4 \times 4 \times 1$ unit cells) to allow for a correct computation of the dispersion relation. From the dispersion relations of diamond (Fig. 3.8) and aluminium (Fig. 3.9) we can discern that for a three-dimensional system at least 16 atoms are necessary for a reasonable result. To derive an accurate dispersion relation the isotropic supercell should include at least ≈ 30 atoms. This can be seen in particular

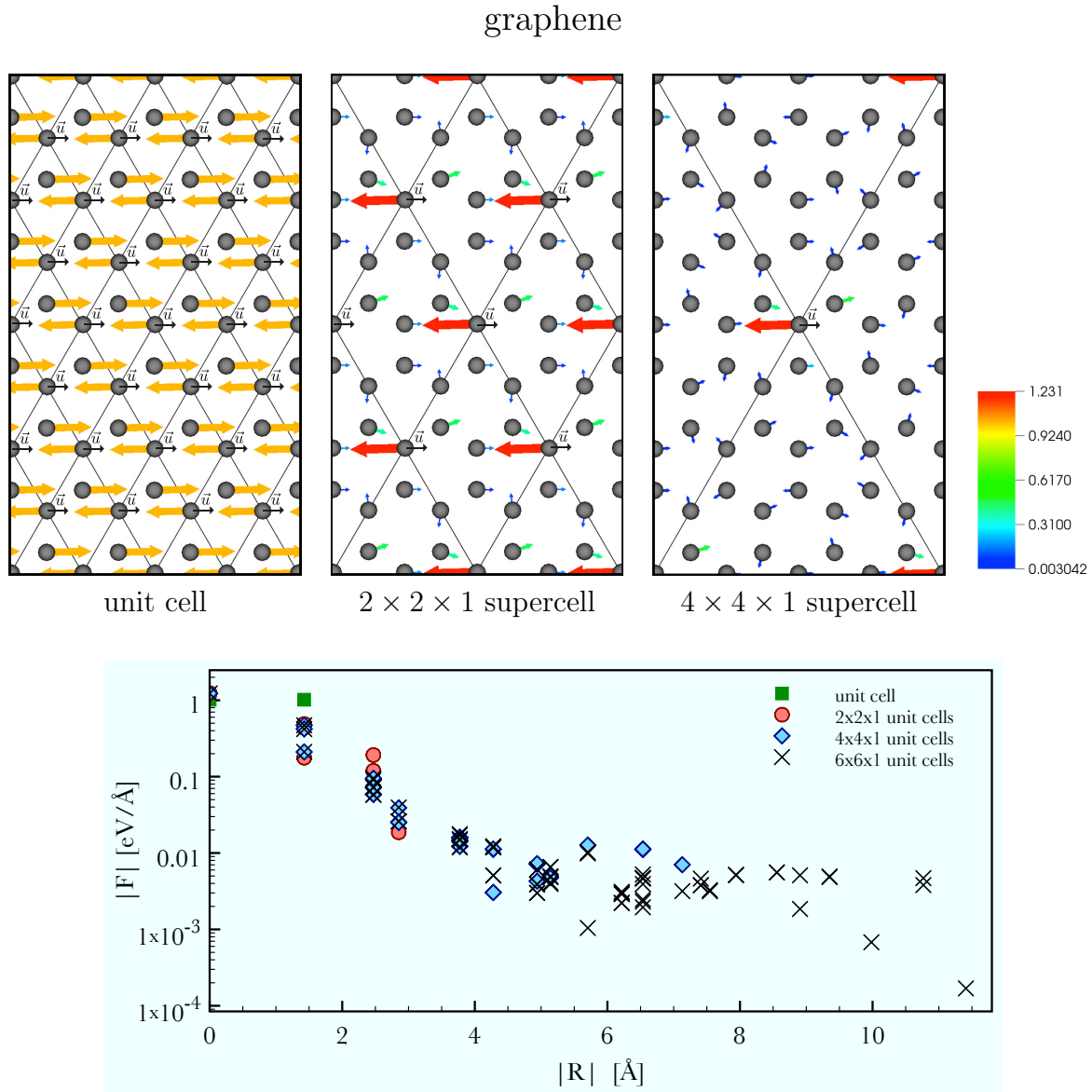


FIGURE 3.6: The force-field of graphene resulting from the displacement $\vec{u} = 0.02\vec{e}_1 \text{ \AA}$ for a unit cell, for a $2 \times 2 \times 1$ supercell and for a $4 \times 4 \times 1$ supercell are shown in the upper panels. In the lower panel the magnitude of the forces $|F|$ as a function of the distance $|R|$ from the displaced atom are compared to those of a $6 \times 6 \times 1$ supercell.

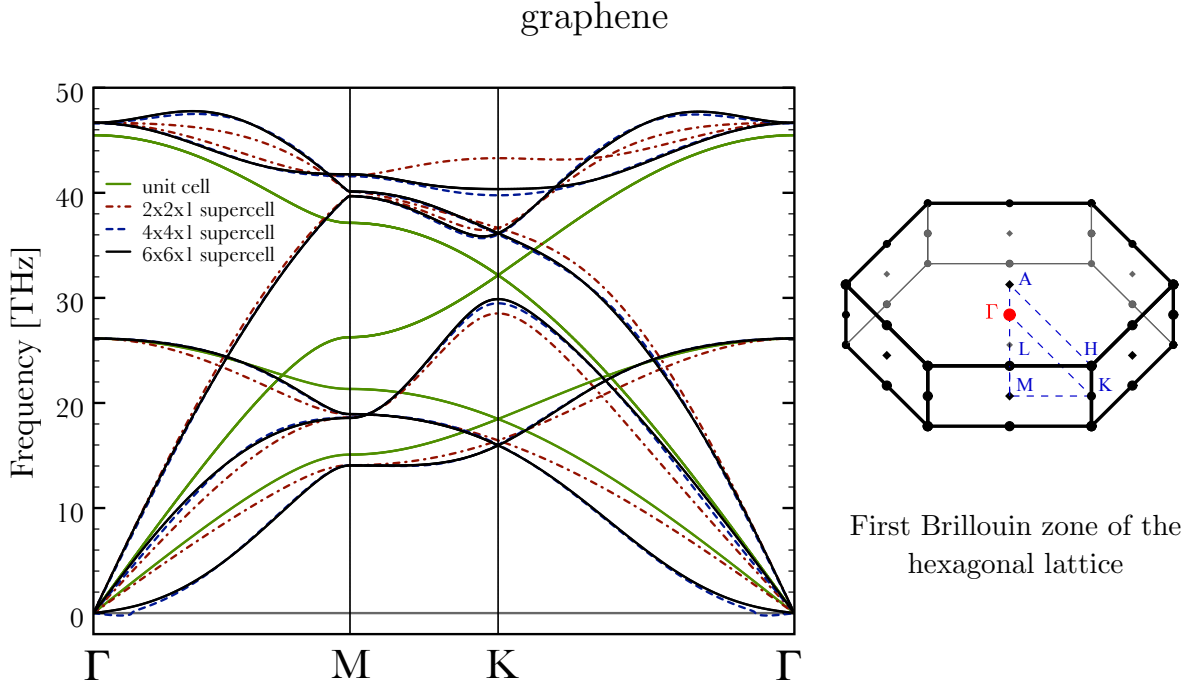


FIGURE 3.7: The dispersion relation of graphene calculated for a unit cell (green solid lines), for a $2 \times 2 \times 1$ supercell (red dashed-dotted lines), for a $4 \times 4 \times 1$ supercell (blue dashed lines) and for a $6 \times 6 \times 1$ supercell (black solid lines).

for diamond (Fig. 3.8) where $\omega(\vec{q})$ is wrong at the high-symmetry points X and W when the supercell consists of only 16 atoms.

Further, one notices that the phonon dispersion for both, graphene (Fig. 3.7) and diamond (Fig. 3.8), is independent of supercell size at the high-symmetry point Γ with a primitive unit cell containing two atoms. The reason for this is that at Γ the phase factor is one for all terms in the sum of Eq. 3.12. Therefore,

$$D^{\kappa\kappa'}(\Gamma) = \frac{1}{\sqrt{M_{\kappa}M_{\kappa'}}} \sum_{l''} \Phi \left(\begin{matrix} l'' \\ \kappa \quad \kappa' \end{matrix} \right) . \quad (3.66)$$

From the symmetry property $\sum_{l''} \Phi \left(\begin{matrix} l-l'' & 0 \\ \kappa & \kappa' \end{matrix} \right) = 0$ (Eq. 3.8) one deduces

$$\sum_{l''} \Phi \left(\begin{matrix} l'' \\ \kappa \quad \kappa \end{matrix} \right) = - \sum_{l'', \kappa' \neq \kappa} \Phi \left(\begin{matrix} l'' \\ \kappa \quad \kappa' \end{matrix} \right) . \quad (3.67)$$

By a longer deduction one arrives at

$$\sum_{l'' \neq 0} \Phi \left(\begin{matrix} l'' \\ \kappa \quad \kappa \end{matrix} \right) = 0 . \quad (3.68)$$

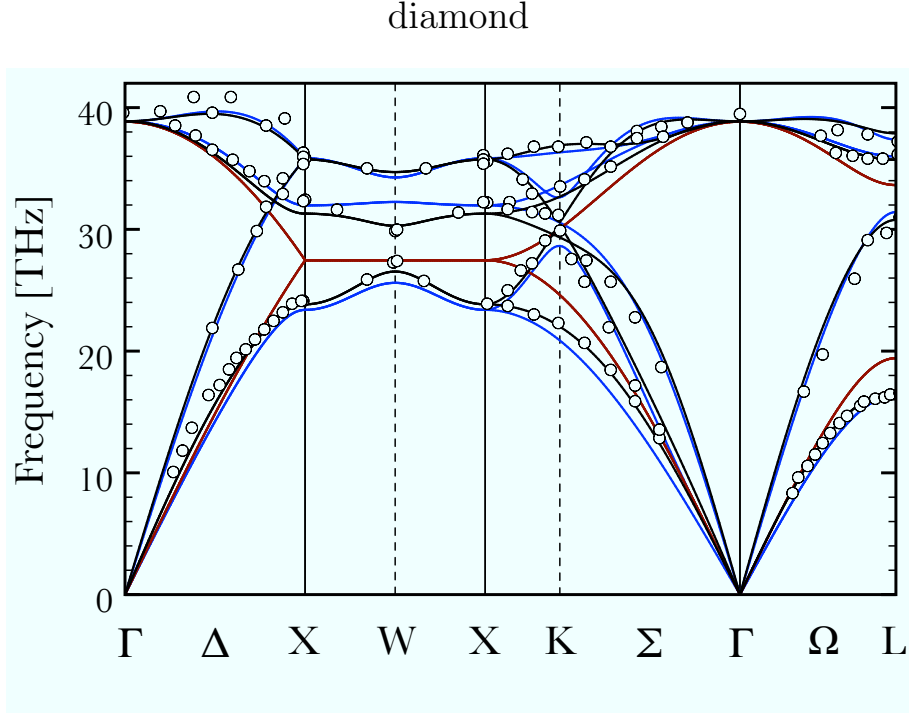


FIGURE 3.8: The phonon dispersions for diamond calculated with *f*PHON and VASP using a supercell with 2 atoms (red lines), 16 atoms (blue lines) and 54 atoms (black lines) are compared to experimental values [26] (circles). The phonons were calculated with a displacement of 0.02 Å.

From this one can deduce that $D^{\kappa\kappa}$ only depends on the acting forces $\vec{F}(u_{l\kappa}\vec{e}_\beta, \vec{R}_{l\kappa})$ of the displaced atom at $\vec{R}_{l\kappa}$ with

$$D^{\kappa\kappa}(\Gamma) = \frac{1}{M_\kappa} \Phi \begin{pmatrix} 0 \\ \kappa \\ \kappa \end{pmatrix} . \quad (3.69)$$

Therefore, deriving

$$D^{\kappa\kappa}(\Gamma) = - \sum_{\kappa' \neq \kappa} \frac{\sqrt{M_\kappa M_{\kappa'}}}{M_\kappa} D^{\kappa\kappa'}(\Gamma) . \quad (3.70)$$

As graphene and diamond have two carbon atoms in the unit cell, i.e. $M_{\text{carbon}} = M_\kappa = M_{\kappa'}$, the relation

$$\begin{aligned} D^{11}(\Gamma) &= -D^{12}(\Gamma) \\ D^{22}(\Gamma) &= -D^{21}(\Gamma) , \end{aligned} \quad (3.71)$$

is valid. Hence, the calculated dispersion at Γ is independent of the supercell size. The slight discrepancy in the calculated dispersion for the single unit cell graphene case (Fig. 3.7) can be attributed to the falsification of the forces due to the force superposition.

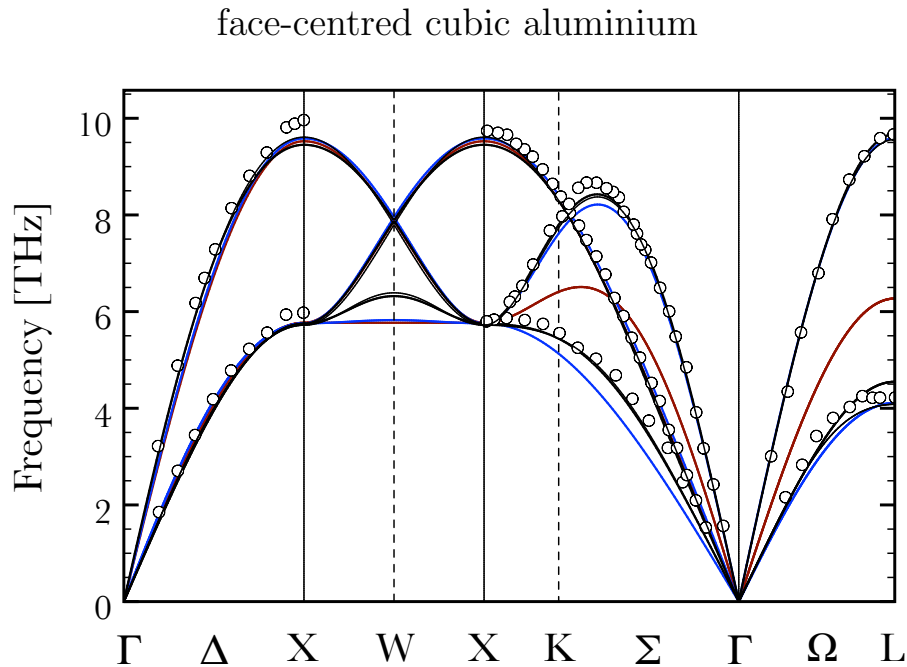


FIGURE 3.9: The phonon dispersions for face-centred cubic aluminium calculated with *f*PHON and VASP using a supercell with 4 atoms (red lines), 8 atoms (blue lines) and 27 atoms (black lines) are compared to experimental values [27] (circles). The phonons were calculated with a displacement of 0.02 Å.

3.5 Imaginary Frequency

If in Eq. 3.12 the eigenvalue ω^2 is negative, then frequency ω is imaginary. Inserting this imaginary ω into the time factor $e^{i\omega t}$ of Eq. 3.10 makes the effect of the imaginary frequency obvious. With the exponent becoming real the exponential function stops oscillating with t . It now describes a non-vibrating mode. Depending on the prefix (+ or -) $\vec{u}(t) \rightarrow 0$ or $\vec{u}(t) \rightarrow \infty$.

*f*PHON distinguishes imaginary frequencies by representing them as negative values, while real frequencies are given as positive values. Furthermore, imaginary frequencies are usually discarded when calculating thermodynamical parameters such as entropy or free energy. Subsequently these parameters are underestimated if the relative number of imaginary modes is high.

There are several reasons for non-vibrating modes: the crystal is dynamically unstable; higher-order anharmonic terms are necessary to describe the lattice dynamics; the displacement amplitude was too small or too large.

body-centred cubic zirconium

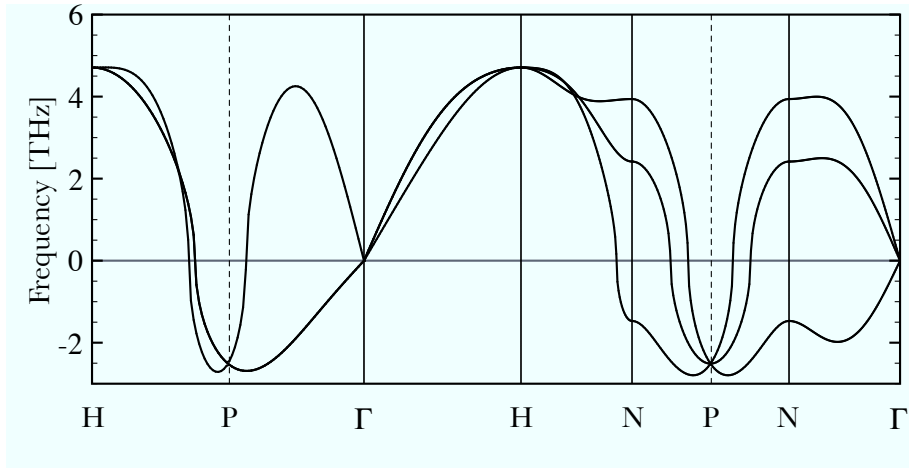


FIGURE 3.10: The phonon dispersions for body-centred cubic zirconium is shown as calculated for a supercell with 32 atoms and using a displacement of 0.02 Å. Imaginary frequencies are indicated by negative values.

In Fig. 3.10 the dispersion relation of body-centred cubic zirconium as calculated by using a $3 \times 3 \times 3$ supercell with 27 atoms is shown. As is well known [28] this system needs anharmonic terms to correctly describe the phonons. Therefore it is not surprising that imaginary modes are found in this calculation.

3.6 Physical Properties

3.6.1 Displacements

Time dependent displacements $\vec{u}_{l\kappa,j}(t)$ can be calculated using $\omega_j(\vec{q})$ with the corresponding polarisation vector $\vec{\epsilon}_{\kappa,j}$ in Eq. 3.10. As the polarisation vectors are orthonormal (see Eq. 3.15) only the real part of the displacement is used (see chapter 22 of Ref. [15]) with

$$u_{l\kappa,j,\alpha}(t) = \frac{1}{\sqrt{M_\kappa}} \operatorname{Re} \left[\epsilon_{\kappa,j,\alpha}(\vec{q}) e^{i(\vec{q} \cdot \vec{R}_{l\kappa} - \omega_j(\vec{q})t)} \right]. \quad (3.72)$$

3.6.2 Density of States

The phonon density of states (DOS) $g(E)$ is defined by an integral over \vec{q} and a sum over modes j (see page 179 in Ref. [15] and page 96 in Ref. [29]) normalised by the volume of

TABLE 3.1: Conversion factors for phonons.

	THz	meV	cm ⁻¹
THz	-	4.1357	33.357
meV	0.2418	-	8.066
cm ⁻¹	0.03	0.124	-

the reciprocal cell $((2\pi)^3/\Omega$ with Ω defining the cell volume) with

$$g(E) = \int_{\vec{q}} \sum_j^{3N} \frac{\Omega}{(2\pi)^3} \delta(E_j(\vec{q}) - E) d^3\vec{q}. \quad (3.73)$$

Deriving the number of states per energy interval $\delta(E_j(\vec{q}) - E)$ in units of meV. As $E_j(\vec{q}) = \hbar\omega_j(\vec{q})$, the phonon density of states can also be given in terms of frequencies, i.e. in unit THz, or as wave length λ in the units cm⁻¹ using the speed of light c as a conversion factor with $\lambda = c/\omega$. One can easily convert from one of the units to another by simply using the correct conversion factors listed in table 3.1. An example for the phonon density of states is shown in Fig. 3.11 for face-centred tetragonal indium.

If the unit cell contains more than one atom, the partial density of states (PDOS) can be useful. These are derived by reformulating Eq. 3.39 to

$$E_\kappa = \sum_{\vec{q}}^{N_q} \sum_j^{3N} |\vec{\epsilon}_{\kappa,j}^*(\vec{q}) \cdot \vec{\epsilon}_{\kappa,j}(\vec{q})| \hbar\omega_j(\vec{q}) \left(\bar{n}_{\vec{q},j} + \frac{1}{2} \right) = \sum_{\vec{q}}^{N_q} \sum_j^{3N} |\vec{\epsilon}_{\kappa,j}^*(\vec{q}) \cdot \vec{\epsilon}_{\kappa,j}(\vec{q})| E_j(\vec{q}). \quad (3.74)$$

As the sum over all eigenvector scalar products is one, the sum of the PDOS

$$g_\kappa(E) = \int_{\vec{q}} \sum_j^{3N} \frac{\Omega}{(2\pi)^3} \delta(E_{\kappa,j}(\vec{q}) - E) d^3\vec{q} \quad (3.75)$$

equals the DOS,

$$g(E) = \sum_{\kappa} g_\kappa(E). \quad (3.76)$$

face-centred tetragonal indium

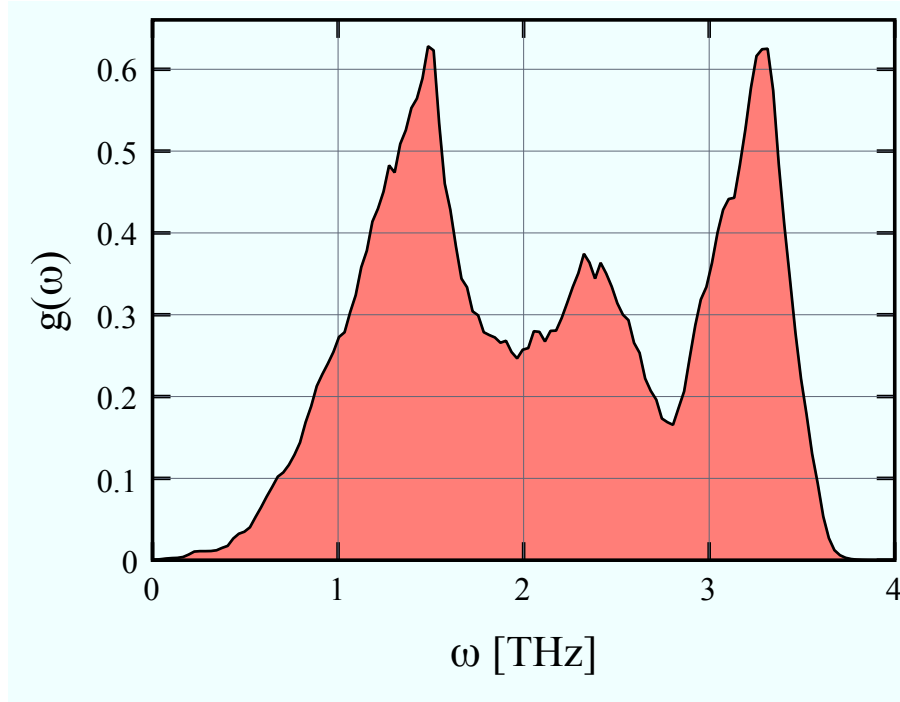


FIGURE 3.11: Phonon density of states (DOS) for face-centred tetragonal indium calculated by *f*PHON and VASP.

3.6.3 Partition Function

Phonons are bosons, hence, their partition function at temperature T is given as the sum over all n phonons with frequency $\omega_j(\vec{q})$ (page 89 in Ref. [30]),

$$Z(T, V, N) = \sum_{\vec{q}}^{N_q} \sum_j^{3N} \sum_{n_{\vec{q},j}} \exp(-\beta n_{\vec{q},j} E_j(\vec{q}, \omega)) \quad \text{with} \quad \beta = \frac{1}{k_B T}. \quad (3.77)$$

One notices that the sum over n is the geometric series of $1/(1 - e^{-\beta \hbar \omega_j(\vec{q})})$. Therefore, the partition function can be rewritten in its final form

$$Z(T, V, N) = \sum_{\vec{q}}^{N_q} \sum_j^{3N} \left(\frac{1}{1 - e^{-\beta \hbar \omega_j(\vec{q})}} \right). \quad (3.78)$$

face-centred tetragonal indium

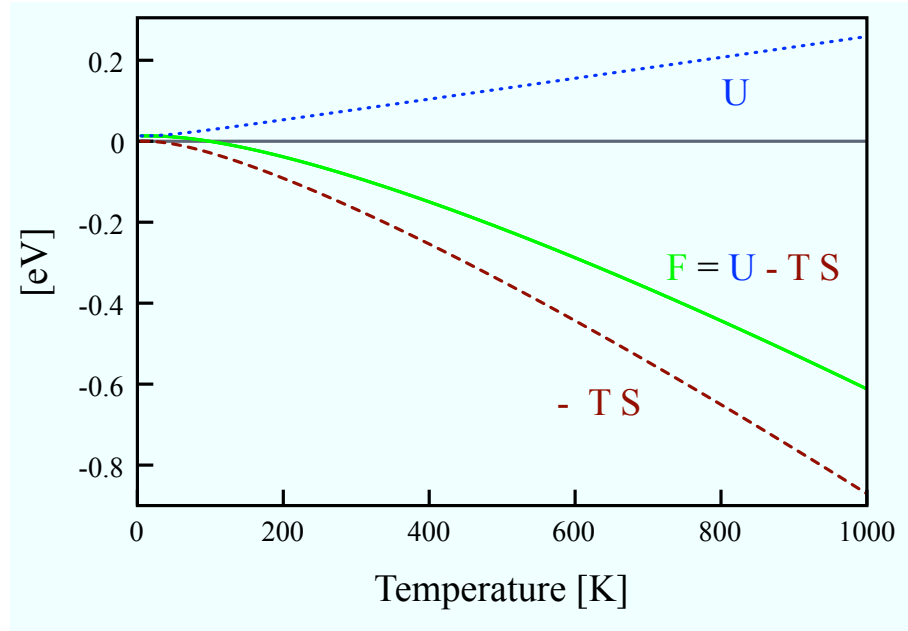


FIGURE 3.12: For face-centred tetragonal indium the vibrational free energy F_{phon} (green solid line) is shown in comparison to the vibrational internal energy U_{phon} (blue dotted line) and the vibrational entropy S_{phon} times temperature T (red dashed line). These values were calculated with *f*PHON and VASP.

3.6.4 Free Energy

Using the partition function (Eq. 3.78) the Helmholtz free energy F is expressed by (see page 62 in Ref. [30])

$$F = -k_B T \ln(Z) . \quad (3.79)$$

Adding the zero point energy $\frac{\hbar\omega}{2}$ of Eq. 3.39 derives

$$F_{\text{phon}} = \sum_{\vec{q}}^{N_q} \sum_j^{3N} \left(\frac{\hbar\omega_j(\vec{q})}{2} + k_B T \ln(1 - e^{-\beta\hbar\omega_j(\vec{q})}) \right) . \quad (3.80)$$

Applying the relation

$$\frac{\hbar\omega_j(\vec{q})}{2} = \beta k_B T \frac{\hbar\omega_j(\vec{q})}{2} = k_B T \ln(e^{\frac{\beta\hbar\omega_j(\vec{q})}{2}}) \quad (3.81)$$

Eq. 3.80 is rewritten to

$$F_{\text{phon}} = k_B T \sum_{\vec{q}}^{N_q} \sum_j^{3N} \ln \left(2 \sinh \left(\frac{\beta \hbar \omega_j(\vec{q})}{2} \right) \right). \quad (3.82)$$

Now the sum over \vec{q} can be replaced by using the DOS $g(\omega)$ (Eq. 3.73), finally leading to the free energy

$$F_{\text{phon}} = k_B T \int_{\omega=0}^{\infty} d\omega g(\omega) \ln \left(2 \sinh \left(\frac{\beta \hbar \omega}{2} \right) \right). \quad (3.83)$$

As an example Fig. 3.12 shows $F_{\text{phon}}(T)$ for face-centred tetragonal indium.

3.6.5 Internal Energy

The internal energy of a system is defined by (see page 182 in Ref. [31])

$$U = -\frac{\partial \ln(Z)}{\partial \beta}. \quad (3.84)$$

Again, using the phonon partition function and taking the zero point energy into account derives the following expression for the internal energy

$$U_{\text{phon}} = \sum_{\vec{q}}^{N_q} \sum_j^{3N} \left(\frac{\hbar \omega_j(\vec{q})}{2} + \frac{\partial \ln(1 - e^{-\beta \hbar \omega_j(\vec{q})})}{\partial \beta} \right) \quad (3.85)$$

Derivating the logarithm term the above equation becomes

$$\begin{aligned} U_{\text{phon}} &= \sum_{\vec{q}}^{N_q} \sum_j^{3N} \left(\frac{\hbar \omega_j(\vec{q})}{2} + \hbar \omega_j(\vec{q}) e^{-\beta \hbar \omega_j(\vec{q})} \frac{1}{1 - e^{-\beta \hbar \omega_j(\vec{q})}} \right) \\ &= \frac{1}{2} \sum_{\vec{q}} \sum_j \hbar \omega_j(\vec{q}) \left(\frac{e^{\beta \hbar \omega_j(\vec{q})} + 1}{e^{\beta \hbar \omega_j(\vec{q})} - 1} \right). \end{aligned} \quad (3.86)$$

Reformulating the sum to an integration over ω using the DOS and substituting the exponential functions by coth the internal energy can be formulated as

$$U_{\text{phon}} = \frac{1}{2} \int_{\omega=0}^{\infty} d\omega g(\omega) \hbar \omega \coth \left(\frac{\beta \hbar \omega}{2} \right), \quad (3.87)$$

plotted again in Fig. 3.12 for face-centred tetragonal indium.

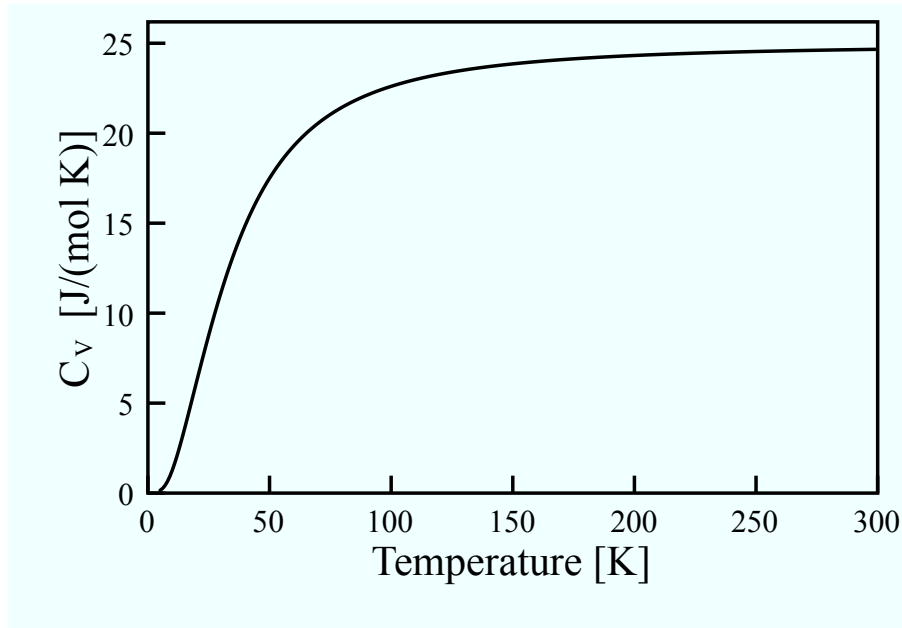


FIGURE 3.13: Vibrational specific heat C_V of face-centred tetragonal indium, calculated using *f*PHON and VASP.

3.6.6 Entropy

The vibrational entropy S_{phon} can be formulated in terms of internal energy U_{phon} and free energy F_{phon} with (see page 185 in [31])

$$F_{\text{phon}} = U_{\text{phon}} - TS_{\text{phon}} . \quad (3.88)$$

Hence,

$$S_{\text{phon}} = \frac{U_{\text{phon}} - F_{\text{phon}}}{T} . \quad (3.89)$$

Inserting U_{phon} (Eq. 3.83) and F_{phon} (Eq. 3.87) leads to the final form

$$S_{\text{phon}} = k_B \int_{\omega=0}^{\infty} d\omega g(\omega) \left[\frac{\hbar\omega}{2k_B T} \coth\left(\frac{\beta\hbar\omega}{2}\right) - \ln\left(2 \sinh\left(\frac{\beta\hbar\omega}{2}\right)\right) \right] . \quad (3.90)$$

3.6.7 Specific Heat

The specific heat at constant volume V is defined as (see page 67 in Ref. [30])

$$C_V = \left. \frac{\partial U_{\text{phon}}}{\partial T} \right|_{V=\text{const}} . \quad (3.91)$$

Using the phonon energy term (Eq. 3.39) the vibrational specific heat is formulated as

$$\begin{aligned} C_V &= \sum_{\vec{q}}^{N_q} \sum_j^{3N} \hbar\omega_j(\vec{q}) \frac{\partial \bar{n}_{\vec{q},j}(T)}{\partial T} \\ &= \sum_{\vec{q}}^{N_q} \sum_j^{3N} k_B (\beta\hbar\omega_j(\vec{q}))^2 \frac{e^{\beta\hbar\omega_j(\vec{q})}}{(e^{\beta\hbar\omega_j(\vec{q})} - 1)^2}, \end{aligned} \quad (3.92)$$

or reformulated in terms of the DOS $g(\omega)$ as

$$C_V = k_B \int_{\omega=0}^{\infty} d\omega g(\omega) (\beta\hbar\omega)^2 \frac{e^{\beta\hbar\omega}}{(e^{\beta\hbar\omega} - 1)^2}. \quad (3.93)$$

The vibrational specific heat of face-centred tetragonal indium at constant volume C_V is shown in Fig. 3.13. As the electronic contribution to the specific heat is not considered the calculated value of 24.7 J/(mol K) at 298.15 K is lower than the experimentally derived value of 26.9 J/(mol K) [32].

3.7 Implementation in *f*PHON

The force-constant phonon program *f*PHON, short for *full-symmetry* PHON, is based on the package PHON, a phonon calculation program written by D. Alfè [5, 6].

The original code was substantially modified.

- The primitive unit cell and its lattice vectors are now automatically identified as well as the space and point group symmetry using the lattice and symmetry subroutines of VASP. These subroutines were written by J. Furthmüller and published as open source (GPL) under *www.freeware.vasp.de*. The program *f*PHON uses these lattice vectors to identify the coordinates of the unit cell atoms.

The benefits of using these VASP subroutines are twofold. It is not anymore necessary to construct the supercell as multiples of the primitive unit cell, as *f*PHON will automatically find the correct cell type and primitive vectors regardless of how the supercell is constructed. Furthermore, *f*PHON can now calculate the phonon dispersion for a greater variety of lattice types, e.g. also for tetragonal lattice structures.

- An error in the symmetrization scheme enforcing of the force-constant matrix Φ has been corrected! This scheme is enforced in two steps. First, by subtracting

$$\delta\Phi = (NC)^{-1} \sum_{l'\kappa'} \Phi \begin{pmatrix} l & l' \\ \kappa & \kappa' \end{pmatrix}_{\alpha\beta} \quad (3.94)$$

(with N defining the number of atoms in the primitive cell and C the number of primitive cells in the supercell) from all force-constants and then by averaging the force-constant matrices $\Phi \begin{pmatrix} l & l' \\ \kappa & \kappa' \end{pmatrix}_{\alpha\beta}$ and $\Phi \begin{pmatrix} l' & l \\ \kappa' & \kappa \end{pmatrix}_{\beta\alpha}$. An error occurred in the previous code where this symmetrization was enforced on the force-constant which should not exist as either one of the two atoms at positions $R_{l\kappa}$ or $R_{l'\kappa'}$ did not exist. This led due to Eq. 3.94 to wrong values for all force-constants and hence to erroneous results for body-centred tetragonal compounds without a centre of inversion like BaPtSi₃, SrPdGe₃ and SrPtGe₃.

*f*PHON now checks if the force-constant really exists before enforcing the symmetrization.

- It is now possible to calculate the vibrational free energies, the vibrational entropies, the vibrational internal energies and the specific heat for a range of temperatures. This is done by calculating the eigenvectors and eigenvalues once, and then using them repeatedly to calculate the thermodynamical parameters at different temperatures. All values are now written temperature dependent into the file ENTRO. Note, the specific heat is now given in J/(mol K).
- If net forces exist in a supercell in equilibrium, i.e. with $\vec{u} = 0$, then this force-field $\mathfrak{F}(\vec{u} = 0)$ is subtracted from all other force-fields $\mathfrak{F}(\vec{u}_{lk})$ by

$$\tilde{\mathfrak{F}}(\vec{u}_{lk}) = \mathfrak{F}(\vec{u}_{lk}) - \mathfrak{F}(\vec{u} = 0) . \quad (3.95)$$

Thereby the accuracy of the phonon calculations for low-symmetry supercells is increased when full atomic relaxation is difficult to obtain.

- The partial density of states (PDOS) of every atom in the primitive unit cell, not just the PDOS of an atom species as implemented in PHON, can now be written out. Furthermore, *f*PHON groups the PDOS according to the atom species or symmetrically equivalent atoms.
- Parts of the code, in which the DOS and the dispersion relation are calculated, are now in separate subroutines. This makes future changes in the code easier to handle.
- The file DYNAMAT, in which VASP writes the force fields from a linear-response calculation, can now be used in *f*PHON.

- The frequencies, eigenvalues, eigenvectors and time-dependent displacement-vectors can be written into the file EIGENPHON. Further it is possible to write POSCAR files at different time steps, where all atoms are displaced using $\vec{u}(t)$.
- The use of symmetry as well as the reduction to the primitive unit cell can now be selectively switched on and off in *f*PHON.

The detailed user manual of *f*PHON is given in [Appendix B](#).

Chapter 4

Isolated Defect Model

Within the supercell approach the defect formation energy ε^{X_i} for a single substitutional defect cluster X_i consisting of n_{X_i} defect atoms is defined by

$$\varepsilon^{X_i} = (n_{X_i} + n_{\text{H}})E_{\text{DFT}}^{X_i+\text{H}} - (n_{X_i}E_{\text{DFT}}^{X_i} + n_{\text{H}}E_{\text{DFT}}^{\text{H}}), \quad (4.1)$$

which is the difference between the DFT total energies of the supercell containing the defect cluster with n_{X_i} defect atoms and n_{H} host atoms and the corresponding reference energies of the ground-state phases of the host and defect atomic species. For substitutional defects the sum $n_{X_i} + n_{\text{H}}$ equals the number of sites in the supercell.

One can go beyond the standard supercell DFT total energies approach by including vibrational free energies derived within the harmonic approximation. Then, the vibrational defect formation energy $f^{X_i}(T)$ is given by

$$f^{X_i}(T) = (n_{X_i} + n_{\text{H}})F_{\text{phon}}^{X_i+\text{H}}(T) - (n_{X_i}F_{\text{phon}}^{X_i}(T) + n_{\text{H}}F_{\text{phon}}^{\text{H}}(T)). \quad (4.2)$$

It should be noted, that the vibrational free energy $F_{\text{phon}}(T) = U_{\text{phon}}(T) - TS_{\text{phon}}(T)$ is temperature dependent and includes the vibrational entropy $S_{\text{phon}}(T)$. The reference free energies entering Eq. 4.2, again, correspond to the ground-state phases of the defect and host atomic species and are subtracted from the vibrational free energy of the supercell.

So far, only ordered phases in terms of the supercell approach are considered. Describing effects of alloying by defects the configurational entropy has to be taken into account (see next section) which allows to derive temperature and concentration dependent free energies.

4.1 Configurational Entropy

In this section a strategy to describe the configurational entropy of non-interacting (independent or isolated) defect clusters that may contain any finite number of defect atoms (including vacancies) is elaborated. In the spirit of Kikuchi *et al.* [33] the configurational entropy is evaluated in terms of bonds rather than sites. Assuming non-interacting defect clusters the number of different distributions probability of cluster X_i is given by the standard binomial distribution

$$W_i(B_i, b_i) = \frac{B_i!}{(B_i - b_i)!b_i!}, \quad (4.3)$$

in which B_i denotes the total number of bonds in the system available for the defect cluster X_i , whereas b_i is the number of bonds occupied by the defect cluster X_i . Then, the total probability for a set of independent defect clusters $X_1 \dots X_i \dots X_m$ occurring $n_1 \dots n_i \dots n_m$ times in the system will be a product of the individual probabilities

$$W_{\text{tot}} = W_1 \cdots W_i \cdots W_m. \quad (4.4)$$

In the corresponding configurational entropy S_{conf} one has to divide by the total number of available bonds B which makes it independent of the actual size of the system.

In the present work combinations of n_1 single-atom defects X_1 with $n_{X_1} = 1$ and n_2 pair-wise defects X_2 with $n_{X_2} = 2$ are taken into account, whereby the pair-wise defects consist of two nearest-neighbour defect atoms. The concept for deriving W_{tot} (and concomitantly S_{conf}) can be generalised to any type of substitutional defect clusters, e.g. pair-wise, 3-atoms, 4-atoms, etc. nearest-neighbour atom clusters. In fact, such elaborate studies were already done for the Fe-Cu system and the results are now prepared for publication.

Each lattice site is connected to its neighbouring sites by ν bonds, whereby ν is one half of the number of nearest-neighbour distances for a given lattice. For example, $\nu = 4$ or 6 correspond to a bcc or fcc lattice, respectively. Hence, the total number of bonds B for a given lattice with N lattice sites is given by $B = \nu N$. Since each single-atom defect is connected by ν bonds to its neighbouring sites, the possible distributions of all these single-atom defects is described by

$$W_1(B_1, b_1) : \quad B_1 = B, \quad b_1 = \nu n_1. \quad (4.5)$$

If no other defects are present the resulting entropy S_{conf} will be the standard mixing entropy for an ideal solution.

Considering pair-wise substitutional defects, it is noted that each pair-wise defect is connected by $2\nu - 1$ bonds to its neighbouring sites, since each substitutional pair-wise defect

contains one complete bond, namely the bond between the two defect atoms. Therefore, for n_2 pair-wise defects the total number of available bonds is reduced to $B_2 = B - n_2$ and the number of different distributions of these pair-wise defects is given by

$$W_2(B_2, b_2) : \quad B_2 = B - n_2, \quad b_2 = (2\nu - 1)n_2. \quad (4.6)$$

The resulting total number of distributions of single-atom and pair-wise defects W_{2+1} is described by the product of the distributions of single-atom and pair-wise defects by

$$W_{2+1} = W_2(B_2, b_2)W_1(B_2 - b_2, b_1) \quad (4.7)$$

$$= \frac{B_2!}{b_1! b_2! (B_2 - b_1 - b_2)!}. \quad (4.8)$$

It should be noted, that the number of available bonds for the single-atom defects is now reduced to $B - 2\nu n_2$, since $2n_2$ sites are occupied by atoms belonging to the pair-wise defects. Making use of Eq. 4.6 this difference is equal to $B_2 - b_2$.

From $S_{\text{conf}} = k_B \ln W_{2+1}$ and applying Stirling's approximation, the configurational entropy for a mixture of independent single-atom and pair-wise substitutional defects is finally given by

$$S_{\text{conf}} = k_B \left[\left(1 - \frac{c_2}{\nu}\right) \ln \left(\frac{1 - \frac{c_2}{\nu}}{1 - c_1 - 2c_2}\right) - \kappa c_2 \ln \left(\frac{\kappa c_2}{1 - c_1 - 2c_2}\right) - c_1 \ln \left(\frac{c_1}{1 - c_1 - 2c_2}\right) \right], \quad (4.9)$$

in which the abbreviation $\kappa = \frac{2\nu-1}{\nu}$ and the concentrations $c_1 = n_1/N, c_2 = n_2/N$ of the single-atom and pair-wise defects are introduced. If the number of pair-wise defects is zero, i.e. $c_2 = 0$, the well-known expression of S_{conf} for the standard mixing entropy of an ideal solution is rederived.

4.2 Grand Canonical Approach

The configurational entropy for the system with single-atom and pair-wise defects is treated by a grand canonical approach writing the total free energy, which depends on the temperature T and the concentrations of point and pair-wise defects c_1 and c_2 , as

$$F_{\text{tot}}(c_1, c_2, T) = c_1 \varepsilon_1^{\text{eff}}(T) + c_2 \varepsilon_2^{\text{eff}}(T) - TS_{\text{conf}}(c_1, c_2). \quad (4.10)$$

In this equation the effective substitution energies are introduced for point defects $\varepsilon_1^{\text{eff}}(T) = \varepsilon^{X_1} + f^{X_1}(T)$ and pair-wise defects $\varepsilon_2^{\text{eff}}(T) = \varepsilon^{X_2} + f^{X_2}(T)$, i.e. the sum of the DFT-derived formation energy ε^{X_i} (Eq. 4.1) and the vibrational formation energy f^{X_i} (Eq. 4.2) which already includes the vibrational entropy.

Using F_{tot} a grand canonical potential can be designed in terms of an Euler-Lagrange equation with the constraint $x = c_1 + 2c_2$ as

$$J'(c_1, c_2, T) = F_{\text{tot}}(c_1, c_2, T) + \mu(x - c_1 - 2c_2). \quad (4.11)$$

The Lagrange parameter μ represents the chemical potential.

Calculating the gradient of J' with respect to the variables c_1 and c_2 leads to,

$$\frac{\partial J'(c_1, c_2, T)}{\partial c_1} = \varepsilon_1^{\text{eff}}(T) - \mu - T \frac{\partial S_{\text{conf}}(c_1, c_2)}{\partial c_1}, \quad (4.12)$$

$$\frac{\partial J'(c_1, c_2, T)}{\partial c_2} = \varepsilon_2^{\text{eff}}(T) - 2\mu - T \frac{\partial S_{\text{conf}}(c_1, c_2)}{\partial c_2}. \quad (4.13)$$

Inserting the entropy from Eq. 4.9 leads to

$$\frac{\partial J'(c_1, c_2, T)}{\partial c_1} = \varepsilon_1^{\text{eff}}(T) - \mu + k_B T \ln \left(\frac{c_1}{1 - c_1 - 2c_2} \right), \quad (4.14)$$

$$\frac{\partial J'(c_1, c_2, T)}{\partial c_2} = \varepsilon_2^{\text{eff}}(T) - 2\mu + 2k_B T \ln \left(\frac{\left(1 - \frac{c_2}{\nu}\right)^{\frac{1}{2\nu}} (\kappa c_2)^{\frac{\kappa}{2}}}{1 - c_1 - 2c_2} \right). \quad (4.15)$$

$$(4.16)$$

Requiring the minimizing condition $\nabla J(c_1, c_2) = \vec{0}$ and abbreviating $\beta = \frac{1}{k_B T}$ gives the final set of coupled equations,

$$\frac{\partial J'}{\partial c_1} = 0 \Rightarrow e^{-\beta(\varepsilon_1^{\text{eff}} - \mu)} = \frac{c_1}{1 - c_1 - 2c_2}. \quad (4.17)$$

$$\frac{\partial J'}{\partial c_2} = 0 \Rightarrow e^{-\frac{\beta}{2}(\varepsilon_2^{\text{eff}} - 2\mu)} = \frac{\left(1 - \frac{c_2}{\nu}\right)^{\frac{1}{2\nu}} (\kappa c_2)^{\frac{\kappa}{2}}}{1 - c_1 - 2c_2}. \quad (4.18)$$

Reformulating Eq. 4.17 for a system containing only single-atom defects ($c_2 = 0$) leads to

$$c_1 = \frac{e^{-\beta(\varepsilon_1^{\text{eff}})}}{1 + e^{-\beta\varepsilon_1^{\text{eff}}}}. \quad (4.19)$$

The reader might notice, that the Lagrange parameter μ has vanished in the above equation. This is a result of the constrain trivially becoming $x = c_1$.

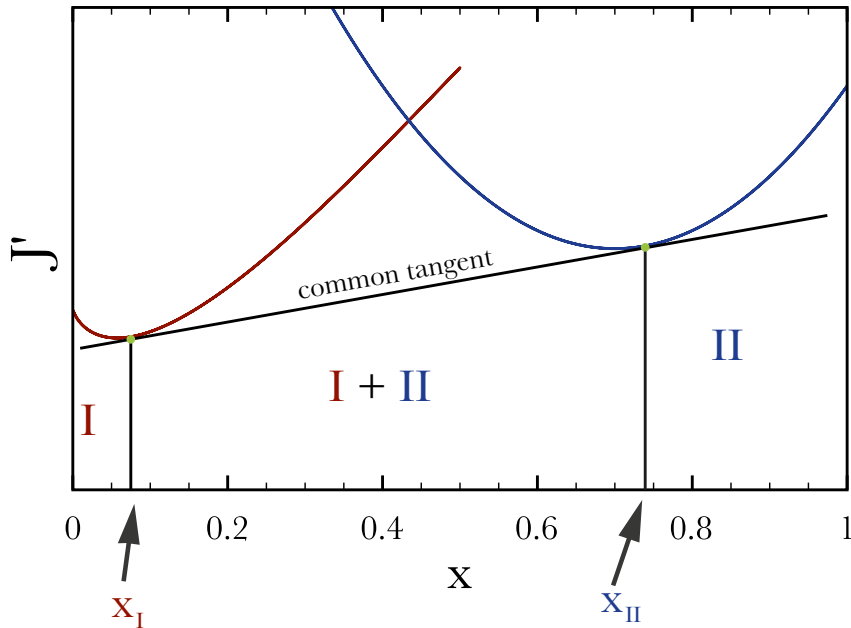


FIGURE 4.1: Example of the grand canonical potential J' for a $A_{1-x}B_x$ alloy at a given temperature for thermodynamically stable solid solutions at the A-rich and B-rich sides. The common tangent defining the limits of solubility touches J' at x_I and x_{II} , between which the alloy decomposes into a mixture of phases with concentrations x_I and x_{II} , respectively. The thermodynamically stable phase I exists in the range $0 \leq x \leq x_I$, whereas phase II is stable for $x_{II} \leq x \leq 1$.

Assuming very small defect point defect concentrations, i.e. $c_1 \approx 0$ and hence $1 \gg e^{-\beta(\epsilon_1^{\text{eff}})}$, one arrives at the well known expression (page 784 in [15])

$$c_1 \approx e^{-\beta\epsilon_1^{\text{eff}}}. \quad (4.20)$$

4.3 Solubility

The phase diagram for a binary system $A_{1-x}B_x$ with two stable phases I and II consisting of A-rich and B-rich solid solutions (i.e. small concentrations of defect atoms) is constructed from Eq.s 4.17 and 4.18. The constraints for the set of coupled equations are $x = c_1^B + 2c_2^B$ $1 - x = c_1^A + 2c_2^A$, and the concentrations c_1^B and c_2^B describe the single-atom and pair-wise defect concentrations of element B in an A host, whereas c_1^A and c_2^A is used to describe A defects in a B host. Solving the equations self-consistently for a given concentration x and temperature T yields the defect concentrations c_1^B , c_2^B , c_1^A and c_2^A with corresponding chemical potentials μ^A and μ^B . Numerically this is done by means of the global convergent Newton-Raphson method (chapter 9.6 in [34]). Inserting these

values into Eq. 4.10 the grand canonical potentials J'_I and J'_{II} for the A-rich and B-rich side, respectively, are found.

As illustrated in Fig. 4.1 the common tangent construction [35] allows to determine the solubility range of defects in the host materials. The common tangent touches the J'_I and J'_{II} at the limiting concentrations x_I and x_{II} , respectively. Thermodynamically stable phases exist in the ranges $0 \geq x \geq x_I$ (phase I) and $x_{II} \geq x \geq 1$ (phase II). Thus, defining the miscibility gap $x_I < x < x_{II}$ where the two phases are mixed with weights

$$w_{II} = \frac{x - x_I}{x_{II} - x_I}, \quad w_I = 1 - w_{II} . \quad (4.21)$$

In the miscibility range the potential becomes the common tangent

$$J'_{\text{tot}}(x) = J'_I(x_I) \frac{x_{II} - x}{x_{II} - x_I} + J'_{II}(x_{II}) \frac{x - x_I}{x_{II} - x_I} . \quad (4.22)$$

Calculating the concentration dependent $J'(x, T)$, as described above, for a set of temperatures and using the common tangent construction the solubility range of defects in A- and B-rich solid solutions can be determined [36].

Chapter 5

Cluster Expansion

By standard DFT approaches systems with cells containing a few hundred atoms can be treated to derive total energies, forces, etc. with typical DFT accuracies.

Furthermore, when describing concentration dependent thermodynamical properties of a multicomponent system one has to sample configuration space, which scales by 2^N for a binary system with N lattice sites. Within DFT this is unfeasible even for small unitcells/supercells. A technique to overcome this size and configuration limitation by maintaining DFT accuracy is the cluster expansion (CE) method. CE applies a set of DFT input structures to fit a set of effective cluster interaction energies (ECI). This set can then be used to calculate the properties of a much larger set of structures at $T = 0$ K maintaining the DFT accuracy of the input structures. This allows for a fast calculation of the formation energy for any given configuration in a large simulation cell making a thermodynamical statistical sampling of configuration space with Monte Carlo (MC) sampling possible. Thus, using thermodynamical statistics built upon *ab-initio* principles it is possible to predict thermodynamical processes at $T > 0$ K in an alloy with DFT accuracy.

All CE calculations in this work were done using the universal cluster expansion (UNCLE) code developed by S. Müller *et al.* [7, 8].

5.1 Theoretical Background

In CE the Hamiltonian of an alloy with atomic configuration σ , i.e. distribution of atoms on a given lattice, is constructed via an Ising-like *ansatz* [37] on a fictitious fixed lattice. For example, in a binary system atom A on the lattice site i is described by a pseudo-spin $s_i = +1$ while atom B on the same site is described by $s_i = -1$. This binary formalism can

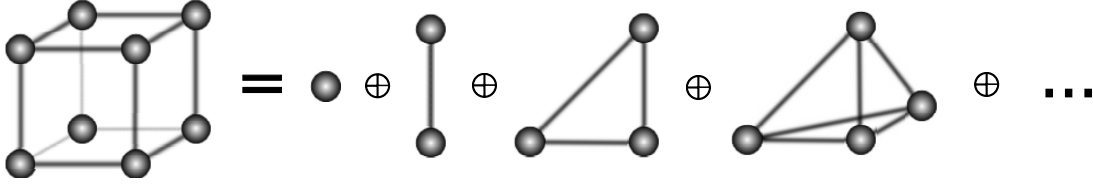


FIGURE 5.1: The CE decomposition of the crystal into points, pairs, triplets and many-body figures is illustrated.

be expanded to ternary, quaternary and larger multicomponent systems using Chebychev polynomials as a orthogonal basis as discussed in Ref. [38].

The energy of any atomic configuration σ , describing a specific distribution of the atoms on the lattice, is constructed in terms of an expansion [39], as illustrated in Fig. 5.1, by

$$E_{\text{CE}}(\sigma) = J_0 + \sum_i J_i s_i(\sigma) + \sum_{j<i} J_{ij} s_i(\sigma) s_j(\sigma) + \sum_{k<j<i} J_{ijk} s_i(\sigma) s_j(\sigma) s_k(\sigma) + \dots, \quad (5.1)$$

with J as the ECI's. J_0 is a configuration independent energy term, while the sum over $J_i s_i(\sigma)$ is the site independent energy of the system depending only on the concentration of the atoms. The summation over $J_{ij} s_i(\sigma) s_j(\sigma)$ includes all possible pair-figures in the alloy while higher order terms reflect many-body interaction, i.e. triplets, quadruplets, etc.

In order to find a more compact formulation of Eq. 5.1 one starts by describing the spin product by

$$\Pi_k(\sigma) = s_{i_1}(\sigma) \cdot s_{i_2}(\sigma) \cdot s_{i_3}(\sigma) \cdots s_{i_{m_k}}(\sigma), \quad (5.2)$$

for figure k with m_k vertices, i.e. over all m_k lattice sites contained within figure k . Using this spin product $\Pi_k(\sigma)$ one introduces the correlation function $\bar{\Pi}_f(\sigma)$ for all figures of class f [40], i.e. all symmetry equivalent figures k collected with a prototype figure f ,

$$\bar{\Pi}_f(\sigma) = \frac{1}{N_{\text{latt}} D_f} \sum_k^{N_{\text{latt}} D_f} \Pi_k(\sigma), \quad (5.3)$$

where N_{latt} describes the number of lattice sites in the system, D_f gives the number of figures that are invariant under the point group symmetry with the sum over all $N_{\text{latt}} D_f$ symmetry equivalent figures in the system.

This correlation function allows for a reformulation of Eq. 5.1 [40],

$$E_{\text{CE}}(\sigma) = N_{\text{latt}} \sum_f^{\infty} D_f J_f \bar{\Pi}_f(\sigma), \quad (5.4)$$

with J_f being the ECI for figure class f .

One should note that the ECI's are fitting parameters obtained by fitting $E_{\text{CE}}(\sigma)$ to values calculated by methods like DFT and, therefore, have no direct physical meaning. The physical nature of the ECI's is determined by the property on which the CE is applied to, e.g. a CE can be done for elastic properties.

However, the CE is only mathematically exact if all possible figures in the crystal are included, i.e. the summations run over an infinite number of figures on an infinite number of sites. Thus, for practical reasons the figure-set $\{f\}$ has to be truncated to a set of N_f figures including all important figures. This problem, i.e. the reasonable truncation of figures, is formulated as a least squares fit procedure of CE derived energies to the energies computed by DFT for N_σ structures (a structure defines a finite cell with fixed configuration σ and periodic boundary conditions) by [8]

$$\sum_{\sigma=1}^{N_\sigma} \left[E_{\text{DFT}}(\sigma) - N_{\text{latt}} \sum_f^{N_f} D_f J_f \bar{\Pi}_f(\sigma) \right]^2 + \sum_f^{N_f} c(\bar{r}_f)^\lambda J_f = \min . \quad (5.5)$$

The last term is a damping term penalising figures with a large spatial extent by using the average figure vertex length \bar{r}_f with scaling parameters c and λ determined internally by UNCLE. This damping is necessary because of the finite size of the input structures and their periodic boundary conditions. Such unphysical figures extending across the periodic boundary condition might correctly reproduce the DFT energies of the input structures but can lead to an artificially periodically ordered system in a larger simulation cell.

When calculating E_{DFT} the structures are allowed to relax fully with respect to atomic positions, cell shape and cell volume. However, the relaxation has to be restricted so that the symmetry of the original lattice is maintained. The fully relaxed DFT energies are then used in the CE on a fixed (i.e. static) lattice. It has been shown by Wolverton and Zunger [41] that this leads to a more accurate CE description of the alloy.

A good figure-set with corresponding ECI's should be able to 'accurately' predict the energies of structures not included in the CE. Of course, determining such a reasonable set is the paramount goal in CE. Thereby one limits oneself to structures that only contain a predefined maximum number of atoms N reducing the maximum number of possible lattice configurations described by these structures. Thus, the total number of possible crystal configurations scales with 2^N for binary systems.

The formation enthalpy of a structure describing configuration σ is given by

$$\Delta H(\sigma) = E_{\text{DFT}}(\sigma) - (xE_{\text{DFT}}^{\text{A}} + (1-x)E_{\text{DFT}}^{\text{B}}) , \quad (5.6)$$

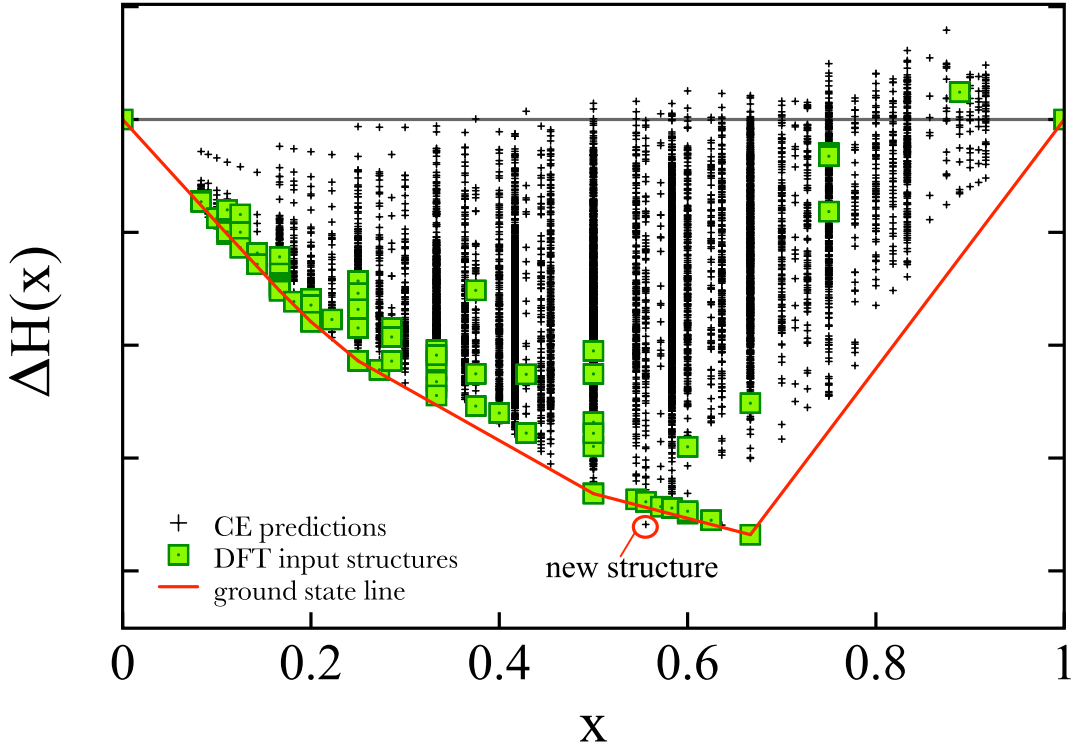


FIGURE 5.2: The formation enthalpy $\Delta H(x)$ versus the concentration of A-atoms x in A_xB_{1-x} is shown for different structures. The red line represents the ground-state line. Note, that the structure below the ground-state line, marked with a red circle, is an important structure and it has to be included as an additional input structure in the CE.

with $E_{\text{DFT}}(\sigma)$ denoting the DFT energy of structure σ , x the A-atom concentration, $E_{\text{DFT}}^{\text{A}}$ the reference energy of the stable A phase and $E_{\text{DFT}}^{\text{B}}$ that of the stable B phase.

Now, in A_xB_{1-x} if for three structures describing configurations α , β and σ with concentrations $x(\alpha) < x(\sigma) < x(\beta)$ the condition

$$\Delta H(\sigma) \leq \frac{x(\sigma) - x(\beta)}{x(\alpha) - x(\beta)} \Delta H(\alpha) + \frac{x(\sigma) - x(\alpha)}{x(\beta) - x(\alpha)} \Delta H(\beta), \quad (5.7)$$

is valid in addition to all three configurations being the ones with the lowest formation enthalpy at their respective concentration and both α and β are ground-state structures, then the structure with configuration σ is also a ground-state structure, as sketched in Fig. 5.2.

In practice a new input structure is found by using a set of structures calculated by DFT as input to a CE. If the CE predicts new structures below the ground-state line that were not included then these are calculated with DFT and subsequently added to the new set

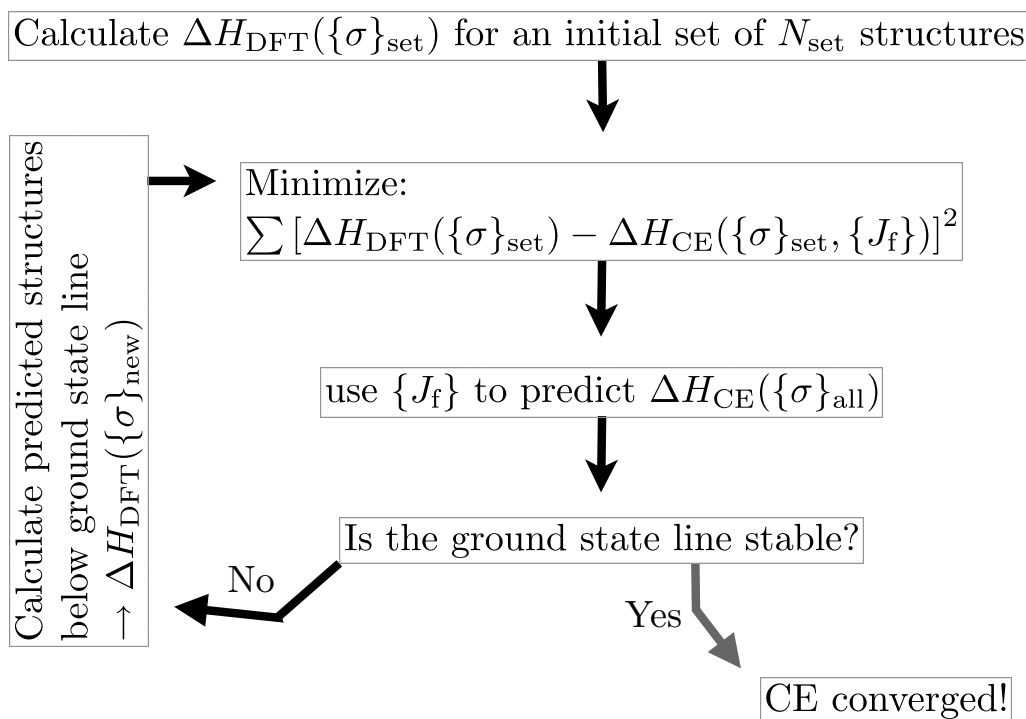


FIGURE 5.3: The standard workflow for the CE is sketched. The formation enthalpies of an initial set of configurations defined by N_{set} input structures calculated with DFT is used for an initial CE. With the fitted set of interaction energies $\{J_f\}$ the enthalpies $\Delta H_{\text{CE}}(\{\sigma\}_{\text{all}})$ of all possible N_{all} configurations (limited by the maximum number of atoms allowed in the structures) are predicted by CE. Configurations predicted to be below the ground-state line defined by the N_{set} input configurations are then identified and the N_{new} structures describing these configurations are calculated with DFT and added to the set of N_{set} input structures. If no new configuration below the ground-state line is found then the CE has converged.

of input structure used for the next CE. This is repeated until no new structure is found below the ground-state line as the work flow illustration in Fig. 5.3 shows.

It should be noted, that because of mathematical reasons the number of input structures N_σ has to be larger than the number of figures N_f in figure-set $\{f\}$.

5.2 Implementation in UNCLE

The question still left unanswered is the minimization method for the multivariable problem. UNCLE uses a genetic algorithm (chapter 10.6.3 in [42]) to find the minimum of Eq. 5.5. Within this genetic algorithm (described in greater detail in the next section)

UNCLE uses a cross validation score (CVS) S_{CV} describing the average error of the CE prediction compared to actual DFT values. However, it is useless to have a set of N_f figures with corresponding ECI's that is only able to accurately reproduce the energies of the input structures. Rather, one wishes to arrive at a set of N_f figures and corresponding ECI's that can accurately predict the energies of structures not used in the fit. The CVS

$$S_{CV} = \sqrt{\frac{1}{nN_{\text{pred}}} \sum_n \sum_{N_{\text{pred}}} [\Delta H_{DFT}(\sigma) - \Delta H_{CE}(\sigma)]^2}, \quad (5.8)$$

is evaluated by dividing the set of N_σ input structures calculated with DFT into n different sets. UNCLE fits the ECI's separately for each set and uses the individual ECI's of a set to predict the energy of N_{pred} structures not included. Therefore, the CVS measures the *predictive* power of a set of ECI's. To evaluate the CVS correctly UNCLE predicts all structures, except the pure phases, at least once.

5.2.1 Genetic Algorithm

A minimization using genetic algorithm was first used for the CE by Hart *et al.* [43]. In this approach the figure list is represented as a binary string. A figure used is marked by the value 1, otherwise the value is 0. Furthermore, the interaction energies are also represented as a binary string. The combination of both binary strings, including figures used and their interaction energies, is now the genetic 'DNA' of a solution, who's fitness is described by the CVS. A higher CVS compared to other solutions means, that this solution has a lower fitness.

Now, a 'population' of n_{pop} different solutions is created, in which the fitness of every individual solution is calculated. Of those n_{pop} individuals only the fittest n_{fit} ($0 < n_{\text{fit}} < n_{\text{pop}}$) individuals are selected to survive to the next iteration process.

The other $n_{\text{pop}} - n_{\text{fit}}$ solutions are replaced by 'descendants' of the surviving fittest 'parent' solutions. Their 'DNA' is created by two different processes as sketched in Fig. 5.4:

- In crossover, the 'DNA' of the 'offspring' is created by mixing the 'DNA' of two randomly selected 'parent' solution. Thereby the 'DNA' of one 'parent' solution is used up to the crossover point. After that point the 'DNA' of the second 'parent' is used.
- In mutation, a random binary bit of the 'DNA' string is flipped from one state to the other, i.e. $1 \Rightarrow 0$ or $0 \Rightarrow 1$.

Note, that one may replace all surviving 'parent' solutions with the 'children', as long as only the fittest 'parent' solutions are used to create them.

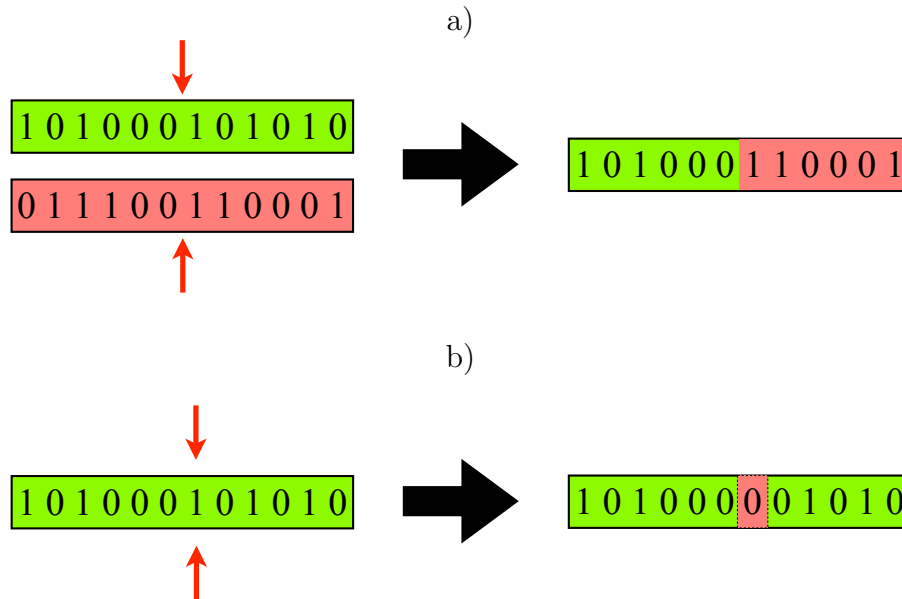


FIGURE 5.4: Illustration of the genetic algorithm: In a) an example of crossover is given. Two ‘parent’ solutions marked red and green are used to create a ‘child’ solution. The sketch in b) shows mutation. A random bit in the binary string is flipped into the opposite state.

Thus, the fitness of the new ‘population’ created by this process can be reevaluated and the whole procedure is repeated until a solution with a small enough CVS is found. This procedure will always find a minimum. But it remains unclear, if a local or global minimum has been found. Therefore, it is advisable to do a number of separate CE and take the solution with the lowest CVS as the final solution. UNCLE can be set up to do this automatically by doing a number of runs sequentially and only storing the best solution at the end.

5.2.2 Monte Carlo

The ECI’s from the CE can be combined with a Monte Carlo (MC) algorithm to statistically sample configuration space allowing for a thermodynamical description of the system.

In principle, MC is based upon a biased random walk of a stationary Markov chain, in which the next state σ_β of the system is only dependent on the previous state σ_α . The probability for a state σ_α is given in MC (chapter 2 in Ref. [44]) by

$$p_\alpha = \frac{1}{Z} e^{\left(-\frac{E(\sigma_\alpha)}{k_B T}\right)}, \quad (5.9)$$

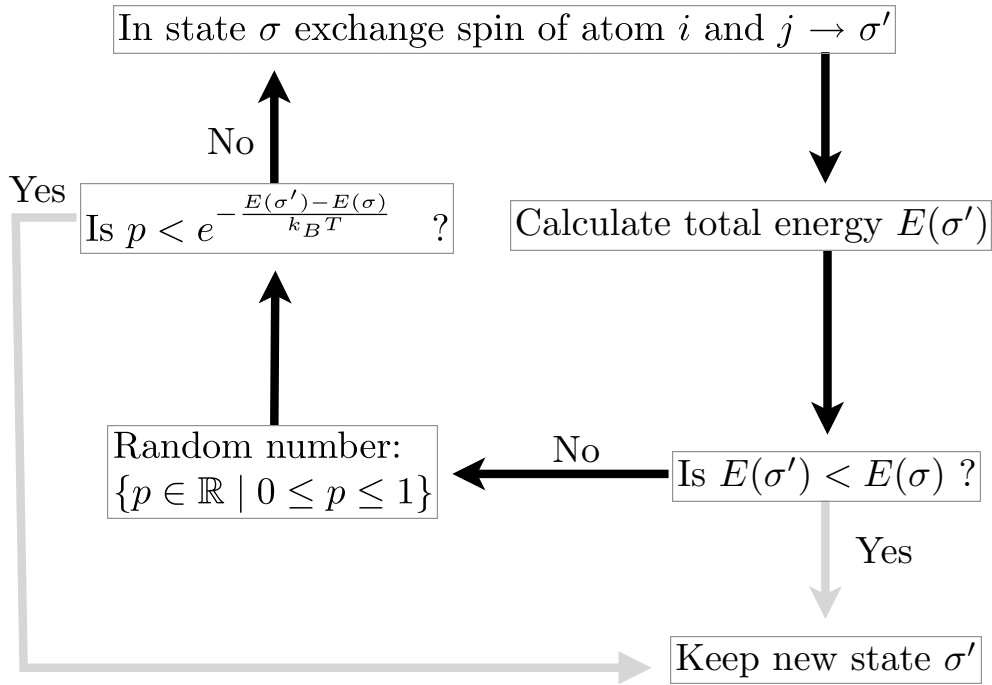


FIGURE 5.5: A standard MC workflow is shown. In the system with state σ the spin of two arbitrary atoms i and j , which have the opposite pseudo spins, is exchanged. If the energy of the new state σ' is lower than the original state, than that state is kept. Otherwise the Boltzmann factor of the energy is calculated and compared to a random number in the range $\{0, 1\}$. If the random number is smaller than the Boltzmann factor, then the new state is kept. If this is not the case the state is discarded and the process is reinitiated.

with $E(\sigma_\alpha)$ denoting the energy of state σ_α . T and k_B are as always temperature and Boltzmann constant and Z describes the grand partition function.

The stationary Markov chain process is reversible and follows the principle of detailed balance (chapter 2 in Ref. [44]), implying that the probability for the transition from state σ_α to σ_β is equal for the reverse process. Hence,

$$p_\alpha p_{\alpha\beta} = p_\beta p_{\beta\alpha} , \quad (5.10)$$

with p_α and p_β for the probabilities of the respective states. The transition probability from one state to the other is given by $p_{\alpha\beta}$ and $p_{\beta\alpha}$.

Reformulating Eq. 5.10 gives

$$\frac{p_{\alpha\beta}}{p_{\beta\alpha}} = \frac{p_{\beta}}{p_{\alpha}} = e^{\left(-\frac{\Delta E}{k_B T}\right)}, \quad (5.11)$$

stating that the probability of the state change $\sigma_{\alpha} \rightarrow \sigma_{\beta}$ and its inverse $\sigma_{\beta} \rightarrow \sigma_{\alpha}$ is only dependent on the energy difference $\Delta E = E(\sigma_{\beta}) - E(\sigma_{\alpha})$.

Note that Eq. 5.11 does not yet give a singular transition probability from one state to another. For that different approaches are applied. One of the most well known is that of Metropolis *et al.* [45], also used in UNCLE, which defines the transition probability as:

$$p_{\alpha\beta} = \begin{cases} e^{\left(-\frac{\Delta E}{k_B T}\right)} & \text{if } \Delta E > 0 \\ 1 & \text{else} \end{cases} \quad (5.12)$$

Therefore, if the energy in the system decreases with the state change, then the change will always happen, otherwise the probability for the change is given by the Boltzmann factor $e^{-\Delta E/k_B T}$. This whole process is sketched in Fig. 5.5.

5.3 Solubility and Phase Boundaries

5.3.1 Grand Canonical Approach

In this approach the number of atoms in the ensemble is not conserved and a chemical potential μ_j is introduced describing the energy change associated with the change in the number of atoms n_j of species j in the ensemble. Hence, μ_j is the derivative of the Gibbs free energy ($G = U - TS + pV$) with

$$\mu_j = \left. \frac{dG}{dn_j} \right|_{p,T}. \quad (5.13)$$

Practically, the grand canonical MC is implemented by including the terms $\mu_j n_j$ for atom species j into the Boltzmann factor used to evaluate the transition probability of a spin flip, i.e. for a binary system the change in occupation from atom A to B or vice versa. Therefore, Eq. 5.12 has to be rewritten for a system with M components:

$$p_{\alpha\beta} = \begin{cases} e^{\left(-\frac{\Delta E + \sum_j^M \mu_j n_j}{k_B T}\right)} & \text{if } \Delta E > 0 \\ 1 & \text{else} \end{cases} \quad (5.14)$$

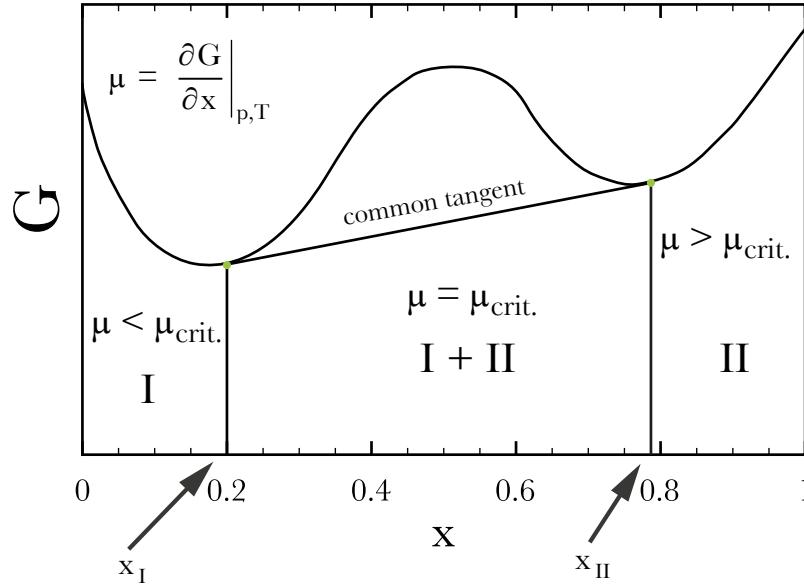


FIGURE 5.6: Sketch of the common tangent method. The effective chemical potential μ , i.e. the derivative of G is a constant in the concentration range where the two phases coexist marked by I + II while it varies in the one phase regions of both phase I and II.

In a binary system the number of atoms of both species can not change independently of each other. Rather, the change of the number of atoms n_A of species A goes in hand with a change of the number of atoms n_B of species B conserving the total number of atoms $N = n_A + n_B$.

Reformulating Eq. 5.13 in terms of $x = n_A/N$ results in

$$\mu_A(x) = \left. \frac{dG(x, p, T)}{dx} \right|_{p, T} . \quad (5.15)$$

By defining the B-atom concentration in terms of x , i.e. $n_B = N - n_A = (1 - x)N$, finds,

$$\mu_B(x) = - \left. \frac{dG(x, p, T)}{dx} \right|_{p, T} . \quad (5.16)$$

Thus, for the chemical potential of both species one can trivially state that

$$\mu_B = -\mu_A . \quad (5.17)$$

Using for a binary system the already discussed common tangent method (chapter 4), sketched in Fig. 5.6, one can deduce that for a single stable phase, i.e. $x < x_I$ or $x > x_{II}$, the chemical potential $\mu(x)$ varies strongly while in the concentration range where the

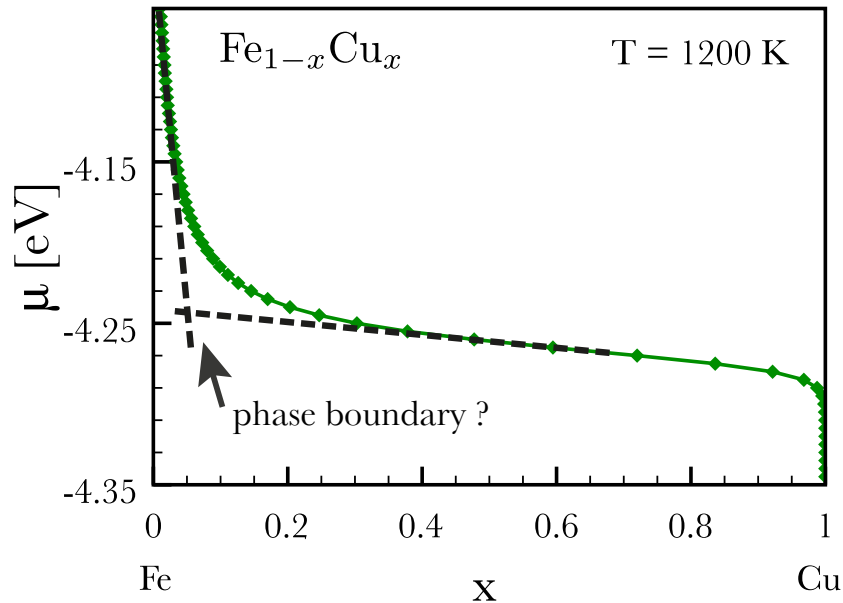


FIGURE 5.7: Effective chemical potential of Cu (μ_{Cu}) versus Cu concentration shown for a grand canonical Monte Carlo simulation with 512000 atoms at $T = 1200$ K. The phase boundary is estimated by fitting two lines onto the curve. At the point where these lines intersect an arrow indicates the phase boundary between the Fe phase and the Fe+Cu phase.

two phases coexist, i.e. $x_I \leq x \leq x_{II}$, the chemical potential $\mu = \mu_{\text{crit.}}$ stays constant. This allows to easily identify the phase boundaries by looking at $\mu(x)$.

Although this approach is part of the standard repertoire to calculate the phase diagram its application to a non-mixing phase diagram (in the present thesis the $\text{Fe}_{1-x}\text{Cu}_x$ alloy) is impractical due to its inaccuracy. This can be observed from Fig. 5.7 for a Fe-Cu grand-canonical MC at 1200K, where the transition from the two phase Fe+Cu area, i.e. μ nearly constant for a large range of x_{Cu} , to the one phase Fe area is ambiguous. This is due to the finite size of the simulation cell.

5.3.2 Canonical Approach

Another standard tool for phase diagram calculations is the canonical MC in which the solubility is obtained by fixing the atomic concentration and varying the temperature. An appropriately large change in the calculated enthalpies then indicates a phase transition. This is shown in Fig. 5.8 for the $\text{Fe}_{1-x}\text{Cu}_x$ system, where $x = 1$ at.% Cu atoms are dissolved in the system by distributing them randomly within the simulation cell. Starting of at 1800 K the system is cooled down in 100 K steps. The phase transition is accompanied by the formation of Cu precipitates at 500 K resulting in a change of the

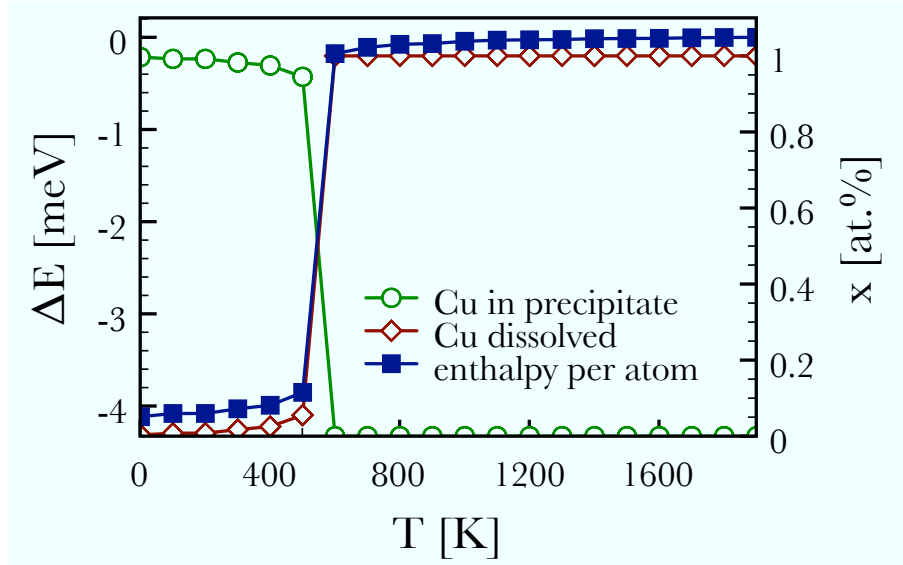


FIGURE 5.8: Concentration of Cu dissolved (red diamonds), Cu in precipitate (green circles) and enthalpy ΔE (blue squares) plotted versus T for a canonical MC simulation with $x = 1$ at. % of Cu in the simulation cell.

dissolved Cu atoms from 1 at.% to 0.05 at.% at 500 K and an energy decrease of ≈ 4 meV/atom. Note, the total number of Cu atoms in the simulation cell remains unchanged as the Cu atoms are either solved or attached onto the Cu precipitate. The Cu solubility was calculated by dividing the number solved, i.e. unattached, Cu atoms through the number of lattice sites. In this thesis an atom was counted as part of a precipitate if one of its nearest neighbours belonged to a precipitate, i.e. a cohesive cluster of more than 10 atoms of the same species.

Two problems have to be dealt with in this approach: First the temperature dependent CE is very costly and has to be done at every temperature step, as will be discussed in greater detail in the next section: Second, as is well known from nucleation theory [46], precipitates need to grow to a critical radius to be stable. Hence, if the probability of removing an atom from a precipitate is comparatively larger than adding an atom to it, then it will take a very long computational timespan or a very large simulation cell will be needed, as the formation of a stable precipitate is unlikely. Therefore, although in the example of dissolved Cu in an Fe host the dissolved Cu might be energetically unfavourable the Cu atoms need a stable Cu precipitate to be removed from the Fe host. This classical metastability problem leads to an overestimation of Cu solubility in this thesis, as visualised in Fig. 5.9.

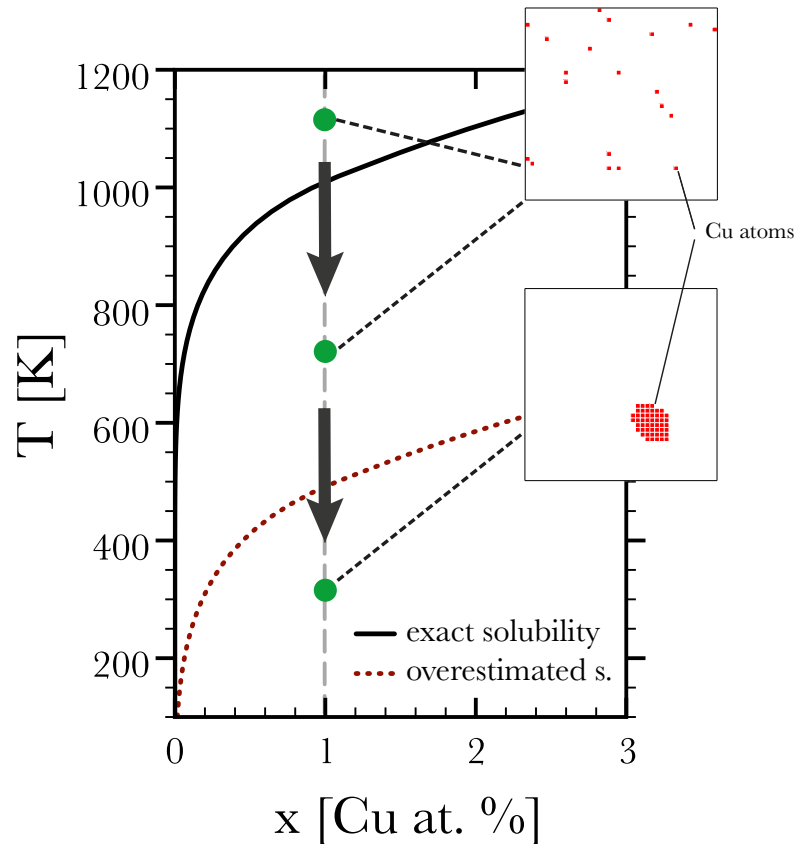


FIGURE 5.9: Sketch of the metastability problem. If the simulation cell with $x = 1$ at. % is cooled below the correct phase boundary (black solid line) the Cu atoms stay in solution, as shown by the simulation cell cross-section in the insets where only the Cu atoms are indicated by red squares, since the formation of a stable Cu precipitate needs a larger computational timespan. This results in an overestimation of the Cu solubility.

5.3.3 Local Grand Canonical Approach

The metastability problem of the canonical MC approach can be circumvented by providing a way for the dissolved atoms to be removed from the solution. For a binary system this is done by modelling a perfect phase separation by dividing the simulation cell into two equal halves each of which is initially fully occupied by one atom species as shown in Fig. 5.10. This local grand canonical setup has a fixed finite reservoir of A and B atoms (i.e. Cu and Fe) allowing an exchange of atoms between the two slabs. Hence, the initial configuration is given at 0 K and the solubility is then determined by counting the dissolved atoms in the host slab at thermodynamical equilibrium for a fixed temperature. However, the boundary between the reservoirs also relaxes. Therefore, to make sure that no atom from the other slab is accidentally counted as dissolved the first three

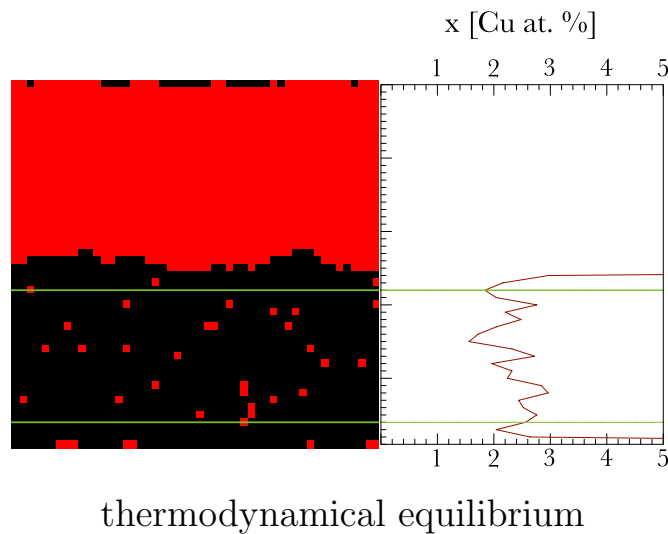
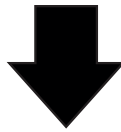
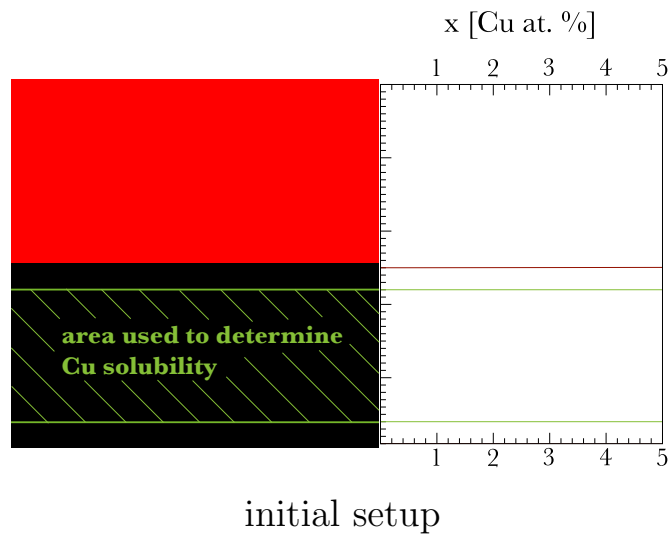


FIGURE 5.10: Cross sections along [111] of the simulation cell with Fe atoms coloured in black and Cu in red. The initial setup (i.e. one slab Cu and one slab Fe) is brought to thermodynamical equilibrium. The volume used to determine the concentration of dissolved Cu (i.e. Cu solubility in Fe) is indicated by the two green lines.

layers around the original slab boundary are not taken into account when determining the solubility.

5.4 Temperature Dependent CE

The inclusion of the vibrational free energy into CE has been discussed in previous works. Notably by Van de Walle *et al.* [47], describing the influence of the vibrational free energy $F_{\text{phon}}(T)$ on the thermodynamics of substitutional alloys. Using the isolated defect model, described in detail in the previous chapter, confirms the importance of the vibrational free energy for the $\text{Fe}_{1-x}\text{Cu}_x$ alloy (chapter 7.2). This provides the necessary motivation to attempt a temperature dependent CE. Yuge *et al.* [48] combined CE with *ab-initio* phonons to calculate the quasi-binary phase diagram of $(\text{BN})_{(1-x)}(\text{C}_2)_x$. This seems to be very similar to the one used in the present thesis, but gives no explanation on the criteria used to reduce the set of 251 CE input structures used in the standard CE to 25 input structure selected for the calculation of the phase diagram with vibrational contributions. This is unsatisfactory.

It should be emphasised, that the DFT energies of the structures used for the CE are strictly defined for $T = 0$ K. Hence, the ECI's are also defined at $T = 0$ K. Finite temperatures are included into Eq. 5.5 by adding the vibrational free energy (Eq. 3.83 in chapter 3) to the CE,

$$\sum_{\sigma=1}^{N_{\sigma}} \left[E_{\text{DFT}}(\sigma) + F_{\text{phon}}(\sigma, T) - N_{\text{latt}} \sum_{\text{f}}^{N_{\text{f}}} D_{\text{f}} J_{\text{f}}(T) \bar{\Pi}_{\text{f}}(\sigma) \right]^2 + \sum_{\text{f}}^{N_{\text{f}}} c(\bar{r}_{\text{f}})^{\lambda} J_{\text{f}}(T) = \min, \quad (5.18)$$

yielding a set of temperature dependent ECI's $\{J_{\text{f}}(T)\}$.

Additionally, to the temperature independent formation enthalpy of configuration σ (Eq. 5.6) a temperature dependent vibrational formation energy term has to be taken into account

$$\Delta f(\sigma, T) = F_{\text{phon}}(\sigma, T) - (x F_{\text{phon}}^{\text{A}}(T) + (1-x) F_{\text{phon}}^{\text{B}}(T)) . \quad (5.19)$$

Hence, this temperature dependent addition to Eq. 5.6 might lead to different sets of ground state structures at different temperatures. Implying that a converged CE at $T = 0$ K might not be converged when temperature dependent contributions of the phonons are included.

Furthermore, the addition of vibrational free energies also results in a temperature dependent increase of $S_{\text{CV}}(T)$ (Eq. 5.8), simply because an increase in $F_{\text{phon}}(\sigma, T)$ also increases the error.

A further important problem is the occurrence of imaginary vibrational modes. Strictly seen, one would have to remove all structures with imaginary modes as these are dynamically unstable. In this thesis the CE has been done for a non-mixing Fe-Cu system with no stable phase between pure Fe and Cu. Hence, all structures used in the CE are

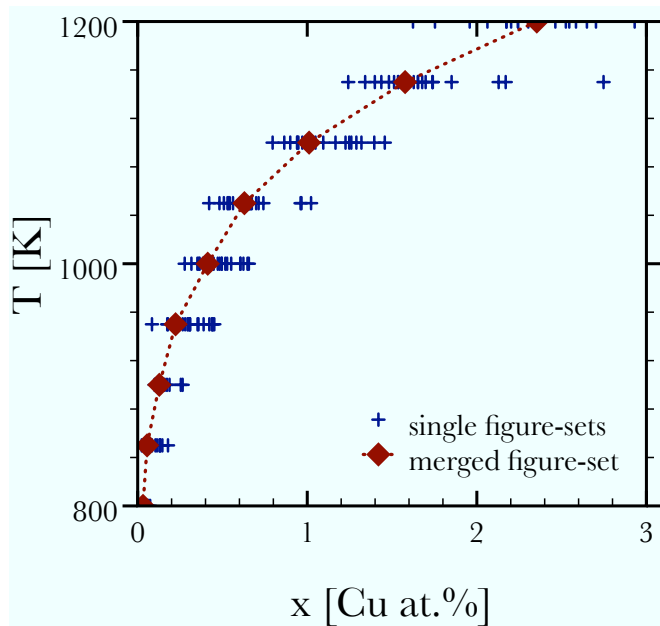


FIGURE 5.11: Cu solubility in bcc Fe calculated from figure-sets of twenty separate CE's (blue crosses) compared to results using a merged figure-set (red diamonds and dotted line).

energetically unstable and, therefore, it is viable to include structures with a low enough percentage (i.e. $i\omega$ below 5%) of imaginary frequencies. As discussed in chapter 3 the imaginary modes are discarded when calculating vibrational free energies. If a temperature dependent CE is done for an alloy with stable phases in-between the pure phases then it is prudent to be more strict and discard all structures with imaginary vibration modes.

In a naive first calculation one immediately notices that the solubility of the dissolved atom scatterers strongly at each temperature step, as seen for dissolved Cu in Fe in Fig. 5.11. This is the case because the figure selection in the CE is not unique. Each CE will select a different set of figures emphasising different structural energetics. This has nothing to do with the temperature dependent CE and also occurs for the CE at $T = 0$ K. But, as all further MC calculations within the standard CE approach are always based on the same figure-set of a single CE, this problem is usually not noticed. However, in the temperature dependent CE where a separate CE has to be done at each temperature step it thus becomes obvious.

It is possible to reliably calculate the solubility of dissolved atoms by averaging over a number of separate CE performed at a fixed temperature. This averaging is done by merging the individual figure-sets of all individual CE's. All figure-sets $\{f(T)\}$ are merged and the corresponding effective interaction energies $\{J_i(T)\}$ are averaged over

N_{CE} independent CE's for a given temperature T by

$$\overline{\{f(T)\}} = \{f\}_1(T) \cup \dots \cup \{f\}_{N_{\text{CE}}}(T) \quad (5.20)$$

and

$$\overline{\{J_{\overline{\{f\}}}(T)\}} = \frac{1}{N_{\text{CE}}} \sum_{\overline{\{f\}}} \{J_f(T)\} . \quad (5.21)$$

This merged figure-set $\overline{\{f(T)\}}$ contains more figures than any one of the individual CE figure-sets used for merging. In the $\text{Fe}_{1-x}\text{Cu}_x$ CE the number of figures is increased from about 40 to more than 100 when merging twenty figure-sets from twenty individual CE's. Ultimately, this merging allows to accurately study the thermodynamics of an alloy using a single merged figure-set by MC. As shown in Fig. 5.11 for the example of Cu solutes in Fe this approach allows for a more accurate description of the Cu solubility in Fe.

Chapter 6

Mo₃Al₂C: Phonons and Phase stability

The compound Mo₃Al₂C (first synthesised in the 1960s [49]) is of particular interest as a superconductor which has a β -Mn-type crystal structure without a centre of inversion. Because of the missing inversion symmetry the classification of Cooper pairs into either spin-singlet or spin-triplet is not possible. In non-centrosymmetric superconductors the electron pairing-process is explained to be a mixture of spin-singlet and spin-triplet pairs states [50, 51] .

The finding of superconductivity in the non-centrosymmetric compound CePt₃Si [52] got a lot of attention. DFT calculations were attempted [53] which, however, encountered the usual DFT problems with localised f-states and therefore the results were inconclusive. On the other hand compounds without inversion symmetry such as BaPt₃Si [54] and Mo₃Al₂C contain no problematic localised states and are therefore an ideal playground for DFT studies. Dealing with superconductivity for these cases with no centre of inversions needs the inclusion of spin-orbit interactions, which are usually (and also in VASP) done in a perturbative way. BaPt₃Si appears to behave like a normal BCS superconductor, because the spin-orbit splitting of states close to the Fermi energy is very small, and the transition temperature $T_c = 2.25$ K is very low. Interestingly, Mo₃Al₂C has a relatively high critical temperature of $T_c = 9.05$ K (see Fig. 6.1) when compared to similar β -Mn compounds and to BaPt₃Si.

The renewed interest in Mo₃Al₂C due to its superconducting and structural properties is manifested by a recent publication by Bauer *et al.* [55]. In the present thesis the focus is put in particular on the vibrational properties of Mo₃Al₂C in order to search for soft phonon modes which might couple with proper pair-forming electronic states. Thermodynamic stability of vacancies on the carbon sites, as elaborated later on, also need to be considered.

TABLE 6.1: Physical properties of Mo_3Al_2C .

crystal structure	Cubic, β -Mn type
space group	P4 ₁ 32
exp. lattice parameter [55]	6.863 Å
DFT lattice parameter	6.890 Å
exp. superconducting transition temperature	9.0K

Experimentally the compound is prepared by cold compacting the elemental powder and reacting it for 24 h at the relatively high temperature of 1500°C. The material is then ball milled and hot pressed at a pressure of 56 MPa with a temperature of 1250°C. [55]. The unit cell of its structure is cubic and contains of 24 atomic positions, of which 12 are Mo, 8 are Al and 4 are C. The structure sketched in Fig. 6.1 shows that the C atoms are placed within trigonal prisms formed by the Mo atoms, resulting in octahedral Mo_6C subunits. Table 6.1 summarises a few properties and compares the experimental lattice constant to the DFT value, which is 0.4 % larger. It should be noted, that for the DFT calculations a PBE flavoured GGA exchange-correlation was considered. In the VASP calculations a $21 \times 21 \times 21$ Monkhorst-Pack [56] \vec{k} -point mesh was used for converging the total energy, and a $13 \times 13 \times 13$ mesh for geometrical relaxations and for deriving force-constants. The integration in \vec{k} -space for the total energies applied the tetrahedron smearing method with Blöchl corrections [57], whereas for the relaxation of the atomic positions and for deriving the force-constants the first order Methfessel-Paxton smearing method [58] with a smearing of 0.2 eV was chosen.

6.1 Vibrational Properties

The structural parameters, i.e. the volume and shape of the unit cell as well as the position of all 24 atoms within this unit cell, were relaxed to residual forces of less than 10^{-4} eV/Å. Furthermore, for a high accuracy of the phonon calculation the force-constants derived from the displaced atoms were corrected by subtracting the still finite force-constants of the fully relaxed structure, as discussed in chapter 3. The perfectly stoichiometric compound Mo_3Al_2C is dynamically not stable, as can be realised from panel a) of Fig. 6.2 due to bands of modes with imaginary frequencies. Particularly noticeable is the situation at Γ where three imaginary optical modes arise. The dynamical instability seems surprising, considering the well-established crystal structure of Mo_3Al_2C and the published experimental data in Ref. [55]. However, one should keep in mind, that the actual content of C on the C sublattice is experimentally not easily accessible, and carbides like to have vacancies on their sublattice.

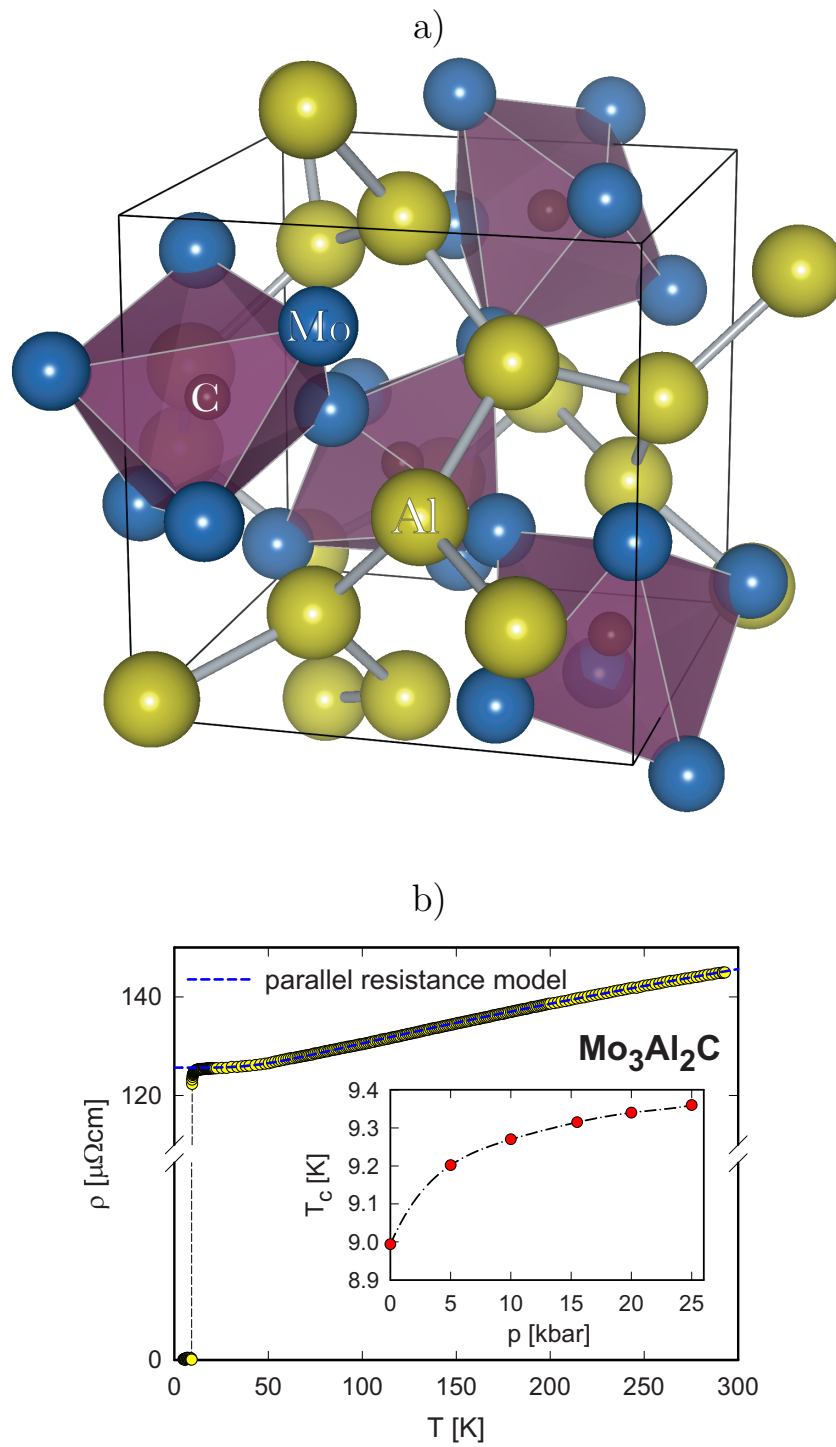


FIGURE 6.1: Properties of Mo_3Al_2C . Panel a): crystal structure; panel b): experimental electrical resistivity (yellow circles) [55]. Inset in panel b) sketches the pressure dependency of conducting transition temperature T_c .

In order to test the numerical accuracy and the reliability of these puzzling imaginary frequencies for the perfectly stoichiometric compound force-constant calculations with several displacements of $|\vec{u}| = 0.05 \text{ \AA}, 0.1 \text{ \AA}, 0.2 \text{ \AA}, 0.3 \text{ \AA}, 0.4 \text{ \AA}$ were done, and furthermore all symmetry were removed. All tests confirm for Mo_3Al_2C the existence of imaginary modes.

Exploiting the calculation with a displacement of $|\vec{u}| = 0.01 \text{ \AA}$ imaginary optical modes with frequencies of $1.62 i$ are found at Γ . A further test was performed by a linear-response calculation directly done by VASP at Γ confirming with $1.65 i$ THz the imaginary frequency. VASP's linear-response results for the force-constants were taken as input for *f*PHON calculations and the thus derived dispersion relation as shown in panel a) of Fig. 6.2 is very similar to the previously derived one based on the force-constant method. To test the structural stability of the atomic distribution all atoms were slightly displaced from their equilibrium positions and allowed to relax without any symmetry constraints. Furthermore, a tetragonal deformation was enforced to the unit cell. In all of these tests the cell relaxed back to the initial crystal structure and atomic distribution. Any significantly different crystal structure seems to be unlikely, because this structure was confirmed by many experiments [49, 55].

A further explanation for the occurrence of imaginary modes for the perfectly stoichiometric compound could be that the experimental samples contain defects, in particular vacancies.

Assuming that a certain C-vacancy concentration is present suitable supercell calculations were done to simulate the defect structures. Calculations with a given displacement of $|\vec{u}| = 0.01 \text{ \AA}$ were done for a single carbon vacancy in a $1 \times 1 \times 1$ supercell, i.e. $Mo_3Al_2C_{0.75}$ containing 23 atoms with 3 out of possible 4 C atoms, for a single carbon vacancy in a $2 \times 1 \times 1$ supercell, i.e. $Mo_3Al_2C_{0.875}$ containing 47 atoms with 7 out of possible 8 C atoms, and in a $2 \times 2 \times 2$ supercell containing 191 atoms, i.e. $Mo_3Al_2C_{0.96875}$. While both $Mo_3Al_2C_{0.75}$ and $Mo_3Al_2C_{0.875}$ were found to be dynamically stable with no imaginary modes, $Mo_3Al_2C_{0.96875}$ was found to be significantly unstable, with imaginary optical modes at Γ quite close to the result for the perfect compound. Comparing $Mo_3Al_2C_{0.875}$ with $Mo_3Al_2C_{0.75}$ in Fig. 6.2 one notices that with a lower carbon vacancy concentration the lowest optical mode at Γ softens from about 3 THz to below 1 THz. Furthermore, a softening of the acoustic modes at R and X occurs. The result for the $2 \times 2 \times 2$ supercell indicates, that there might be a critical concentration of carbon vacancies below which the compound becomes dynamically unstable. Assuming that the frequency of the lowest optical mode at Γ scales linearly with the carbon vacancy concentration $x_{vac} = 1 - x$ the critical carbon vacancy is estimated, using the values of Γ in $Mo_3Al_2C_1$, $Mo_3Al_2C_{0.96875}$ and $Mo_3Al_2C_{0.875}$ as input (Fig. 6.3), to be $x_{crit} = 0.089$.

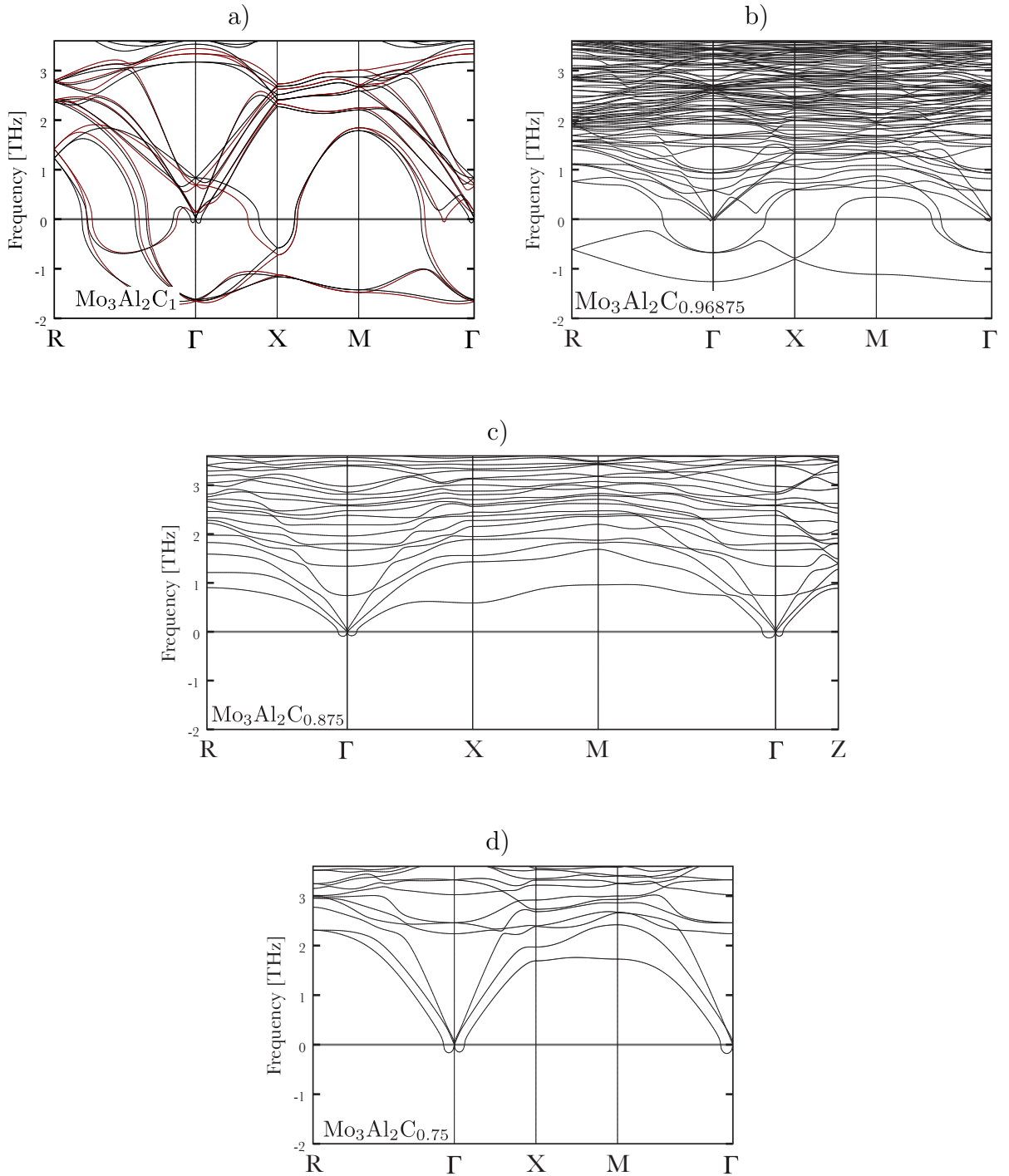


FIGURE 6.2: Vibrational properties of $Mo_3Al_2C_x$ with $x \leq 1$, i.e. vacancies on the C sublattice. In panel a) for Mo_3Al_2C the calculated phonon dispersion derived from the displaced-atoms force-constant method (black line) is compared to a calculations with force-constants derived from linear response (red line). In panels b), c) and d) the dispersion relation, as calculated directly from the displaced-atoms force-constants, are presented for $Mo_3Al_2C_{0.96875}$, $Mo_3Al_2C_{0.875}$ and $Mo_3Al_2C_{0.75}$, respectively. It should be noted, that the paths in reciprocal space are different, because for $Mo_3Al_2C_{0.875}$ a $2 \times 1 \times 1$ simple tetragonal supercell has been used but for the other cases a $1 \times 1 \times 1$ or a $2 \times 2 \times 2$ simple cubic supercell.

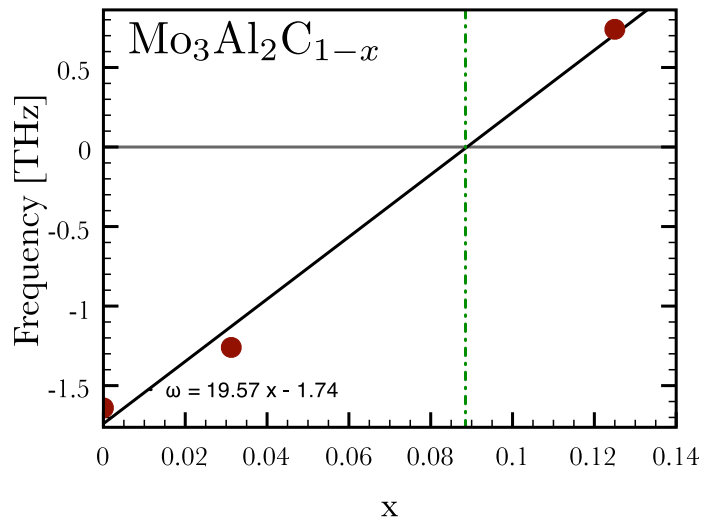


FIGURE 6.3: Carbon vacancy concentration x versus the frequency of the lowest optical mode at Γ .

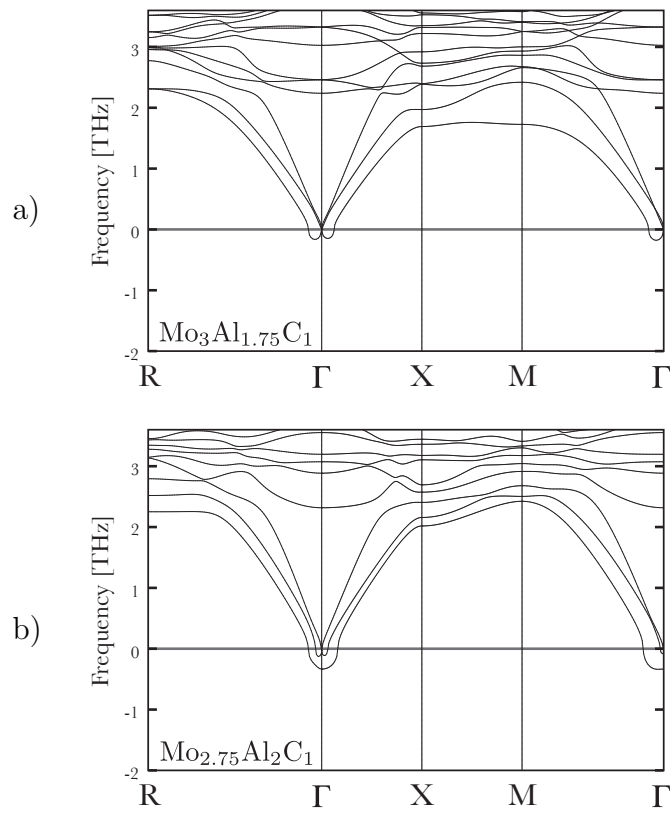


FIGURE 6.4: Panels a) and b) present the dispersion relation, as derived from the displaced-atoms force-constant method for $Mo_{2.75}Al_2C_1$ and $Mo_3Al_{1.75}C_1$.

Further stoichiometries were studied, enforcing vacancies on the other two sublattices. As a result, Fig. 6.4 shows two different phonon dispersion relations for two different stoichiometries, namely $Mo_{2.75}Al_2C$ and $Mo_3Al_{1.75}C$. Clearly, the phonon dispersion relations in Figs 6.2 and 6.4 reveal that no significant imaginary modes exist for the other two vacancy stoichiometries. The small dip below the zero line (i.e. imaginary axis) close to Γ is a numerical artifact.

All these results indicate that the compound might be stabilised by vacancy formation. However, both molybdenum and aluminium have a comparatively large X-ray cross section [59] and can be easily detected by experiment, and so far no vacancies on these sublattices have been measured. The situation is different for carbon, which is a light atom, and one may speculate that carbon vacancies exist in the experimental samples.

Two questions then remain: what is the true ground state structure of Mo_3Al_2C , and is it thermodynamically possible that vacancies are formed under the given conditions, i.e. preparation temperature? The discussion in the next subchapter deals with the second point, which at the moment is of particular interest.

Coming back to the vibrational properties, in Fig. 6.5 the normalised phonon DOS of unstable Mo_3Al_2C and $Mo_3Al_2C_{0.96875}$ are compared to the stable compounds $Mo_3Al_2C_{0.875}$ and $Mo_3Al_2C_{0.75}$. While no Debye-like ω^2 behaviour of the DOS is observed close to Γ for Mo_3Al_2C and $Mo_3Al_2C_{0.96875}$, it can be found for the other presented cases. For $Mo_3Al_2C_{0.875}$ the Debye-like behaviour occurs in a rather narrow range up to ≈ 0.5 THz due to the softening of the acoustical and optical modes, for $Mo_3Al_2C_{0.75}$ the Debye-feature is more strongly pronounced up to 1.5 THz. The partial DOS reveals that Mo, as the heaviest atom species, dominates in the spectrum the lower frequencies (up to 7 THz) whereas carbon, being the lightest atom, contributes only at frequency higher than 13.5 THz. A direct comparison of the DOS of Mo_3Al_2C with that of $Mo_3Al_2C_{0.875}$ and $Mo_3Al_2C_{0.75}$ shows that the large Al dominated peak at ≈ 12.2 THz is strongly reduced by the carbon vacancy from 0.55 to 0.12 for $Mo_3Al_2C_{0.96875}$. With increasing carbon vacancy concentration this peak increases to 0.21 and 0.36 for $Mo_3Al_2C_{0.875}$ and $Mo_3Al_2C_{0.75}$. Furthermore, the carbon dominated frequencies mode are shifted down by the introduction of vacancies from above 15 THz to about 13.5 THz.

For the sake of completeness the phonon DOS of the remaining of $Mo_{2.75}Al_2C_1$ and $Mo_3Al_{1.75}C_1$ are presented in Fig. 6.6. They reveal a similar behaviour, namely a Debye-like ω^2 increase in the frequency range 0 – 1.5 THz and the reduction of the aluminium dominated peak at ≈ 12.2 THz. In both cases one observes that the carbon frequencies are shifted to lower values. Furthermore, for $Mo_{2.75}Al_2C_1$ a hybridisation of the carbon modes with aluminium modes between 11.5 – 13 THz is observed.

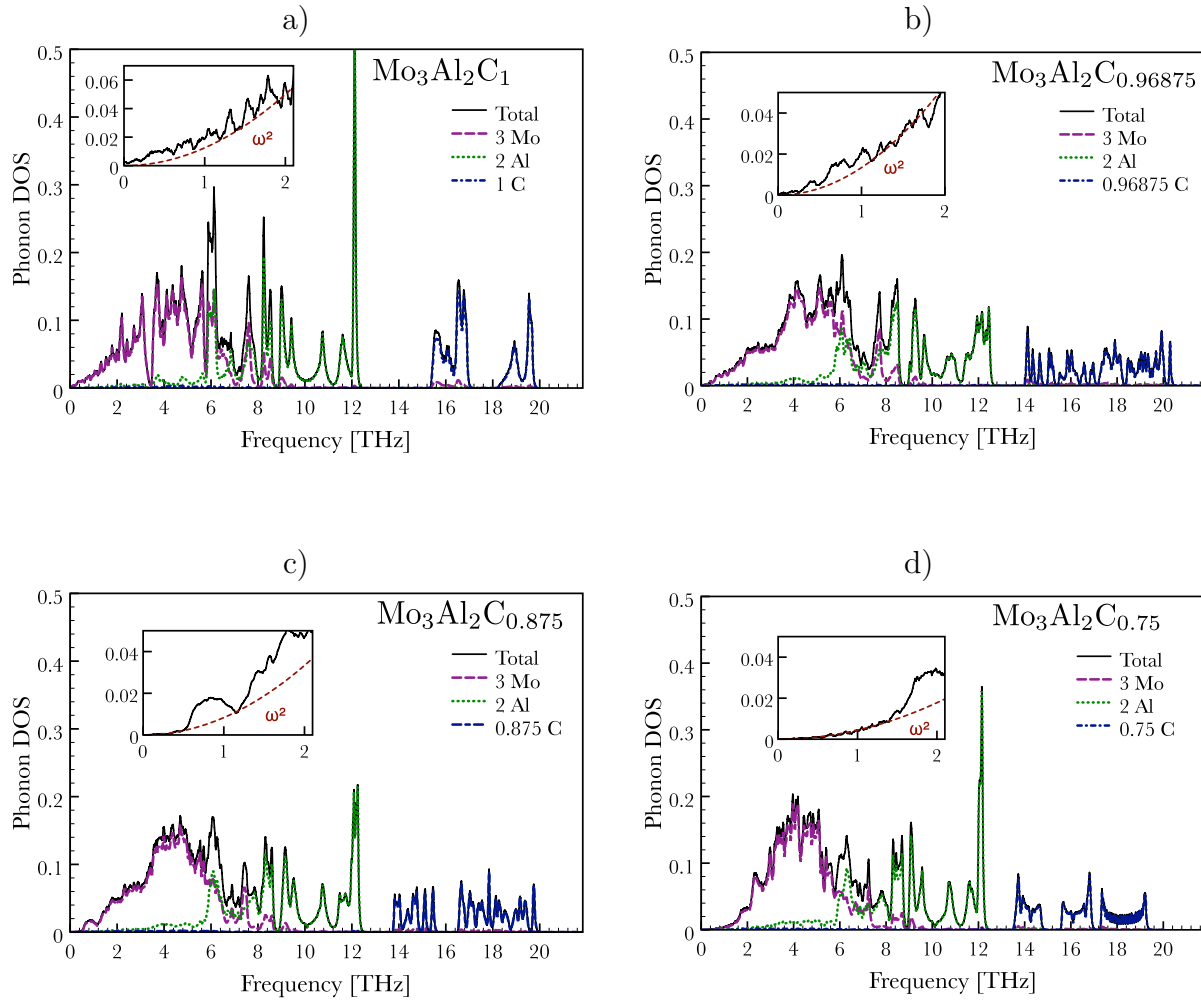


FIGURE 6.5: Vacancies on the C sublattice: Phonon DOS (black solid line) and the partial phonon DOS of Mo (purple dashed line), Al (green dotted line) and C (blue dashed-dotted line) are shown in panels a), b), c) and d) for $\text{Mo}_3\text{Al}_2\text{C}$, $\text{Mo}_3\text{Al}_2\text{C}_{0.96875}$, $\text{Mo}_3\text{Al}_2\text{C}_{0.875}$ and $\text{Mo}_3\text{Al}_2\text{C}_{0.75}$, respectively. In the inset the total DOS at low frequencies is compared to a Debye-like ω^2 behaviour (red dashed line).

Returning to the discussion of the carbon vacancies the question about the mechanism behind the stabilisation of the optical low-frequency molybdenum modes arises. Obviously, the Mo-C bonding in the Mo_6C subunits is very important for this phenomenon. This can be tested by removing a C atom from one of the four Mo_6C subunits in the unit cell of $\text{Mo}_3\text{Al}_2\text{C}$. The removal strongly influences the Mo-C bonds in all the remaining three Mo_6C subunits because they share a common Mo atom with the defect subunit. By relaxing the Mo atoms in all subunits the carbon shifts into an off-center position, by which the average molybdenum carbon bond length of the three perfect Mo_6C subunits is increased by 1.4 %, and the corresponding octahedral volume is increased by 3.6 %. It seems that this distortion is the stabilizing factor for the vibrational modes.

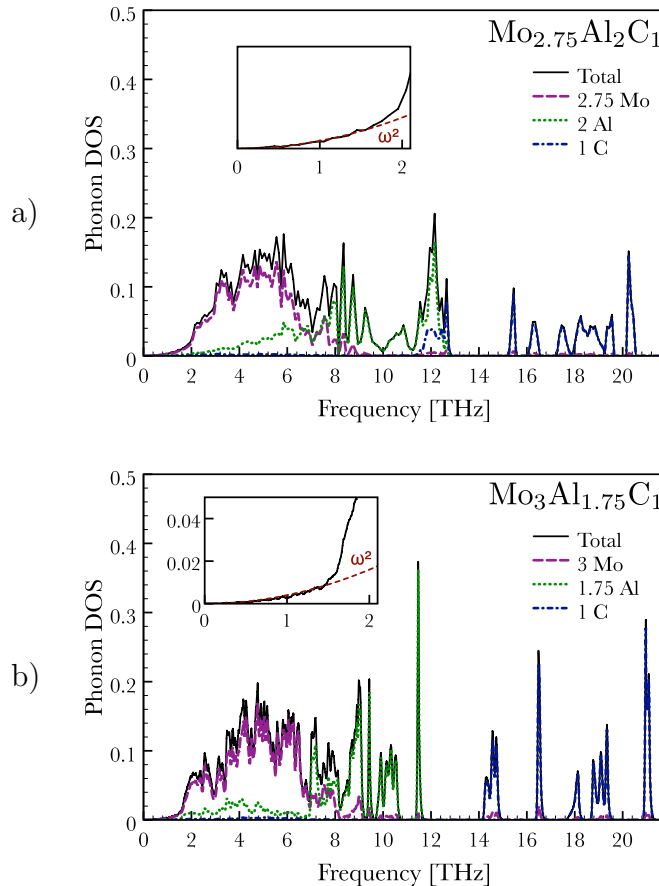


FIGURE 6.6: Vacancies on the Mo or Al sublattice: Phonon DOS (black solid line) and the partial phonon DOS of Mo (purple dashed line), Al (green dotted line) and C (blue dashed-dotted line) are shown in a) for $Mo_{2.75}Al_2C_1$ and in b) for $Mo_3Al_{1.75}C_1$. The inset compares the increase of the total DOS at low frequencies is compared to a Debye-like ω^2 behaviour (red dashed line).

6.2 Formation Energy

As discussed above, a certain amount of C-vacancies is needed in order to stabilise some of the optical modes, which indicates that the experimental samples are not perfectly stoichiometric. The question now arises, if the formation of vacancies is thermodynamically possible. Investigating this key question the vacancy formation energy is calculated by subtracting the total energy $E_{\text{DFT}}(Mo_{12}Al_8C_4)$ of the stoichiometric compound from the total energy $E_{\text{DFT}}(Mo_{12}Al_8C_4 - X)$ of the compound with vacancy X and the ground state reference energy $E_{\text{DFT}}(X)$ of the removed atom X by

$$\varepsilon^{X(\text{vac})} = E_{\text{DFT}}(Mo_{12}Al_8C_4 - X) + E_{\text{DFT}}(X) - E_{\text{DFT}}(Mo_{12}Al_8C_4). \quad (6.1)$$

TABLE 6.2: Formation energies for vacancies in Mo_3Al_2C for $1 \times 1 \times 1$ and $2 \times 1 \times 1$ unit cells without vibrational contributions (DFT $T=0$ only), adding $f^X(T)$, and finally completing with the configurational entropy

$S_{\text{conf}}(c_X) = -[c_X \ln(c_X) + (1 - c_X) \ln(1 - c_X)]$ at temperatures of 1250°C and 1500°C.

	Mo(vac)	Al(vac)	C(vac)	C(vac)
	[meV]	[meV]	[meV]	[meV]
supercell size	$1 \times 1 \times 1$	$1 \times 1 \times 1$	$1 \times 1 \times 1$	$2 \times 1 \times 1$
$\varepsilon^{X(\text{vac})}$	1738	855	595	561
T=1250°C: $\varepsilon^{X(\text{vac})} + f^{X(\text{vac})}(T)$	1582	497	196	-393
T=1500°C: $\varepsilon^{X(\text{vac})} + f^{X(\text{vac})}(T)$	1506	387	75	-661

Suitably replacing the DFT total energies (E_{DFT}) with vibrational free energies (F_{phon}) leads to the vibrational vacancy formation energy

$$f^{X(\text{vac})}(T) = F_{\text{phon}}(\text{Mo}_{12}\text{Al}_8\text{C}_4 - X) + F_{\text{phon}}(X) - F_{\text{phon}}(\text{Mo}_{12}\text{Al}_8\text{C}_4) - F_{\text{phon}}(X). \quad (6.2)$$

The reference energies $E_{\text{DFT}}(X)$ and $F_{\text{phon}}(X)$ were calculated for the ground states of bcc-Mo, fcc-Al and C in the graphene structure. The formation energy of the carbon vacancy in the $2 \times 1 \times 1$ supercell (as needed for small vacancy concentrations) was calculated by doubling the value of the reference $\text{Mo}_{12}\text{Al}_8\text{C}_4$ compound that is subtracted from $\text{Mo}_{24}\text{Al}_{16}\text{C}_7$.

Comparing the vacancy formation energies in Table 6.2 for one notices that at $T = 0$ K (DFT only) they are all strongly positives, whereby the Mo vacancy with a formation energy of 1738 meV is by far the most unfavourable one. As hoped, carbon vacancies are the most favourable ones, with a formation energy of 595 meV for $1 \times 1 \times 1$ supercell corresponding to $\text{Mo}_3\text{Al}_2\text{C}_{0.75}$. This value is reduced by only 34 meV for the $2 \times 1 \times 1$ supercell corresponding to a composition of $\text{Mo}_3\text{Al}_2\text{C}_{0.875}$.

It should, however, be noted that the experimental samples were synthesised at 1500°C and heat treated at 1250°C. Therefore, theory should consider temperature dependent vacancy formation energies $f^{X(\text{vac})}$ combined with the composition dependent configurational entropy $S_{\text{conf}}(x)$. For this derivation the fully stoichiometric compound $\text{Mo}_3\text{Al}_2\text{C}_1$ was chosen with its imaginary modes, as described above. Concerning the vibrational free energy, its imaginary modes were not included because only 3% of all vibrational states are imaginary.

Table 6.2 and Fig. 6.7 show that the vibrational contribution reduces the strongly positive values of the vacancy formation energies as derived directly from the DFT total energies.

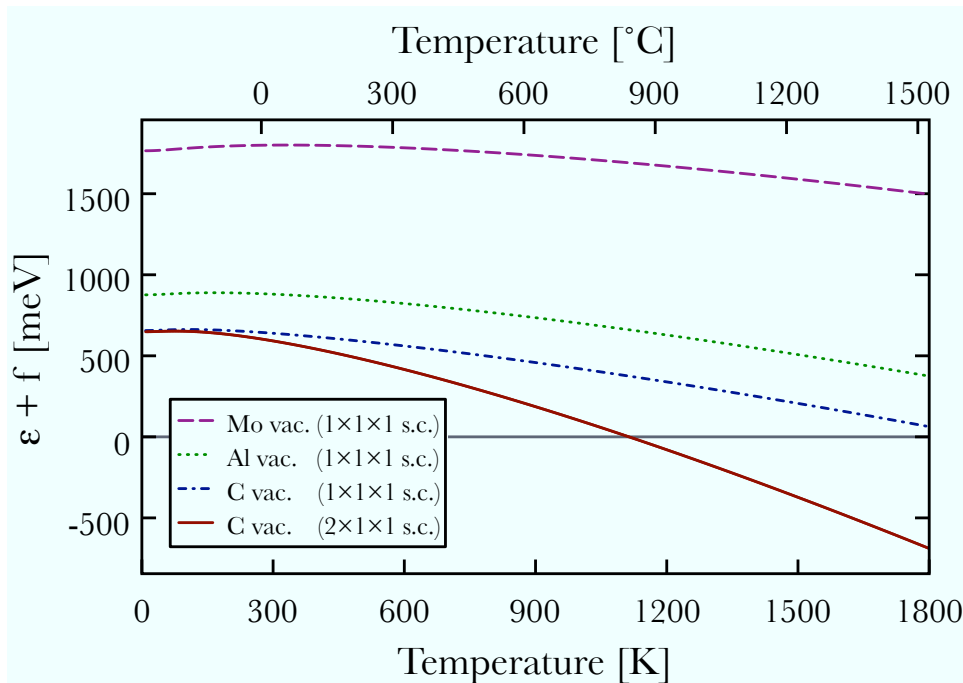


FIGURE 6.7: Total vacancy formation energy (sum of the DFT ε and vibrational f formation energies) versus temperature for a Mo vacancy (purple dashed line), an Al vacancy (green dotted line) and a C vacancy (blue dashed-dotted line) in a unit cell ($1 \times 1 \times 1$ supercell). Also the result for a carbon vacancy in a $2 \times 1 \times 1$ supercell is shown (red solid line).

While this reduction is comparatively small for the Mo vacancy, (from 1738 meV to 1506 meV at 1500°C) it is much larger for the other two types of vacancies.

In particular, the formation energy of the carbon vacancy for the single unit cell, i.e. $Mo_3Al_2C_{0.75}$, decreases from 595 meV to 75 meV at 1500°C. Remarkably, this reduction is much larger for the larger supercell, i.e. the composition $Mo_3Al_2C_{0.875}$ with the vacancy formation energy decreasing by more than 1 eV down to -661 meV. As a conclusion, the sum of DFT and vibrational vacancy formation energy, $\varepsilon + f(T)$, strongly depends on x and T .

From the isolated defect model of chapter 4 (Eq. 4.19) the temperature dependent equilibrium vacancy concentration x can be calculated. However, as the formation energy per vacancy, $\varepsilon + f(T)$, is strongly dependent on x the model of chapter 4 cannot be applied directly here. The total vacancy formation energy $U(x, T) = (\varepsilon + f(T))x$ is not a linear function of x any more, but is described as

$$U(x, T) = ax^2 + bx, \quad (6.3)$$

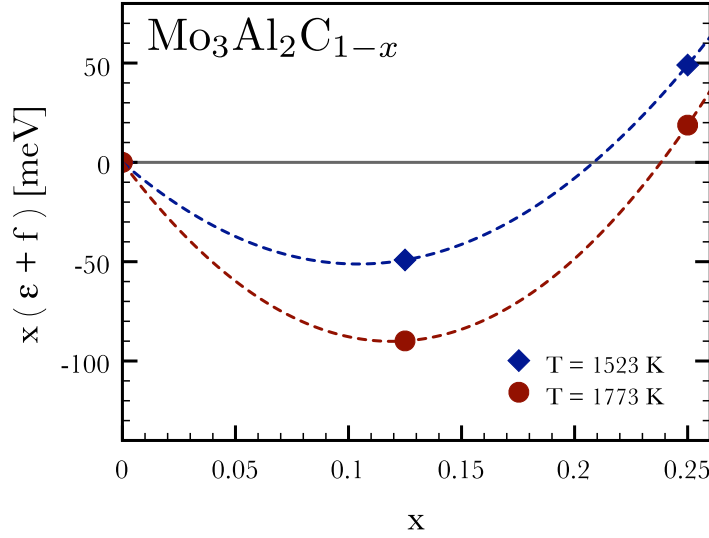


FIGURE 6.8: Total vacancy formation energy, $\varepsilon + f(T)$, times carbon vacancy concentration x versus x at temperatures of 1250°C (blue diamond) and 1500°C (red circles). The dashed lines (blue for 1250°C and red for 1500°C) are obtained by parabolic interpolation between the calculated data.

wherein a and b are parameters fitted to the directly calculated vacancy formation energies, as shown in Fig. 6.8.

Thus, the total free energy including the configurational entropy is now described as,

$$F(x, T) = ax^2 + bx - Tk_B S_{\text{conf}}(x) . \quad (6.4)$$

Defining S_{conf} as the mixing entropy of an ideal solution,

$S_{\text{conf}}(x) = x \ln(x) + (1 - x) \ln(1 - x)$ the derivative of F with respect to x becomes,

$$\frac{\partial F(x, T)}{\partial x} = 2ax + b - Tk_B [\ln(x) - \ln(1 - x)] . \quad (6.5)$$

Searching for the concentration x minimising the free energy, i.e. $\partial F(x, T)/\partial x = 0$ one obtains

$$\frac{\partial F(x, T)}{\partial x} = 0 \quad \Rightarrow \quad x = \frac{e^{-\beta(2ax+b)}}{1 + e^{-\beta(2ax+b)}} , \quad (6.6)$$

with $\beta = \frac{1}{k_B T}$. This allows for the numerical calculation of x using a simple bracketing root finding algorithm (page 445 in [34]).

Considering experimental preparation temperatures the likely carbon vacancy concentration of the sample is 0.13–0.14., according to the model described by Eq. 6.6. From

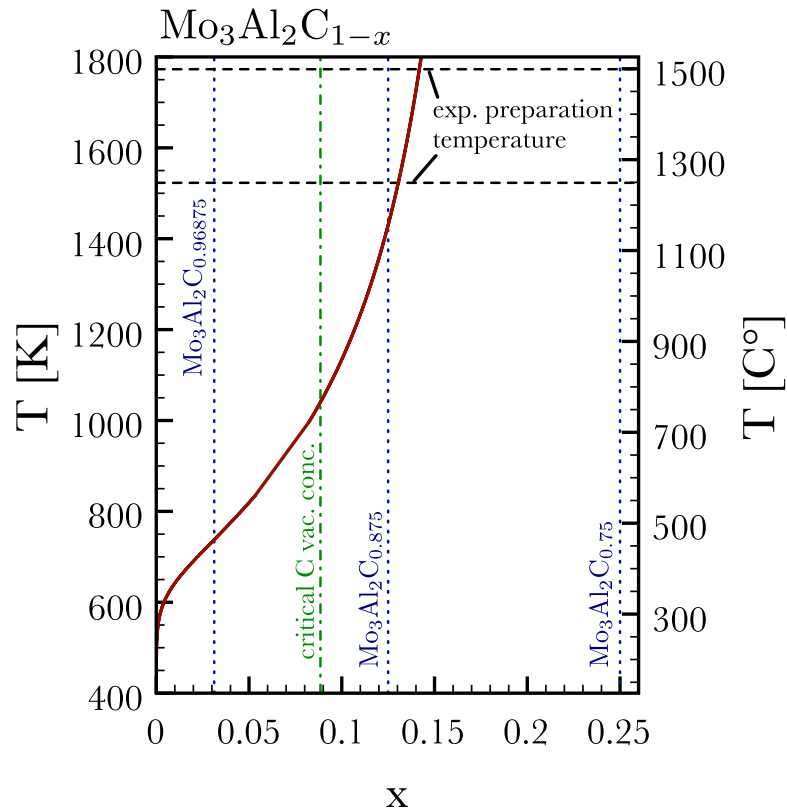


FIGURE 6.9: Temperature dependent carbon vacancy concentration plotted as a solid red line. Experimental preparation temperatures are indicated as dashed black lines. The critical carbon vacancy concentration, below which the structure becomes dynamically unstable, is shown by a green dash-dotted line, while the carbon vacancy concentrations of the calculated supercells are drawn as blue dotted lines.

these findings, it seems plausible that the superconducting transition temperature might be altered by annealing the sample at a different temperatures

However, one should be aware that only three input values were considered when calculating x . It is probable that as the concentration dependent phonon softening over a large part of BZ occurs according to Figs 6.2 and 6.3 the vibrational entropy increases. This makes a vacancy concentration close to the critical x more favourable as the total vacancy formation energy increases. Therefore, the sample might have a vacancy concentration of $x \approx 0.09$.

6.3 Conclusions

As a result of the investigations it turns out that the perfectly stoichiometric compound Mo_3Al_2C is dynamically unstable, i.e. imaginary frequencies appear in the phonon dispersion. This finding is of particular importance because its superconducting properties, as recently published [55], are phonon mediated. On the other hand, Mo_3Al_2C is not a simple BCS-like superconductor because its crystal structure has no centre of inversion making the description of the electron-pairing process more complicated.

If, however, carbon vacancies are introduced (by means of supercell calculations) then the corresponding phonon dispersions may consist of only real frequencies provided the vacancy concentration x in the compound $Mo_3Al_2C_{1-x}$ is larger than a critical value. Thus, as a result it appears that phonon softening might be controlled by the carbon stoichiometry although experimentally this might be hard to achieve.

The key question is now if the formation of carbon vacancies is thermodynamically possible. The answer is no, if only the DFT energies (i.e. formation enthalpies at $T = 0$ K) are considered. Based on a thermostatistical model including also the vibrational free energies it is found that at the elevated temperatures at which the experimental samples were fabricated carbon vacancies formation becomes favourable. Assuming that the cooling down of the sample freezes in the vacancies it becomes plausible, that the measurements for the superconducting properties for $T < 10$ K are done with carbon deficient samples.

Of course, also the electronic structure are needed for more detailed discussion on superconductivity. This would involve calculations of the electronic band structures and Fermi surfaces of the vacancy structures including spin-orbit coupling (because of the missing centre-of-inversion) and an elaborate discussion of the results. This is, however, beyond the scope of the present thesis which focusses on dynamic and thermodynamic stabilities. Nevertheless, all the necessary calculations were done also for the electronic structure and the results are currently prepared for publication.

Chapter 7

$\text{Fe}_{1-x}\text{Cu}_x$

In the steel production elements are added to Fe in order to improve its material properties. One of these elements is Cu which hardens steel. Fig. 7.1 depicts Cu precipitates in an Fe matrix whose formation is essential for the hardening effect. The precipitation formation is stimulated by the correct heat treatment. Once formed the precipitates hinder the movements of dislocations and thus makes the steel more resistant against mechanical loads. The hardening effect is demonstrated by Fig. 7.2 in which experimental data [60] for the change of Vicker's hardness versus ageing time for an $\text{Fe}_{1-x}\text{Cu}_x$, $x = 1.17$ at. % alloy is presented. The alloy hardens because of precipitate formation by annealing at 773 K. If the heat treatment is too long then a softening is observed which is attributed

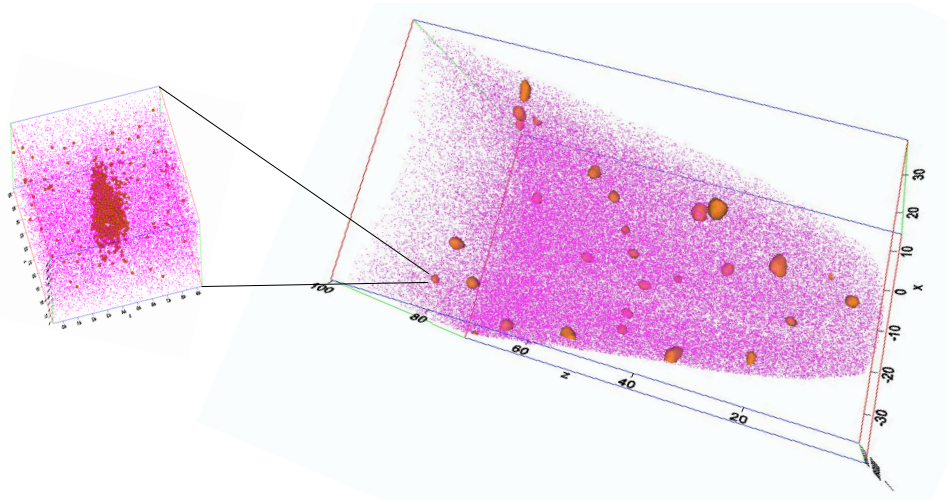


FIGURE 7.1: Atom probe microscope image as derived by Harald Leitner and Michael Schober at the Montan University of Leoben of Cu precipitates in Fe after the alloy has been annealed for 500000 seconds at 773 K.

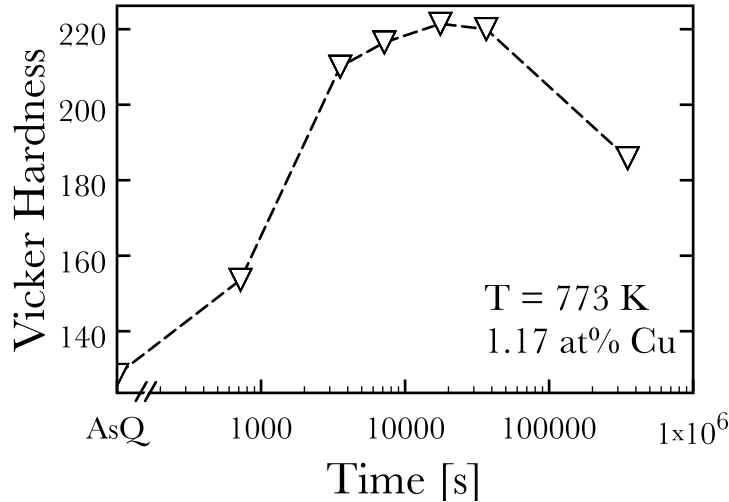


FIGURE 7.2: Change in hardness versus time at $T = 773$ K for $Fe_{1-x}Cu_x$, $x = 1.17$ at.%. Experimental data of Ref. [60].

to Oswald ripening [61]: a well known precipitate ageing process by which larger precipitates grow at the cost of smaller ones thus decreasing the number precipitates in the alloy. Further softening can also occur when the interaction of the dislocations with the precipitates changes due to the size change of the precipitates.

The industrial interest in controlling the hardening process in steel is enormous. Therefore, Fe-rich Fe-Cu alloys are well studied by a large number of publications but *ab-initio* DFT studies are still rather scarce. As will be demonstrated in the present work, these studies mostly do not take into account all the important material properties, i.e. vibrational free energies. The aim of this work is now to model the precipitation formation by two different concepts maintaining DFT accuracy in both of them and taking into account vibrational properties. The first approach deals with independent one- and two-atom defects whereas the second, much more elaborate task, fully derives concentration dependent interaction energies between atoms of the alloy. The *ab-initio* results in terms of phase boundaries and miscibility range are compared to data of the semi-empirical CALPHAD (computer coupling of phase diagrams and thermochemistry) method [62] much loved by the technologically based material's scientist. However, while often the parameters which enter CALPHAD simulations are empirical the mechanisms behind them are not well understood. The experimental results are just used to fudge the simulations to more or less well-defined values. One of the major goals of the present thesis is to demonstrate that purely based on DFT total energies (and related quantities such as force-constants) thermodynamical stabilities can be modelled rather well with the advantage that the fundamental mechanisms of bonding and stability can be analysed and understood comprehensively.

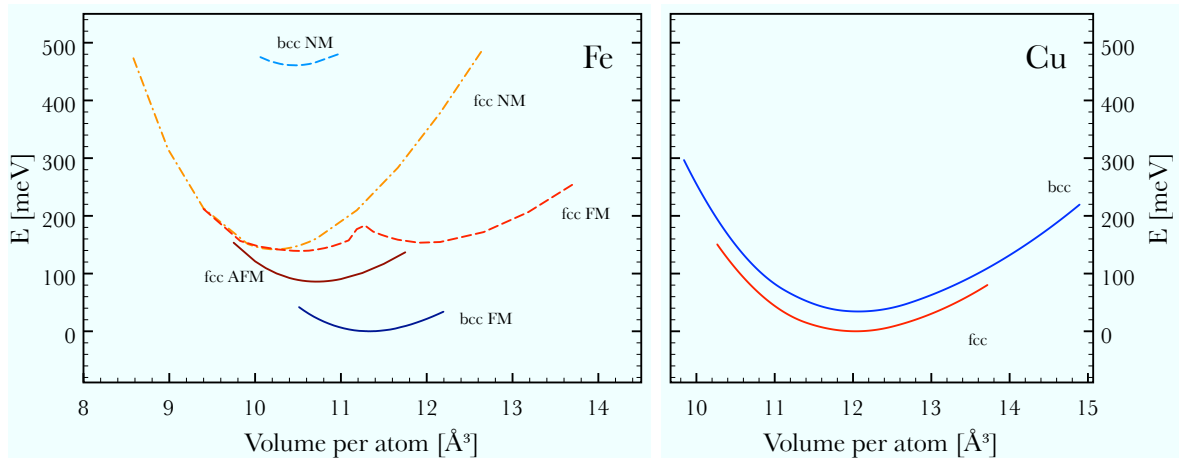


FIGURE 7.3: DFT total energies E_{DFT} (PBE parametrisation) for Fe and Cu as a function of volume V , whereby the energy zero corresponds to the minimum of E_{DFT} . The ground states are bcc ferromagnetic (FM) Fe and fcc Cu. Left panel: results for Fe bcc and fcc non-spinpolarised (NM), antiferromagnetic (AFM) and ferromagnetic (FM). Right panel: results for fcc and bcc Cu.

7.1 Bulk Fe and Cu

Fig. 7.3 presents volume dependent total energies, E_{DFT} for bcc and fcc structures and in case of Fe for several magnetic orders. As it is obvious, bcc ferromagnetic (FM) Fe and fcc Cu are the equilibrium ground states at $T = 0$ K.

Table 7.1 summarises a variety of results for both metals. To test the accuracy of the present DFT results they are compared to other recent DFT studies (also applying VASP) [63, 64] as well as to experimental data. For further cross-checks the full-potential linearised augmented plane-wave (FLAPW) approach *flair* [65, 66] was also applied. Summarising, the *flair* and VASP results of the present work agree very well between each other and with the data of Ref. [63]. For Fe in particular, however, there is a significant difference to the published data of Domain *et al.* [64] which can be ascribed to difference in constructing the pseudopotential. Liu *at. al* [63] and the present study utilised projector augmented wave (PAW) potentials whereas in Ref. [64] ultrasoft pseudopotentials (USPP) were chosen. It is well known, that USPP potentials exaggerate magnetic effects as can be seen from table 7.1 for Fe, a result of the larger volume.

Considering the bulk results it is reasonable to continue from now on by using VASP with a PBE parametrisation as basis.

TABLE 7.1: Results of several VASP and *flair* calculations and experimental data for ground state properties of bcc Fe and fcc Cu: lattice parameter a_0 , total magnetic moment M and bulk modulus B . PAW: projected augmented wave pseudopotentials, USPP: ultrasoft pseudopotentials. GGA parametrisations of the exchange-correlation functionals according to Ref. [12] (PBE) and Ref. [67] (PW91).

Method		a_0 [Å]	M [μ_B]	B [GPa]
bcc Fe	<i>flair</i> (PBE)	2.838	2.24	199
	<i>flair</i> (PW91)	2.837	2.23	199
	VASP (PAW:PBE)	2.831	2.19	198
	VASP (PAW:PW91) ¹	2.827	2.16	194
	VASP (USPP:PW91) ²	2.856	2.32	160
	exp. ³	2.8662	2.18	168
fcc Cu	VASP (PAW:PBE)	3.636	-	147
	<i>flair</i> (PBE)	3.627	-	143
	VASP (PAW:PW91) ¹	3.634	-	134
	VASP (USPP:PW91) ²	3.641	-	140
	exp. ³	3.614	-	137

7.1.1 Vibrational Properties

For both Fe and Cu the phonon dispersions and density of states (DOS) were calculated at their most stable states, namely bcc FM Fe and fcc Cu. The force constant matrices were derived using a 64 atom supercells (i.e. the primitive cells vectors were enlarged by a factor of 4) in which the forces acting on displaced atoms were directly derived from VASP calculations using the Methfessel-Paxton [58] method for the \vec{k} -space integration.

In Fig. 7.4 the dispersion relation for bcc FM Fe with two different lattice parameters is presented. There is hardly any difference between both DFT results and both agree rather well with the experimental dispersions with the exception of a measured softening at the N point. This well known phenomena of temperature dependent phonon softening in bcc Fe is described in Ref.s [70–73]. Also including thermal expansion in terms of the slightly enlarged lattice parameter of $a = 2.841$ Å (about 0.3 % larger than a_0) has hardly any effect on the dispersion N . (For more details about calculating the thermal expansion, see next section.) Therefore, the discrepancy to experiment has to be attributed to some temperature dependency of the magnetic ordering, which is not taken into account in the present work.

For fcc Cu, the dispersions as presented in Fig. 7.5 were calculated for the $T = 0$ K lattice constant, $a = 3.636$ Å. It shows, that the agreement with experiment is excellent.

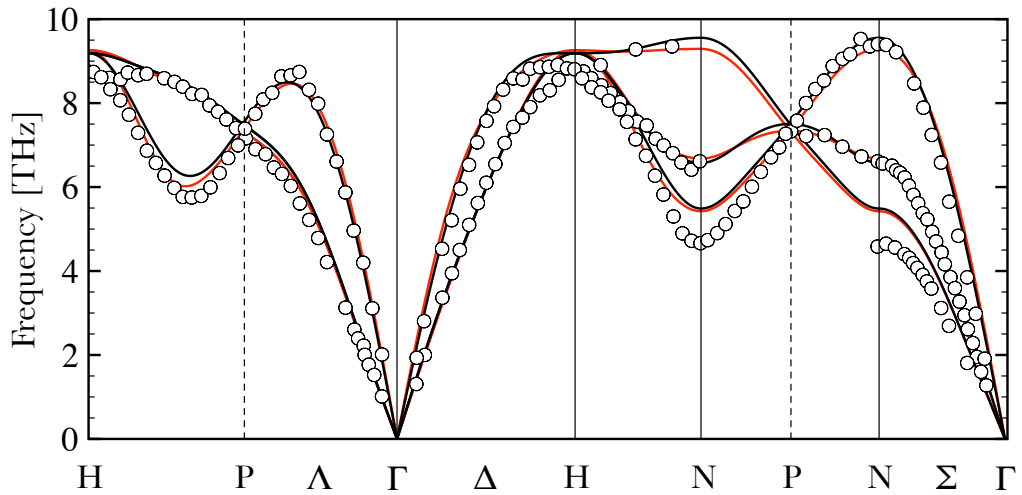


FIGURE 7.4: Phonon dispersion for bcc FM Fe along some high symmetry directions. DFT results (black line) for the equilibrium lattice parameter at $T = 0$ K, $a_0 = 2.831$ Å are compared to experiment [69] (circles), as measured at $T = 296$ K. A further DFT calculation was made for $a = 2.841$ Å (red line), corresponding to the DFT derived thermal expansion at $T = 296$ K. For details see text.

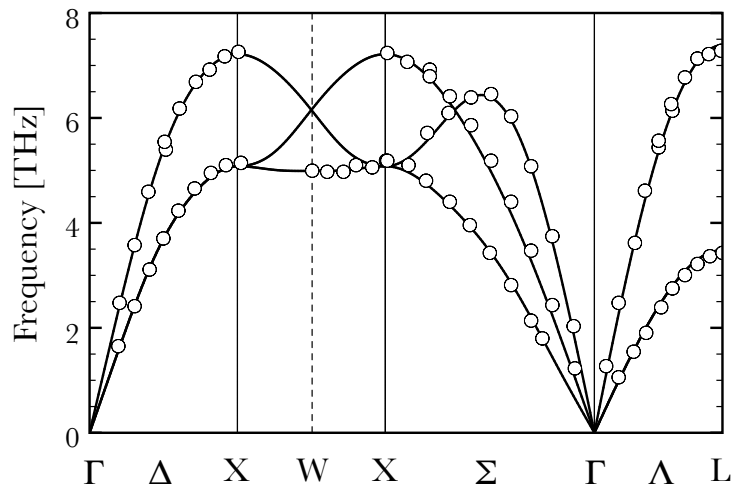


FIGURE 7.5: Phonon dispersion relation for fcc Cu along high-symmetry paths. DFT results (black line) are compared to experiment measured at $T = 49$ K [74] (circles).

7.1.2 Thermal Expansion - Quasiharmonic Approach

Thermal expansion is modelled within the quasiharmonic approach, as based on volume dependent phonon DOS from which volume and temperature dependent vibrational free energies $F_{\text{phon}}(a, T)$ (see Eq. 3.83, Ref.s [75–78]) can be derived. For the actual calculations supercells consisting of 27 atoms were constructed by multiplying each primitive lattice vector by 3. These supercells are due to the computational costs smaller than the ones used to derive the very accurate phonon dispersions. For each lattice parameter a the total free energy $F_{\text{tot}}(a, T) = E_{\text{DFT}}(a) + F_{\text{phon}}$ is summed up, and then for a given fixed temperature $T = T_f$ the minimum of $F_{\text{tot}}(a, T_f)$, as a function of a , is searched for. By this procedure temperature dependent equilibrium lattice parameter $a(T)$ are obtained.

The phonon DOS was calculated by using a $25 \times 25 \times 25$ \vec{q} -point mesh according to Monkhorst and Pack [56] for the \vec{q} -space integration. In general, the phonon dispersion relation at different lattice constants reveal volume dependent shifts. Discussing this effect for Cu, Fig. 7.6 shows the differences of the normalised phonon DOS

$$\Delta g(E) = g_{a_0}(E) - g_a(E) , \quad (7.1)$$

with respect to the $T = 0$ K equilibrium lattice parameter $a_0 = 3.636 \text{ \AA}$. As can be seen for the larger lattice spacing, there is a negative peak in the energy range up to 20 meV followed by a positive peak with a smaller range. This implies that the DOS $g(\omega)$ of the larger lattice parameter is enhanced in this range and reduced in the subsequent smaller range. Therefore, for larger lattice parameters the vibrational entropy is enhanced (according to Eq. 3.90) or the free energy is lowered when compared to the reference spacing at least up to a certain temperatures corresponding to the DOS changes in the discussed energy ranges. This makes it plausible that at increased temperatures the system will tend to a larger equilibrium volume, i.e. the minimum of the volume dependent free energy occurs at larger volumes.

The thermal expansion is derived from the lattice parameter $a(T)$ at which $F_{\text{tot}}(a, T)$ has a minimum for the fixed temperature T , and the equilibrium parameter a_{RT} corresponding to $T = 298.15$ K,

$$\delta l(T) = \frac{a(T) - a_{\text{RT}}}{a_{\text{RT}}} . \quad (7.2)$$

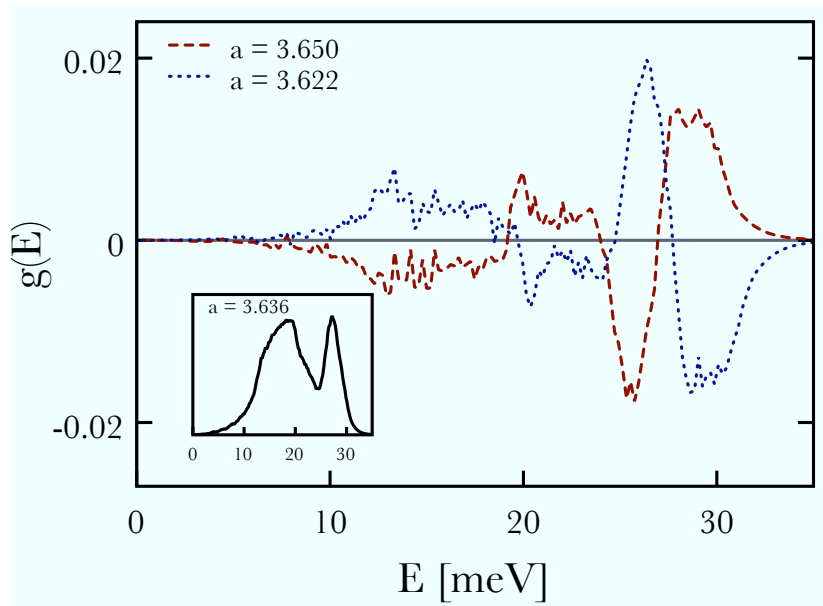


FIGURE 7.6: Differences $\Delta g(E) = g_{a_0}(\omega) - g_a(\omega)$ of normalised phonon DOS of fcc Cu. Blue dotted line: result for the lattice constant $a = 3.622$ Å; red dashed line: $a = 3.650$ Å. The inset shows the phonon DOS for the $T = 0$ K equilibrium lattice constant of $a_0 = 3.636$ Å.

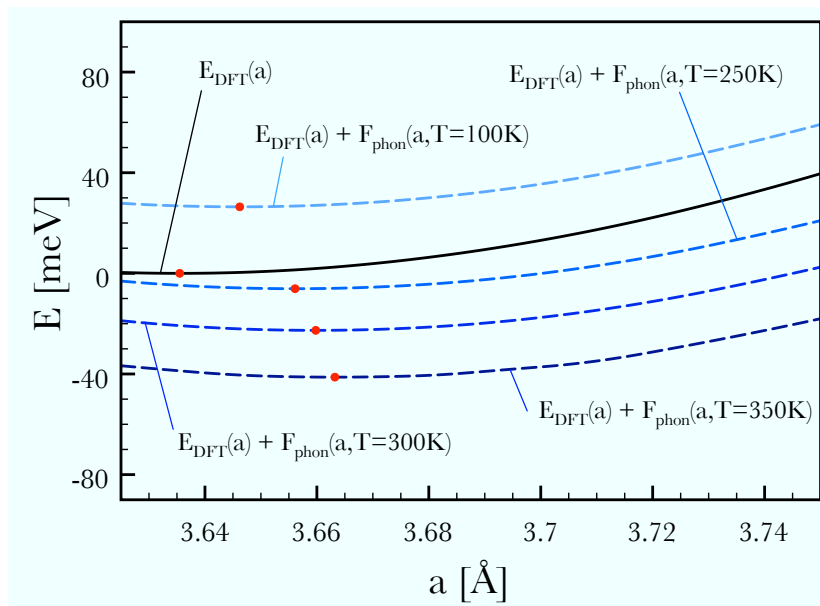


FIGURE 7.7: Volume dependent DFT total energy $E_{\text{DFT}}(a)$ (black solid line) and the total free energy $F_{\text{tot}}(a, T) = E_{\text{DFT}}(a) + F_{\text{phon}}(a, T)$ (dashed lines) for $T = 100$ K, 250 K, 300 K and 350 K vs. the lattice parameter a . For each curve the lattice constant at minimum energy is indicated by a red dot. The energy zero coincides with the minimum of $E_{\text{DFT}}(a_0)$.

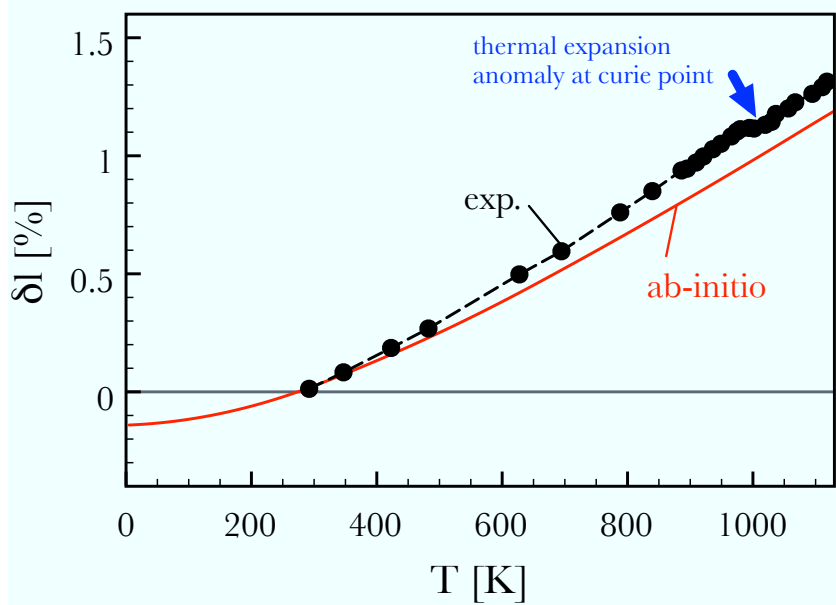


FIGURE 7.8: DFT derived thermal expansion of Fe (red solid line) in comparison to experiment [79] (black circles and dashed line). The Curie temperature T_C is indicated by an arrow.

7.2 Independent Defect Model for Fe-Cu

For Cu defects in Fe and Fe defects in Cu the influence of the vibrational free energy on the thermodynamic properties within the independent defect model of 4 is studied. In particular, the effect of the vibrational free energy on the solubility of the defects is investigated, which is comparable to previous studies [84–86].

7.2.1 Formation Energies

The relation introduced in chapter 4, as Eq. 4.1,

$$\varepsilon^{X_i} = (n_i + n_H)E_{\text{DFT}}^{X_i+H} - (n_i E_{\text{DFT}}^{X_i} + n_H E_{\text{DFT}}^H), \quad (7.3)$$

is now used to derive the formation energies of single and pair-wise Cu defects in a bcc Fe-matrix and Fe single and pair-wise defects in a fcc Cu-matrix. For the reference energies E_{DFT}^H and $E_{\text{DFT}}^{X_i}$ the energies per atom of fcc Cu and bcc Fe are taken.

The formation energy of one substitutional Cu defect in bcc Fe, $\varepsilon^{\text{Cu}_1}$, is presented in more detail in table 7.3. Compared to previous DFT results [64] the table reveals a significant difference. The formation energies of this work are always larger than 750 meV, independent of the chosen numerical conditions. On the other hand, the published data

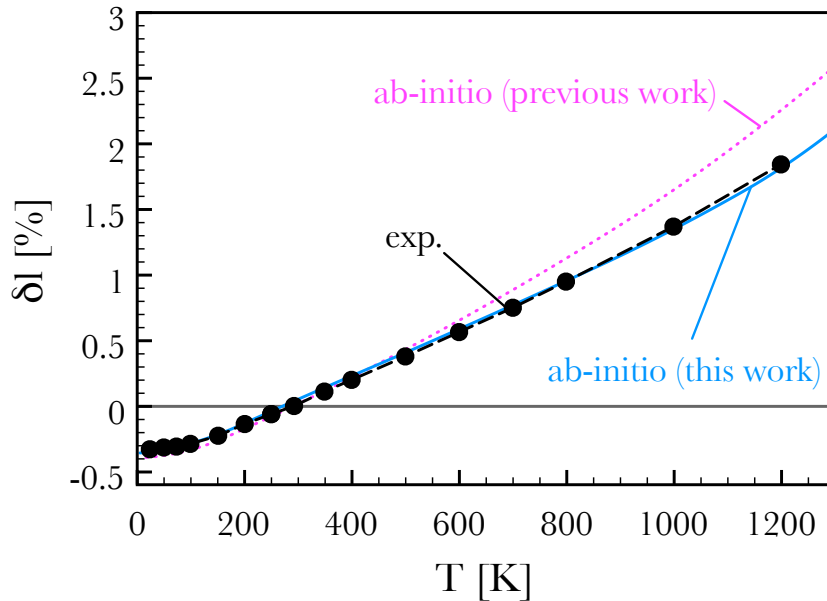


FIGURE 7.9: DFT derived thermal expansion of Cu. Present study: blue solid line; other calculation [78]: magenta dotted line; experiment [80]: black circles and dashed line.

Fig. 7.8 shows the results for Fe in comparison with experiment [79]. There are two significant differences between theory and experiment: The experimental expansion grows faster with increasing temperature, and there is a kink at the Curie Temperature ($T = 978 \text{ K} - 1043 \text{ K}$) reflecting the order-disorder phase transition of the ferromagnetic ordering. Both effects are attributed to temperature effects of the magnetic ordering which are not included in the present quasiharmonic approach.

For non-magnetic Cu, however, DFT theory and experiment agree very well according to Fig. 7.9. The present result for Cu matches experiment better than the data of a previous DFT work of Nara *et al.* [78]. The authors used the plane wave code PWSCF [81] and derived the vibrational properties within perturbation theory [82, 83].

Taking into account the thermal expansion the phonon free energies are not significantly affected, as can be seen in Fig. 7.10. There, $F_{\text{phon}}(a(T), T)$ is compared to $F_{\text{phon}}(a_0, T)$, in which a_0 is the $T = 0 \text{ K}$ equilibrium parameter (i.e. at which E_{DFT} has its minimum). Therefore, from now on all DFT calculations are done without considering thermal expansion considerably reducing computational cost.

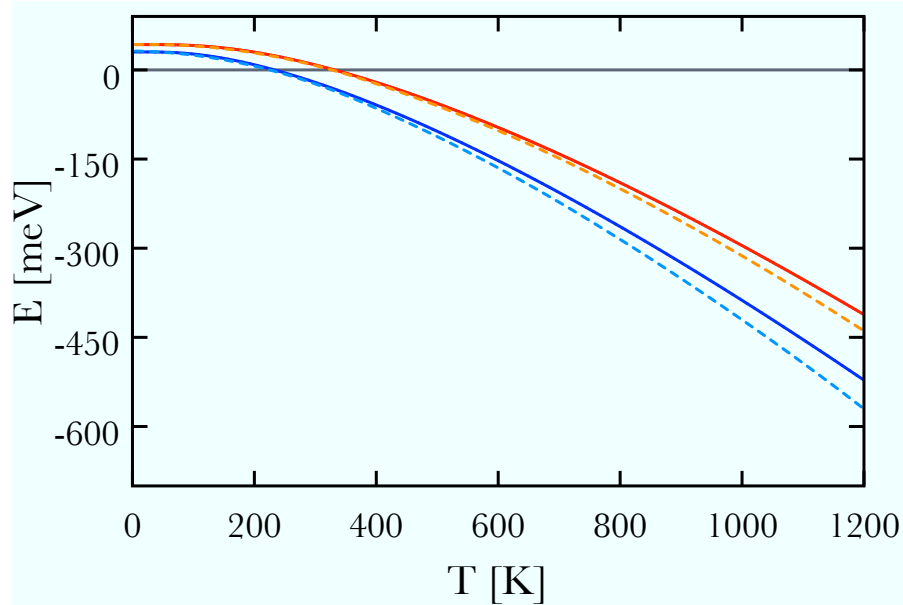


FIGURE 7.10: Phonon free energies for temperature dependent equilibrium parameters $a(T)$, $F_{\text{phon}}(a(T), T)$ (solid lines) are compared to $F_{\text{phon}}(a_0, T)$ (dashed lines) for both Fe (red and orange) and Cu (dark blue and light blue). The lattice parameter a_0 corresponds to the DFT minimum.

of Domain *et al.* are by at least 200 meV significantly smaller, which of course strongly alters the thermodynamical properties. To test for accuracy in the present study various test calculations were performed using VASP as well as *flair*. Table 7.3 shows results for two sizes of supercells (16 and 64 atoms) for three different cases, namely with and without relaxation of atomic positions and with all structural parameters relaxed including volume. In all these test cases the defect formation energies agree within 3%. Indicating that the relaxation effect on the defect formation energies is rather small. This can be expected since the atomic sizes are quite similar: the atomic volume of Cu is only 0.5% smaller than the one of Fe. Further test were done by recalculating the ground state properties of some intermetallic Cu-Fe compounds needed for the CE and given in Ref. [63], namely FeCu (B2 structure), FeCu₃ and Fe₃Cu with the DO₃ structure. In all these cases the energies and structural parameters calculated agree within 3% rather well with Ref. [63]. Although Liu *et al.* [63] applied a different exchange-correlation GGA potential [67] (according to Perdew and Wang, PW91) compared to the present work [12] (according to Perdew, Burke and Ernzerhof, PBE) all the results are very similar. Similar test calculations were done using a completely different code. Namely, *flair* which is based on the all-electron full potential linearised augmented plane wave method and considered to be one of the most precise DFT concepts as no pre-constructed pseudopotential are necessary. Thus, it is concluded that the discrepancies to Domain *et al.*'s results are not due the different choice of the GGA parametrisation but due to the construction of the

pseudopotentials. In the work of Ref.[64] the so-called ultrasoft pseudopotentials (USPP) was used provided in older versions of VASP. It is well-known that USPP exaggerates magnetic properties with too large volumes and local moments [87].

TABLE 7.2: Formation energy per atom for the single atom defect, ε^{X_1} , and pair-wise substitutional defects, $\varepsilon^{X_2}/2$ per atom for Cu in bcc Fe and Fe in Cu. All geometrical parameters are relaxed.

	ε^{X_1} [meV]	$\varepsilon^{X_2}/2$ [meV]	$\varepsilon^{X_2}/2 - \varepsilon^{X_1}$ [meV]
Cu in Fe	773	682	-91
Fe in Cu	853	531	-322

Table 7.2 lists the results for the single and pair-wise defects of Cu in bcc Fe and Fe in fcc Cu. For the pair-wise defects the energy is reduced considerably, in comparison to the single atom defects, which is due to the bonding between the defects atoms in the nearest-neighbour pairwise arrangement, but nevertheless all values are strongly positive. The bonding effect is particularly strong for the Fe defect pairs, which is attributed to the ferromagnetic coupling. A calculation with antiferromagnetic coupling resulted in a by about 320 meV significantly higher formation energy compared to the ferromagnetic case. Anticipating the discussion about thermodynamical stability and solubility one would expect, that because of the substantially lower formation energy of Fe defect pairs compared to Cu pairs the miscibility of Fe defects in fcc Cu would be higher than the miscibility of Cu defects in bcc Fe. This is indeed the case as long as vibrational free energies are *not* taken into account, as illustrated in Fig. 7.14. If, however, they *are* taken into account the situation reverses dramatically demonstrating the strong and unpredictable (as far as predictions based on $T = 0$ K values) effect of vibrational free energies and entropies in particular on thermodynamic properties. This finding is elaborated later on.

	method	nr. atoms	total nr. k points	ϵ no rel. [meV]	ϵ pos. rel. [meV]	ϵ all rel. [meV]
ϵ^{Cu_1} :	VASP (PAW:PBE)	16	8192	768	758	-
	flair (PBE)	16	8192	767	756	-
	VASP (USPP:PW91)	54	6750	-	540	500
	VASP (PAW:PBE)	64	4096	790	778	773
ϵ^{Fe_1} :	VASP (PAW:PBE)	64	1728	858	857	853

TABLE 7.3: DFT derived formation energy of one Cu defect in bcc-Fe, ϵ^{Cu_1} , for several test cases for 16 and 64 atoms supercells. The corresponding defect energy of Fe in fcc Cu, ϵ^{Fe_1} , was calculated only for a 64 atom supercell. Results are shown for no relaxation, relaxation of atomic positions, as well as relaxation of volume and positions. Several \vec{k} -point sets were also tested, the number given is the total number of all \vec{k} -points in the BZ. A comparison with the data of Ref. [64] is made for the calculations of ϵ^{Cu_1} with a supercell of 16 atoms. Abbreviations for potentials and methods are given as in Table 7.1

TABLE 7.4: Temperature dependence of the differences of vibrational free energy, f^{X_1} and $f^{X_2}/2$, according to Eq. 7.6.

	T	f^{X_1}	$f^{X_2}/2$
	[K]	[meV]	[meV]
Cu in Fe:	0	-43	-23
	400	-118	-69
	800	-227	-130
	1200	-339	-191
Fe in Cu:	0	-5	29
	400	-14	80
	800	-28	178
	1200	-40	288

7.2.2 Vibrational Formation Energies

Figs 7.11 and 7.12 show the differences of normalised phonon densities of states g ,

$$\Delta g(\omega) = g^{X_i+H}(\omega) - g^H(\omega) . \quad (7.4)$$

The results for Δg for single atom and pair-wise Cu defects in Fe show a very similar behaviour for both types of defects. For Cu defects in Fe, the phonon DOS is significantly enhanced at lower energies between 14 and 22 meV with respect to pure Fe. This red shift might be understood by the replacement of Fe with heavier Cu atoms, assuming that the spring constants, i.e. bonding strength, remain unchanged. The fluctuations of Δg at larger energies are a consequence of the normalisation $\int \Delta g d\omega = 0$. The negative peaks are centred at the higher energy of about 37 meV indicating that the spectrum of the defect modes is restricted to lower frequencies. Δg is also shown in Fig. 7.12 for single atom and pair-wise Fe defects in fcc Cu. The prominent features are more pronounced for the pair-wise defect, which can be attributed to the strong ferromagnetic bonding between the two Fe atoms. In contrast to the Cu defects, there is a blue shift, i.e. loss of states, in the defect phonon DOS at energies between 12 and 20 meV. In the high energy region above 28 meV Δg is positive, as the defect Fe atoms are lighter than the Cu host atoms. In both cases of Δg , a significant negative peak arises at medium energies centred at 25 meV, which is more pronounced with the pair-wise defect.

The temperature dependent vibrational free energy F_{phon} is derived by integration over the phonon DOS $g(\omega)$, as derived in chapter 3, with

$$F_{\text{phon}}(T) = k_B T \int_0^\infty g(\omega) \ln \left(2 \sinh \left(\frac{\hbar\omega}{2k_B T} \right) \right) d\omega. \quad (7.5)$$

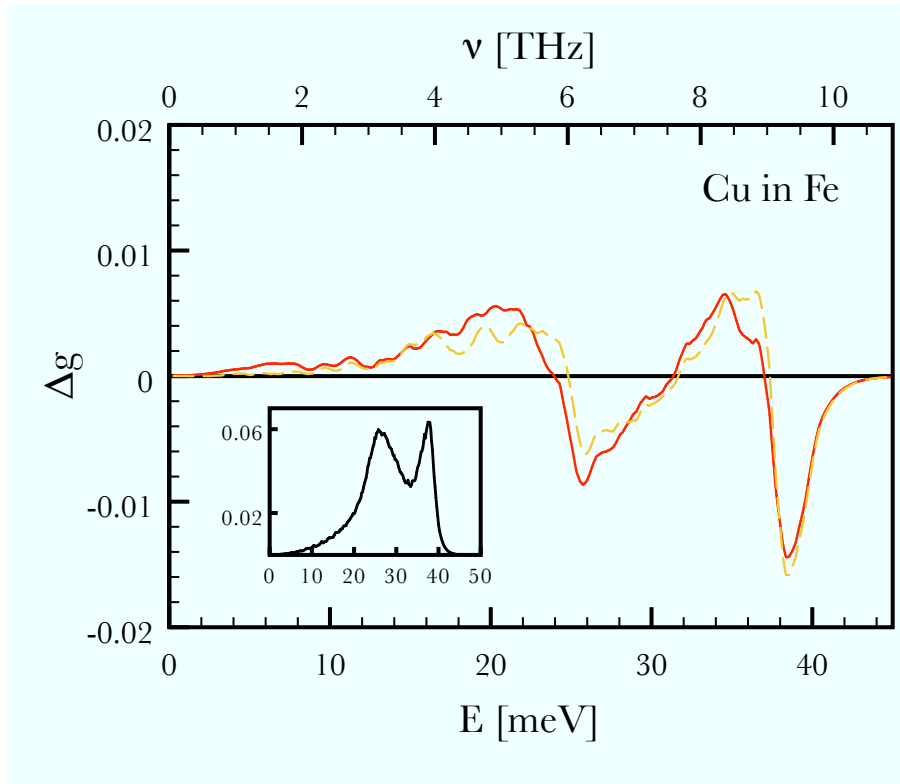


FIGURE 7.11: Differences Δg of normalised phonon DOS for substitutional Cu defects in comparison to pure bcc Fe: single-atom Cu defect (yellow dashed line) and pair-wise Cu defect (red solid line). The phonon DOS for bcc Fe is shown in the inset.

The change of the free vibrational energy $f^{X_i}(T)$ is calculated by (Eq. 7.6)

$$f^{X_i}(T) = F_{\text{phon}}^{X_i+H}(T) - (n_i F_{\text{phon}}^{X_i}(T) + n_H F_{\text{phon}}^H(T)), \quad (7.6)$$

using, as with the calculation of the formation energies, the corresponding reference pure phases, bcc-Fe and fcc-Cu.

Inspecting Fig. 7.13 and table 7.4, one realizes that the temperature dependency of the defect vibrational free energies are very different for the respective defects. For Cu defects in bcc Fe (single atom as well as pair-wise defects) the behaviour is very similar for both cases, namely a strong decrease of f with increasing temperature, which means thermodynamical stabilisation of these defects according to Eq. 4.10. For Fe defects in fcc Cu, however, the difference energies f behave totally different. For the single defect f is rather zero over the whole temperature range. On the other hand, for the pair-wise Fe defects the vibrational free energy difference increases very strongly, which in turn reduces the thermodynamical stability of pairwise Fe-defects.

Volume relaxation has a noticeable influence on $f(T)$. The energies f^{Cu_1} and f^{Cu_2} are

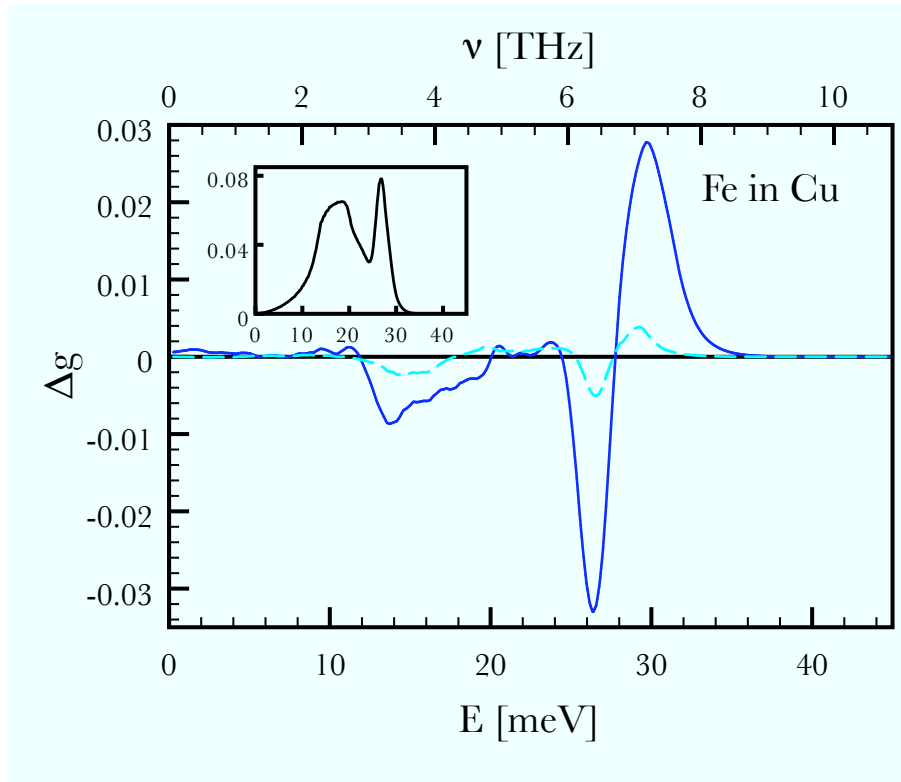


FIGURE 7.12: Differences Δg of normalised phonon DOS for substitutional Fe defects in comparison to pure fcc Cu: single-atom Fe defect (turquoise dashed line) and pairwise Fe defect (blue solid line). The phonon DOS for bulk fcc Cu is shown in the inset.

less negative when the volume is not relaxed: for example, the difference to the volume relaxed defects at 1200 K is ≈ 240 meV, and for $T = 800$ K it is ≈ 160 meV. This effect can also be observed on the Cu rich side where f^{Fe_1} and f^{Fe_2} are by about 30 meV less negative at 800 K and f^{Fe_1} is by 40 meV less negative at 1200 K while it is 130 meV less for f^{Fe_2} .

It should be noted, that in all the studied cases the temperature dependence of f comes exclusively from the differences of the vibrational entropies. The corresponding differences of internal energies are rather independent of temperature (at least on the energy scale of Fig. 7.13).

All values of $f(T)$ have been calculated for each of the defects at the equilibrium lattice constants at $T = 0$ K. Effects of thermal expansion were not taken into account and it is assumed that the *differences* of free energies $f(T)$ are only weakly affected by thermal expansion.

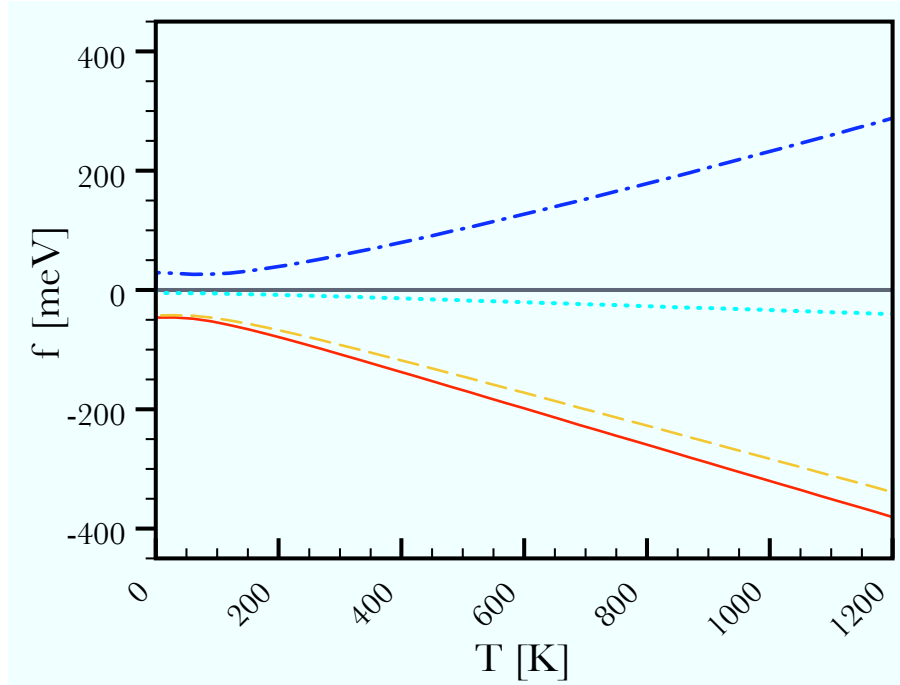


FIGURE 7.13: Temperature dependence of changes of differences of vibrational free energies $f(T)$ (see Eq. 7.6). Defects in bcc Fe: single Cu atom (yellow dashed line) and pairs of Cu atoms (red solid line); defects in fcc Cu: single Fe atom (turquoise dashed line) and pairs of ferromagnetic Fe atoms (blue dashed-dotted line). The plotted values for pair-wise defects correspond to the vibrational defect energy of the two atoms (not divided by 2).

TABLE 7.5: Relative distribution of one atom and pair-wise defects (in % of x) at 800 K and 1200 K, and the corresponding total concentration x of the solute species.

	T [K]	without vibr.		with vibr.		c_1	$2c_2$
		x [at. %]	c_1	$2c_2$	x [at. %]		
Cu in Fe	800	0.003	49	51	0.047	75	25
	1200	0.115	48	52	1.940	75	25
Fe in Cu	800	0.024	2	98	0.006	9	91
	1200	0.419	6	94	0.124	30	70

7.2.3 Phase diagram

Including the calculated formation energies and the change in the free vibrational energy of single and pair-wise defects into the thermodynamical model discussed in chapter 4, yields the phase diagram for the dilute Fe-Cu alloy. Fig. 7.14 shows this phase diagram at both, the Fe-rich side and the Cu-rich side. No other stable phases exist over the whole range of concentrations, as is clearly evident by the rather large and positive, i.e. nonbonding, formation energies derived from DFT calculations for Fe-Cu

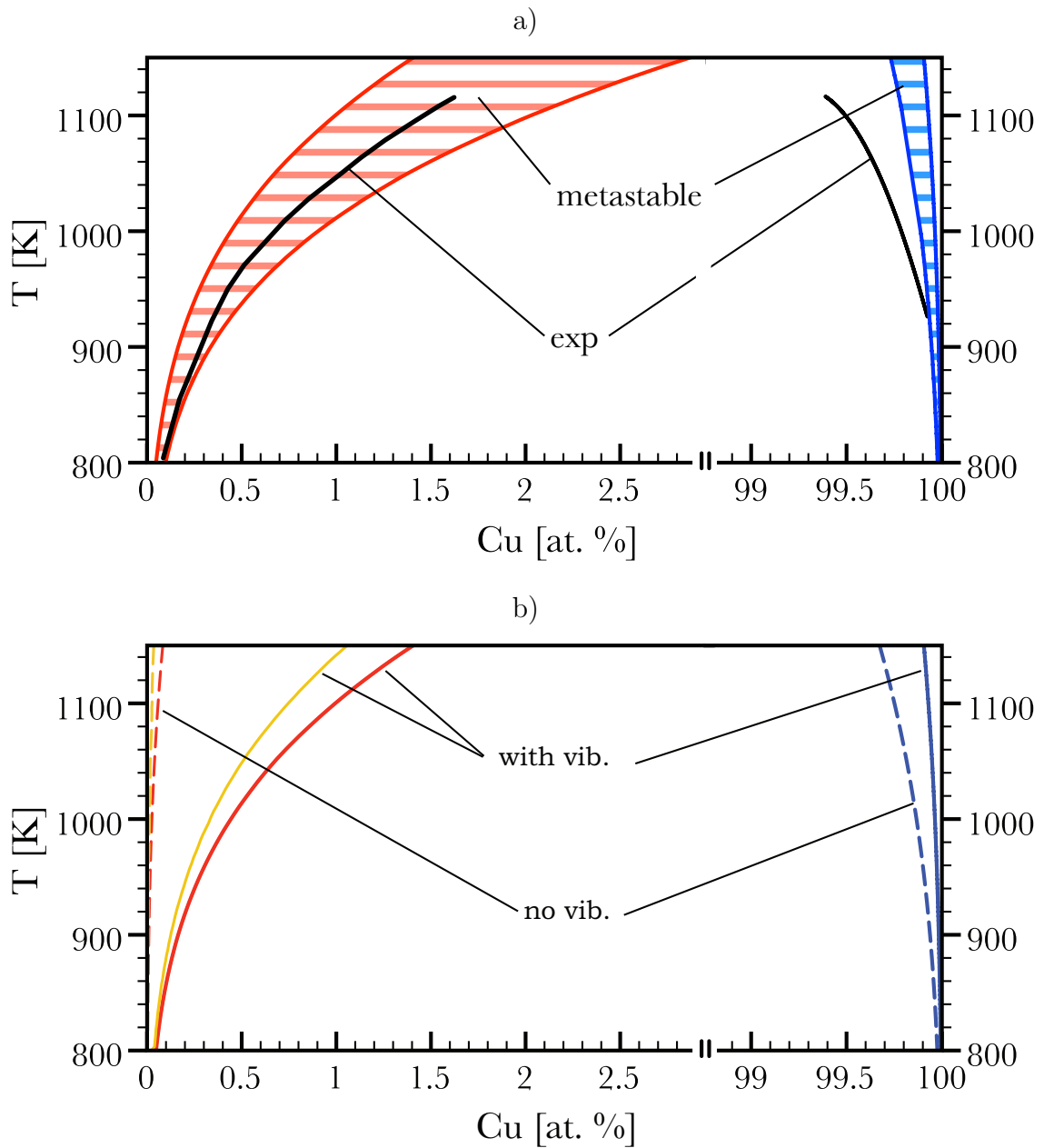


FIGURE 7.14: Phase diagram of the Fe-Cu system at the Fe-rich and Cu-rich side. Panel a: Comparison between the experimental data of Ref. [62] (black solid line) to the calculations including the vibrational energy according to Eq. 4.10. Hatched areas: regions of metastable phases. The upper boundaries of the hatched areas mark the thermodynamically stable phase boundaries. Panel b: Analysis the calculated results for the thermodynamically stable phase boundaries. Without vibrational energies: dashed lines, with vibrational energies: full lines. Results for single and both (single and pair-wise) defects at the Fe-rich side are shown in yellow and red colours, correspondingly. On the Cu-rich side only the results for both (or rather pair-wise) defects are shown (blue colour), because the effect of single defects is hardly visible.

ordered compounds [63]. Therefore, only solid solutions and defect clusters might be thermodynamically stabilised by entropy.

In Fig. 7.14 a) the Fe-rich alloy experimental data [62] (black line) indicates, that a significant amount of Cu can be added. These results are in good agreement as they lie within the hatched region. It should, however, be noted that the model only covers single and pair-wise defects. Larger Cu-clusters might lead to even more favourable lower boundaries, if there is a sufficient gain in bonding energy for larger clusters compared to pairs of Cu-atoms. On the other hand, considering Fig. 7.14 b) and comparing the yellow and red lines, there is almost no change of the phase boundary when pair-wise defects are added to the mixture with single atom Cu-defects.

The situation is very different at the Cu-rich side, where the miscibility range is rather narrow, as indicated by the experimental boundary [62].

From the calculated results in Fig. 7.14 b) *without* vibrational free energies, one derives a very narrow miscibility range at the Fe-rich side (coloured dashed lines), and a wider range at the Cu-rich side (blue dashed line). The mixing entropy alone is obviously totally insufficient for a reasonable estimate of the phase boundaries. Including vibrational free energies changes the calculated results dramatically. Fig. 7.14 b) emphasises these findings: for the Fe-rich side by looking at the dashed and solid lines the miscibility range widens significantly, whereas at the Cu-rich side it is strongly narrowed. This asymmetric behaviour of the miscibility ranges is due to the asymmetry of the total free energies F_{tot} of both phases. Whereas at the Fe-rich side the vibrational energy (i.e. the vibrational entropy) lowers F_{tot} , the effect is opposite on the Cu-rich side as illustrated in Fig. 7.13.

For a truly quantitative description of the phase boundary on the Fe-rich side for temperatures $T > T_C = 1043$ K larger than the Curie temperature of Fe, the change of magnetic ordering also needs to be included. Nevertheless, the most important effects occur already far below T_C (see Fig. 7.14) underlying the important role of vibrational entropy for the modelling of the Fe-Cu alloys. This is also manifested by table 7.5. For the Fe-rich side it shows, that *without* vibrational energies the Cu concentrations c_1 and $2c_2$ are rather equal, at least in the given temperature range of $800 \text{ K} < T < 1200 \text{ K}$. This balance changes dramatically when vibrational entropies are included, as single atom defects are much more abundant than pairs, the ratio is now 3 to 1. In both cases the mixture of defects remains rather constant in the studied temperature range. At the Cu-rich side the mixture of defects for the calculation *with* vibrational energies depends much stronger on temperature: for 800K the ratio $c_1 : 2c_2$ is 1:10, and it changes to 3:7 at 1200K. Clearly, the magnetic coupling of the Fe-pairs manifests itself in the dominance of the pair-wise defects.

Summarising, the vibrational free energies (in particular their entropy contributions) are indeed very important. By including them one reproduces the main features of the

experimental phase diagram, which consists of a wide miscibility range at the Fe rich side and a very narrow range at the Cu-rich side. So far, non-interacting independent defects were considered with their formation energies independent of the concentration of defects in the host. Clearly, a much more general approach would be to derive concentration dependent thermodynamical properties on a truly *ab-initio* level, which is the subject of the next section dealing with the CE. In which, as for the independent defect case also vibrational free energies will be taken in a more elaborate study into account.

7.3 Cluster Expansion

In a first step towards a temperature dependent CE a standard CE utilising only DFT energies was made. The formation enthalpy $\Delta H(\sigma)$ of the Fe-Cu system within the CE was derived by

$$\Delta H(\sigma) = E_{\text{DFT}}(\sigma) - \left(x E_{\text{DFT}}^{\text{Cu}(\text{fcc})} + (1-x) E_{\text{DFT}}^{\text{Fe}(\text{bcc})} \right) , \quad (7.7)$$

using DFT total energies of bcc Fe $E_{\text{DFT}}^{\text{Fe}(\text{bcc})}$ and fcc Cu $E_{\text{DFT}}^{\text{Cu}(\text{fcc})}$ as reference values. No stable phases for any atomic configurations σ between the pure elemental phases are found, i.e. the formation enthalpies are always positive. Hence, at $T = 0$ K the system completely decomposes in to the two elemental phases. This causes a technical problem for the CE procedure as presented in chapter 5, because the input structures cannot be selected automatically. The structures with the lowest formation enthalpies $\{\sigma\}_{\text{min}}$ between the pure phases are those representing Fe-Cu phase-separation, i.e. two slabs of pure Cu and Fe orientated along some arbitrary direction. Hence, it is unlikely that the important interactions needed for a useful CE are present in the set of structures $\{\sigma\}_{\text{min}}$. It was therefore necessary to include structures which are energetically unfavourable. Still, the familiar procedure could be pursued. New structures predicted by CE with lower energies than the ones already calculated by DFT were included into the set $\{\sigma\}$ until no new ones were found.

Furthermore, it should be noted that the two parent lattices, bcc for Fe and fcc for Cu, are different. Since the main interest lies in Fe-rich Fe-Cu alloys the bcc parent lattice was chosen as basis for the CE. To correctly calculate ΔH the energy of pure fcc Cu was taken as reference. Proceeding with this approach a set of 53 input structure was obtained resulting in a cross validation score S_{CV} (see Eq. 5.8 in chapter 5) of 3.74 meV. For unit cells up to 8 atoms UNCLE can set up, on the bcc parent lattice, 631 possible configurations σ , i.e. structures for the CE. The CE predicted energies of these structures are shown in Fig. 7.15. From these 631 structures the random mixing energy (see Fig. 7.15) can be calculated, which agrees very well with a previous CE by Liu *et al.* [63].

On the basis of the chosen set of CE structures other physical alloy properties, such as the average magnetic moment per atom, can be derived for the random alloy. The result for the averaged moment for the $Fe_{1-x}Cu_x$ alloy system is shown in Fig. 7.16 and was recently published in Ref. [88]. The change of the average moment with Cu concentration is not linear and can be fitted by a third-order polynomial,

$$M(x) = (0.51x^3 - 1.437x^2 - 1.272x + 2.199) \mu_B . \quad (7.8)$$

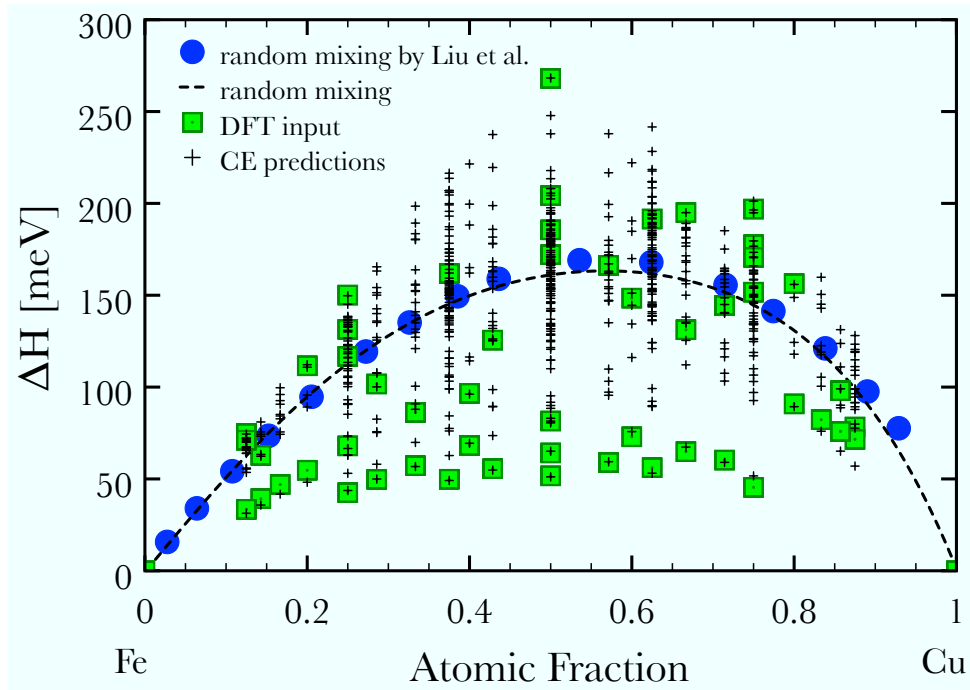


FIGURE 7.15: Enthalpy of formations vs. atomic fraction x of the $Fe_{1-x}Cu_x$ alloy system. Comparison of DFT input values (green squares) to CE predictions (black crosses). The random mixing energy of this work (dashed black line) is compared to a CE of Liu *et al.* [63] (blue circles). The averaging is done over all 8 atom unit cell structures with a bcc parent lattice.

The nonlinearity at higher Fe concentrations, i.e. for $x < 0.5$, may be ascribed to the ever so slight volume mismatch of Fe and Cu with a calculated DFT volume (see table 7.1) of 11.35 \AA^3 and 12.02 \AA^3 , respectively. Thus, with the volume expansion due to the mixing of Fe and Cu the Fe atoms have with increasing x in the interval $x = \{0, 0.5\}$ more space available leading to a slightly higher local magnetic moment for Fe. At smaller Fe concentrations, i.e. $x > 0.5$, the behaviour of the average magnetic moment becomes a linear function of x as the change in the Fe atomic volume becomes marginal.

7.3.1 Temperature Dependent CE

In a second, much more elaborate step, the CE was extended by taking vibrational free energies for all structures under consideration into account. This makes the ECI's temperature dependent which has, as will be discussed in greater detail, the consequence that for different temperatures *different* CE's have to be done. Furthermore, one has to deal with a variety of structures where parts of the vibrational spectrum consists of imaginary frequencies.

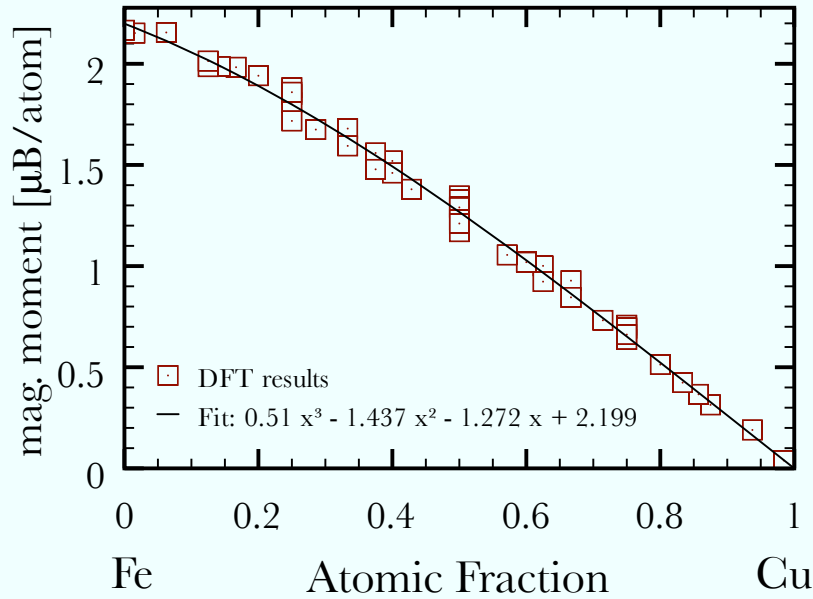


FIGURE 7.16: Magnetic moment per atom versus Cu concentration x for $Fe_{1-x}Cu_x$.

The standard Fe-Cu CE is now extended by adding the relative vibrational free energy

$$\Delta f(\sigma, T) = F_{\text{phon}}(\sigma, T) - xF_{\text{phon}}^{\text{Cu}(\text{fcc})}(T) - (1-x)F_{\text{phon}}^{\text{Fe}(\text{bcc})}(T), \quad (7.9)$$

again using bcc Fe ($F_{\text{phon}}^{\text{Fe}(\text{bcc})}$) and fcc Cu ($F_{\text{phon}}^{\text{Cu}(\text{fcc})}$) as references.

From Figs 7.17 and 7.18 one notices that most of the input structures have imaginary vibration modes, with the structures on the Cu bcc rich side having a bias towards a higher imaginary frequency percentage. This can be easily explained by fcc Cu being more stable than bcc Cu resulting in Cu rich structures being more likely to be dynamically unstable. It is not necessary to remove all imaginary structures because of their dynamical instability from the CE as these structures are already energetically unstable and no alternatives exist. Still, to reduce the error contributions from imaginary phonon modes two structures where the amount of imaginary frequencies ($i\omega$) were found to be greater than 5 % had to be removed, thereby reducing the number of input structures to 51 as shown in Figs 7.17 and 7.18.

Using the sum of both $\Delta f(T)$ and ΔH in the CE now yields, as discussed in chapter 5, a set of temperature dependent figures $\{f(T)\}$ with the corresponding interaction energies $\{J_f(T)\}$. At each temperature step twenty separate CE were done and the separate figure-sets $\{f\}$ merged into a single set $\overline{\{f\}}$ (see Eq.s 5.20 and 5.21 in chapter 5). The merged $\overline{\{f\}}$ now contains more than 100 figures, making it much larger than any individual set

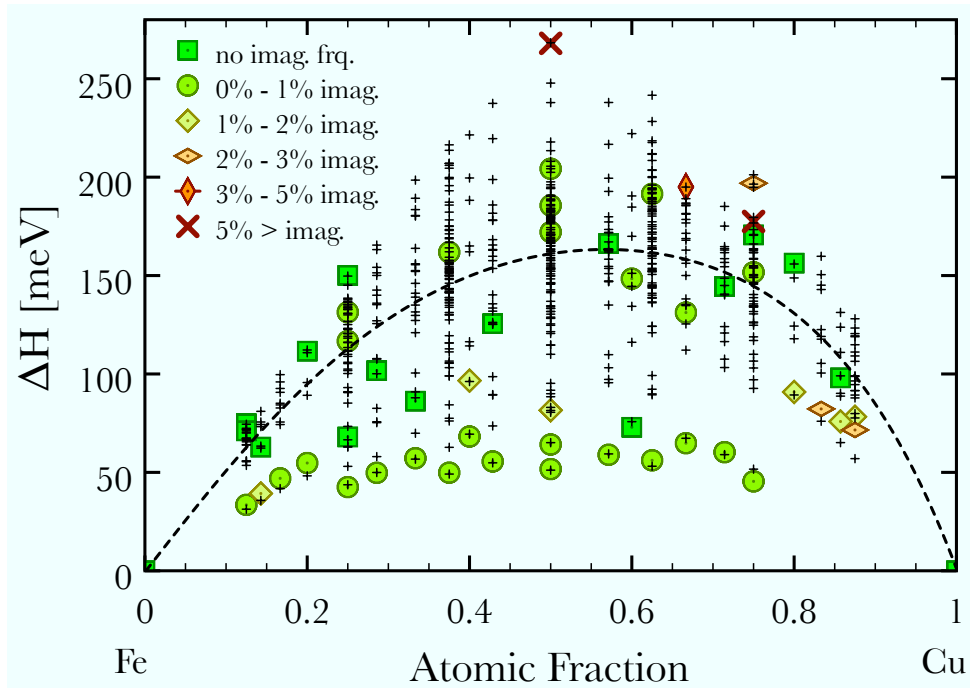


FIGURE 7.17: Enthalpy of formation ΔH as derived from temperature dependent CE by taking into account vibrational free energies, representation similar to Fig. 7.15. The percentage of imaginary frequency indicates how much of the total vibrational spectrum is affected by the non-vibrational modes.

which only included between 30 to 40 figures. As discussed previously this is most likely stems from the choice of figures being ambiguous.

In general, it is disputable by which way modes with imaginary frequencies should be taken into account in the vibrational free energy, i.e. in the entropy. In this work the most common recipe was taken: the imaginary modes were just *not* taken into account.

The next crucial point concerns the quality of the temperature dependent CE.

The temperature dependent cross validation score $S_{CV}(T)$ of the original twenty unmerged figure-sets now increases from 3.74 ± 0.11 meV for the standard CE without phonons to 5.48 ± 0.08 meV for the temperature dependent CE at 1200 K, as sketched in Fig. 7.19 and table 7.6. It should be noted, that S_{CV} is evaluated for each figure-set separately within the UNCLE code during the CE fitting procedure. It is impossible to evaluate S_{CV} for the merged figure-sets (see chapter 5).

The temperature dependency of the effective interaction energy after merging the figure-sets is demonstrated in Figs 7.20 and 7.21. The ECI's $J(\bar{T})$ of the figures are shown without and with vibrational contributions at $T=600$ K and 1200 K. For the sake of clarity only the figures with $|\bar{J}| > 5$ meV are shown. The symbol \bar{J} refers to the interaction energy of the merged figure-set. Each figure is classified by its average vertex-vertex

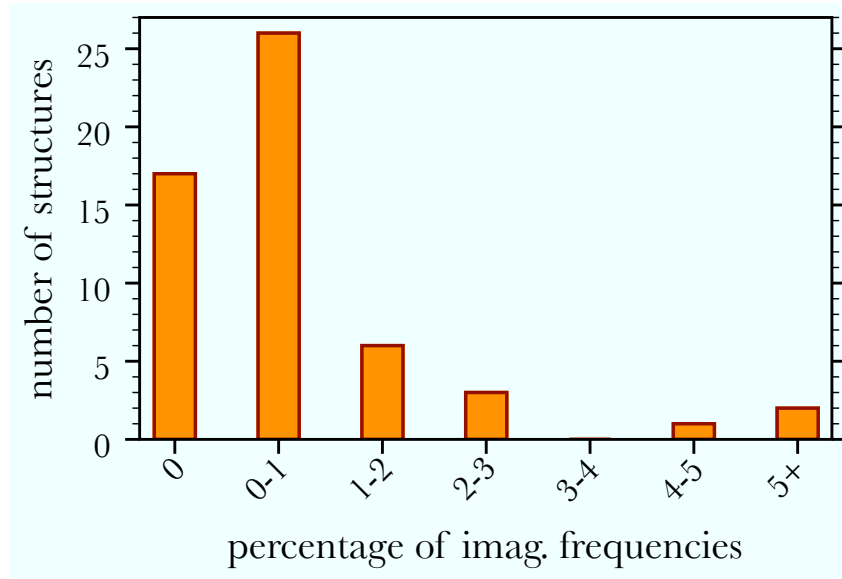


FIGURE 7.18: Frequency of imaginary modes occurring in Fig. 7.17.

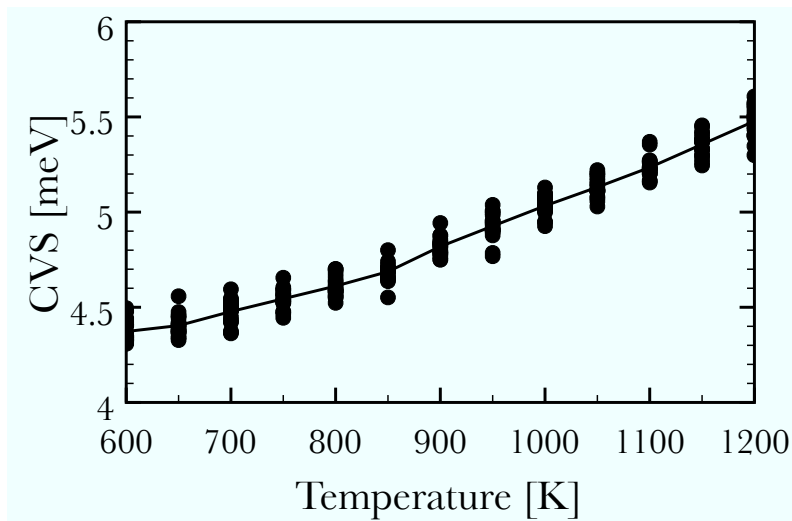
FIGURE 7.19: Temperature dependency the cross validation score $S_{CV}(T)$. At each temperature several figure-sets with varying $S_{CV}(T)$ are obtained. Average of $S_{CV}(T)$ indicated by solid line.

TABLE 7.6: Cross validation score $\bar{S}_{CV}(T)$ averaged over twenty figure-sets for CE's without the vibrational contributions and with vibrational contributions at 600 K, 900 K and 1200 K.

	T [K]	$\bar{S}_{CV}(T)$ [meV]
CE without vib.:	-	3.74 ± 0.11
CE with vib.:	600	4.37 ± 0.05
	900	4.82 ± 0.05
	1200	5.48 ± 0.08

distances v , i.e. the average distance between each corner point of the figure. For example, for pairs the (now exact) distance between the atoms is given by $d_{\text{pair}} = 2v$ as the pair-figures consist of two vertices.

Inspecting Figs 7.20 and 7.21 shows that adding the vibrational free energy decrease the value of the strongly negative nearest neighbour pair-interaction energy, namely from -115.25 meV (no vibrational free energy) to -92.43 meV (with vibrational free energy) at 1200 K. and similarly the 2. nearest neighbour pair-interaction increases from -20.7 meV to -10.5 meV. The changes in the higher-order interaction energies is less distinctive. The kink in Fig. 7.21 for the pair-figures ECI's at 650 K has by itself no physical meaning as it may be compensated by higher-order figures, i.e. triplet, quadruplet, etc. which are not shown. This underlies the importance of viewing the pair figures not independently but as part of the larger figure-set, i.e. Fig. 7.21 only reflects a general trend.

The results when using the merged figure-set for the random mixing energy at $T = 0$ K (no vibrational contribution), 5 K, 300 K, 600 K, 900 K and 1200 K are shown in Fig. 7.22. It is obvious that the higher the temperature the more the maximum is shifted towards higher Cu concentrations, and also that the value of the maximum is lowered with increasing temperature. This leads to a decrease of the random solution gradient at the Fe-rich side, while increasing the gradient weakly on the Cu-rich side. Clearly, this has the effect of increasing the solubility of Cu at the Fe-rich side, whereas on the Cu-rich side the effect is opposite. This mirrors the results found with the independent defect model where the same influence of the vibrational free energies on the solubilities has been observed.

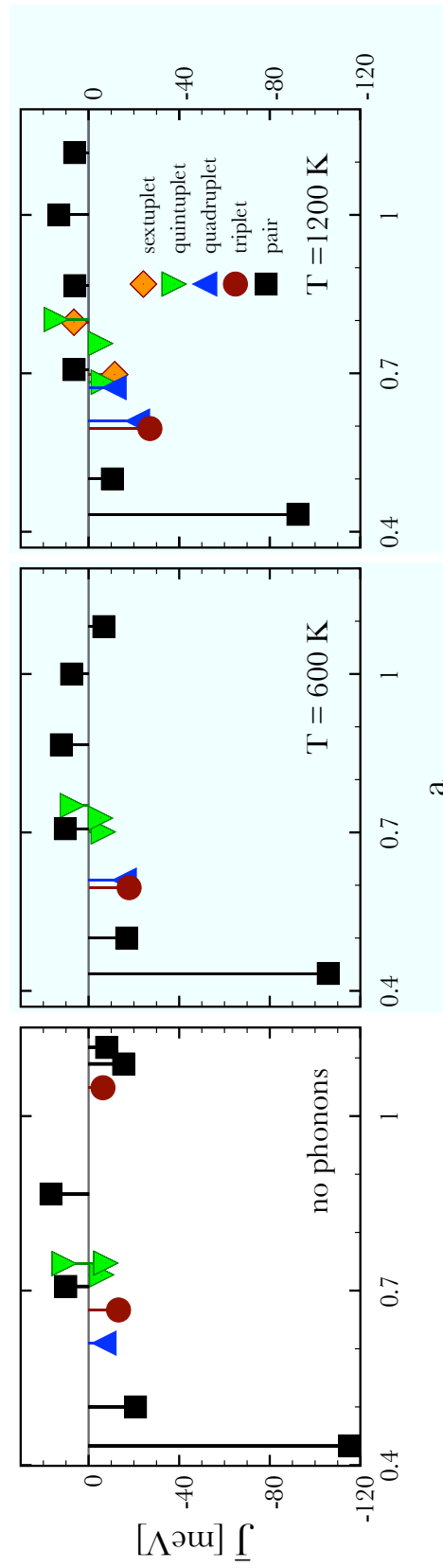


FIGURE 7.20: Effective cluster interaction energies \bar{J} of the merged figure-set for $|\bar{J}| > 5$ are shown for the cases without and with vibrational free energies for $T = 600$ K and 1200 K. The vertex-vertex v distance is given in multiples of the lattice constant a , i.e. the correct distance of the pair figures is described by $d_{\text{pair}} = 2v$.

7.3.2 Monte Carlo simulation: Solubility of Cu

To determine the Cu solubility x in Fe-rich alloys the quasi grand-canonical Monte Carlo approach described in chapter 5 was applied. For the accurate determination of the Cu solubility it has to be ensured that only atoms dissolved in the Fe host are counted. Therefore, the first three layers of the Fe block forming the interface were discarded in order to avoid that Cu atoms from the Cu block are counted as dissolved.

Fig. 7.23 shows cross-sections through the simulation for $T = 900$ K, 1050 K and 1200 K without and with vibrational contributions. The Fe-Cu interface is oriented in the [111] direction of the bcc lattice. Clearly Fig. 7.23 demonstrates that the solubility of Cu in Fe increases with temperature and most importantly, that the Cu solubility is much higher when vibrational free energies are included into the CE. On the other hand, hardly any Fe is dissolve in Cu as already observed for the independent defect model. It should be noted, that applying the defect model for the Cu-host the fcc lattice was correctly chosen, whereas now in the CE the bcc parent lattice is underlying the calculations. Nevertheless, the trend of solubility at the Cu-rich side is similar in both cases.

At this point it should be emphasised that the MC simulation is statistical and suitable averages have to be taken. Therefore, the correct solubility was determined by five separate MC calculations using different random-number generator seeds. The resulting standard-deviation for the solubility of Cu was smaller than 4% which is very small compared to the standard-deviation of the calculations with the 20 individual unmerged figure-sets.

For example, for the CE with twenty unmerged figure-sets at $T = 1150$ K a rather bad standard deviation of 18% is obtained and for $T = 0$ K (no vibrational free energies) the deviation is even worse, namely 21%. Table 7.7 reveals a small difference between the average solubility of the 20 unmerged CE calculations and the value for the merged figure-set, listed for $T = 850$ K, 1000 K and 1150 K. This small difference can be explained by the standard-deviation of 4% from the five separate MC calculations.

Finally, the standard deviation of the 20 unmerged figure-set for each temperature step (see table 7.7) are now included in the phase diagram shown in Fig. 7.24, replacing the MC standard deviation where the merged figure-set are used as they are much larger. A comparison of the CE derived solubility to the CALPHAD data of Ref. [62] and to the model of independent defects shows in Fig. 7.24 that there is a very good agreement between CE and the defect model. However, at larger temperatures the deviation of the Cu concentrations is getting more significant, because concentration dependent interactions, as included in the CE, now become more important. The agreement to the (semi)-empirical CALPHAD results is rather good, demonstrating the power and reliability of the applied *ab-initio* DFT+CE+MC+vibrational energy approach. This is done

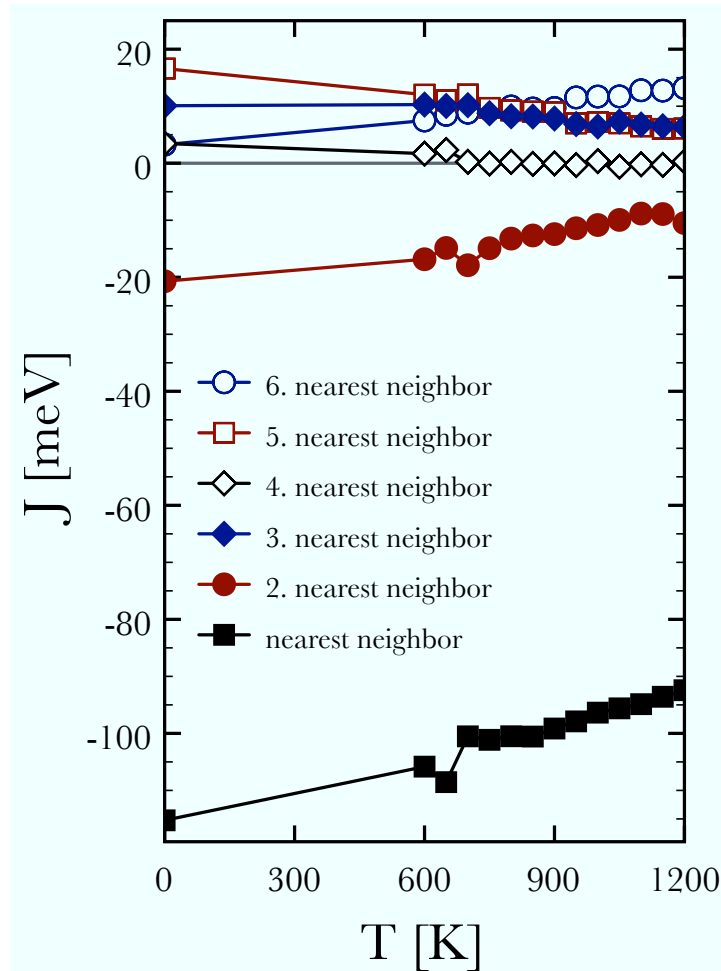


FIGURE 7.21: Pair figure ECI's of the merged figure-set \bar{J} versus temperature up to the sixth nearest neighbour pair interactions.

without any empirical parameter. (Note, the exchange-correlation functional was parameterised by a standard GGA model.) Summarising, Fig. 7.24 demonstrates very clearly that the solubility of Cu in the Fe-rich alloy is very strongly underestimated and therefore very wrong when vibrational free energies are not included.

7.3.3 Supersaturation and Precipitations

Technologically, the most important effect is the formation of precipitates [89]. This can be simulated from first-principles by using CE and MC, but requires two major extensions dealing with the migration of Cu atoms which are not available at present. To make space available for the migration, vacancies have to be introduced enlarging the CE to a ternary case. To connect the MC steps to physical time a kinetic MC approach with a residence time algorithm [90] is needed in which migration barriers are also included

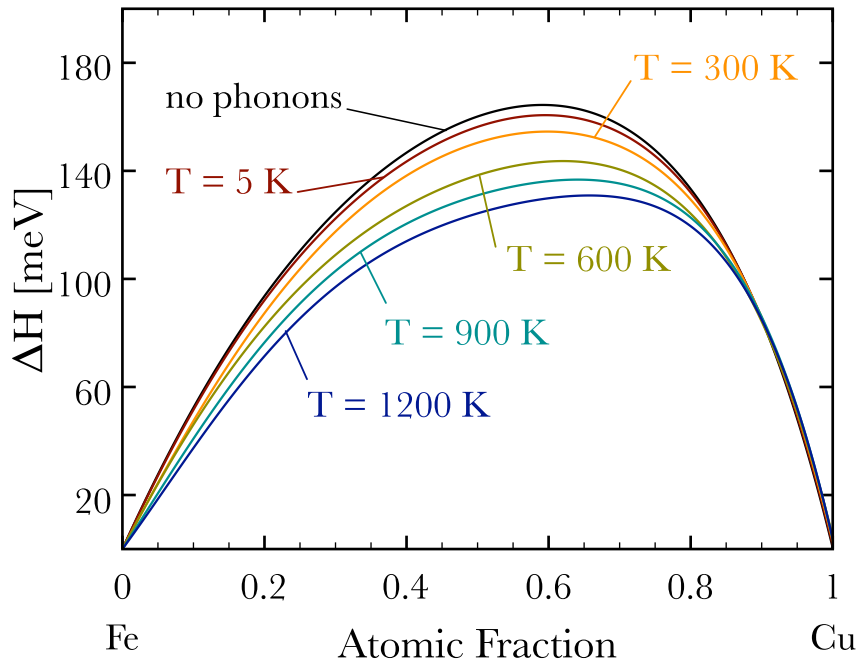


FIGURE 7.22: Random mixing energies without and with vibrational free energies for temperatures $T = 0$ K (no phonons), 5 K, 300 K, 600 K, 900 K and 1200 K.

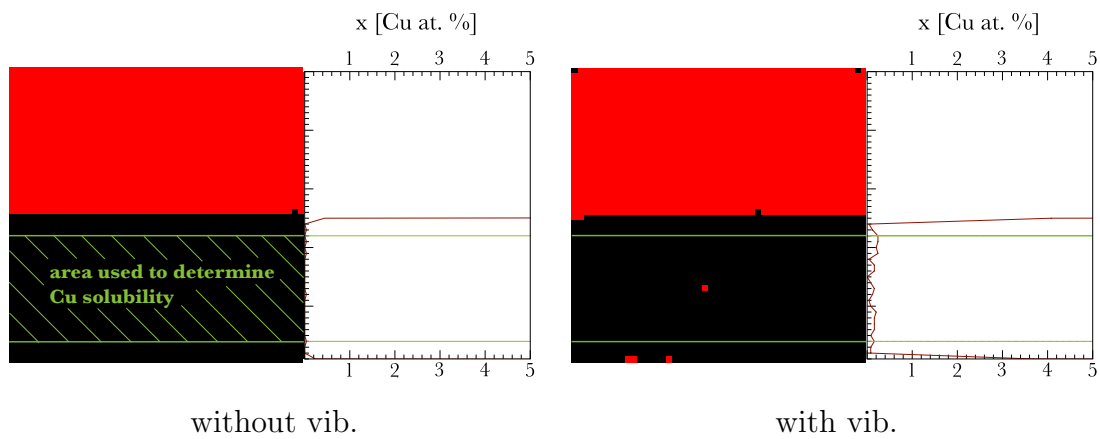
TABLE 7.7: Mean solubility of Cu $\bar{c}_{Cu}(F)$ as derived from 20 individual CE fits in comparison to the value $c_{Cu}(\bar{F})$ corresponding to the merged figure-sets.

	T [K]	$\bar{c}_{Cu}(F)$ Cu [at. %]	$c_{Cu}(\bar{F})$ Cu [at. %]
E without phonons:	1150	0.19 ± 0.04	0.18
CE with phonons:	850	0.08 ± 0.04	0.06
	1000	0.48 ± 0.11	0.43
	1150	1.69 ± 0.33	1.58

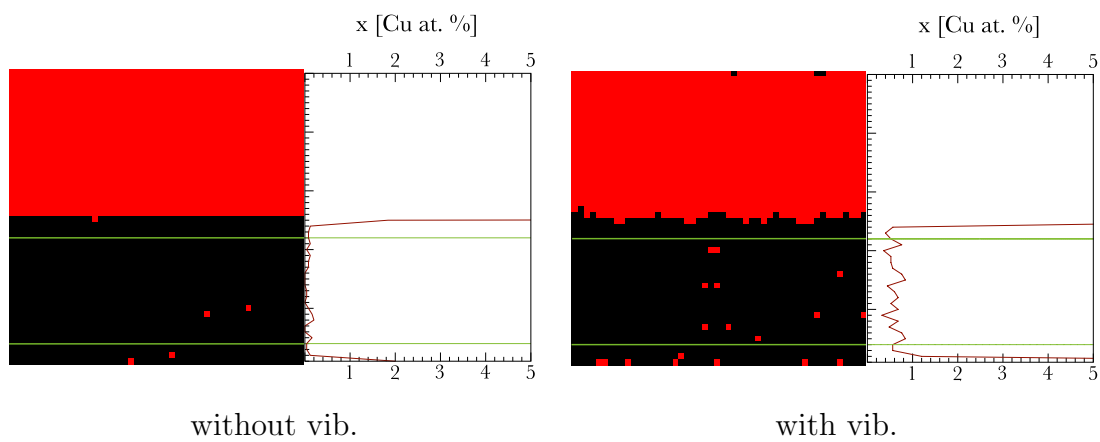
correctly. All this can be done in principle (and is done at the moment within a major FWF project) with DFT accuracy but goes beyond the scope of the present thesis. The thermodynamical MC technique in this work is based on the direct exchange between any two atoms of different species within an defined cutoff radius, which in the present case covers the whole simulation cell. A qualitative description of the precipitation process is possible by the thermodynamic MC as long as as one accepts that the number of MC steps, i.e. the number of times an atom exchange is attempted, is not directly connected to any real time scale and that the diffusion process itself is unphysical.

The definition of the size of a precipitate is arbitrary and must be defined beforehand, as also done by the experimentalists when, e.g. analysing the results of an atom probe

900K



1050K



1200K

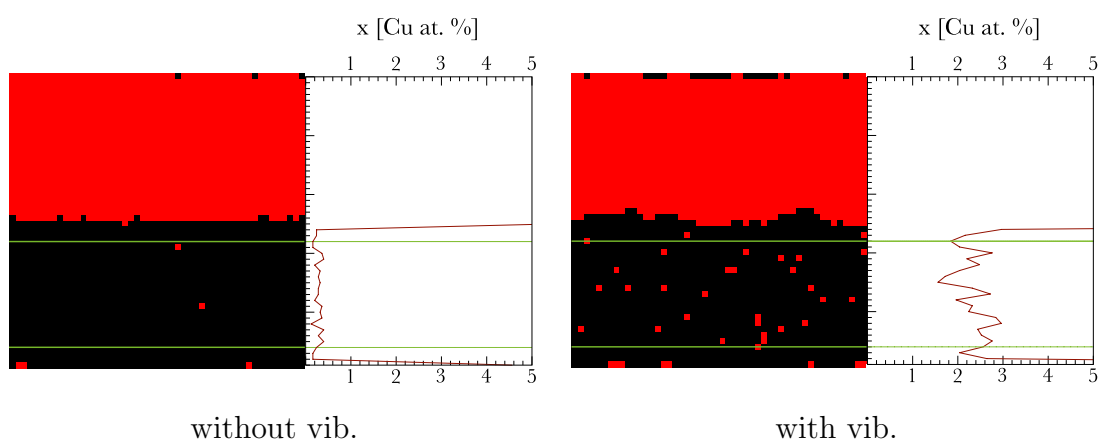


FIGURE 7.23: Cross-sections of the simulation box the in $[111]$ direction with and without vibrational contributions as well as the layer concentration of Cu at the $T = 900$ K, 1050 K and 1200 K. The Fe atoms are coloured black and Cu atoms red. Area (volume) in which the Cu atoms were counted is marked by two green lines (planes).

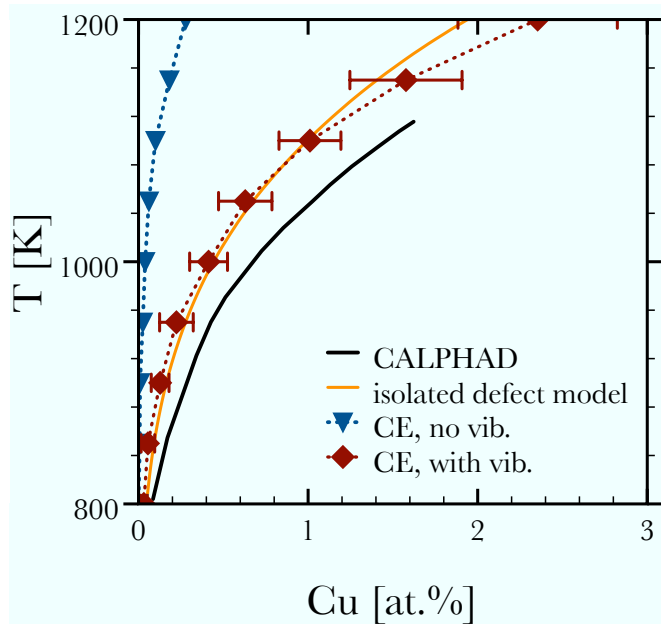


FIGURE 7.24: Fe-Cu phase diagram at the Fe-rich side: CALPHAD according to Landolt and Börnstein [62] (black solid line); CE results with vibrational contributions (red dashed line and diamond) and without the (blue dashed line and triangle). Independent defect model indicated by (orange solid line).

experiment. In this work the definition is that any cluster consisting of more than 10 nearest-neighbour linked Cu atoms is a precipitate and each Cu in this cluster belongs to this specific precipitate. All other smaller objects of Cu atoms are considered to be Cu dissolved in the matrix of the Fe host. The chosen precipitate size is close to 12 Cu atoms, the size estimated by Yuge *et al.* [91] for the critical size of a Cu precipitate. Of course, the periodic boundary condition must be taken into account properly for a correct counting of precipitates.

This procedure is in contrast to the one used for finding the thermodynamical equilibrium, i.e. the solubility, as discussed in the previous section. In the search for the equilibrium one had to start at $T = 0$ K and when at a given temperature equilibrium was reached, the dissolved atoms in a locally predefined Fe-box were counted. Now, the starting state is prepared at high temperature in order to simulate the effect of supersaturation upon cooling down. The simulations starts now by randomly filling the box in Fig. 7.25 by n_{Cu} . When cooling the box down the Cu atoms start to be either included in a precipitate or remain dissolved in the Fe matrix.

The total number of Cu atoms defines the concentration of available Cu, $x = n_{Cu}/N_{tot}$ whereby N_{tot} is the total number of Fe and Cu atoms in the box. Consequently, the concentration of atoms dissolved in the matrix is defined as $x_{mat} = n_{dis}/N_{tot}$ and the concentration of atoms in the precipitates $x_{prec} = n_{prec}/N_{tot}$ is given accordingly. The

assignment, if a Cu object and its atoms belong to the matrix or to a precipitate was described above.

In Fig. 7.25 the $50 \times 50 \times 50$ simulation cell with 125000 lattice sites has as an initial starting configuration of 3750 Cu atoms, which are randomly distributed. The number of Cu atoms corresponds to $x = 3$ at.%, which at the beginning is equal to x_{mat} . By annealing the simulation cell at 800 K a decomposition reaction takes place: precipitates first form via nucleation and then grow. This decomposition reaction is illustrated in more detail by the two panels of Fig. 7.26. Panel a) shows the change of Cu concentrations x_{mat} and x_{prec} as well as the enthalpy per atom ΔH versus the number of Monte Carlo steps whereas panel b) demonstrates the change of the average size of precipitates and the change of the number of precipitates in the simulation cell.

One can roughly distinguish between three separate processes. In a first step, in the supersaturated mixture Cu precipitates are formed by a nucleation process, for which panel a) reveals the largest enthalpy change of -8.36 meV per atom and a sharp drop of x_{mat} from the initial 3 at.% to 0.43 at.% with the accompanying rise in x_{prec} from 0 at.% to 2.57 at.%. For this situation panel b) shows an exponential growth of precipitate size. The second process is a rather fast Ostwald ripening [61]: larger precipitates grow by swallowing smaller ones. This process is accompanied by a change in the average precipitate size from 111 to 498 and a large fluctuation of precipitate size as well as a reduction in the number of precipitates from 24 to 7. The enthalpy changes by -2.06 meV while x_{mat} drops further down to 0.22 at.%. In the last phase the Ostwald ripening process slows down considerably as all smaller precipitates have been consumed. The change in precipitate size becomes much slower and each time before the number of precipitates is decreased by one the standard deviation of the average precipitation size increases. After 25×10^6 MC steps Cu is still oversaturated in the simulation cell with a x of 0.16 at. % as the equilibrium solubility in Fig. 7.24 is $x = 0.03$ at.%.

Although the discussion of the precipitation process is only a qualitative assessment it becomes clear that the timespan for Cu to reach equilibrium concentration is much larger than the observation timespan, i.e. final number of MC steps. The value of x also depends on the size of the Cu precipitates in the simulation cell. The larger the Cu precipitate the more it resembles bulk Cu and the more favourable it becomes for the Cu atoms to attach to the precipitate. This might point to an overestimation of x in the semi-empirical CALPHAD calculations [62] as they are based on empirical data with a limited observation timespan.

$T = 800\text{K}$, $x = 3 \text{ Cu at.}\%$

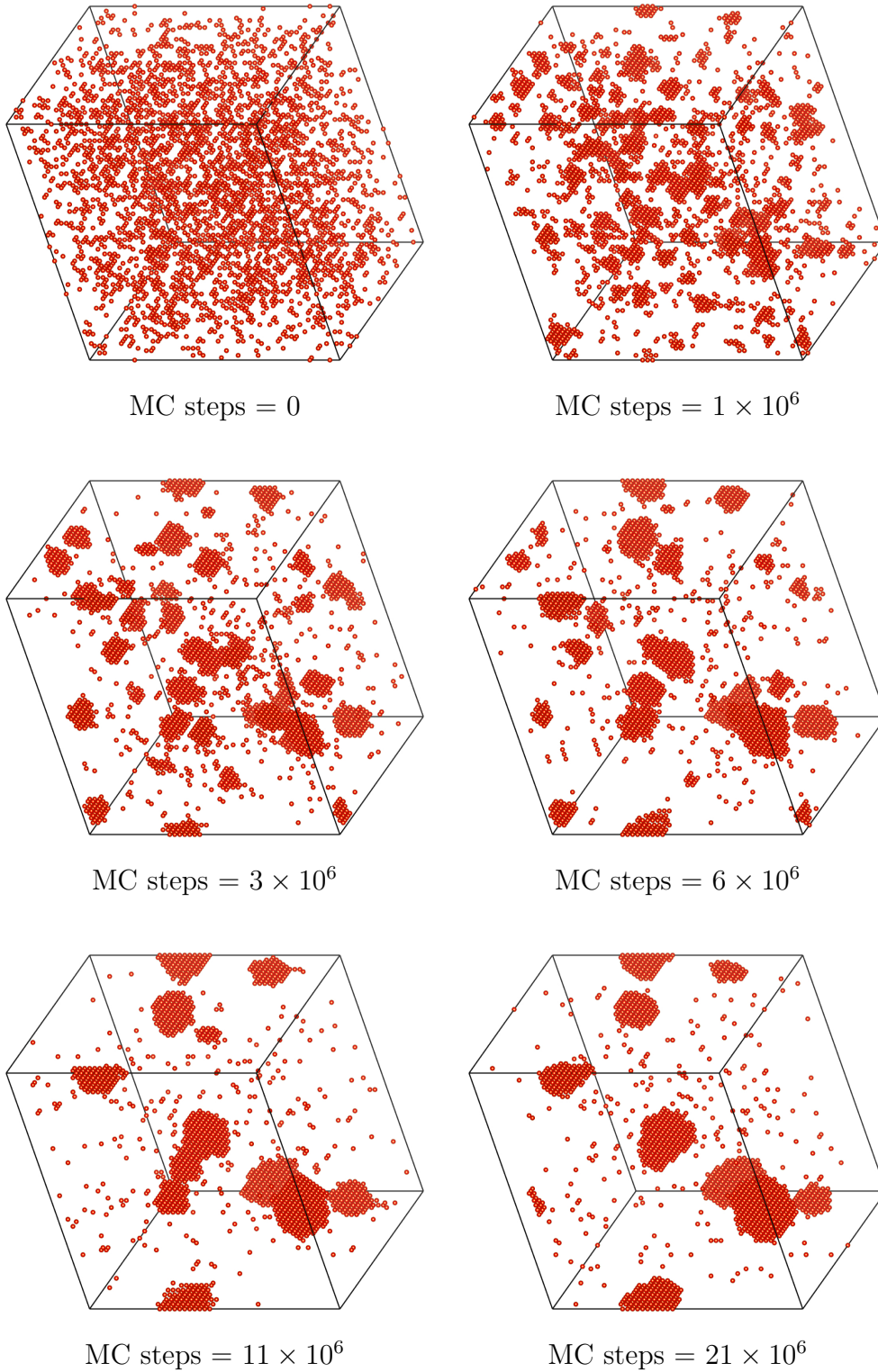


FIGURE 7.25: Cu distribution in a $50 \times 50 \times 50$ simulation cell with $x = 3 \text{ at.}\%$ at $T = 800 \text{ K}$ is shown at different MC steps. The initially randomly distributed Cu atoms (red spheres) coalesce into Cu precipitates as time progresses.

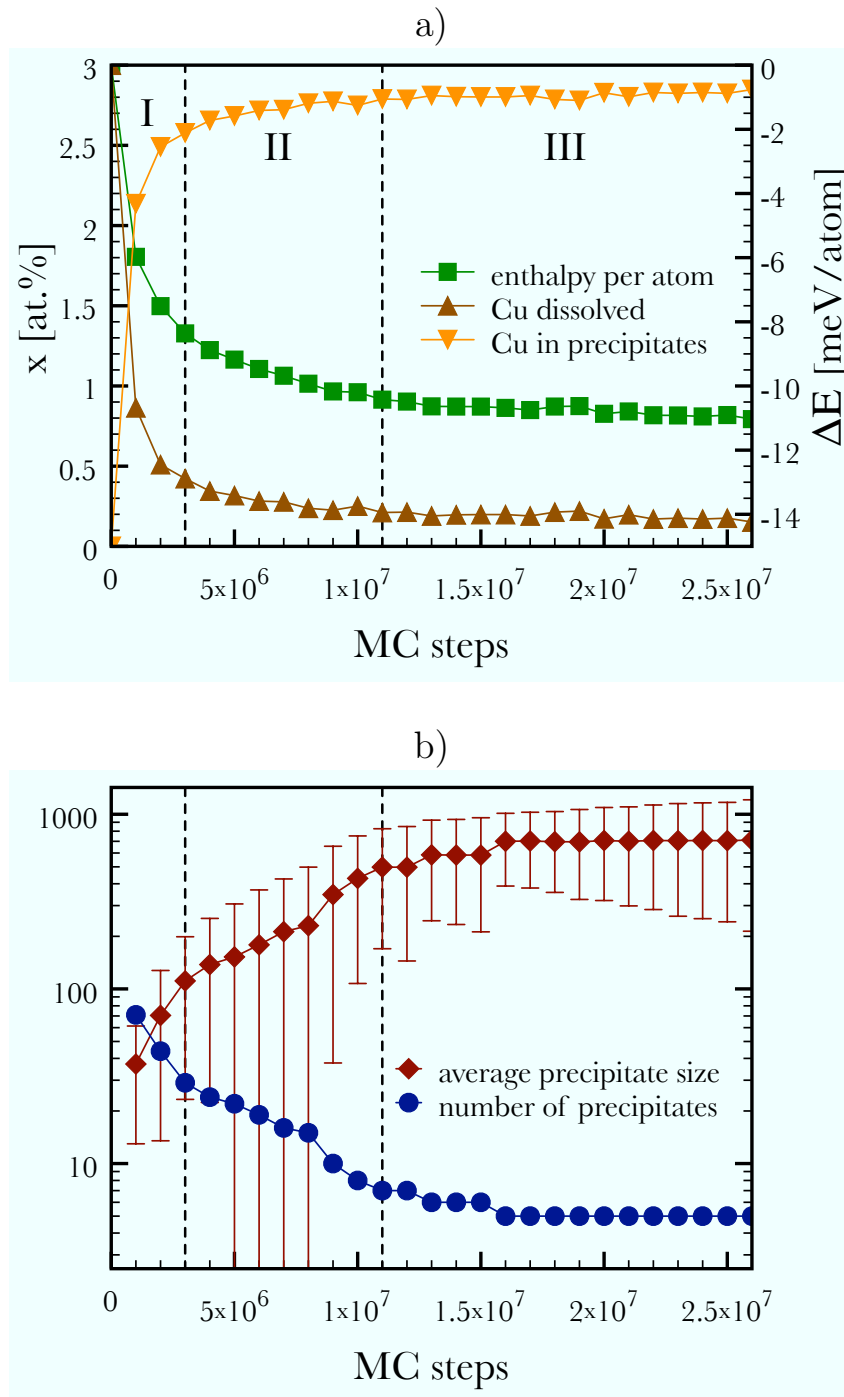


FIGURE 7.26: Panel a) plots the concentration of dissolved Cu atoms in the Fe-matrix and the concentration of Cu atoms in precipitates as well as the the energy change per atom versus MC steps. In panel b) the change in average precipitate size and its standard deviation and the number of precipitates are shown. In the 'time' regions distinguished by I, II and III a nucleation and two separate Ostwald ripening processes, a fast and a slow one, are shown.

7.4 Interface Entropy

Doing MC (in the present case with temperature dependent ECI's from the CE) one can derive the entropy change of a thermodynamical system at constant pressure and temperature T as [92],

$$S_{\text{CE}} = \frac{E_{\text{CE}}^{\text{equ}} - E_{\text{CE}}^{\text{ini}}}{T}, \quad (7.10)$$

with $E_{\text{CE}}^{\text{ini}}$ being the free energy at the start of the MC simulation and $E_{\text{CE}}^{\text{equ}}$ the energy at equilibrium reached at the end of the MC runs. This section considers the interface system as sketch in Fig. 7.23. The starting point of a MC run for a given temperature T is perfectly ordered because the atoms are exclusively located in their respective blocks. Then, starting the MC simulation atoms are exchanged until the final equilibrium distribution is obtained. Thus, the change in disorder is directly proportional to the change in entropy.

The same methodology was applied for the independent defect case as elaborated in section 7.2 because the defect model yields solubilities which are very similar to the one derived by CE+MC. A comparison between both cases, with and without vibrational free energy, is shown in Fig. 7.27. The configurational entropy S_{def} of the isolated defect model as constructed in chapter 4 is given by

$$S_{\text{def}} = k_B \left[\left(1 - \frac{c_2}{\nu}\right) \ln \left(\frac{1 - \frac{c_2}{\nu}}{1 - c_1 - 2c_2} \right) - \kappa c_2 \ln \left(\frac{\kappa c_2}{1 - c_1 - 2c_2} \right) - c_1 \ln \left(\frac{c_1}{1 - c_1 - 2c_2} \right) \right], \quad (7.11)$$

with c_1 and c_2 being the concentrations of Cu or Fe single and pair-wise defects in the respective hosts. The expression $\kappa = \frac{2\nu-1}{\nu}$ contains ν which denotes the number of bonds per site. It is important to consider that the interface system contains the same number of Fe and Cu atoms. Therefore one has to average the corresponding entropies,

$$S_{\text{def}}^{\text{av}} = \frac{S_{\text{def}}^{\text{Cu}}(c_1^{\text{Fe}}, c_2^{\text{Fe}}) + S_{\text{def}}^{\text{Fe}}(c_1^{\text{Cu}}, c_2^{\text{Cu}})}{2}, \quad (7.12)$$

with $S_{\text{def}}^{\text{Cu}}(c_1^{\text{Fe}}, c_2^{\text{Fe}})$ for the entropy of the Cu-rich phase and $S_{\text{def}}^{\text{Fe}}(c_1^{\text{Cu}}, c_2^{\text{Cu}})$ for that of the Fe-rich phase. It should be noted that $S_{\text{def}}^{\text{av}}$ refers to a slightly different system as the one used for CE+MC. For the independent defect case the fcc lattice was taken for the Cu-rich phase, whereas in the CE+MC simulations only a bcc parent lattice was used. Another, more important difference is that the defect model refers to a bulk system, whereas the CE+MC simulation is done for an interface system in which the interface separates two bulk-like blocks. Therefore, the entropy resulting from the CE+MC calculations also contains the interface entropy and it seems plausible that in general S_{CE} is larger than $S_{\text{def}}^{\text{av}}$.

TABLE 7.8: Estimated interface entropy S_{intf} versus temperature without and with vibrational free energy ($\Delta f(T)$). The value in the bracket is given under the assumption that the interface entropy with vibrational free energy increases continuously.

T [K]	without $\Delta f(T)$ [$\mu\text{J}/(\text{m}^2 \text{ K})$]	with $\Delta f(T)$ [$\mu\text{J}/(\text{m}^2 \text{ K})$]
900	5.5	38.0
1050	22.1	68.4
1200	57.8	45.3 (101.1)

At $T = 1050$ K the CE+MC calculations yield a value of $0.56 \mu\text{eV}/\text{K}$ without vibrational free energy and $2.85 \mu\text{eV}/\text{K}$ with it. These values are much higher than the values for the isolated defect model with $S_{\text{def}}^{\text{av}} = 0.03 \mu\text{eV}/\text{K}$ and $2.04 \mu\text{eV}/\text{K}$, respectively with and without vibrational free energy. The difference of the entropy models, as shown in the inset in Fig. 7.27, may therefore be used to derive the interface entropy S_{intf} , i.e. $S_{\text{intf}} = S_{\text{CE}} - S_{\text{def}}^{\text{av}}$, as listed in table 7.8 resulting in values of $22.1 \mu\text{J}/(\text{m}^2 \text{ K})$ respectively $68.4 \mu\text{J}/(\text{m}^2 \text{ K})$, with and without $\Delta f(T)$ at $T = 1050$ K.

The inset in Fig. 7.27 shows that S_{intf} as the entropy difference between CE+MC and defect model behaves similar for both cases, i.e. with and without vibrational contributions, up to ≈ 1050 K. Above this temperature the entropy difference S_{intf} decreases strongly for the case with vibrational free energy. This might be interpreted by the bulk entropy becoming dominant at a sufficiently high temperatures presumably because the interface is getting dissolved. However, this interpretation should be accepted with some reservation because the entropies of two quite different models enter the derivation of S_{intf} . Nevertheless, it might be worthwhile to analyse this mentioned effect at 1050 K more deeply in the future, which interestingly enough does not occur for the case without vibrational free energies.

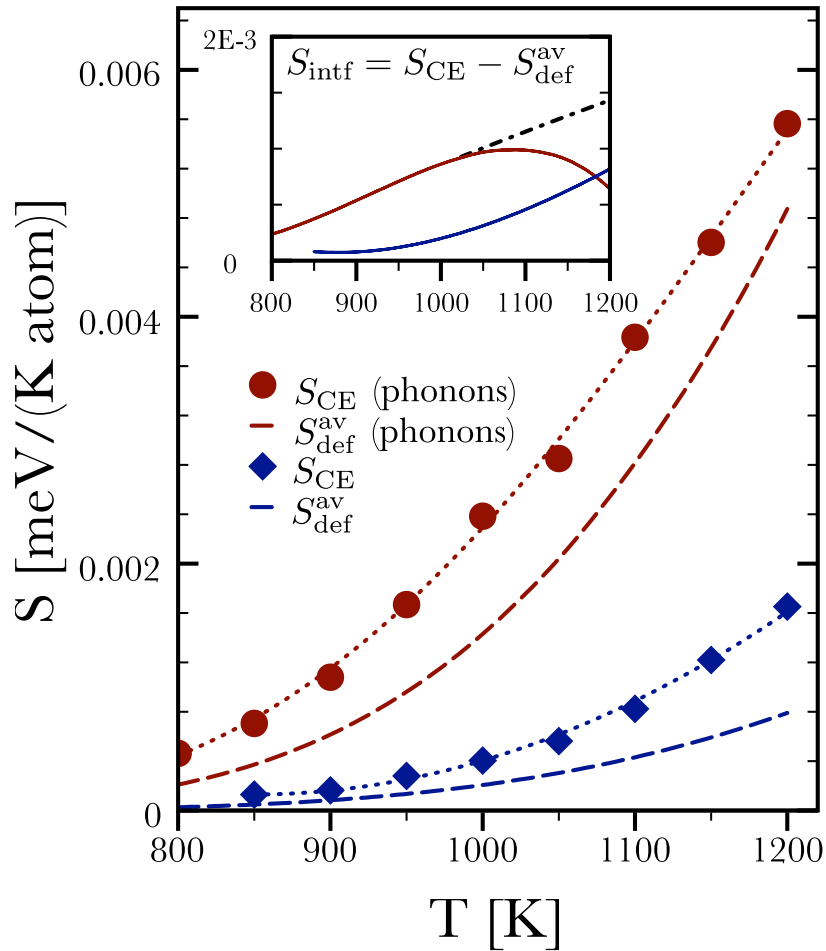


FIGURE 7.27: Entropy versus temperature calculated using CE without vibrational free energy (blue diamonds and blue dotted line) and with vibrational free energy (red circles and red dotted line) compared to values calculated using the isolated defect model without vibrational free energy (blue dashed line) and with (red dashed line). The inset gives the difference $S_{\text{intf}} = S_{\text{CE}} - S_{\text{def}}^{\text{av}}$ for both, without (blue line) and with (red line) vibrational free energy. The black dashed-dotted line extrapolates the values for the case with vibrational free energy assuming that it has a similar behavior to the one without.

7.5 Conclusion

The Fe-Cu system was chosen to demonstrate the power of DFT based approaches when dealing with vibrational, thermodynamical and concentration dependent properties. By DFT supercell calculations and thermodynamical modelling using the isolated defect model of chapter 4 for the dilute Fe-Cu alloys it was demonstrated that vibrational free energies have a substantial influence on the thermodynamical stability and miscibility range. The Fe-Cu alloy system is very well suited for such a task, as the rather wide miscibility range at the Fe-rich and the Cu-rich side of the phase diagram can only be described realistically by entropic effects: no stable intermetallic phases exist and the formation energies of Cu and Fe defects in Fe and Cu derived from DFT are highly positive and non bonding. In the dilute alloys model single atom defects and pair-wise substitutional defects were considered, for which a formulation of the entropy of mixing was worked out in chapter 4. Applying a DFT approach to determine vibrational properties within the harmonic approximation the temperature dependent free vibrational energies for each defect species was calculated. These were entered in a grand canonical thermodynamical *ansatz* of the total free energies. Magnetic interactions were included in terms of spin-polarised total energies, but a temperature induced change of magnetic ordering of the ferromagnetically aligned Fe moments was not taken into account. Using the isolated defect model it was found, that indeed, vibrational free energies and in particular their entropy contributions are very important. By including them one can reproduce in terms of Cu solubility in the Fe-matrix the main features of the experimental phase diagram.

The much more demanding task consisted in the concentration dependent treatment of phase stability and solubility which goes far beyond the isolated, independent defect model. The concentration dependent modelling was done by the CE elaborated in chapter 5. For that it was necessary to calculate the vibrational free energy for each structure entering the CE. Thereby a basic problem arises in how dynamically unstable structures should be dealt with, i.e. structures with imaginary frequency modes in the phonon dispersions. An ad hoc criterion based on experience was applied: structures with more than 5 % imaginary modes were removed from the input data set for the CE. It is found that the strongly binding interactions are reduced, i.e. the energies are less negative, when the vibrational free energy contribution increase with temperature. For example, the nearest-neighbour pair interaction is reduced from -115.25 meV, without the vibrational free energy, to -92.43 meV with vibrational free energies at 1200 K. Finally, with the much more elaborate CE plus MC simulation procedure the same main effect was found, namely that vibrational free energies (and their entropy contribution) have a very strong influence on the solubility by substantially increasing the miscibility of Cu in an Fe-rich matrix.

Furthermore, the ECI's from the temperature dependent CE were used in a MC with supersaturated Cu in Fe. However, as vital ingredients are still missing, i.e. vacancies and a correct diffusion mechanism, this assessment was purely qualitative. Nevertheless, the nucleation and Ostwald ripening process could be observed. The timespan for Cu to reach equilibrium concentration is observed to be much larger than the observation timespan.

Comparing the entropy derived from MC simulations based on the CE ECI's, which included the interface entropy between Fe and Cu slabs, to that of the entropy of the isolated defect model, which represents a bulk system, it is possible to estimate the temperature dependent Fe-Cu interface entropy at, e.g. 1050 K to be $68.4 \mu\text{J}/(\text{m}^2 \text{K})$ including the vibrational free energy. This value is by $46 \mu\text{J}/(\text{m}^2 \text{K})$ larger than when the vibrational free energies are not considered. Again demonstrating the important role of the vibrational free energy.

Summarised, this study emphasises the fundamental importance of vibrational entropy in determining the correct solubilities in the Fe-Cu alloy and thus the correct energetics. Not considering F_{phon} greatly underestimates the Cu solubility (and overestimates Fe solubility).

Appendix A

Brillouin Zone Sampling

One of the most widely used schemes to create a \vec{k}/\vec{q} -point mesh is that of Monkhorst and Pack [56], in which \vec{k}/\vec{q} -points are uniformly distributed within the first Brillouin Zone (BZ). This is done by defining the interval along the reciprocal vectors as

$$d_{r_i} = (2r_i - R_i - 1)/2R_i \quad r_i = 1, \dots, R_i \quad i = 1, 2, 3 \quad (\text{A.1})$$

with R_i as an input integer defining the number of \vec{k}/\vec{q} -points along \vec{B}_i . All uniformly distributed \vec{k}/\vec{q} -points within the BZ are then given by

$$\vec{k}_{r_1 r_2 r_3} = d_{r_1} \vec{B}_1 + d_{r_2} \vec{B}_2 + d_{r_3} \vec{B}_3 . \quad (\text{A.2})$$

This scheme is used to construct the \vec{k} -point mesh for all DFT calculations and the \vec{q} -point mesh for the lattice vibration calculations.

Appendix B

*f*PHON Manual

B.1 Files used by *f*PHON

A short overview:

INPHON	contains all controlling parameters	IN
OUTPHON	main log file	OUT
POSCAR	defines the crystal structure	IN
SPOSCAR	supercell to be used for the force-field calculations	OUT
DISP	displacements for the force-field calculations	OUT
FORCES	force-fields for the phonon calculations	IN
DYNMAT	dynamical matrix from VASP's linear response calculation (used instead of FORCES)	IN
QPOINTS	defines the irreducible \vec{q} -point mesh	IN&OUT
DOS, DOS.meV, DOS.cm	phonon density of states	OUT
ENTRO	vibrational entropy, free energy, internal energy and specific heat	OUT
FREQ, FREQ.meV, FREQ.cm	phonon dispersion	OUT
FPROJ, EIGENPHON	projector, eigenvalues and eigenvectors	OUT
HARMONIC	force-constant matrices	OUT
DYNPHON	dynamical matrices	OUT

B.1.1 INPHON

This is the main input file of *f*PHON containing all controlling parameters. Check section [B.2](#) for a detailed description of these parameters as well as section [B.3](#) for some examples

on its usage.

B.1.2 OUTPHON

OUTPHON is the output log file and will always be created. This file provides all relevant information necessary to understand what *fPHON* has done. Most importantly, the primitive unit cell vectors and the atom positions in that unit cell are given and additionally a list of the symmetry operations can be found.

B.1.3 POSCAR

This input file defines the lattice geometry and the atomic positions and it is the same file used by the latest version of VASP. For example, a file containing the $D0_3$ Fe_3Al structure will look like this:

```
D03
2.77136
  0.0 1.0 1.0
  1.0 0.0 1.0
  1.0 1.0 0.0
Al   Fe
  1   3
Direct
0.0  0.0  0.0
0.5  0.5  0.5
0.75 0.75 0.75
0.25 0.25 0.25
```

The first line is a comment line. The second line provides a scaling factor (usually the lattice constant) with which all lattice vectors and atomic coordinates are scaled. As in VASP *fPHON* interprets a negative value as the total cell volume of the supercell/unit cell.

The following three lines define the three lattice vectors of the supercell/unit cell in row form, i.e. the first line corresponds to the first, the second to the second and the third line to the third lattice vector.

The next line is optional and describes the atom types (as in VASP versions greater than 5). The sixth (or seventh) line supplies the number of atoms per atom type.

The seventh (or eighth) line specifies whether the atomic positions are provided in direct or cartesian coordinates. Note, that *fPHON* only checks if the first letter in this line starts with a 'c' or 'C' to switch to the cartesian coordinate system. The subsequent lines define the three coordinates for each atom in the coordinate system specified above.

B.1.4 SPOSCAR

This output file has to be used as input for the DFT force-field calculations and subsequent *fPHON* phonon calculations.

The setup of this file concerning lattice geometry and atomic positions is identical to the POSCAR file (see section B.1.3 for more information). The atomic positions are always given in direct coordinates. *fPHON* creates a new SPOSCAR file when

```
LDISP = .TRUE.
```

has been set in the INPHON file. The form of the SPOSCAR file is defined by the INPHON parameters NDIM and IBCELL.

If IBCELL = 0 the SPOSCAR file is nearly identical to the original POSCAR file, with the only difference being a possible reordering of the atomic coordinates list.

With IBCELL = 1 the SPOSCAR file is constructed using the lattice vectors of the primitive unit cell \vec{A}_i^{PRIM} found by *fPHON* multiplied by the values provided by NDIM = n1 n2 n3, i.e.

$$\vec{A}_i^{\text{SPOSCAR}} = n_i \vec{A}_i^{\text{PRIM}} \quad \text{for } i = \{1, 2, 3\} . \quad (\text{B.1})$$

Setting IBCELL = 2 results in a SPOSCAR for a supercell constructed from lattice vectors of the POSCAR file $\vec{A}_i^{\text{POSCAR}}$ multiplied by the values provided by NDIM = n1 n2 n3, i.e.

$$\vec{A}_i^{\text{SPOSCAR}} = n_i \vec{A}_i^{\text{POSCAR}} \quad \text{for } i = \{1, 2, 3\} . \quad (\text{B.2})$$

In both cases, i.e. IBCELL = 1, 2, the total number of atoms in SPOSCAR is naturally a multiple of n1 n2 n3 times the atoms in the unit cell respectively the POSCAR file.

In order to obtain an accurate dispersion relation one should create a SPOSCAR file containing at least thirty atoms. For more details please refer to the discussion on the supercell size in chapter 3.4.3.

B.1.5 DISP

This output file is written if the parameter

```
LDISP = .TRUE.
```

has been set in the INPHON file and it looks as follows:

```
" 0 0.00000000 0.00000000 0.00000000 " \  
" 1 -0.00174362 0.00174362 0.00174362 " \  
" 9 -0.00174362 0.00174362 0.00174362 " \  
" 17 -0.00174362 0.00174362 0.00174362 " \
```

The first integer value in a line indicates which atom in the SPOSCAR has to be displaced by the displacement vector given by the next columns. This displacement vector is always given in direct coordinates based on the lattice vectors defined in the corresponding SPOSCAR file.

If LZFORCE=.TRUE. has been set in INPHON then DISP will contain in the first line:

```
" 0 0.00000000 0.00000000 0.00000000 " \!
```

This indicates that the force-field $\mathfrak{F}(\vec{u} = 0)$ should be calculated without displacing any atoms. *fPHON* then subtracts this force-field from all other force-fields by

$$\tilde{\mathfrak{F}}(\vec{u}_{lk}) = \mathfrak{F}(\vec{u}_{lk}) - \mathfrak{F}(\vec{u} = \vec{0}) . \quad (\text{B.3})$$

The resulting corrected force-fields $\tilde{\mathfrak{F}}(\vec{u}_{lk})$ are then used for the construction of the force-constant matrices. This setting increases the accuracy of the phonon calculations for supercells where not all atomic positions have been fully relaxed.

B.1.6 FORCES

This input file contains all force-fields necessary for the construction of the force-constant matrices:

```
1 # number of force-fields  
5 -0.0028 0.0028 0.0056 # displ. atom & disp. vector (dir.)  
0.39111343 0.11218241 0.00167954 # forces (cart.) of 1. atom
```

0.18083650	-0.05489937	-0.03701212	# forces (cart.) of 2. atom
0.18902986	-0.06238748	0.06383136	# ...
-0.01683632	0.00760789	0.00946216	# ...
-0.83191269	0.06451551	-0.00966764	# ...
0.00748872	0.00006703	-0.07662493	# ...
0.00691357	-0.00021969	0.05768324	# ...
0.07336694	-0.06686630	-0.00935160	# forces (cart.) of 8. atom

The integer in the first line indicates the number of force-fields contained in FORCES. Each force-field block starts with a line similar to the DISP file indicating which atom has been displaced and providing the displacement vector in direct coordinates based on the lattice vectors defined in the SPOSCAR file. Note, the SPOSCAR file has to be copied to POSCAR since *fPHON* only reads from the POSCAR file. The following lines provide the three component force-vectors given in cartesian coordinates corresponding to the atoms in the (new) POSCAR file. Hence, it is vital that the POSCAR file read in is the same POSCAR file, without displacements, that was used for the DFT force-field calculations (i.e. the SPOSCAR file created with `LDISP = .TRUE.`).

B.1.7 DYNMAT

The DYNMAT file is read in instead of FORCES if the parameter

```
LDYNMAT = .TRUE.
```

has been set in INPHON. DYNMAT is a VASP output file resulting from a DFT *linear response* calculation. For this calculation a VASP version greater than 5 is needed and the parameter `IBRION = 8` has to be set in the INCAR file. For further details please refer to the VASP manual.

B.1.8 QPOINTS

This output file contains a list of irreducible \vec{q} -points created by the Monkhorst and Pack [56] scheme (see appendix A) that is needed for the DOS and free energy calculations. The QPOINT file is created when `LFREE = .TRUE.` and `LDISP = .FALSE.` are set in the INPHON file:

6			
-0.3750000000000000	-0.3750000000000000	-0.3750000000000000	8.000000
-0.3750000000000000	-0.3750000000000000	-0.1250000000000000	12.000000
-0.3750000000000000	-0.3750000000000000	0.3750000000000000	6.000000
-0.3750000000000000	-0.1250000000000000	0.1250000000000000	24.000000
-0.3750000000000000	0.1250000000000000	0.1250000000000000	8.000000
-0.1250000000000000	-0.1250000000000000	0.1250000000000000	6.000000

The integer in the first line specifies the number of \vec{q} -points provided in the file. In the subsequent lines a \vec{q} -point is defined by the first three values of the line in direct coordinates. The last value in each line specifies the weight of that \vec{q} -point.

The size of the \vec{q} -points mesh is controlled in INPHON by the integer values of QA, QB and QC.

B.1.9 DOS, DOS.meV and DOS.cm

These output files contain the phonon density of states (DOS) in the units states/THz, states/meV and states/cm⁻¹ (see table 3.1 for the conversion factors) and are created when parameter LDISP = .FALSE. is set in INPHON. If LFREE = .TRUE. then the phonon DOS is integrated over all \vec{q} -points in the BZ as given in the QPOINTS file otherwise the phonon DOS is only integrated over the \vec{q} -points of the paths defined by QI and QF.

In the output files the first column represents the energy while the second column gives the normalised DOS.

All INPHON parameters concerning the DOS are given in the units THz. The INPHON parameter DOSIN sets the DOS startpoint while DOSEND sets its endpoint. DOSSTEP sets the step size and DOSSMEAR is the smearing parameter σ of a Gaussian smearing function $\exp\left(-\frac{\omega^2}{\sigma^2}\right)$.

B.1.10 ENTRO

This output file is written when the INPHON parameter LFREE = .TRUE. and LDISP = .FALSE. have been set.

The first column gives the temperature in K. The second column gives the vibrational entropy $S = \frac{U-F}{k_B T}$ of the primitive unit cell in 1/K and the third and fourth column give the vibrational free energy F and the vibrational internal energy U of the primitive unit

cell in eV. The next three columns give S , F and U per atom, and the last column gives the specific heat C_V at constant volume of the primitive unit cell in J/(mol K).

If the parameter `LDELTAT` has not been set or `LDELTAT = .FALSE.` then `ENTRO` will only contain one line with S , F , U and C_V given at the temperature in K defined in the `INPHON` file by `TEMPERATURE`.

If `LDELTAT = .TRUE.` has been set then the lowest temperature has to be defined using `TMIN` and the highest temperature using `TMAX`. The number of steps in between is then defined by `ITSTEP`.

B.1.11 `FREQ`, `FREQ.meV` and `FREQ.cm`

The output files `FREQ`, `FREQ.meV` and `FREQ.cm` contain the phonon dispersion relation in the units THz, meV and cm^{-1} , respectively, (see table 3.1 for the conversion factors) and are created when parameters `LFREE = .FALSE.` and `LDISP = .FALSE.` are set.

The paths in \vec{q} -space are defined by the following parameters in `INPHON`:

```
IND = 2;  INPOINTS = 100
QI =  0.0 0.5 0.0    0.0 0.0 0.0
QF =  0.0 0.0 0.0   -0.5 0.5 0.5
```

Parameters `IND` and `INPOINTS` define the number of paths and the number of \vec{q} -points on each of these paths, respectively. `QI` defines sequentially the three components of each initial \vec{q} -point of a path while the components of each final point is defined by `QF`.

These initial and final \vec{q} -points are to be given in direct coordinates of the reciprocal lattice if the parameter `LRECIP = .FALSE.` is not explicitly set. If `LRECIP = .FALSE.` then the \vec{q} -points are interpreted as cartesian coordinates given in the units $2\pi a^{-1}$ with a for the scaling parameter provided in the `POSCAR` file.

In the `FREQ` files at the beginning of each path a line is written

```
#  1 path from  0.000  0.500  0.000 to  0.000  0.000  0.000
```

indicating the path number and the start and end points in the specified coordinate system. After which the phonon dispersion relation along the path is listed. The value in the first column defines the absolute path length already covered in units of $2\pi a^{-1}$ with the scaling parameter a from the `POSCAR` file. The frequency of the vibrational modes are given in the other columns. If more than three vibrational modes exist then the vibration

modes are written in sets of three into the files **FREQ1-FREQ999** in THz, whereby the first column in all files describes the absolute path length in units $2\pi a^{-1}$.

B.1.12 FPROJ and EIGENPHON

These output files are created if **LPFREQ = .TRUE.** is set in addition to **LFREE = .FALSE.** and **LDISP = .FALSE.** in the **INPHON** file.

The files **FPROJ1-FPROJ999** contain in the first column the absolute path in units of $2\pi a^{-1}$ and in the subsequent columns the projectors $\mathbf{p}_{\kappa,j}$ of all the atoms in the primitive unit cell for vibrational mode j .

The **EIGENPHON** file contains the eigenvalues and eigenvectors of each \vec{q} -point and vibrational mode as well as the corresponding displacement vectors in the time interval 0 ps to 2 ps.

Warning, the size of these files can quickly become enormously large. Using small values for **IND** and **INPOINTS** is recommended.

B.1.13 HARMONIC

With the parameters **LHARMONIC = .TRUE.** and **LDISP = .FALSE.** the output file **HARMONIC** is created. It contains the atomic positions in a **POSCAR** like manner and the force-constant matrices.

B.1.14 DYNPHON

The dynamical matrices are written into **DYNPHON** if the parameters

<code>LDPHON = .TRUE. ; LDISP = .FALSE. ; LFREE = .FALSE.</code>
--

have been set in the **INPHON** file.

Warning, the size of this file can quickly become enormously large. Using small values for **IND** and **INPOINTS** is recommended.

B.2 Configuration Options in INPHON

B.2.1 MASS

This array assigns to each atom type, in the same order as specified in the POSCAR file, the corresponding atom mass in the unified atomic mass units (amu). It is not necessary to set this parameter when calculating displacements (i.e. `LDISP = .TRUE.`).

Usage example:

```
MASS = 87.62000 106.42000 72.61000
```

B.2.2 RMAX

Default:

```
RMAX = 15.0
```

This parameter defines the cutoff radius in Å in real space of the shell lattice vector $|\vec{R}_{l-l'} + \vec{\tau}_\kappa - \vec{\tau}_{\kappa'}|$ used to search for equivalent atoms in the supercell.

If the value for `RMAX` is too small then *fPHON* will have a problem constructing the force-constant matrix. Hence, one should set `RMAX` larger than the maximum diameter of the supercell.

B.2.3 ISYM

Default:

```
ISYM = 3
```

This parameter controls the symmetry routine used by *fPHON* in the calculation of the displacement vectors and in the construction of the force-constant matrix. Furthermore, `ISYM` controls the search for the primitive unit cell.

The possible settings are:

ISYM	use symmetry	reduce to primitive unit cell
0	no	no
1	no	yes
2	yes	no
3	yes	yes

If there exists doubt about the quality of the phonon calculations with the standard value of `ISYM`, i.e. imaginary phonon modes, then a calculation with `ISYM = 1` should be done to crosscheck the results.

Warning, the `ISYM` setting has to be the same for the displacements calculation (`LDISP = .TRUE.`) and for the force-constant matrices construction (`LDISP = .FALSE.`) of the phonon calculations.

B.2.4 LHARMONIC

Default:

`LHARMONIC = .FALSE.`

The force-constant matrix is written into the file `HARMONIC` if parameter `LHARMONIC = .TRUE.` is set in `INPHON`.

B.2.5 INTI and LSYMM

Default:

`INTI = 100`
`LSYMM = .TRUE.`

With these two parameters one can control if and how *fPHON* imposes the symmetries

$$\sum_{l'' \kappa'} \Phi \left(\begin{matrix} l'' \\ \kappa \kappa' \end{matrix} \right)_{\alpha\beta} = 0 \quad (\text{B.4})$$

and

$$\Phi \left(\begin{matrix} l & l' \\ \kappa & \kappa' \end{matrix} \right)_{\alpha\beta} = \Phi \left(\begin{matrix} l' & l \\ \kappa' & \kappa \end{matrix} \right)_{\beta\alpha} \quad \text{crystal with no centre of inversion} \quad (\text{B.5})$$

$$\Phi \left(\begin{matrix} l & l' \\ \kappa & \kappa' \end{matrix} \right)_{\alpha\beta} = \Phi \left(\begin{matrix} l' & l \\ \kappa' & \kappa \end{matrix} \right)_{\alpha\beta} \quad \text{crystal with centre of inversion} \quad (\text{B.6})$$

onto the force-constant matrices (see chapter 3.1).

The parameter INTI controls the maximum number of iteration steps. If the error is sufficiently small (i.e. when $10^{-8} > \sum_{\alpha,\beta} \sum_{\kappa\kappa'} \left| \Phi \left(\begin{smallmatrix} \kappa\kappa' \\ \alpha\beta \end{smallmatrix} \right) \right|$) then *fPHON* will stop before it reaches this limit.

Setting INTI=0 will not enforce any symmetries onto the force-constant matrices. If LSymm = .FALSE. then only the translational symmetry, i.e. Eq. B.4, is enforced in the iterative procedure upon the force-constant matrices.

B.2.6 Finding Displacements and Constructing Supercells

Important parameters:

```
LDISP, DISP, IBCELL, NDIM
```

In all the calculations for finding the displacements and constructing the supercells the parameter LDISP = .TRUE. has to be set. If LZFORCE (see section B.2.6.2) is set to .TRUE. (advisable for supercells with low symmetries) then *fPHON* will write in addition a ‘zero displacement’ into the first line of the DISP file.

B.2.6.1 LDISP and DISP

Default:

```
LDISP = .FALSE.
DISP = 0.02
```

If the parameter LDISP = .TRUE. *fPHON* calculates all displacements necessary for the force-constant method and writes them into the file DISP (see section B.1.5).

Furthermore, *fPHON* writes the supercell on which the displacements are based into the file SPOSCAR. The form of the supercell written into SPOSCAR depends on the values of the parameters IBCELL and NDIM. It is absolutely *vital*, that the displacements in the file DISP are applied to the output SPOSCAR and not to the input POSCAR as the order of atoms might differ even when no new supercell is created.

The parameter DISP defines the size of the displacements in Å. Usually, the default size should be sufficient. When increasing displacement size one should always check if the

displacements are still within the harmonic regime. A too small value for DISP might result in an inaccurate phonon dispersion due to numerical inaccuracies of the DFT calculated force-fields calculated by DFT.

B.2.6.2 LZFORCE

Default:

LZFORCE = .FALSE.

With the setting LZFORCE = .TRUE. *fPHON* writes as the first displacement a ‘zero displacement’, displacing atom 0 with vector $\vec{u} = (0.0, 0.0, 0.0)$, into the file DISP (if LDISP=.TRUE.). This indicates that the force-fields without any displacements has to be calculated.

If *fPHON* finds in FORCES this zero displacement for the first displacement then the force-field $\mathfrak{F}(\vec{u} = 0)$ is subtracted from all other force-fields $\mathfrak{F}(\vec{u}_{lk})$ in FORCES. Hence, correcting the force-fields with

$$\tilde{\mathfrak{F}}(\vec{u}_{lk}) = \mathfrak{F}(\vec{u}_{lk}) - \mathfrak{F}(\vec{u} = 0) . \quad (\text{B.7})$$

This will greatly improve the phonon calculations for supercells with low symmetry where not all atomic positions have been fully relaxed.

B.2.6.3 IBCELL and NDIM

Default:

IBCELL = 0
NDIM = 1 1 1

IBCELL controls how the new supercell, written into SPOSCAR (see section B.1.4), is do be constructed. The settings are:

IBCELL	
0	<i>fPHON</i> writes the original cell, as defined in the POSCAR file, into SPOSCAR. Note, that the order of atoms in SPOSCAR might differ.
1	<i>fPHON</i> builds the supercell using multiples, defined by NDIM, of the <i>primitive unit cell vectors</i> .
2	<i>fPHON</i> builds the supercell using multiples, defined by NDIM, of the <i>lattice vectors</i> from the POSCAR.

If `IBCELL`≠0 then the multiples `n1`, `n2` and `n3`, defined by parameter `NDIM`, i.e. `NDIM = n1 n2 n3`, are used to construct the new lattice vectors of the new supercell by,

$$\vec{A}_i^{\text{SPOSCAR}} = n_i \vec{A}_i \quad i = \{1, 2, 3\}, \quad (\text{B.8})$$

with \vec{A}_i either being a primitive unit cell vector or a lattice vector from the POSCAR file depending on `IBCELL`.

In order to accurately calculate the phonons the supercell should contain at least ≈ 30 atoms and it should be as cubic as possible as discussed in greater detail in chapter 3.4.3.

B.2.7 Phonon Density of States, F , U , S and C_V Calculations

Important parameters:

`LFREE`, `QA`, `QB`, `QC`, `TEMPERATURE`

For all phonon DOS calculations `LFREE = .TRUE.` and `LDISP = .FALSE.` has to be set. Furthermore, the temperature has to be defined with `TEMPERATURE` or with `LDELTA`, `TMIN`, `TMAX` and `ITSTEP` and the \vec{q} -mesh has to be defined with `QA`, `QB` and `QC`.

B.2.7.1 LFREE

Default:

`LFREE = .FALSE.`
`LGAMMA = .FALSE.`

fPHON will calculate the phonon DOS if `LFREE = .TRUE.` is set and writes the results into the files `DOS`, `DOS.meV` and `DOS.cm` (see section B.1.9). Furthermore, the vibrational free energy F , the vibrational internal energy U , the vibrational entropy S and the specific heat at constant volume C_V are evaluated at the temperature defined by `TEMPERATURE` in K and written to the file `ENTRO` (see section B.1.10).

B.2.7.2 QA, QB, QC and LGAMMA

The size of the \vec{q} -mesh within the Monkhorst and Pack scheme is defined by the integer values of the parameters `QA`, `QB` and `QC`. If `LGAMMA = .TRUE.` is set then the \vec{q} -mesh is shifted so that one \vec{q} -point coincides with the Γ -point.

B.2.7.3 TEMPERATURE, LDELTAT, TMIN, TMAX, ITSTEP

Default:

```
LDELTAT = .FALSE.
```

The temperature in K is set with `TEMPERATURE` and has to be defined if `LFREE = .TRUE.` and `LDELTAT = .FALSE..`

If `LDELTAT = .TRUE.` is set then *fPHON* will calculate F , U , S and C_V (file `ENTRO` see section [B.1.10](#)) for a range of temperatures. Thereby, the lowest temperature is set by `TMIN`, the highest temperature by `TMAX` and the number of steps between these two by the integer `ITSTEP`.

B.2.7.4 DOSIN, DOSEND, DOSSTEP and DOSSMEAR

Default:

```
DOSIN = 0.0  
DOSEND = 25.0  
DOSSTEP = 0.1  
DOSSMEAR = 0.02
```

Although these parameters influence the computation of the phonon DOS that is written into the files `DOS`, `DOS.meV` and `DOS.cm` (see section [B.1.9](#)) the values of these parameters are only given in THz.

`DOSIN` defines the lowest frequency of the DOS and `DOSEND` the highest frequency. The interval between these two values is defined by `DOSSTEP`. The smearing parameter σ of a Gaussian smearing function $\exp\left(-\frac{\omega^2}{\sigma^2}\right)$ is defined by `DOSSMEAR`.

B.2.7.5 IPDOS

Default:

```
IPDOS = 0
```


The integer value of IPDOS controls if and how the partial phonon DOS's is written in states/THz into the files DOS1, DOS2, etc. when LFREE = .TRUE.. Thereby one should note that the number of the created DOS* files depends on the setting of IPDOS.

IPDOS	write partial phonon DOS's
0	no
1	for each atom type
2	for all non-equivalent atoms in the primitive unit cell
3	for every atom in the primitive unit cell

B.2.8 Calculating the Phonon Dispersion Relation

Important parameters:

```
IND, INPOINT, QI, QF
```

To calculate the phonon dispersion relation the parameters LFREE = .FALSE. and LDISP = .FALSE. have to be set in addition to the parameters IND, INPOINT, QI and QF.

B.2.8.1 IND, INPOINT, LRECIP, QI and QF

Default:

```
LRECIP = .TRUE.
```

The path through \vec{q} -space for the phonon dispersion relation is defined by these parameters for example:

```
IND = 2;  INPOINTS = 100
QI =  0.0 0.5 0.0    0.0 0.0 0.0
QF =  0.0 0.0 0.0   -0.5 0.5 0.5
```

Parameters IND and INPOINTS define the number of paths and the number of \vec{q} -points on each path, respectively. QI defines sequentially the three components of each initial starting \vec{q} -point of a path while the components of each end point are defined by QF.

These initial and end \vec{q} -points have to be given in direct coordinates of the reciprocal lattice if the parameter LRECIP = .FALSE. is not explicitly set. If LRECIP = .FALSE.

then the \vec{q} -points are interpreted in cartesian coordinates given in units of $2\pi a^{-1}$ whereby a is the scaling factor from the file POSCAR.

The output is written into the files `FREQ`, `FREQ.cm`, `FREQ.meV` and `FREQ*` (see section [B.1.11](#) for more details).

B.2.8.2 LPFREQ and LDPHON

Default:

```
LPFREQ = .FALSE.
LDPHON = .FALSE.
```

The output files `FPROJ*` and `EIGENPHON` (see section [B.1.12](#) for more details) containing projector and eigenvalues are created if `LPFREQ = .TRUE.` is set in addition to `LFREE = .FALSE.` and `LDISP = .FALSE.` in the `INPHON` file.

The dynamical matrices are written into `DYNPHON` when parameter `LDPHON = .TRUE.` is set.

Warning, the size of these files can become huge for large values of `IND` and `INPOINTS`.

B.2.9 IMOV, ISTEP, TSTEP, IBRANCH and Q

Default:

```
IMOV = 0
ISTEP = 0
TSTEP = 1.0
IBRANCH = 1
Q = 0.0 0.0 0.0
```

With the setting `IMOV = 1` `fPHON` will calculate the displacements and atomic positions over `ISTEP` iterations for the vibrational mode `IBRANCH` at \vec{q} -point `Q`. The time interval of each iteration is defined by `TSTEP` in picoseconds.

B.2.10 LO–TO Splitting

In ionic semiconducting or insulating crystals electric dipoles are created when ions are displaced by longitudinal optical vibrations at the long-wavelength limit. Resulting in a splitting of the longitudinal optical (LO) and transversal optical (TO) phonon modes. At $\vec{q} \rightarrow 0$ the dynamical matrix can be split into an analytical part $D_{\alpha\beta}^{\kappa\kappa'}$ and a non-analytical part $D_{\alpha\beta}^{\kappa\kappa',NA}$, i.e.

$$D_{\alpha\beta}^{\kappa\kappa'} = D_{\alpha\beta}^{\kappa\kappa'} + D_{\alpha\beta}^{\kappa\kappa',NA} . \quad (\text{B.9})$$

In the subroutine written by M. Hieckel [93] the non-analytical part is calculated at \vec{q} by,

$$D_{\alpha\beta}^{\kappa\kappa',NA} = \frac{4\pi e^2}{\Omega \sqrt{M_\kappa M_{\kappa'}}} \frac{(\vec{q} \cdot Z_\kappa)_\alpha (\vec{q} \cdot Z_{\kappa'})_\beta}{\vec{q} \cdot \epsilon^\infty \cdot \vec{q}} , \quad (\text{B.10})$$

with the born effective charge tensor Z_κ and atomic mass M_κ of atom κ , the dielectric tensor ϵ , elemental charge e and cell volume Ω . For more details please refer to Ref. [93, 94]. This correction is applied to both cases, the integration over \vec{q} -space for the DOS, U , S , F and C_V calculations and for the dispersion relation calculation.

B.2.10.1 LBORN

Default:

```
LBORN = .FALSE.
```

Setting `LBORN = .TRUE.` activates the LO–TO splitting subroutine.

B.2.10.2 BORN

If `LBORN = .TRUE.` is set the born effective charge tensor of each atomic species has to be defined in the `INPHON` file by:

```
BORN001 = Z(1,1) Z(1,2) Z(1,3) Z(2,1) Z(2,2) Z(2,3) Z(3,1) Z(3,2) Z(3,3)
.
.
.
BORN999 = Z(1,1) Z(1,2) Z(1,3) Z(2,1) Z(2,2) Z(2,3) Z(3,1) Z(3,2) Z(3,3)
```

For example, in a system with two atomic species the born effective charge tensors $Z_1 = \begin{pmatrix} -2.07 & 0 & 0 \\ 0 & -2.07 & 0 \\ 0 & 0 & -2.07 \end{pmatrix}$ and $Z_2 = \begin{pmatrix} 2.07 & 0 & 0 \\ 0 & 2.07 & 0 \\ 0 & 0 & 2.07 \end{pmatrix}$ are defined as follows;

```
BORN001= -2.07 0.0 0.0 0.0 -2.07 0.0 0.0 0.0 -2.07
BORN002=  2.07 0.0 0.0 0.0  2.07 0.0 0.0 0.0  2.07
```

B.2.10.3 INELEC, RDIELECTRIC and RDIETENSOR

Default:

```
INELEC = 0
```

If INELEC = 1 then the dielectric tensor ϵ is read in by

```
RDIETENSOR=e(1,1) e(1,2) e(1,3) e(2,1) e(2,2) e(2,3) e(3,1) e(3,2) e(3,3)
```

otherwise (i.e. INELEC = 0) a scalar value for ϵ^∞ is defined with RDIELECTRIC.

B.2.10.4 RESIGMA

In the subroutine a Gaussian weighting function

$$f(q) = \exp\left(-\frac{q^2}{\sigma^2}\right), \quad (\text{B.11})$$

is used to define the weight with which $D_{\alpha\beta}^{\kappa\kappa',NA}(\vec{q})$ is added to the dynamical matrix. The Gaussian function has to vanish at the BZ boundary. This condition is determined by the RESIGMA parameter which defines the width of the Gaussian function $0 < f(q_{\max}) \ll 1$ with

$$f(q_{\max}) = \exp\left(\frac{-q_{\max}^2}{\sigma^2}\right) = \text{RESIGMA} . \quad (\text{B.12})$$

B.3 Example

The standard *fPHON* workflow is outlined for the example of Fe_3Al in the structure D0_3 defined by the following POSCAR:

```
D03
2.880
  0.0 1.0 1.0
  1.0 0.0 1.0
  1.0 1.0 0.0
Al   Fe
  1   3
Direct
0.00 0.00 0.00
0.50 0.50 0.50
0.75 0.75 0.75
0.25 0.25 0.25
```

The supercell and displacements necessary to construct the FORCES file are calculated using the INPHON file settings:

```
LDISP=.TRUE. #calculate displacements
IBCELL=1     #use the vectors of unit cell
NDIM=2 2 2   #build a 2x2x2 supercell
```

Running *fPHON* with

```
:~/> fphon
```

creates a SPOSCAR file containing 32 atoms, i.e. 8 Al and 24 Fe atoms, and the DISP file:

```
"  1 -0.00173611  0.00173611  0.00173611 " \
"  9 -0.00173611  0.00173611  0.00173611 " \
" 17 -0.00173611  0.00173611  0.00173611 " \
```

The python script

```
:~/> ./phonon_disp
```

then creates the directories $\sim/00$, $\sim/01$ and $\sim/02$ and copies the VASP files INCAR, KPOINTS, POTCAR into these directories. Furthermore, the file SPOSCAR is copied to these directories as POSCAR and the atoms identified in DISP are displaced by the given vector, i.e. in $\sim/00$

the 1st atom is displaced by $\vec{d} = \begin{pmatrix} -0.00174362 \\ 0.00174362 \\ 0.00174362 \end{pmatrix}$ etc.

After running VASP the forces are extracted with the python script

```
:~/> ./phonon_forces
```

and written to $\sim/PHON/FORCES$. The file $\sim/SPOSCAR$ is copied by the script to $\sim/PHON/POSCAR$. This brings all the necessary ingredients together for the next step, the phonon calculation.

B.3.1 Dispersion Relation

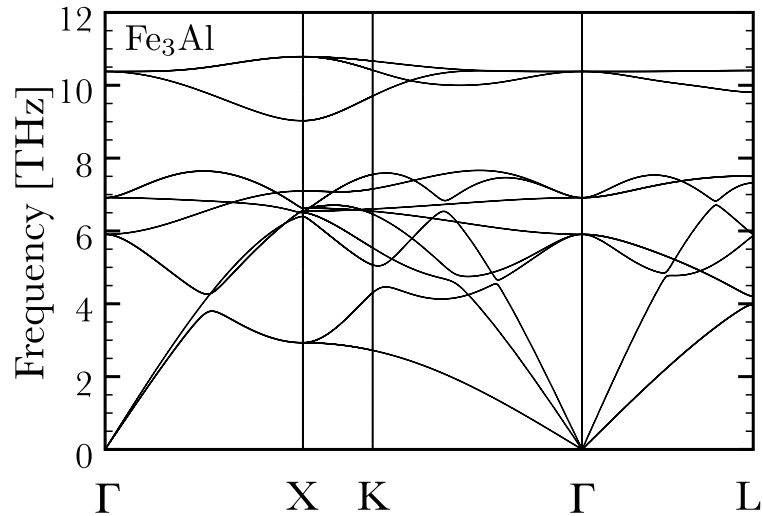
As the primitive unit cell is face-centred cubic the dispersion relation along a path connecting the special points in the BZ is set up in $\sim/PHON/INPHON$ with

```
LDISP = .FALSE.      #do not calculate displacements
LFREE = .FALSE.      #do not calculate DOS etc.
MASS = 26.982 55.847 #mass of both atom species
IND = 4               #calculate dispersion relation for 4 path
INPOINTS = 200       #each path consists of 200 points
QI = 1.0 1.0 1.0    0.500 1.000 0.500    0.375 0.750 0.375    0.0 0.0 0.0
QF = 0.5 1.0 0.5    0.375 0.750 0.375    0.000 0.000 0.000    0.5 0.5 0.5
# Gamma' -> X' -> K -> Gamma -> L
```

Executing *fPHON* in $\sim/PHON$ with

```
:~/PHON> fphon
```

calculates the dispersion relation which can be found in the file **FREQ** in units of THz as plotted in Fig. B.1.

FIGURE B.1: Phonon dispersion relation for $D0_3$ Fe_3Al .

B.3.2 Phonon DOS

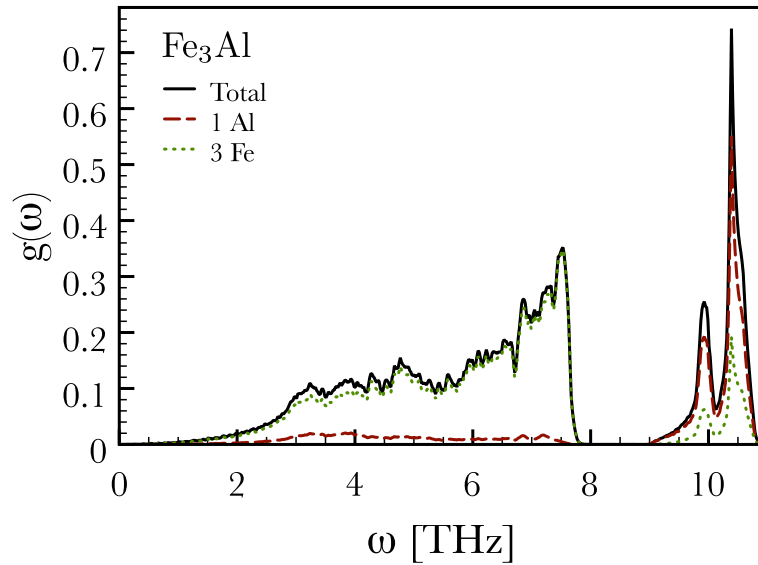
The phonon DOS calculation is initialised using the `~/PHON/INPHON` file:

```
LDISP = .FALSE.      #do not calculate displacements
LFREE = .TRUE.       #calculate DOS etc.
MASS = 26.982 55.847 #mass of both atom species
TEMPERATURE = 200    #temperature in K
IPDOS = 1            #calculate the partial DOSes of each species
QA = 30; QB = 30; QC = 30 #q-mesh
DOSIN = 0; DOSEND = 11; DOSSTEP = 0.02; DOSSMEAR = .05 #DOS smearing
```

Thus, with

```
:~/PHON> fphon
```

the phonon DOS is calculated and the total DOS is written to `DOS` in `states/THz` and the partial DOS's of Al and Fe can be found in the files `DOS1` and `DOS2`, respectively. These results are shown in Fig. B.2.

FIGURE B.2: Density of states for D0₃ Fe₃Al.

B.3.3 F, U, S and C_V

To calculate the vibrational free energy, internal energy, entropy and specific heat for a temperature range the `~/PHON/INPHON` file of the previous calculation has to be modified to:

```
LDISP = .FALSE.      #do not calculate displacements
LFREE = .TRUE.       #calculate DOS etc.
MASS = 26.982 55.847 #mass of both atom species
IPDOS = 1            #calculate the partial DOS's of each species
QA = 30; QB = 30; QC = 30 #q-mesh
LDELTAT = .TRUE.     #calculate F, U, S and C_V for a temperature range
TMIN = 5; TMAX = 1800 #starting and end temperature in K
ITSTEP = 400         #number of temperature intervals
DOSIN = 0; DOSEND = 11; DOSSTEP = 0.02; DOSSMEAR = .05 #DOS smearing
```

The values of the vibrational free energy F and internal energy U are given in the units eV/atom and eV/cell and the entropy in K⁻¹/atom and K⁻¹/cell in the file `ENTRO` as plotted in Fig. B.3. Furthermore, the specific heat C_V is also given in `ENTRO` in J/(K mol cell) as shown in Fig. B.4.

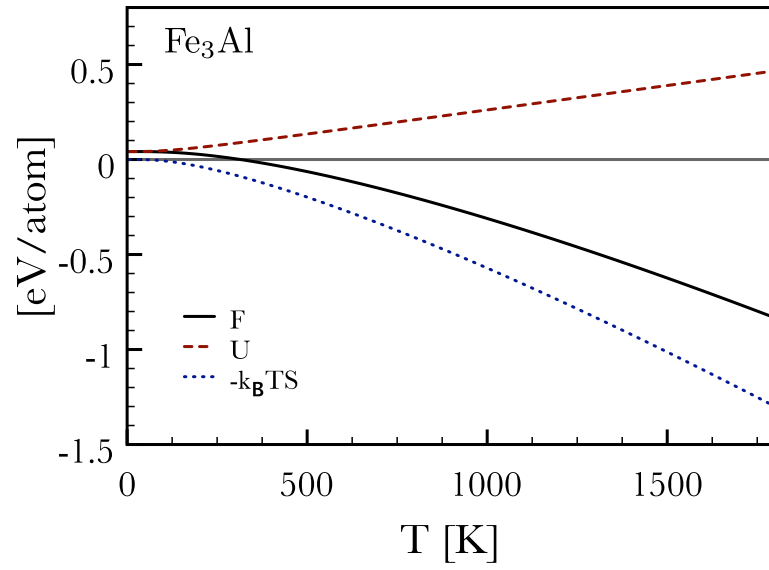


FIGURE B.3: Vibrational free energy F , internal energy U and entropy times temperature $-k_B T S$ for $\text{D0}_3 \text{Fe}_3\text{Al}$.

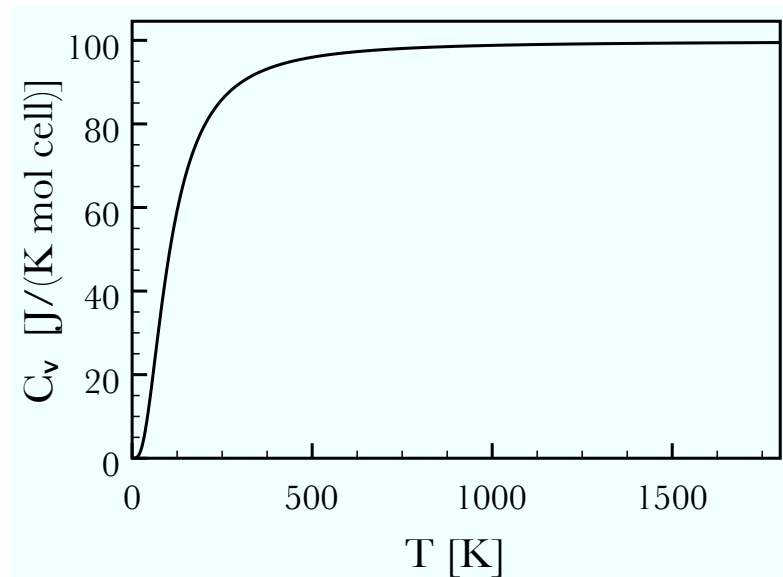
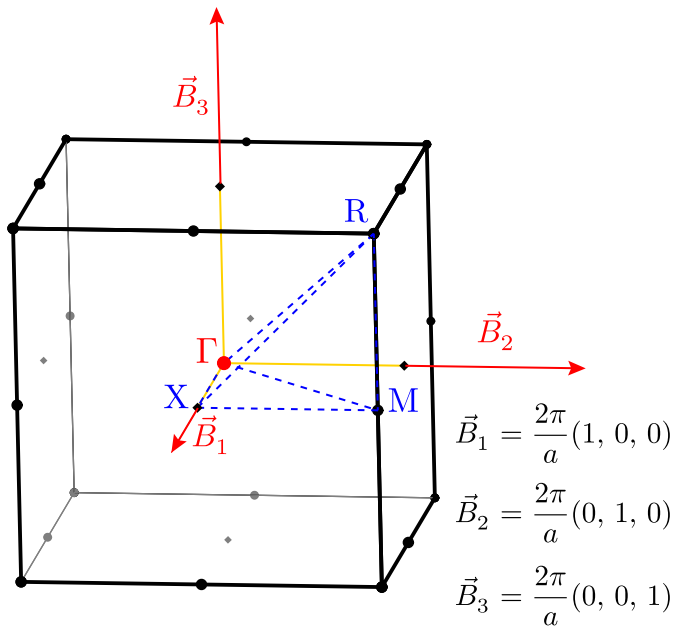


FIGURE B.4: Specific heat C_V for $\text{D0}_3 \text{Fe}_3\text{Al}$.

Appendix C

Special Points in the First Brillouin Zone

C.1 Simple Cubic (sc)



lattice vectors:

$$\vec{A}_1 = a(1, 0, 0)$$

$$\vec{A}_2 = a(0, 1, 0)$$

$$\vec{A}_3 = a(0, 0, 1)$$

high-symmetry points:

	direct	cartesian [$2\pi a^{-1}$]
Γ	(0, 0, 0)	(0, 0, 0)
X	($\frac{1}{2}$, 0, 0)	($\frac{1}{2}$, 0, 0)
M	($\frac{1}{2}$, $\frac{1}{2}$, 0)	($\frac{1}{2}$, $\frac{1}{2}$, 0)
R	($\frac{1}{2}$, $\frac{1}{2}$, $\frac{1}{2}$)	($\frac{1}{2}$, $\frac{1}{2}$, $\frac{1}{2}$)

high-symmetry paths (cartesian coordinates in units of $2\pi a^{-1}$):

Δ : $\Gamma \rightarrow X$ described by $[\xi 0 0]$ with $0 < \xi < 1/2$

Σ : $\Gamma \rightarrow M$ described by $[\xi \xi 0]$ with $0 < \xi < 1/2$

Λ : $\Gamma \rightarrow R$ described by $[\xi \xi \xi]$ with $0 < \xi < 1/2$

C.2 Body-Centred Cubic (bcc)

lattice vectors:

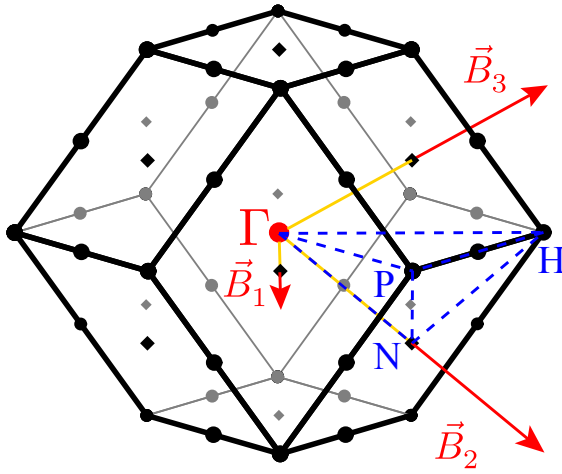
$$\vec{A}_1 = a \begin{pmatrix} -\frac{1}{2} & \frac{1}{2} & \frac{1}{2} \\ \frac{1}{2} & -\frac{1}{2} & \frac{1}{2} \\ \frac{1}{2} & \frac{1}{2} & -\frac{1}{2} \end{pmatrix}$$

$$\vec{A}_2 = a \begin{pmatrix} \frac{1}{2} & -\frac{1}{2} & \frac{1}{2} \\ \frac{1}{2} & \frac{1}{2} & -\frac{1}{2} \\ -\frac{1}{2} & \frac{1}{2} & \frac{1}{2} \end{pmatrix}$$

$$\vec{A}_3 = a \begin{pmatrix} \frac{1}{2} & \frac{1}{2} & -\frac{1}{2} \\ \frac{1}{2} & -\frac{1}{2} & \frac{1}{2} \\ -\frac{1}{2} & \frac{1}{2} & \frac{1}{2} \end{pmatrix}$$

high-symmetry points:

	direct	cartesian [$2\pi a^{-1}$]
Γ	(0, 0, 0)	(0, 0, 0)
N	(0, $\frac{1}{2}$, 0)	($\frac{1}{2}$, 0, $\frac{1}{2}$)
H	($-\frac{1}{2}$, $\frac{1}{2}$, $\frac{1}{2}$)	(1, 0, 0)
P	($\frac{1}{4}$, $\frac{1}{4}$, $\frac{1}{4}$)	($\frac{1}{2}$, $\frac{1}{2}$, $\frac{1}{2}$)



$$\vec{B}_1 = \frac{2\pi}{a} (0, 1, 1)$$

$$\vec{B}_2 = \frac{2\pi}{a} (1, 0, 1)$$

$$\vec{B}_3 = \frac{2\pi}{a} (1, 1, 0)$$

high-symmetry paths (cartesian coordinates in units of $2\pi a^{-1}$):

Δ : $\Gamma \rightarrow \text{H}$ described by $[\xi 0 0]$ with $0 < \xi < 1$

Σ : $\Gamma \rightarrow \text{N}$ described by $[\xi 0 \xi]$ with $0 < \xi < 1/2$

Λ : $\Gamma \rightarrow \text{P}$ described by $[\xi \xi \xi]$ with $0 < \xi < 1/2$

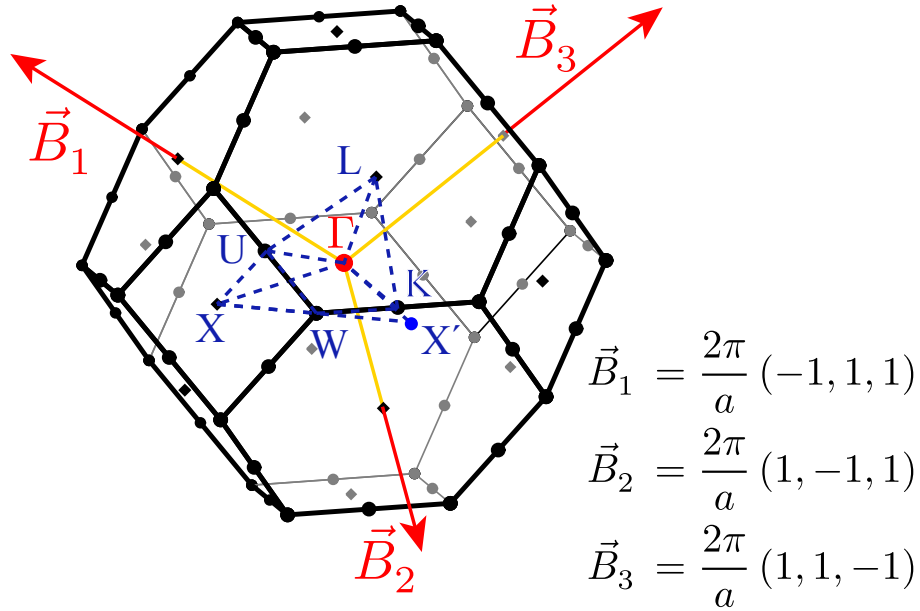
C.3 Face-Centred Cubic (fcc)

lattice vectors:

$$\begin{aligned}\vec{A}_1 &= a \left(0, \frac{1}{2}, \frac{1}{2} \right) \\ \vec{A}_2 &= a \left(\frac{1}{2}, 0, \frac{1}{2} \right) \\ \vec{A}_3 &= a \left(\frac{1}{2}, \frac{1}{2}, 0 \right)\end{aligned}$$

high-symmetry points:

	direct	cartesian [$2\pi a^{-1}$]
Γ	(0, 0, 0)	(0, 0, 0)
X	($\frac{1}{2}$, $\frac{1}{2}$, 0)	(0, 0, 1)
L	($\frac{1}{2}$, $\frac{1}{2}$, $\frac{1}{2}$)	($\frac{1}{2}$, $\frac{1}{2}$, $\frac{1}{2}$)
W	($\frac{1}{2}$, $\frac{3}{4}$, $\frac{1}{4}$)	($\frac{1}{2}$, 0, 1)
U	($\frac{5}{8}$, $\frac{5}{8}$, $\frac{1}{4}$)	($\frac{1}{4}$, $\frac{1}{4}$, 1)
K	($\frac{3}{8}$, $\frac{3}{4}$, $\frac{3}{8}$)	($\frac{3}{4}$, 0, $\frac{3}{4}$)
X'	($\frac{1}{2}$, 1, $\frac{1}{2}$)	(1, 0, 1)



high-symmetry paths (cartesian coordinates in units of $2\pi a^{-1}$):

Δ : $\Gamma \rightarrow X$ described by $[00\xi]$ with $0 < \xi < 1$

Σ, S' : $\Gamma \rightarrow K \rightarrow X'$ described by $[\xi 0 \xi]$ with $0 < \xi < 1$

Λ : $\Gamma \rightarrow L$ described by $[\xi \xi \xi]$ with $0 < \xi < 1/2$

C.4 Hexagonal and Hexagonal Close-Packed (hcp)

lattice vectors:

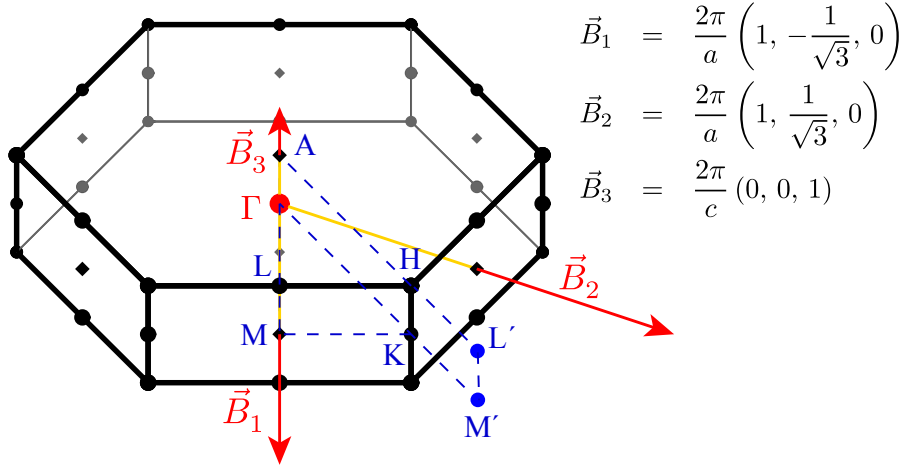
$$\vec{A}_1 = a \left(\frac{1}{2}, -\frac{1}{2}\sqrt{3}, 0 \right)$$

$$\vec{A}_2 = a \left(\frac{1}{2}, \frac{1}{2}\sqrt{3}, 0 \right)$$

$$\vec{A}_3 = c(0, 0, 1)$$

high-symmetry points:

	direct	cartesian
Γ	$(0, 0, 0)$	$(0, 0, 0)$
M	$(\frac{1}{2}, 0, 0)$	$(\frac{\pi}{a}, -\frac{\pi}{\sqrt{3}a}, 0)$
K	$(\frac{1}{3}, \frac{1}{3}, 0)$	$(\frac{4\pi}{3a}, 0, 0)$
M'	$(\frac{1}{2}, \frac{1}{2}, 0)$	$(\frac{2\pi}{a}, 0, 0)$
A	$(0, 0, \frac{1}{2})$	$(0, 0, \frac{\pi}{c})$
L	$(\frac{1}{2}, 0, \frac{1}{2})$	$(\frac{\pi}{a}, -\frac{\pi}{\sqrt{3}a}, \frac{\pi}{c})$
H	$(\frac{1}{3}, \frac{1}{3}, \frac{1}{2})$	$(\frac{4\pi}{3a}, 0, \frac{\pi}{c})$
L'	$(\frac{1}{2}, \frac{1}{2}, \frac{1}{2})$	$(\frac{2\pi}{a}, 0, \frac{\pi}{c})$



high-symmetry paths (cartesian coordinates):

$\Delta : \Gamma \rightarrow A$ described by $[00\xi]$ with $0 < \xi < \pi c^{-1}$

$\Sigma : \Gamma \rightarrow M$ described by $[\xi\sigma 0]$ with $0 < \xi < \pi a^{-1}$ and $0 > \sigma > -\pi(\sqrt{3}a)^{-1}$

$\Lambda, T : \Gamma \rightarrow K \rightarrow M'$ described by $[\xi 00]$ with $0 < \xi < 2\pi a^{-1}$

C.5 Simple Tetragonal (st)

lattice vectors:

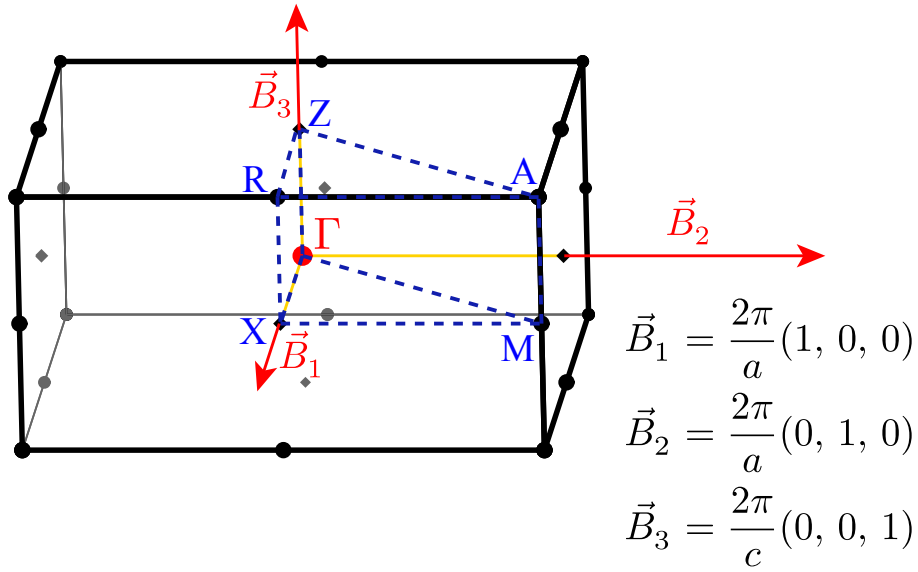
$$\vec{A}_1 = a(1, 0, 0)$$

$$\vec{A}_2 = a(0, 1, 0)$$

$$\vec{A}_3 = c(0, 0, 1)$$

high-symmetry points:

	direct	cartesian
Γ	$(0, 0, 0)$	$(0, 0, 0)$
X	$(\frac{1}{2}, 0, 0)$	$(\frac{\pi}{a}, 0, 0)$
M	$(\frac{1}{2}, \frac{1}{2}, 0)$	$(\frac{\pi}{a}, \frac{\pi}{a}, 0)$
Z	$(0, 0, \frac{1}{2})$	$(0, 0, \frac{\pi}{c})$
R	$(\frac{1}{2}, 0, \frac{1}{2})$	$(\frac{\pi}{a}, 0, \frac{\pi}{c})$
A	$(\frac{1}{2}, \frac{1}{2}, \frac{1}{2})$	$(\frac{\pi}{a}, \frac{\pi}{a}, \frac{\pi}{c})$



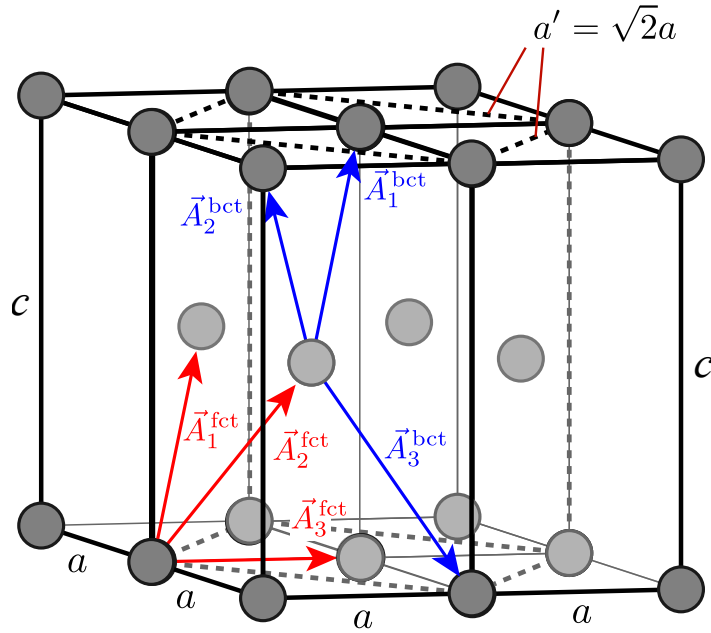
high-symmetry paths (cartesian coordinates):

$$\Delta : \Gamma \rightarrow X \quad \text{described by } [\xi 0 0] \text{ with } 0 < \xi < \pi a^{-1}$$

$$\Sigma : \Gamma \rightarrow M \quad \text{described by } [\xi \xi 0] \text{ with } 0 < \xi < \pi a^{-1}$$

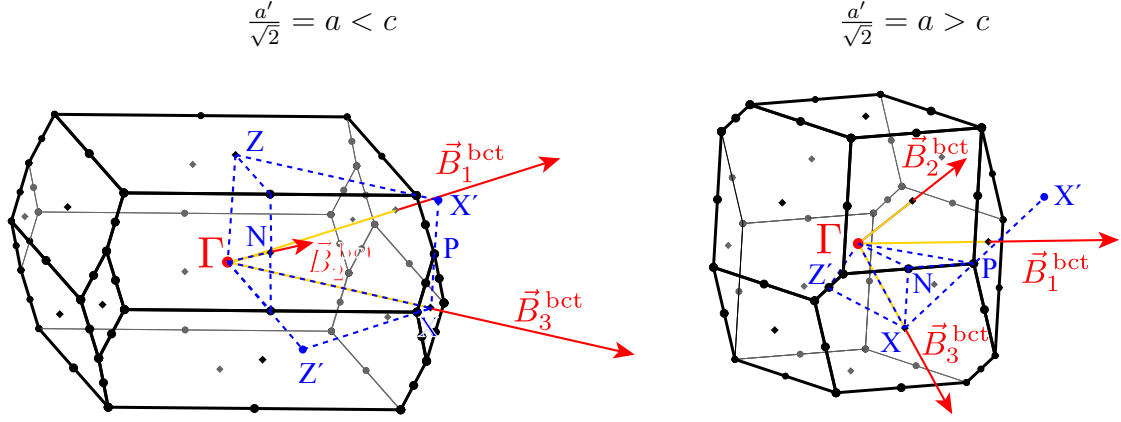
$$\Lambda : \Gamma \rightarrow Z \quad \text{described by } [0 0 \xi] \text{ with } 0 < \xi < \pi c^{-1}$$

C.6 Body-Centred Tetragonal (bct) and Face-Centred Tetragonal (fct)



$$\begin{aligned}
 \vec{A}_1^{\text{bct}} &= \frac{1}{2}(-a, a, c) & \vec{A}_1^{\text{fct}} &= \frac{1}{2}(0, a', c) \\
 \vec{A}_2^{\text{bct}} &= \frac{1}{2}(a, -a, c) & \vec{A}_2^{\text{fct}} &= \frac{1}{2}(a', 0, c) \\
 \vec{A}_3^{\text{bct}} &= \frac{1}{2}(a, a, -c) & \vec{A}_3^{\text{fct}} &= \frac{1}{2}(a', a', 0)
 \end{aligned}$$

The crystal structure can be described by both an bct or fct lattice. However, the coordinate system of the fct lattice is rotated by 45° around the z-axis and the lattice constant a is rescaled by $\sqrt{2}$.



C.6.1 Body-Centred Tetragonal (bct):

$$\vec{B}_1^{\text{bct}} = \left(0, \frac{2\pi}{a}, \frac{2\pi}{c}\right) \quad \vec{B}_2^{\text{bct}} = \left(\frac{2\pi}{a}, 0, \frac{2\pi}{c}\right) \quad \vec{B}_3^{\text{bct}} = \left(\frac{2\pi}{a}, \frac{2\pi}{a}, 0\right)$$

high-symmetry points:

	direct	cartesian
Γ	$(0, 0, 0)$	$(0, 0, 0)$
X	$(0, 0, \frac{1}{2})$	$(\frac{\pi}{a}, \frac{\pi}{a}, 0)$
P	$(\frac{1}{4}, \frac{1}{4}, \frac{1}{4})$	$(\frac{\pi}{a}, \frac{\pi}{a}, \frac{\pi}{c})$
N	$(0, \frac{1}{2}, 0)$	$(\frac{\pi}{a}, 0, \frac{\pi}{c})$
Z	$(\frac{1}{2}, \frac{1}{2}, -\frac{1}{2})$	$(0, 0, \frac{2\pi}{c})$
X'	$(\frac{1}{2}, \frac{1}{2}, 0)$	$(\frac{\pi}{a}, \frac{\pi}{a}, \frac{2\pi}{c})$
Z'	$(-\frac{1}{2}, \frac{1}{2}, \frac{1}{2})$	$(\frac{2\pi}{a}, 0, 0)$

high-symmetry paths

(cartesian coordinates):

$\Delta : \Gamma \rightarrow X$ described by $[\xi \xi 0]$ with $0 < \xi < \pi a^{-1}$

$\Sigma, (F'(a < c)) : \Gamma \rightarrow Z'$ described by $[\xi 0 0]$
with $0 < \xi < 2\pi a^{-1}$

$\Lambda, (V'(a > c)) : \Gamma \rightarrow Z$ described by $[0 0 \xi]$
with $0 < \xi < 2\pi c^{-1}$

C.6.2 Face-Centred Tetragonal (fct):

$$\vec{B}_1^{\text{fct}} = \left(-\frac{2\pi}{a'}, \frac{2\pi}{a'}, \frac{2\pi}{c}\right) \quad \vec{B}_2^{\text{fct}} = \left(\frac{2\pi}{a'}, -\frac{2\pi}{a'}, \frac{2\pi}{c}\right) \quad \vec{B}_3^{\text{fct}} = \left(\frac{2\pi}{a'}, \frac{2\pi}{a'}, -\frac{2\pi}{c}\right)$$

high-symmetry points:

	direct	cartesian
Γ	$(0, 0, 0)$	$(0, 0, 0)$
X	$(0, \frac{1}{2}, \frac{1}{2})$	$(\frac{2\pi}{a'}, 0, 0)$
P	$(\frac{1}{4}, \frac{3}{4}, \frac{1}{2})$	$(\frac{2\pi}{a'}, 0, \frac{\pi}{c})$
N	$(0, \frac{1}{2}, 0)$	$(\frac{2\pi}{a'}, -\frac{2\pi}{a'}, \frac{2\pi}{c})$
Z	$(\frac{1}{2}, \frac{1}{2}, 0)$	$(0, 0, \frac{2\pi}{c})$
X'	$(\frac{1}{2}, 1, \frac{1}{2})$	$(\frac{2\pi}{2a'}, 0, \frac{2\pi}{c})$
Z'	$(-\frac{1}{2}, \frac{1}{2}, 0)$	$(\frac{2\pi}{a'}, -\frac{2\pi}{a'}, 0)$

high-symmetry paths

(cartesian coordinates):

$\Delta : \Gamma \rightarrow X$ described by $[\xi 0 0]$ with $0 < \xi < 2\pi a'^{-1}$

$\Sigma, (F'(\frac{a'}{\sqrt{2}} < c)) : \Gamma \rightarrow Z'$ described by $[\xi -\xi 0]$
with $0 < \xi < 2\pi a'^{-1}$

$\Lambda, (V'(\frac{a'}{\sqrt{2}} > c)) : \Gamma \rightarrow Z$ described by $[0 0 \xi]$
with $0 < \xi < 2\pi c^{-1}$

Bibliography

- [1] G. Kresse, J. Furthmüller, and J. Hafner, *Europhysics Letters* **32**, 729 (1995).
- [2] G. Kresse and J. Furthmüller, *Physical Review B* **54**, 11169 (1996).
- [3] G. Kern, G. Kresse, and J. Hafner, *Physical Review B* **59**, 8551 (1999).
- [4] G. Kresse and D. Joubert, *Physical Review B* **59**, 1758 (1999).
- [5] D. Alfè, *Computer Physics Communications* **180**, 2622 (2009).
- [6] D. Alfè (1998), the program is available at <http://chianti.geol.ucl.ac.uk/~dario>.
- [7] S. Müller, *Journal of physics: condensed matter* **15**, R1429R1500 (2003).
- [8] D. Lerch, O. Wieckhorst, G. Hart, R. Forcade, and S. Müller, *Modelling Simul. Mater. Sci. Eng.* **17**, 055003 (2009).
- [9] P. Hohenberg and W. Kohn, *Physical Review* **136**, B864 (1964).
- [10] W. Kohn and L. J. Sham, *Physical Review* **140**, A1133 (1965).
- [11] R. G. Parr and W. Yang, *Density-functional theory of atoms and molecules* (Oxford University Press, 1989).
- [12] J. P. Perdew, K. Burke, and M. Ernzerhof, *Phys. Rev. Lett.* **77**, 3865 (1996).
- [13] P. E. Blöchl, *Physical Review B* **50**, 1759317979 (1994).
- [14] G. Kresse, M. Marsman, and J. Furthmüller, *Vasp the guide*, this document can be retrieved from <http://cms.mpi.univie.ac.at/VASP/>.
- [15] N. W. Ashcroft and N. D. Mermin, *Festkörperphysik* (Oldenbourg Verlag München Wien, 2001), translation by Jochen Gress.
- [16] V. Pierron-Bohnes and T. Mehaddene, *Alloy Physics* (WILEY-VCH Verlag GmbH & Co. KGaA Weinheim, 2007).
- [17] E. Rebhan, *Theoretische Physik II* (Spektrum Akademischer Verlag München, 2005).

- [18] R. M. Martin, *Physical Review* **186**, 871 (1969).
- [19] J. C. Phillips, *Physical Review* **166**, 832 (1968).
- [20] S. Baroni, P. Giannozzi, and A. Testa, *Physical Review Letters* **58**, 1861 (1987).
- [21] R. D. King-Smith and R. J. Needs, *Journal Physical Condensed Matter* **2**, 3431 (1990).
- [22] X. Gonze, D. C. Allan, and M. Teter, *Physical Review Letters* **68**, 3603 (1992).
- [23] W. Frank, C. Elsässer, and M. Fähnle, *Physical Review Letters* **74**, 1791 (1995).
- [24] J. M. Thijssen, *Computational Physics second edition* (Cambridge University Press, 2007).
- [25] H. Bruus and K. Flensberg, *Many-Body Quantum Theory in Condensed Matter Physics, An Introduction* (Oxford University Press, 2010).
- [26] J. L. Warren, J. L. Yarnell, G. Dolling, and R. A. Cowley, *Physical Review* **158**, 805 (1967).
- [27] H. R. Schober and P. H. Dederichs, *The Landolt-Börnstein Database* (<http://www.springermaterials.com>), vol. 13a (SpringerMaterials, 1981), al.
- [28] P. Souvatzis, O. Eriksson, M. Katsnelson, and S. Rudin, *Computational Materials Science* **44**, 888 (2008).
- [29] R. M. Martin, *Electronic Structure* (Cambridge University Press, 2004).
- [30] L. K. Nash, *Elements of statistical thermodynamics* (Addison-Wesley Reading, Massachusetts, 1974).
- [31] F. Mandl, *Statistical Physics* (John Wiley & Sons Ltd. Chichester, 1977).
- [32] F. Gronvold, *Journal of Thermal Analysis* **13**, 419 (1978).
- [33] R. Kikuchi, *Physical Review* **81**, 988 (1951).
- [34] W. H. Press, B. P. Flannery, S. A. Teukolsky, and W. T. Vetterling, *Numerical Recipes: The Art of Scientific Computing* (Cambridge University Press, 2007).
- [35] B. Fultz and J. J. Hoyt, *Alloy Physics* (WILEY-VCH Verlag GmbH & Co. KGaA Weinheim, 2007).
- [36] D. Reith and R. Podloucky, *Physical Review B* **80**, 054108 (2009).
- [37] E. Ising, *Zeitschrift für Physik A Hadrons and Nuclei* **31**, 253 (1925).

-
- [38] C. Wolverton and D. de Fontaine, *Physical Review B* **49**, 8627 (1994).
- [39] J. Sanchez, F. Ducastelle, and D. Gratias, *Physica A* **128**, 334 (1984).
- [40] Z. W. Lu, S. H. Wei, A. Zunger, S. Frota-Pessoa, and L. G. Ferreira, *Physical Review B* **44**, 512 (1991).
- [41] C. Wolverton and A. Zunger, *Physical Review Letters* **75**, 3162 (1995).
- [42] J. M. Thijssen, *Computational Physics* (Cambridge University Press, 2007).
- [43] G. L. W. Hart, V. Blum, M. J. Walorski, and A. Zunger, *Nature Materials* **4**, 391 (2005).
- [44] K. Binder and D. W. Heermann, *Monte Carlo Simulation in Statistical Physics* (Springer Verlag Berlin Heidelberg, 2002).
- [45] N. Metropolis, A. W. Rosenbluth, M. N. Rosenbluth, and A. H. Teller, *The Journal of Chemical Physics* **21**, 1087 (1953).
- [46] F. F. Abraham, *Homogeneous nucleation theory* (Academic Press New York, 1974).
- [47] A. V. D. Walle and G. Ceder, *Rev. Mod. Phys.* **74**, 11 (2002).
- [48] K. Yuge, A. Seko, Y. Koyama, F. Oba, and I. Tanaka, *Physical Review B* **77**, 094121 (2008).
- [49] L. E. Toth, *Transition Metal Carbides and Nitrides. Refractory Materials Monographs.*, vol. 7 (Academic Press New York, 1971).
- [50] L. P. Gor'kov and E. I. Rashba, *Physical Review Letters* **87**, 037004 (2001).
- [51] M. Sigrist, D. Agterberg, P. Frigeri, N. Hayashi, R. Kaur, A. Koga, I. Milat, and K. W. Y. Yanase, *Journal of Magnetism and Magnetic Materials* **310**, 536 (2007).
- [52] E. Bauer, G. Hilscher, H. Michor, C. Paul, E. W. Scheidt, A. Griбанov, Y. Seropegin, H. Noël, M. Sigrist, and P. Rogl, *Physical Review Letters* **92**, 027003 (2004).
- [53] M. Marsman, W. Wolf, and R. Podloucky, private communication.
- [54] E. Bauer, R. T. Khan, H. Michor, E. Royanian, A. Grytsiv, N. Melnychenko-Koblyuk, P. Rogl, D. Reith, R. Podloucky, E.-W. Scheidt, et al., *Physical Review B* **80**, 064504 (2009).
- [55] E. Bauer, G. Rogl, X.-Q. Chen, R. T. Khan, H. Michor, G. Hilscher, E. Royanian, K. Kumagai, D. Z. Li, Y. Y. Li, et al., *Physical Review B* **82**, 064511 (2010).

- [56] H. Monkhorst and J. Pack, *Physical Review B* **13**, 5188 (1976).
- [57] P. E. Blöchl, O. Jepsen, and O. K. Andersen, *Physical Review B* **49**, 16223 (1994).
- [58] M. Methfessel and A. T. Paxton, *Physical Review B* **40**, 3616 (1989).
- [59] W. H. McMaster, K. K. D. Grande, J. H. Mallett, and J. H. Hubbell, *Lawrence Livermore National Laboratory Report* (available from <http://cars9.uchicago.edu/newville/mcbook/mcbook-l.pdf>, 1969).
- [60] K. Osamura, H. Okuda, S. Ochiai, M. Takashima, K. Asano, M. Furusaka, K. Kishida, and F. Kurosawa, *ISIJ International* **34**, 359 (1994).
- [61] W. Oswald, *Lehrbuch der Allgemeinen Chemie*, vol. 2 (Wilhelm Engelmann Leipzig, 1896).
- [62] P. Franke and D. Neuschütz, *Cu-Fe*, vol. IV/19B3 of *Landolt-Börnstein New Series* (Springer Verlag, Berlin, 1994).
- [63] J. Z. Liu, A. van de Walle, G. Ghosh, and M. Asta, *Physical Review B* **72**, 144109 (2005).
- [64] C. Domain and C. S. Becquart, *Physical Review B* **65**, 024103 (2001).
- [65] M. Weinert, E. Wimmer, and A. J. Freeman, *Physical Review B* **26**, 4571 (1982).
- [66] M. Weinert, G. Schneider, R. Podloucky, and J. Redinger, *J. Phys.: Condens. Matter* **21**, 084201 (2009), <http://www.uwm.edu/~weinert/flair.html>.
- [67] J. P. Perdew and Y. Wang, *Physical Review B* **45**, 13244 (1992).
- [68] *Landolt – Börnstein New Series*, vol. III/6, III/19c and III/29a (Springer Verlag, 1994).
- [69] C. V. Dijk and J. Bergsma, *Neutron Inelastic Scattering*, vol. 1 (IAEA Vienna, 1968).
- [70] H. Hasegawa, M. W. Finnis, and D. G. Pettifor, *Journal of Physics F: Metal Physics* **17**, 2049 (1987).
- [71] J. A. Rayne and B. S. Chandrasekhar, *Physical Review* **122**, 1715 (1961).
- [72] D. J. Dever, *Journal of Applied Physics* **43**, 3293 (1972).
- [73] S. K. Satija, R. P. Comes, and G. Shirane, *Physical Review B* **32**, 3309 (1985).
- [74] R. M. Nicklow, G. Gilat, H. G. Smith, L. J. Raubenheimer, and M. K. Wilkinson, *Physical Review* **164**, 922 (1967).

-
- [75] J. Xie, S. de Gironcoli, S. Baroni, and M. Scheffler, *Physical Review B* **59**, 965 (1999).
- [76] S. Biernacki and M. Scheffler, *Physical Review Letters* **63**, 290 (1989).
- [77] A. Quong and A. Liu, *Physical Review B* **56**, 7767 (1997).
- [78] S. Narasimhan and S. de Gironcoli, *Physical Review B* **65**, 064302 (2002).
- [79] N. Ridley and H. Stuart, *Journal of Physics D Applied Physics* **1**, 1291 (1968).
- [80] *American Institute of Physics Handbook*, vol. 3rd ed. (McGraw-Hill New York, 1982).
- [81] S. Baroni, A. D. Corso, S. de Gironcoli, and P. Giannozzi, *Quantum espresso*, the program is available at <http://www.pwscf.org>.
- [82] S. Baroni, P. Giannozzi, and A. Testa, *Physical Review Letters* **58**, 1862 (1987).
- [83] S. Baroni, S. de Gironcoli, A. D. Corso, and P. Giannozzi, *Reviews of Modern Physics* **73**, 515 (2001).
- [84] C. Colinet, W. Wolf, R. Podloucky, and A. Pasturel, *Applied Physics Letters* **87**, 041910 (2005).
- [85] X.-Q. Chen, W. Wolf, R. Podloucky, and P. Rogl, *Physical Review B* **76**, 014424 (2007).
- [86] X.-Q. Chen, W. Wolf, R. Podloucky, and P. Rogl, *Physical Review B* **76**, 092102 (2007).
- [87] E. Moroni, G. Kresse, and J. Hafner, *Physical Review B* **56**, 15629 (1997).
- [88] M. Schober, E. Eidenberger, H. Leitner, P. Staron, D. Reith, and R. Podloucky, *Applied Physics A* **99**, 697704 (2010).
- [89] C. P. Flynn, *Point Defects and Diffusion* (Clarendon Press, Oxford, 1972).
- [90] U. Burghaus, *A practical guide to kinetic Monte Carlo simulations and classical molecular dynamics simulations: an example book* (Nova Science Publishers, 2006).
- [91] K. Yuge, A. Seko, I. Tanaka, and S. R. Nishitani, *Physical Review B* **72**, 174201 (2005).
- [92] P. Atkins and J. de Paula, *Atkins' Physical Chemistry 8. edition* (Oxford University Press, 2006).
- [93] M. Hieckel, Master's thesis, Friedrich-Schiller-Universität Jena, Germany (2011).
- [94] K. Parlinski, Z. Li, and Y. Kawazoe, *Physical Review Letters* **81**, 3298 (1998), reply.

List of Publications

- 2011 K. Miliyanchuk, F. Kneidinger, C. Blaas-Schenner, D. Reith, R. Podloucky, P. Rogl, T. Khan, L. Salamakha, G. Hilscher, H. Michor, E. Bauer and A. D. Hillier, *Platinum metal silicides and germanides: superconductivity in non-centrosymmetric intermetallics*, Journal of Physics: Conference Series **273**, 012078 (2011)
- 2011 P. Warczok, D. Reith, M. Schober, H. Leitner, R. Podloucky, E. Kozeschnik *Investigation of Cu precipitation in bcc-Fe - Comparison of numerical analyses with experiment*, International Journal of Materials Research **06/2011**, 709-716 (2011)
- 2010 M. Schober, E. Eidenberger, H. Leitner, P. Staron, D. Reith and R. Podloucky, *A critical consideration of magnetism and composition of (bcc) Cu precipitates in (bcc) Fe*, Appl. Phys. A **99**, 697704 (2010)
- 2009 E. Bauer, R. T. Khan, H. Michor, E. Royanian, A. Grytsiv, N. Melnychenko-Koblyuk, P. Rogl, D. Reith, R. Podloucky, E.-W. Scheidt, W. Wolf and M. Marsman, *BaPtSi₃: A noncentrosymmetric BCS-like superconductor*, Physical Review B **80**, 064504 (2009)
- 2009 D. Reith and R. Podloucky, *First-principles model study of phase stabilities of dilute Fe-Cu alloys: Role of vibrational free energy*, Physical Review B **80**, 054108 (2009)
- 2005 D. Reith, W. Püschl, W. Pfeiler, F. Haider and W. A. Soffa, *Phase Transformations in Inorganic Solids*, PTM 2005, The Minerals, Metals and Material Society, Warrendale, PA, p. 765 (2005)

to be submitted:

- D. Reith, M. Stöhr, T. Kerscher and R. Podloucky, *Concentration and temperature dependent first-principles modelling of $Fe_{1-x}Cu_x$ alloys.*
- D. Reith, C. Blaas-Schrenner and R. Podloucky, *First-principle study of thermodynamic and vibrational stabilities of $Mo_3Al_2C_{1-x}$ in its corresponding electronic structure.*
- M. Hieckel, G. Kastlunger, D. Reith, M. Leitner and R. Podloucky, *First-principles study of the solubility of Cu in Fe by isolated defects including thermal expansion and vibrational properties.*
- D. Reith, G. Kastlunger, M. Leitner, R. Podloucky, and G. Kresse, *First-principles study of the phase stabilities of FeAl and Fe_3Al compounds.*
- D. Reith and R. Podloucky, *A generalized entropy model for non-interacting defect clusters on a crystal lattice.*
- M. Hieckel, D. Reith, C. Blaas-Schrenner, C. Franchini, R. Podloucky and F. Bechstedt, *Post-DFT study of the LO-TO phonon mode splitting in MnO and NiO.*
- T. Ali, S. Manalo, H. Michor, C. Ritter, D. Reith and R. Podloucky, *Nitrogen vacancies in superconducting $La_3Ni_2B_2N_{3-\delta}$: effects on structural and electronic properties*

Talks and Conference Contributions

- 03/2011 *Deutsche Physikalische Gesellschaft, Frühjahrstagung*
Dresden, Germany, D. Reith, M. Stöhr and R. Podloucky, *Extending the Cluster Expansion by Vibrational Free Energies Cluster Expansion (CE): basic concept*
- 10/2010 *VICOM Workshop*
Stadt Schlaining, Burgenland, Austria, D. Reith and R. Podloucky, *Multi-scale simulations of multi-component phases*
- 12/2008 *Intermetallics Workshop*
Vienna, Austria, D. Reith and R. Podloucky, *Ab initio modelling of Fe-rich Fe-Cu alloys*
- 03/2008 *American Physical Society, March Meeting*
New Orleans, USA, D. Reith and R. Podloucky, *Ab initio study of Fe-rich Fe-Cu alloys*
- 03/2006 *Deutsche Physikalische Gesellschaft, Frühjahrstagung*
Dresden, Germany, D. Reith, W. Püschl, W. Pfeiler und F. Haider, *The influence of vacancy movement on the character of phase transformations*
- 03/2005 *Deutsche Physikalische Gesellschaft, Frühjahrstagung*
Berlin, Germany, D. Reith, W. Püschl, W. Pfeiler und F. Haider, *Leerstellenpfad und Ordnungskinetik*

Curriculum Vitae

Personal Data

Name	Mag. David Reith
Date of birth	24.10.1979
Place of birth	Vienna, Austria
Marital status	married

Studies

since 10/2006	Universität Wien, Vienna, Austria Doctoral student at the Department of Physical Chemistry Thesis on ‘Towards first principle material design: The role of lattice vibrations’, supervisor Ao. Univ.-Prof. tit. Univ.-Prof. Dr. Raimund Podloucky.
03/1999 – 01/2006	Universität Wien, Vienna, Austria Degree in Physics Diploma thesis on ‘Lokalisierte Ordnungsumwandlung durch eingeschränkte Leerstellenbeweglichkeit – eine Monte Carlo Studie’ at the Institut für Materialwissenschaft, supervisor Ao. Univ.-Prof. Dr. Wolfgang Püschl.

Education

08/1993 – 11/1998	Deutsche Schule Kapstadt (DSK), Capetown, South Africa
1990 – 1993	Deutsche Schule Pretoria (DSP), Pretoria, South Africa
1989 – 1990	Josef Krainer Volksschule, Donnersbach, Austria
1987 – 1989	Deutsche Internationale Schule (DIS), Jakarta, Indonesia
1986 – 1987	Deutsche Schule Neu Delhi, New Delhi, India